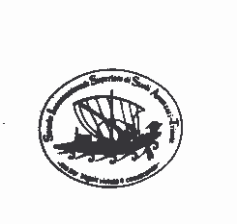

ISAS - INTERNATIONAL SCHOOL FOR ADVANCED STUDIES

GENERAL RELATIVISTIC HYDRODYNAMICS OF COMPRESSIBLE MULTICOMPONENT FLUIDS: DEVELOPMENTS AND APPLICATIONS

A Thesis submitted for the degree of
Doctor Philosophiae

SISSA - International School for Advanced Studies

Astrophysics Sector

Candidate:

Luciano Rezzolla

Supervisor:

John C. Miller

Academic Year 1995—1996

Contents

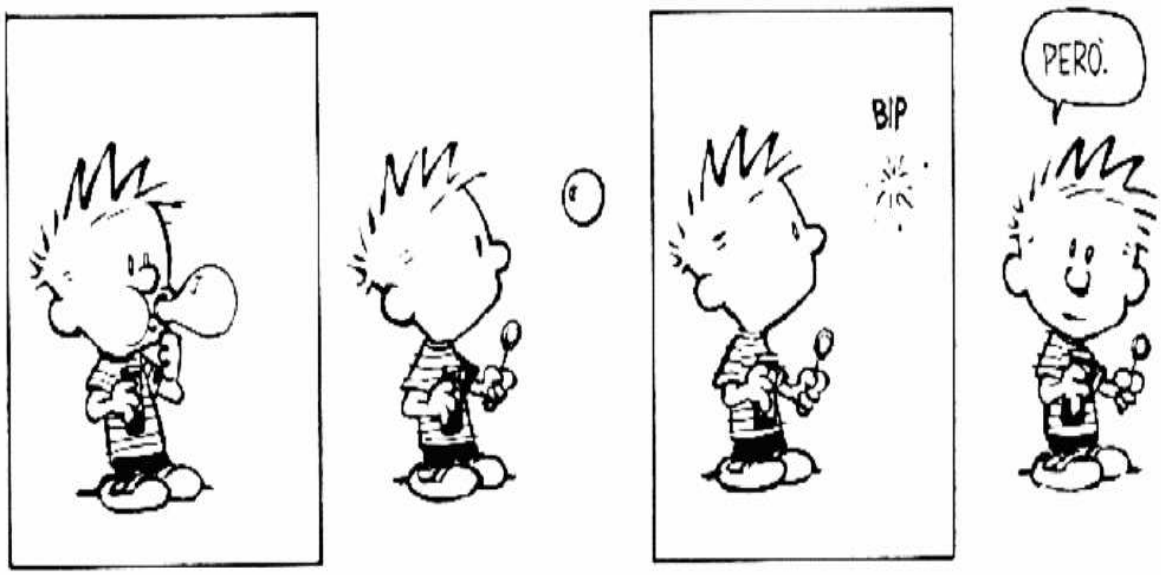
BIP
PERÒ.

Ringraziamenti

Questa Tesi è essenzialmente il frutto degli sforzi congiunti di due gruppi di persone che mi hanno dato l'entusiasmo e la forza di completare questo lavoro.

Tra le persone del primo gruppo, i miei sinceri ringraziamenti vanno al mio relatore ed amico John Miller che durante questi anni mi ha fornito della sua attenta e calma guida e del cui intuito fisico ho sempre beneficiato. È inoltre un piacere ringraziare i miei colleghi ed amici qui alla SISSA ed, in particolare, vorrei esprimere i miei ringraziamenti a Dennis Sciama per il suo caldo supporto ed incoraggiamento, a Pablo-Paul Haines, Antonio Lanza, Ornella Pantano ed a Marek Abramowicz che ha letto attentamente il Capitolo 7.

Il secondo gruppo di persone è composto da non-scienziati, i quali molto probabilmente non leggeranno mai questo lavoro al quale hanno così tanto contribuito. Prima tra tutte, devo esprimere la mia più profonda gratitudine alla mia amante, amica e moglie Carolin, che ha condiviso con me le gioie e le pene di questi anni (e che, in verità, ha letto e corretto questa Tesi !). Voglio anche ringraziare i miei genitori Emilia e Domenico per la libertà di pensiero nella quale mi hanno allevato e le mie sorelle Lucia e Loredana, per la loro pazienza ed amore. Alla fine ma non ultima, vorrei ringraziare tutte la "brava gente" e gli amici che ho incontrato a Trieste e nella mia città d'origine Bari. Tra queste vi è la mia compagna di vela Fabia che ha conservato la mia sanità mentale e mi ha insegnato che i buoni marinai non sono necessariamente uomini.

Acknowledgments

This Thesis is essentially the result of the joint efforts of two groups of people who have given me the enthusiasm and the strength to complete this work.

Among people in the first group, my sincere thanks are due to my supervisor and friend John Miller who has given me his careful and calm guidance during these years and whose physical insight I have always benefitted from. It is also a pleasure to thank my colleagues and friends here at SISSA and, in particular, I would like to express my thanks to Dennis Sciama for his warm support and encouragement, to Pablo-Paul Haines, Antonio Lanza, Ornella Pantano and Marek Abramowicz, who carefully read Chapter 7.

The second group of people is composed of non-scientists, who probably will never read this work to which they contributed so much. First among them, I need to express my deepest gratitude to my lover, friend and wife Carolin who has shared with me the happiness and the hard times of these years (and who, indeed, has read and corrected this Thesis !). I also want to thank my parents Emilia and Domenico for the freedom of thought in which they have educated me and my sisters Lucia and Loredana for their patience and care. Last but not least, I would like to thank all of the "good people" and friends I have met in Trieste and in Bari, my hometown. Among them is my sailing partner Fabia, who kept me mentally sane and taught me that good sailors are not necessarily men.

Overview

Relativistic hydrodynamics represents one of the most powerful tools by means of which it is possible to unveil the physical mechanisms behind the past history of our Universe and behind many of the high energy astrophysics phenomena observed nowadays. This Thesis is focussed on the formalism and techniques of relativistic hydrodynamics of compressible single and multicomponent fluids both in the case when they are considered as ideal gases and when viscous effects are not neglected.

The work contained here has a two-fold aspect and the layout of the Thesis is organized so as to reflect this double structure. *General results* that we have derived from investigations on the theoretical framework of relativistic hydrodynamics of discontinuous flows, have then been implemented for *specific* cosmological and astrophysical *applications* to the study of the hydrodynamics of the cosmological quark–hadron phase transition and the definition of a new set of relativistic non-stationary hydrodynamical equations for an accreting slim disk model. As a result, while Chapters 1, 2 and 3 are focussed on the analysis of general topics of relativistic hydrodynamics of compressible fluids, Chapters 4, 5 and 6 deal with the more specific study of relativistic hydrodynamics of a first order cosmological quark–hadron phase transition and benefit from the general tools and mathematical techniques introduced and discussed in the previous chapters. Chapter 7 presents an application of relativistic hydrodynamics to another astrophysical problem: that of slim disk accretion.

Chapter 1 is partly devoted to a general introduction to relativistic shock fronts and reaction fronts (Sections 1.1–1.2.2) and partly devoted to the very important subject of *hydrodynamic stability* of discontinuity surfaces (Sections 1.3–1.3.3). There, we discuss the delicate problem of the causal structure and determinacy of relativistic detonations and deflagrations and show, after rather lengthy algebra, the linear stability properties of relativistic detonations and deflagrations. The importance of our calculations should

be considered in view of some recent less rigorous stability analysis of cosmological detonations appeared in the literature and whose results we have here corrected. We warn the reader that Subsections 1.3.2 and 1.3.3 are heavily technical and the details in them could be skipped without serious consequences for understanding the rest of the Thesis.

Chapter 2 is dedicated to a general discussion of self similar solutions for spherical deflagrations. There, we first introduce the importance of spherical self similar solutions for the dynamics of "bubbles" and "drops" during cosmological first order phase transitions and subsequently derive analytic similarity solutions for bubble growth and drop evaporation. The latter, in particular, are original and some aspects of them are presented in this Thesis for the first time. Apart from the importance related to the generality of the assumptions under which they are derived, the concepts and solutions of this chapter will be encountered in Chapter 6 during the presentation of numerical computations of hadron bubble growth and quark drop evaporation.

In Chapter 3 we introduce the concepts of multicomponent hydrodynamics and concentrate, in particular, on the problem of the long range energy and momentum transfer between a standard fluid (meant as a collection of relativistic particles with short interaction scale length) and a radiation fluid (meant as a collection of relativistic particles with much longer interaction scale length). This is a relativistic radiative transfer problem that we here solve by rewriting the radiative transfer equation in terms of Projected Symmetric Trace Free tensors. The mathematical apparatus developed in this chapter is general and while it is implemented here for numerical computations of the quark–hadron transition, other applications of it in astrophysical contexts have been produced by other authors.

Chapter 4 starts the part of this Thesis which is dedicated to the application of the theoretical tools developed in the previous chapters to the specific study of the hydrodynamics of the cosmological quark–hadron phase transition. In this chapter, therefore, we discuss a number of different issues regarding the physics of cosmological phase transitions and aimed at providing the necessary physical background for the study of the quark–hadron transition. Apart from a general introduction to the thermodynamics of first order phase transitions, we discuss arguments in support of the hypothesis that the phase interface should move as a weak deflagration front and present suitable equations of state for the quark-gluon plasma and the hadron plasma. We conclude the chapter with a discussion of the debated and fundamental issue of bubble nucleation and present

a schematic description of the various stages of the transition.

Chapter 5 is entirely focussed on the hydrodynamics of the quark–hadron transition and is dedicated to the derivation of a new complete set of relativistic equations describing the hydrodynamics of a multicomponent fluid in a spherical flow. In particular, the mathematical apparatus developed in this chapter allows for a consistent treatment of: *a)* the long range energy and momentum transfer between a standard fluid and a radiation fluid; *b)* the dynamics of a superposed fluid component of baryon number carriers which is collisionless and subject to diffusion only; *c)* the dynamics of a discontinuity surface moving as a weak deflagration front; *d)* general relativistic junction conditions across the discontinuity surface for the metric, the energy and the momentum of each of the three fluid components; *e)* a characteristic form of the relevant hydrodynamical equations along the several different characteristic directions present. As a result, Chapter 5 embodies all of the concepts and tools presented in this Thesis, which will find a concrete application in the numerical computations discussed in the subsequent chapter.

In Chapter 6, in fact, after a brief discussion of the numerical strategies that have been introduced in order to solve the hydrodynamical equations, we present results obtained from hydrodynamical calculations of different stages of the cosmological quark–hadron phase transition. In particular, four distinct numerical codes have been constructed and implemented for studying respectively : *i*) bubble dynamics and long range energy and momentum transfer during the growth of an isolated spherical hadron bubble; *ii*) the evaporation of a quark drop at the end of the transition and the stability of the analytic solution for a self similar evaporating system; *iii*) drop dynamics and radiation decoupling during the final stages of the evaporation of a cosmological quark drop; *iv*) baryon number segregation produced during the very final stages of the transition by evaporating quark drops. These numerical computations cover a wide range of the different stages of the transition and provide a new consistent and sometimes unexpected picture of the physical properties of hadron bubble growth and quark drop evaporation. Apart from the intrinsic interest of knowing how the transition might have proceeded, the results of our computations have also a cosmological significance and the role played by the inhomogeneities produced at the end of the transition for the subsequent nucleosynthesis is also discussed in this chapter.

Finally, Chapter 7 marks the end of the Thesis and represents a "*variazione sul tema*" of relativistic hydrodynamics. There, we discuss the problem of relativistic viscous

flows in the different physical and geometrical scenario of axisymmetric slim disk accretion onto a rotating black-hole. In particular, we extend previous Newtonian and relativistic slim disk models and derive an original set of non-stationary relativistic hydrodynamical equations for this problem. This new set of equations, which could unveil many of the properties of slim disk models when implemented in a numerical computation, could also set the basis for a more realistic study of relativistic magnetohydrodynamic flows onto black-holes, behind which most probably lie the physical mechanisms for the formation of the extragalactic jets.

Symbols and Conventions

In view of our application to a problem involving input from particle physics, we use in the first six chapters of this Thesis a system of units in which $c = \hbar = k_{_B} = 1$. This also has the advantage that the gravitational source terms are clearly identified because of retention of the constant G in the equations. Chapter 7, on the other hand, is related to a relativistic astrophysical problem and there we use units in which $c = G = 1$. We use a space-like signature $(-, +, +, +)$. Greek indices are taken to run from 0 to 3 and Latin indices from 1 to 3. Covariant derivatives in the four-dimensional spacetime are denoted with a semicolon ";", while covariant derivatives on space-like three-dimensional hypersurfaces are denoted with "$\|$". Partial derivatives are either indicated with a comma or with the standard "∂" notation.

All of the figures in this Thesis (with the only exception of Figure 4.2) are original and either extracted from papers published by the author or presented here for the first time.

Chapter 1

Relativistic Shock Waves and Reaction Fronts

1.1 Introduction to Discontinuity Surfaces

The concept of *discontinuity surfaces* appears naturally within the framework of compressible fluids hydrodynamics and expresses the fact that the quantities describing a compressible fluid (*i.e.* velocity, temperature, pressure, density) do not need to be continuous everywhere in the flow when viewed on a suitably large scale. We here refer to as a *fluid* a continuum collection of particles so numerous that the dynamics of individual particles cannot be followed. However, this continuum can be described in terms of quantities averaged over representative *"elements"* of the continuum which are large enough so as to contain a relevant number of particles and small enough so as to guarantee homogeneity within the element[1].

We should underline that the concept of "discontinuity" both in the mathematical and in the pictorial representation of this type of phenomena is an just artifact of the scale of the fluid description. From a microscopical point of view, the relevant physical variables across these discontinuity surfaces are certainly continuous although they experience very large gradients over extremely short length scales. Within these regions, they are subject to complex irreversible thermodynamical processes caused by dissipation and heat conduction. However, outside those regions, the flow is much more regular and is usually governed by the standard laws of adiabatic reversible hydrodynamics.

This fortunate circumstance allows then the introduction of fictitious infinitesimal surfaces across which the fluid variables are assumed to be discontinuous (*i.e.* the dis-

[1]Note that the above definition effectively refers to a *simple fluid*, *i.e.* to a collection of identical particles or of particles of the same species. Such a definition can be extended if the fluid is composed of particles of different species (Section 3.1).

continuity surfaces). As a result, the mathematical description of these phenomena is greatly simplified and the overall approximation of this approach is extremely good when the shock front has a constant width which is much smaller than the typical length scale for the variation of the flow variables and when the thermal and the viscous time scales are much smaller than the one set by the motion of the front. In general, discontinuity surfaces can be distinguished in *contact surfaces*, which are surfaces separating two parts of a medium without any fluid flow through the surface, and in *shock fronts* and *reaction fronts*[2] which are discontinuity surfaces that are crossed by a fluid flow.

A consistent hydrodynamical description of the flow changes across a shock or reaction front can be performed after imposing the conservation of baryon number, energy and momentum across the front, or equivalently, after requiring that "what goes into the shock front must come out". The above conditions are often called *jump* or *junction conditions* and allow to express quantities on one side of the shock front in terms of the same quantities on the other side. The general relativistic treatment of the junction conditions across a discontinuity surface needs particular care in the case of a phase interface which has intrinsic physical properties (*e.g.* surface energy density or surface tension). In this case, the shock front can no longer be considered as a fictitious mathematical surface and its influence on the local curvature of spacetime needs to be taken into account. Subsection 5.2.2 discusses how this can be done by using the Gauss-Codazzi equations.

In the following we review the main aspects of the relativistic theory of hydrodynamical shocks which was first developed by Taub [159] and then subsequently extended by Lichnerowicz [93, 94, 95]. Most of the arguments discussed here will be used in the next section, in which the properties of reaction fronts are presented.

It is important to stress that the standard analysis of relativistic shocks with no intrinsic physical properties is valid in curved spacetimes as well as flat. Indeed, this is the case for any theory with a metric in whose local Lorentz frames the nongravitational laws of physics assume their standard special relativistic form (equivalence principle, Thorne [163], Steinhardt [153]). This is equivalent to saying that in a curved spacetime one can choose an event $\mathcal{P}$ on the shock front worldline and then introduce in its neighbourhood a local Lorentz frame (the rest frame of the shock). This frame can always be chosen so that *i)* the shock is momentarily at rest, *ii)* there are no three-velocity components tangent to the front (hereafter we shall refer to the three-velocity vectors simply as velocities) and *iii)* the shock is taken to be at rest on the (y, z) plane.

---

[2] A comment on terminology is needed. Here we follow the convention of Courant and Friedrichs and denote with "shock wave" the flow region comprising the discontinuity surface (which we also refer to as "front") and its downstream flow. A similar convention will be assumed with the terms "compression wave" and "rarefaction wave". Other authors, however, (*e.g.* Landau and Lifshitz) call "shock wave" the discontinuity surface itself, so that "wave" and "front" become equivalent terms for them.

In this comoving reference frame, we can think of the front as a planar discontinuity surface which divides the three-space into a region 1 and a region 2 and which is crossed by positive velocities from left to right when the front is left propagating in the inertial frame (see Figure 1.1). This allows then to define as *ahead* or *upstream* or *"1"* the region from which the fluid moves to reach the shock front and as *behind* or *downstream* or *"2"* the region in which the fluid moves after having passed across the shock.

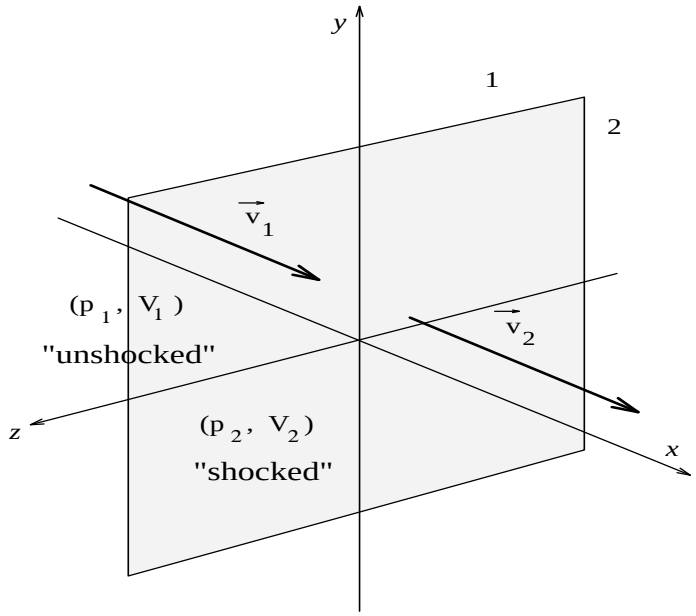

Figure 1.1 Spatial configuration of a left propagating shock wave

Consider now the fluids on either side of the front to be ideal and described by the standard stress energy tensor of a relativistic perfect fluid

$$T^{\alpha\beta} = (e+p)u^{\alpha}u^{\beta} + pg^{\alpha\beta} \ , \tag{1.1}$$

where $u^{\alpha} \equiv \gamma(1,\ \vec{v})$ is the fluid four-velocity and $\gamma = (1 - v^i\, v^j\, \delta_{ij})^{-1/2}$, with $v^i = dx^i/dt$. Here e is the energy density, p is the pressure and $g^{\alpha\beta}$ is the metric tensor. Referring to the shock configuration shown in Figure 1.1 and using the stress energy tensor (1.1), we can express the laws of conservation of energy and momentum respectively as

$$T_1^{0\ x} = T_2^{0\ x} \ , \qquad\qquad T_1^{x\ x} = T_2^{x\ x} \ , \tag{1.2}$$

with the lower indices indicating quantities on the two sides of the shock. Equations (1.2) need to be supplemented with the continuity equation of baryon number density

$$(nu^{\alpha})_{;\,\alpha} = 0 \ , \tag{1.3}$$

where n is the number density of baryons. Defining the enthalpy density on either side of the front as $w_k = e_k + p_k$, (with $k = 1,\ 2$), we can write the following junction conditions across a relativistic shock[3] (see Subsection 5.2.2 for the general relativistic form of the junction conditions).

$$w_1\gamma_1^2 v_1 = w_2\gamma_2^2 v_2 \ , \tag{1.4}$$

$$w_1\gamma_1^2 v_1^2 + p_1 = w_2\gamma_2^2 v_2^2 + p_2 \ , \tag{1.5}$$

$$j \equiv n_1\gamma_1 v_1 = n_2\gamma_2 v_2 \ . \tag{1.6}$$

Besides equations (1.4)–(1.6), a further condition is needed in order to eliminate unphysical solutions and this condition is strictly related to the complex irreversible processes that take place in the small region of the shock front and basically excludes as physically realistic those shocks which do not produce an entropy increase. In other words, the values of the specific entropy on either side of a physical shock have to satisfy the inequality

$$s_2 > s_1 \tag{1.7}$$

where $s_{1,\,2}$ is the specific entropy on either side of the front.

It is now convenient to introduce the chemical potentials on either side of the front $\mu_k = (\partial e_k/\partial n_k)_s = [(e+p)/n]_k$ and rewrite the conservation of momentum (1.5) and the continuity equation (1.6) as the single expression

$$j^2 = -\frac{p_2 - p_1}{\mu_2 V_2 - \mu_1 V_1} \ , \tag{1.8}$$

where $V_k = 1/n_k$ are the specific volumes on either side of the front. Similarly, by using the continuity equation (1.6), we can rewrite the conservation of energy (1.4) as

$$\mu_1\gamma_1 = \mu_2\gamma_2 \ . \tag{1.9}$$

[3]Unless specified, all the velocities are meant to be referred to the front rest frame.

Multiplying (1.8) by $(\mu_1 V_1 + \mu_2 V_2)$, and combining it with the new form of the continuity equations

$$\gamma_1 v_1 = jV_1 \ , \qquad\qquad \gamma_2 v_2 = jV_2 \ , \tag{1.10}$$

we obtain

$$(\mu_2 \gamma_2 v_2)^2 - (\mu_1 \gamma_1 v_1)^2 = (p_1 - p_2)(\mu_1 V_1 + \mu_2 V_2) \ . \tag{1.11}$$

Subtracting then (1.9) from (1.11) we finally obtain the equation for the *Taub Adiabat*

$$\mu_2^2 - \mu_1^2 = (p_2 - p_1)(\mu_1 V_1 + \mu_2 V_2) \ , \tag{1.12}$$

which represents the relativistic generalization of the classical *Hugoniot Adiabat.*[4]

Equations (1.8), (1.10) and (1.12) are also called *Taub's junction conditions* for shock waves and represent the relativistic generalization of the corresponding *Rankine–Hugoniot* junction conditions for classical shocks (Courant and Friedrichs [35], Landau and Lifshitz [90]) . The Newtonian limit of these equations is readily taken by substituting the generalized volume μV with its classical equivalent V and by setting equal to one the Lorentz gamma factor in the relativistic current $j = n\gamma v$.

The study of the Taub adiabat in a $(p, \mu V)$ plane represents a very useful tool for extracting information on the variation of the relevant hydrodynamical quantities across a shock front. Once the state of the fluid ahead of the front "1" is assigned in terms of a pressure p_1 and of a generalized volume $\mu_1 V_1$, the condition (1.11) constraints the possible states of the fluid behind "2" to lie on the adiabat.

Another important curve in the $(p, \mu V)$ plane is represented by the *Poisson Adiabat* (or "constant entropy curve") which is a solution of (1.7) when the equality holds. It is possible to show (Thorne [163]) that the Poisson adiabat through "1" is here tangent to the Taub adiabat at point "1" and that the two curves have the same second derivative there. In this way, the Poisson adiabat selects the "physical" branch of the Taub adiabat as the one that always lies above the constant entropy curve (see Figure 1.2).

[4] We recall that the Hugoniot adiabat is a curve on a (p, V) plane in terms of which all of the properties of a classical shock can be derived.

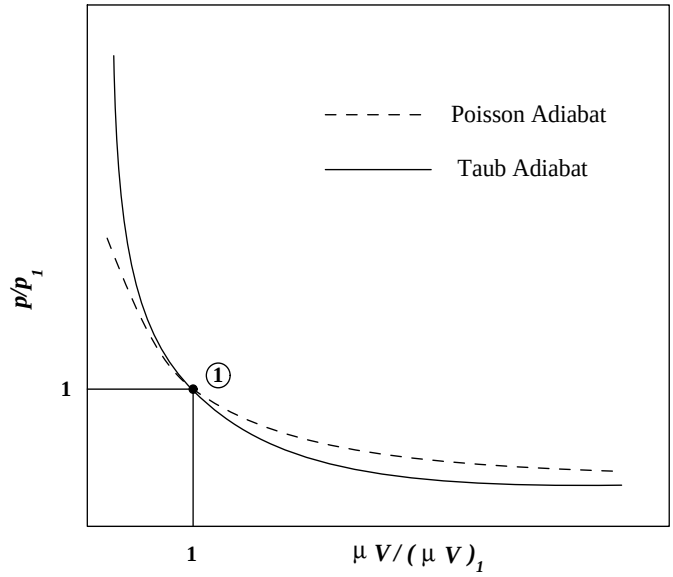

Figure 1.2 Schematic representation of the Taub Adiabat and of the Poisson Adiabat on a $(p,\, \mu V)$ plane.

The condition on the entropy increase (1.7) establishes that the state "2" of the fluid behind the shock wave must be above the state "1" on the $(p,\, \mu V)$ plane, or equivalently, that for a physical shock:

$$p_2 > p_1 \ , \tag{1.13}$$

$$\mu_2 > \mu_1 \ , \tag{1.14}$$

$$V_2 < V_1 \ . \tag{1.15}$$

Since equation (1.8) expresses the fact that j^2 is the slope of the chord connecting "1" with "2", one can make use of the condition (1.15) to deduce a further condition for the occurrence of a physical shock, *i.e.*

$$v_2 < v_1 \ . \tag{1.16}$$

Further important information that can be extracted from the study of the Taub adiabat is given by the magnitudes of the flow velocities on either side of the shock as compared to the local sound speeds. Using the first law of thermodynamics in the form

$$de = \left(\frac{w}{n}\right) dn + nTds \ , \tag{1.17}$$

and rewriting it as

$$d\left(\frac{w}{n}\right) = Vdp + Tds \ , \tag{1.18}$$

it is possible to see that the tangent to the Poisson adiabat is given by

$$\left[\frac{\partial p}{\partial(\mu V)}\right]_s = -\left(\frac{c_s}{V}\right)^2 < 0 \ . \tag{1.19}$$

where $c_s = (\partial p/\partial e)_s^{1/2}$ is the local sound speed. Equation (1.19) allows then to interpret the slope of the Taub adiabat at any given point as proportional to the local sound speed and to the fluid's specific volume. Using (1.19) together with the condition (1.16), it is easy to show that the flow entering a shock front is always supersonic and, similarly, that the flow out of a physical shock is necessarily subsonic, *i.e.*

$$v_1 \ \geq \ c_{s1} \quad (\propto \text{tangent at "1"}) \ , \tag{1.20}$$

$$v_2 \ \leq \ c_{s2} \quad (\propto \text{tangent at "2"}) \ . \tag{1.21}$$

These inequalities can be readily verified by looking at the schematic representation of the fluid velocities at the different states on the Taub adiabat presented in Figure 1.3.

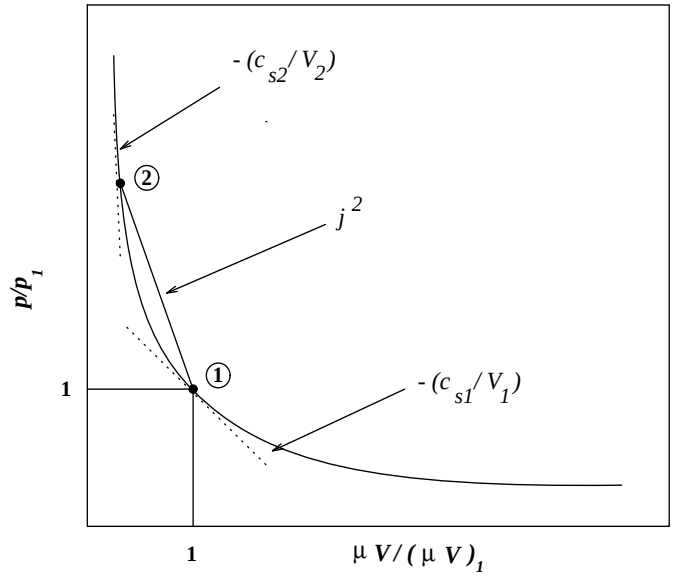

Figure 1.3 Schematic representation of the Taub Adiabat and of the magnitude of the fluid velocities at the states "1" and "2". The tangents to the adiabat at "1" and "2" are proportional to the local sound speeds, while the slope of the chord between the two states is proportional to the fluid velocities ahead of and behind the front.

After a manipulation of the junction conditions (1.4)–(1.5), we can write relations expressing the fluid velocities on either side of the front in terms of the physical state there, *i.e.*

$$v_1^2 = \frac{(p_2 - p_1)(e_2 + p_1)}{(e_2 - e_1)(e_1 + p_2)} , \tag{1.22}$$

$$v_2^2 = \frac{(p_2 - p_1)(e_1 + p_2)}{(e_2 - e_1)(e_2 + p_1)} , \tag{1.23}$$

and from their combination we can have information about the velocity jump across the front in terms of the relative velocity

$$v_{rel} = \frac{v_1 - v_1}{1 - v_1 v_2} = \left[\frac{(p_2 - p_1)(e_2 - e_1)}{(e_2 + p_1)(e_1 + p_2)}\right]^{1/2} , \tag{1.24}$$

and of the velocities ratio and product

$$\frac{v_1}{v_2} = \frac{e_2 + p_1}{e_1 + p_2} \ , \qquad\qquad v_1 v_2 = \frac{p_2 - p_1}{e_2 - e_1} \ . \tag{1.25}$$

In the case of a relativistic fluid,[5] $p_k = e_k/3$, $c_s = 1/\sqrt{3}$ and (1.25) then become

$$v_1 = \left(\frac{3e_2 + e_1}{3e_1 + e_2}\right) v_2 \ , \qquad\qquad v_1 = \frac{1}{3v_2} \ . \tag{1.26}$$

It is instructive to consider the expressions that equations (1.25) and (1.26) assume in the limiting situations of *weak* and *strong shocks*. In the first case, $e_2 \sim e_1$ and from (1.26) it is possible to deduce that

$$v_1 \to c_{s1} = c_s \ , \qquad\qquad v_2 \to c_{s2} = c_s \ , \tag{1.27}$$

and, in agreement with our common sense, this is equivalent to saying that an asymptotically weak shock wave tends to resemble a *sound wave*. On the other hand, in the case of strong shocks $e_2 \to \infty$ (*i.e.* the state "2" moves upwards on the Taub adiabat) and then

$$v_1 \to 1 \ , \qquad\qquad v_2 \to \frac{1}{3} < c_{s2} = c_s \ . \tag{1.28}$$

Note that in this latter case $v_2/c_{s2} \to 1/\sqrt{3}$.

1.2 Relativistic Reaction Fronts

In the classical theory of reaction fronts (Courant and Friedrichs [35], Landau and Lifshitz [90], Buckmaster and Ludford [26], Fickett and Davis [46], Friedrichs [47]), these discontinuities in the flow are described as moving surfaces by means of which a suitable fluid mixture undergoes a chemical *transformation* with liberation of heat. As a result of the transformation, the fluid behind the reaction front can be either compressed and decelerated or decompressed and accelerated. The study of the microphysics in the narrow region where the reaction processes take place is extremely complicated and an exhaustive theory of it within the context of relativistic reaction fronts has not been reached yet.

[5] Here and in the following we will consider as relativistic a fluid whose internal energy is much larger than its rest mass energy. In this case, a one-parameter equation of state can be used and a precise relation between pressure and energy density can be established. Such a relativistic fluid is different from one which is said to be "relativistic" because it has bulk motions close to the speed of light, but for which a two-parameter equation of state needs to be used.

Nevertheless, just as for shock waves, a satisfactory hydrodynamical description of reaction fronts can be achieved when these are treated as discontinuity surfaces of infinitesimal and constant width across which rapid changes in the fluid variables occur. Once again this approximation is certainly good if the front has a thickness which is much smaller than the typical length scale for the variation of the flow variables and if the thermal and the viscous time scales are much smaller than the one set by the motion of the front (we shall assume that these requirements are always met within the scenarios discussed in this work). In this respect, reaction fronts are very similar to shock fronts and can be essentially described by means of the same mathematical theory (Courant and Friedrichs [35], Landau and Lifshitz [90], Fickett and Davis [46], Friedrichs [47], Buckmaster and Ludford [26], Zeldovich et al. [172]).

The main difference between shock fronts and reaction fronts is to be found in the fact that the fluids on either side of a reaction front are chemically and physically *different*. We have seen (Section 1.1) that as a fluid goes across a shock front it can be compressed and decelerated so as to change its state. However, the irreversible processes occurring across the front *do not* produce a change in its chemical and physical properties and the *same* equation of state will hold on either side of the shock. This is not the case for a reaction front, for which the irreversible processes taking place at the front *do* produce a radical change in the chemical and physical properties of the fluid. As a result, fluid elements on either side of a reaction front are described by *different* equations of state, each accounting for the different internal binding energies (as in the case of a nonrelativistic fluid) or for the different number of degrees of freedom or vacuum energies (as in the case of a relativistic fluid).

Given this difference, the analysis of reaction fronts proceeds in close analogy to the analysis of shock fronts and the relevant differences can be easily pointed out by means of the *Reaction* or *Transition* or *Detonation/Deflagration Adiabat* and which represents equivalent of the Taub adiabat (1.12) for a relativistic reaction front. It is now convenient to introduce the *compression coefficient* (Danielewicz and Ruuskaneen [39], Bonometto and Pantano [24])

$$x = \frac{w_1 \gamma_1^2 v_1^2}{w_2 \gamma_2^2 v_2^2} \ , \tag{1.29}$$

by means of which the reaction adiabat can be written as

$$w_2 x - w_1 - (p_2 - p_1)(x + 1) = 0 \ . \tag{1.30}$$

Physical solutions of (1.30) need to satisfy the conservation of momentum in the new form

$$\gamma_2^2 v_2^2 = (x/w_2)(p_2 - p_1)/(x-1) \tag{1.31}$$

and are given respectively by

$$p_1 < p_2 \qquad \text{and} \qquad v_2 < v_1 \quad (x < 1)\,, \tag{1.32}$$

or

$$p_1 > p_2 \qquad \text{and} \qquad v_2 > v_1 \quad (x > 1)\,. \tag{1.33}$$

Inequalities (1.32) and (1.33) distinguish the reaction adiabat into two different branches which are called *Detonation Branch* and *Deflagration Branch* respectively (see Figure 1.4).

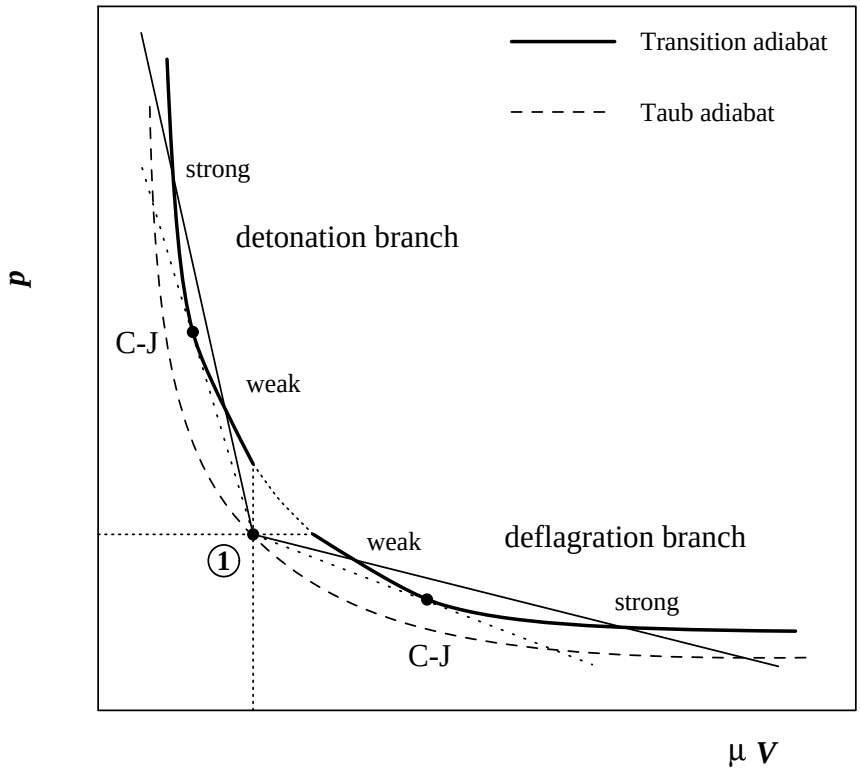

Figure 1.4 Reaction adiabat for the state "1" and the distinction between the Detonation and the Deflagration Branches. Weak, Strong and Chapman-Jouguet (C–J) processes are also pointed out, with the latter being marked by heavy dots.

The part of the reaction adiabat between the two branches is indicated with a dotted line and refers to a non a physical region since there $p_2 > p_1$, $\mu_2 V_2 > \mu_1 V_1$ and therefore j is imaginary [*cf.* equation (1.8)].

Making use of Figure 1.4 and of the relations (1.8) and (1.19), it is possible to realize that in a detonation the reaction front always moves at a *supersonic* speed relative to the medium ahead. On the other hand, the reaction front always moves at a *subsonic* speed relative to the medium ahead in the case of a deflagration. Deflagrations (and detonations) can be further classified as *weak* or *strong* according to whether the velocity of the medium behind is subsonic (supersonic) or supersonic (subsonic) [6].

An additional and special class of reaction fronts is the one for which the velocity of the fluid behind the front is exactly equal to the local sound speed. These fronts are called *Chapman-Jouguet* deflagrations or detonations, and represent a specifically interesting class of phenomena. (The classification of the various reaction fronts is summarized in Table I). The following sections are devoted to a brief review of the main properties of detonation and deflagration fronts.

	DETONATIONS $(v_1 > v_2\,,\ p_1 < p_2)$	DEFLAGRATIONS $(v_1 < v_2\,,\ p_1 > p_2)$
Weak	$v_1 > c_{s1},\quad v_2 > c_{s2}$	$v_1 < c_{s1},\quad v_2 < c_{s2}$
Chapman–Jouguet	$v_1 > c_{s1},\quad v_2 = c_{s2}$	$v_1 < c_{s1},\quad v_2 = c_{s2}$
Strong	$v_1 > c_{s1},\quad v_2 < c_{s2}$	$v_1 < c_{s1},\quad v_2 > c_{s2}$

Table I The various combinations of the fluid velocities for the different types of reaction front. The velocities are referred to the front rest frame, with v_1 being the fluid velocity ahead of the front and v_2 the fluid velocity behind the front. Similarly c_{s1} and c_{s2} are the sound speeds on either side of the front (see also Figures 1.1 and 1.4).

[6] A useful mnemonic rule is to remember that *weak* reaction fronts are those for which the velocities ahead and behind the front are both either subsonic or supersonic. The opposite holds for *strong* reaction fronts.

1.2.1 Detonations

As mentioned in the previous section, detonation fronts propagate supersonically relative to their medium ahead. As a consequence, no causal influence from the front is possible on its upstream region of the flow which cannot be perturbed (see also Subsection 1.3.1 for an extended discussion of the causal structure of reaction fronts). When unperturbed fluid at rest is crossed by a detonation front, it is compressed, heated and set into motion. In general, the motion immediately behind the front is characterized by a flow region in which the fluid is smoothly decompressed and decelerated (see Figure 1.5).

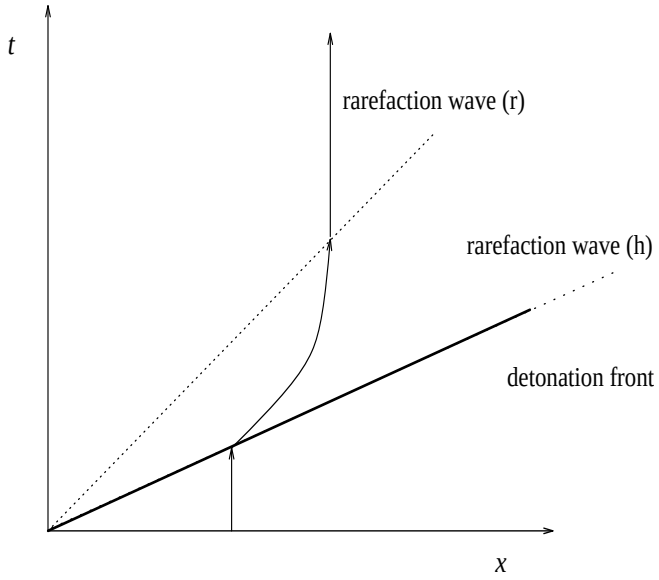

Figure 1.5 Schematic spacetime diagram of a 1+1 dimensional flow across a detonation wave. The heavy line curve traces the worldline of the detonation front, while the dotted lines represent the heading (h) and rear (r) fronts of the rarefaction wave. Note that within this treatment the head of the rarefaction wave and the detonation front are coincident and are here represented as distinguished for clarity only. The continuous arrowed line represents the worldline of a fiducial fluid element, while t and x are fiducial time and space coordinates.

This flow region is called *rarefaction wave* and is limited by a supersonic leading front and by a rear edge or "tail" of the rarefaction wave (this moves at the local sound speed in the case where the velocity is zero at the downstream boundary of the flow)[7].

[7]Here we will always be using boundary conditions which set the velocity to zero (in a suitable reference frame) at both ends of the calculational domain.

The rear edge of the rarefaction wave behaves as a *weak discontinuity* and represents the locus of points at which the fluid variables and their first derivatives are continuous, but have discontinuous higher order derivatives.

As shown in Table I, detonations can be distinguished according to the magnitude of the fluid velocity behind the detonation front (measured in the rest frame of the front) as compared with the local sound speed. In this sense, they are defined as weak, strong and Chapman-Jouguet those detonations having respectively supersonic, subsonic, and sonic downstream flows. It is worth mentioning here that a formal similarity exists between detonations and another class of reaction fronts called *condensation discontinuities*. Classically, these are discontinuity surfaces across which a supersaturated vapour undergoes a phase transformation becoming a condensed vapour (*e.g.* fog). It is relevant to underline that condensation discontinuities are distinct phenomena and do not simply result from the compression of a fluid across a shock wave. In general, in fact, the compression of a fluid element across a shock wave produces a local increase of the temperature larger than the local increase of the degree of supersaturation. This is the reason for which only those fluids with large heat capacities are able to undergo this type of phase transformation. Similar to detonation fronts, condensation discontinuities are exothermic processes and their formal description closely resembles the one of detonations with which they share many of their properties (Landau and Lifshitz [90], Thompson and Kim [161], Thompson et al. [162]). Condensation discontinuities have not been very fully investigated up to now but they have been mentioned in connection with the cosmological first order phase transitions (Applegate and Hogan [6], Laine [85]) which we will be discussing in the later chapters of this Thesis.

Important features of detonations can be deduced by counting the number of "unknowns" which are typical of the hydrodynamical solution of a detonation wave. In general, we need to calculate the energy densities and the velocities on each side of the discontinuity surface and the velocity at which this front moves relative to some coordinate system. In the case of a detonation, these represent five unknowns (*i.e.* e_1, v_1, e_2, v_2 and v_{det}) and can be balanced by the two equations expressing the conservation of energy and momentum. Boundary conditions (depending on the specific geometry of the front) will usually allow to specify the velocity and the state of the unreacted fluid, thus reducing to one the number of unknowns.

However, there is a special class of detonations whose hydrodynamical solution is completely determined *only* in terms of the boundary conditions and of the energy–momentum conservation. This is the case of the Chapman-Jouguet detonations, for which the velocity out of the front equals the local sound speed. Chapman-Jouguet detonations represent a particularly relevant class of reaction fronts, for which it can be shown that

the fluid velocity ahead of the front and the entropy of the fluid behind the front are at a minimum (Chapman-Jouguet detonations are then the slowest of all possible detonations). Moreover, the entropy jump across a Chapman-Jouguet detonation front is at a maximum.

The peculiar nature of Chapman-Jouguet detonations is underlined in the "Chapman-Jouguet hypothesis", according to which detonations in chemical combustion should occur *only* under the form of Chapman-Jouguet detonations and a proof of this for an ideal self similar detonation can be found in Courant and Friedrichs [35] or in Landau and Lifshitz [90]. Although in nature detonations in chemical combustion often appear accompanied by nonlinear effects (such as transverse shock waves or turbulence: Fickett and Davis [46]), it seems that the hypothesis is generally verified to a good approximation, with detonation fronts which although complicated, propagate at a constant velocity close to the theoretical Chapman-Jouguet value (Lewis and von Elbe [98], Williams [169], Lee [97]).

It should be underlined that although weak detonations in chemical combustion satisfy the conservation laws, they cannot be realized in practice[8]. A simple proof of this can come from considering a detonation front as a region of finite width across which the reaction takes place and whose forward layer is represented by a shock front moving into the unreacted fluid (Landau and Lifshitz [90])[9]. In this case, the evolution of the hydrodynamical quantities across the reaction front can be followed by using a shock adiabat through a point a representing the unreacted fluid and a transition adiabat as shown in Figure 1.6.

When the fluid moves across the shock wave, it is heated and compressed and effectively moves on the chord ab from point a to point b. The physical conditions have therefore been created for the reaction to take place and as this proceeds the fluid state moves downwards from point b along the chord ba. In doing this, the heat of the reaction is released, the fluid expands and its pressure decreases until the whole heat of the reaction has been evolved. The final physical state will then correspond to the point c on the transition adiabat which is representative of a strong detonation [10]. If the reaction involves

---

[8]Reaction fronts have been recently considered for studying the hydrodynamics of the phase interface during cosmological first order phase transitions and this will be further discussed in Chapter 2 and 4. However, because of the differences between chemical combustion and phase transitions, neither the validity of the Chapman-Jouguet hypothesis nor the arguments about weak detonations can be extended to the context of cosmological phase transitions (Laine [85], Kurki-Suonio and Laine [82]).

[9]Courant and Friedrichs [35] have also suggested the mathematical equivalence between a detonation and a deflagration initiated by a shock front. In this sense, a strong detonation would be equivalent to a shock front followed by a weak deflagration and a weak detonation would be equivalent to a shock front followed by a strong deflagration.

[10]We are here assuming that diffusion and viscosity may be neglected in the reaction zone, so that the

chemical combustion, then the condition on the entropy increase across the detonation front does not allow the lower point d (that would correspond to a weak detonation) to be reached, thus excluding weak detonations.

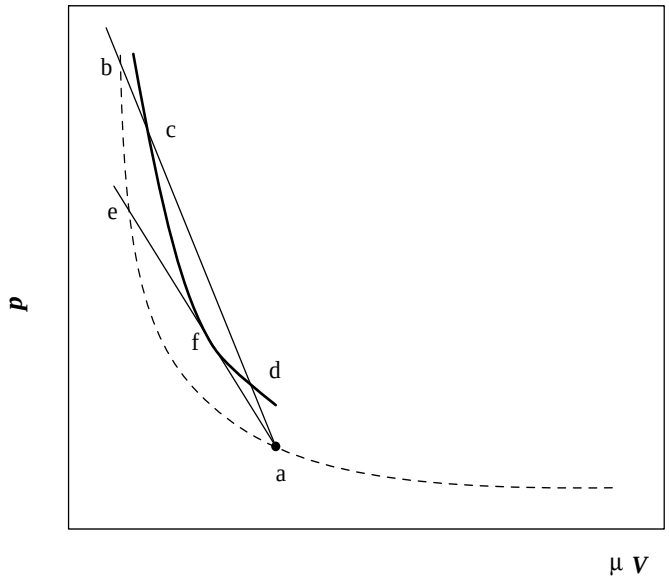

Figure 1.6 Schematic diagrams showing the impossibility of weak detonations in chemical burning. The dashed line hyperbola is the shock adiabat through the point a, while the continuous line hyperbola is the transition adiabat.

In Subsection 1.3.2, we shall prove that strong and Chapman-Jouguet detonations are evolutionary and linearly stable to corrugations of the detonation front. However, we shall also give a brief proof that, in general, boundary conditions do not allow for strong detonations to be produced in practice. From this and the above arguments about weak detonations in chemical combustion, an indirect proof of the Chapman-Jouguet hypothesis can be deduced.

1.2.2 Deflagrations

Deflagration waves (or *slow combustion* waves) have been extensively investigated within the classical theory of combustion and laminar flames. Quite differently from detonations, deflagration fronts move subsonically relative to their medium ahead and this is then

---

mass and momentum transfer can take place only by means of fluid flow. This, in turn, establishes that the motion of the physical state has to take place along a constant j (*i.e.* slope) curve.

equivalent to have, in the rest frame of the front, the velocity of the fluid behind the front being larger than that ahead of it. Being a subsonic front, the deflagration does perturb the fluid ahead of it by means of a *precompression wave* which travels in the unreacted medium ahead of the deflagration front. At the leading edge of the precompression wave there is a shock front at least in principle (it may have essentially vanishing amplitude in practice) which moves supersonically relative to the medium ahead of it and has the effect of accelerating, compressing and heating the fluid before it is swept by the deflagration front. Its role is therefore that of establishing suitable hydrodynamical and chemical conditions under which the reaction or combustion can take place (the same role is played by the supersonic reaction front itself in a detonation). It is worth underlining that the fluid undergoes a chemical or physical transformation only when it is swept by the deflagration front and that there is no chemical difference between the fluids on the two sides of the precompression shock front.

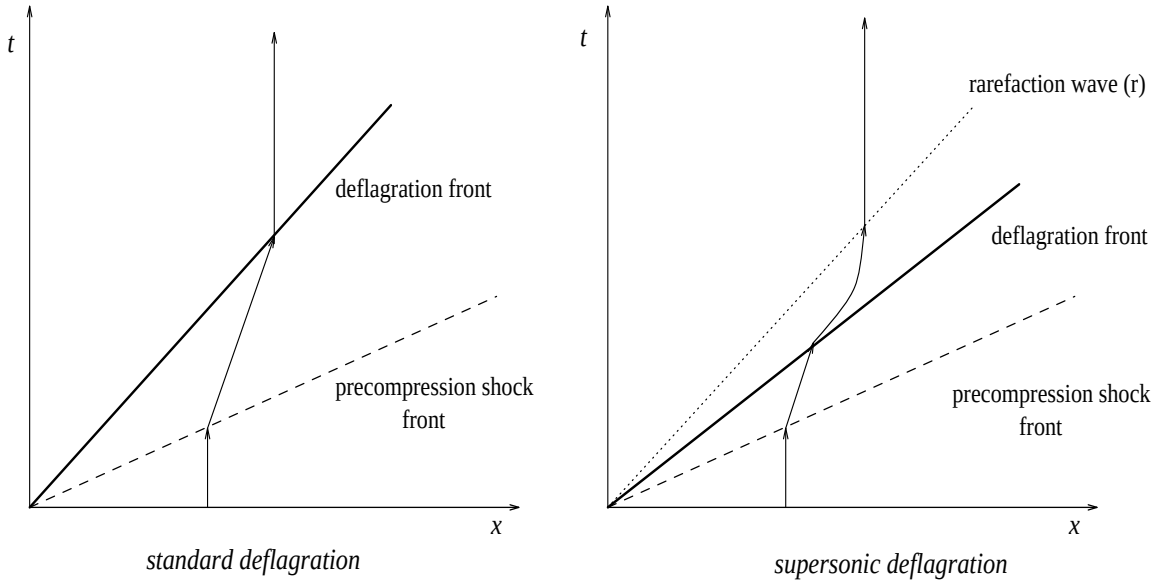

Figure 1.7 Schematic spacetime diagrams of 1+1 dimensional flows across deflagration waves. The left diagram refers to a standard (subsonic) deflagration, while the right one to a supersonic deflagration. The heavy line curves trace the worldline of the deflagration fronts, while the long-dashed lines are the worldlines of the precompression shock front. The dotted line in the right diagram represents the rear (r) front of the rarefaction wave. The continuous arrowed lines represent the worldlines fiducial fluid elements, while t and x are fiducial time and space coordinates.

Relative to the front, the fluid behind the deflagration can either be at rest (as in the case of a standard subsonic deflagration) or have a finite subsonic velocity. This is the case for a *supersonic deflagration* (Kurki-Suonio and Laine [82]), for which the deflagration front moves supersonically relative to the a fixed coordinate system[11] (see Figure 1.7).

In their computations, Kurki-Suonio and Laine have considered the supersonic deflagration as composed of a Chapman-Jouguet deflagration followed by a rarefaction wave. While in their models Kurki-Suonio and Laine have assumed that the downstream flow is sonic relative to the front (*i.e.* $v_2 = c_{s2}$), we here note that this restrictive hypothesis does not need to be made. Indeed, it is in principle possible to construct solutions for supersonic deflagrations in which $v_2 < c_{s2}$ and $v_2 > c_{s2}$ corresponding respectively to supersonic weak and strong deflagrations followed by rarefaction waves. It should be noted that a supersonic deflagration could eventually evolve into a detonation if the deflagration front would coalesce with its precompression shock. This could happen, for instance, when the strength of the precompression shock front increases so much that its speed would equal that of a detonation front (Courant and Friedrichs [35]).

As for detonations, deflagrations can be further distinguished into weak, strong and Chapman-Jouguet deflagrations according to whether the fluid velocity behind the deflagration front is supersonic, subsonic, or sonic respectively. The count of the unknowns in the hydrodynamical solution of a deflagration front is somewhat more elaborate as a consequence of the higher number of discontinuity surfaces that could be present. Nevertheless, it is straightforward to show that there are ten different unknowns (*i.e.* e and v ahead of the shock, e and v behind the shock, e_1, v_1, e_2, v_2, v_{shock} and v_{def}) in the case of a standard deflagration wave and twelve (*i.e.* the same as before plus the energy density behind the tail of the rarefaction wave and its velocity) in the case of a supersonic deflagration (Kurki-Suonio [80]). The junction conditions across the discontinuity surfaces together with the boundary and initial conditions allow to determine nine of the unknowns for a standard deflagration and eleven of the unknowns for a supersonic deflagration.

As a result, deflagration waves represent intrinsically underdetermined fronts and this reflects the impossibility of defining the velocity of the detonation front from the initial conditions and the conservation equations (Landau and Lifshitz [90]). The further equation required in order to close the system of equations and eliminate the degeneracy in the solution is usually defined starting from microscopic considerations about the processes taking place at the detonation wall and effectively expresses the rate at which the reaction takes place at the front. Because of its microscopic nature, this equation can represent a

[11] Note that also in this case the front moves subsonically relative to medium ahead of it, which however, can have a considerable velocity relative to the fluid at rest.

delicate point in the whole hydrodynamical treatment of a deflagration wave and this is particularly true in the case in which the front is taken to mimic the dynamics of a phase interface in a cosmological first order phase transition. The way this problem has been solved for the cosmological quark–hadron phase transition will be discussed in detail in Subsection 5.2.3.

A final comment should be made on strong deflagrations which, similarly to weak detonations, cannot be realized in practice in spite of the fact that they satisfy conservation laws. There are a number of ways of proving this claim for chemical combustion. A rigorous treatment in which the combustion front is described as a changing mixture of the reacted and unreacted fluid can show that strong deflagrations would include regions of negative entropy production and are therefore impossible (Courant and Friedrichs [35]). Other proofs involve the investigation of the stability properties of a strong deflagration (see next subsection) and show that if a strong deflagration could be momentarily produced it would be totally unstable and would then split into a similarity rarefaction wave and into a weak deflagration (Landau and Lifshitz [90], Laine [85]). Once the impossibility of strong deflagration is assessed, it is also possible to exclude weak detonations in chemical combustion when the latter are considered as equivalent to a shock front followed by a strong deflagration (Courant and Friedrichs [35] and see also Subsection 1.2.1).

1.3 Stability of Relativistic Reaction Fronts

An aspect which deserves great attention when studying the evolution of a *thermodynamically stable* reaction front (*i.e.* of a front which satisfies conservation laws and can be momentarily produced) is that of *hydrodynamic stability*. For this purpose, stability analyses are carried out so as to establish whether, once the front is produced, this can evolve in time without radically changing its properties. Stability analyses of reaction fronts represent a large area of research both from the experimental and the theoretical point of view and a number of important results have been established especially within a linear regime. In the next Subsections (1.3.2, 1.3.3) we will discuss in detail some recent linear stability analyses of relativistic detonation fronts (Rezzolla [143]) and of relativistic deflagration fronts (Huet et al. [60])[12]. In both cases the analyses have been made having in mind an application to the motion of a phase interface during a cosmological phase transition and comments on these applications will be made often during the discussion.

[12]Note that these subsections are heavily technical and, if the reader so wishes, they can be safely skipped without creating difficulties for reading the rest of the Thesis.

Before going into details, a couple of comments should be made on the concept of evolutionarity of a discontinuity surface and on the properties and the validity of a linear stability analysis. A discontinuity surface is usually considered as *evolutionary* if any infinitesimal perturbation of the initial state produces only an infinitesimal change in the flow over a sufficiently short time interval (Landau and Lifshitz [90]). This means that an evolutionary front can be momentarily produced and can *possibly* have a regular evolution in time. However, an evolutionary front is not necessarily a stable front since it might well develop instabilities over a long enough time scale. In order to verify that an evolutionary front is also hydrodynamically stable a rigorous stability analysis is necessary. It is important to stress that the ultimate onset of the instabilities cannot be fully assessed within a linear analysis, since it might also be that the instability modes possibly found could be controlled by intervening nonlinear effects which would limit the energy transfer into the unstable modes and counteract their growth. However, in the case of reaction fronts, a necessary and sufficient condition for the validity of the above arguments is that a *mutual causal connection* should be maintained between the front and the upstream or the downstream regions of the flow. In order to clarify this concept for the various cases of deflagrations and detonations, we dedicate the next subsection to the discussion of the causal structure of reaction fronts and introduce the concept of *degree of underdeterminacy* of a discontinuity surface, which can provide a simple indication of whether the surface can be stable or not.

1.3.1 Causal Structure and Determinacy of Reaction Fronts

The degree of underdeterminacy of a discontinuity surface (*e.g.* either a shock or a reaction front) can be easily calculated by counting the number of free parameters which could be associated with a small perturbation of the front (Landau and Lifshitz [90], Friedrichs [47]). These are determined by the difference between the number of unknown parameters (which in general are given by the number of sonic perturbations that can be transmitted from the front, by the entropy perturbation propagated in the downstream region of the flow and by the surface displacement) and the number of boundary conditions that the perturbation has to satisfy (which in general are given by the conservation of baryon number, energy and momentum). While a discontinuity with a zero degree of underdeterminacy can be shown to be linearly stable, the opposite is not true for a discontinuity with a finite degree of underdeterminacy. This is because the further equation necessary to close the system of equations and determine the solution (and which usually specifies the velocity of the front in terms of the thermodynamical variables on either side) could or could not lead to an unstable configuration (see Subsection 1.3.3).

Since all of the reaction fronts presented so far satisfy the same boundary conditions, their different degree of underdeterminacy is then simply due to the different number of perturbations that can be transmitted from the front. In order to calculate this number there are at least two efficient ways, one of which makes use of the concept of the characteristic curves [13] (Rezzolla [143]), while the other requires the calculation the of the difference between the local fluid velocity and the perturbation velocity as seen in the front rest frame [*i.e.* $u_1 = (v_1 \pm c_{s1})/(1 \pm v_1 c_{s1})$ and $u_2 = (v_2 \pm c_{s2})/(1 \pm v_2 c_{s2})$, Landau and Lifshitz [90], Seibert [151]]. Since the perturbations must propagate away from the front, it follows that for all of the different classes of reaction front the following inequalities $u_1 < 0$ and $u_2 > 0$ must hold.

We here adopt the first of the two methods and for this purpose we have represented in Figure 1.8 the causal structure of the six types of reaction fronts which were summarized in Table I. The figure consists of six different spacetime diagrams, (all referred to the front rest frame), with time on the vertical axis and the space coordinate on the horizontal one. For each diagram, the thick solid line represents the worldline of a fluid element passing from region 1 to region 2, the thin solid and arrowed lines denote the characteristic curves relative to the front [$\mathcal{C}^j_\pm$ are the forward (+) and the backward (−) characteristics of the regions ahead of the front ($j = 1$) and behind it ($j = 2$)], the dotted line shows the sound speed in the frame of the front and the dashed line represents the worldline of the front. The characteristic curves are drawn so to reach the front when the fluid element crosses it and to depart from the front at the same instant; note that for simplicity we have assumed the sound speeds to be the same on both sides of the front.

Deflagrations are represented in the left column, detonations in the right one and the different diagrams refer respectively to AA: weak deflagration, AB: Chapman-Jouguet deflagration, AC: strong deflagration, CC: weak detonation, CB: Chapman-Jouguet detonation and CA: strong detonation. (The letters A, B, C, express the fact that the fluid element can move, relative to the front, at a speed smaller, equal or larger than the sound speed, with the first letter referring to the medium ahead and the second one to the medium behind.)

With this representation, the diagrams in Figure 1.8 show that when the medium ahead of a reaction front is subsonic (*e.g.* as in the diagrams AA, AB and AC), the front can always transmit a perturbation upstream in region 1 by means of the backward characteristic $\mathcal{C}^1_-$.

---

[13] We recall that the characteristic curves can be interpreted as the directions in spacetime along which sonic perturbations are transmitted, as well as the fluid flowlines (advective characteristics). It is then possible to define the "region of determinacy" of an event $\mathcal{P}$ as the region of spacetime included between the characteristic curves converging to the point $\mathcal{P}$ (see also Subsection 5.2.4 for a more extended discussion).

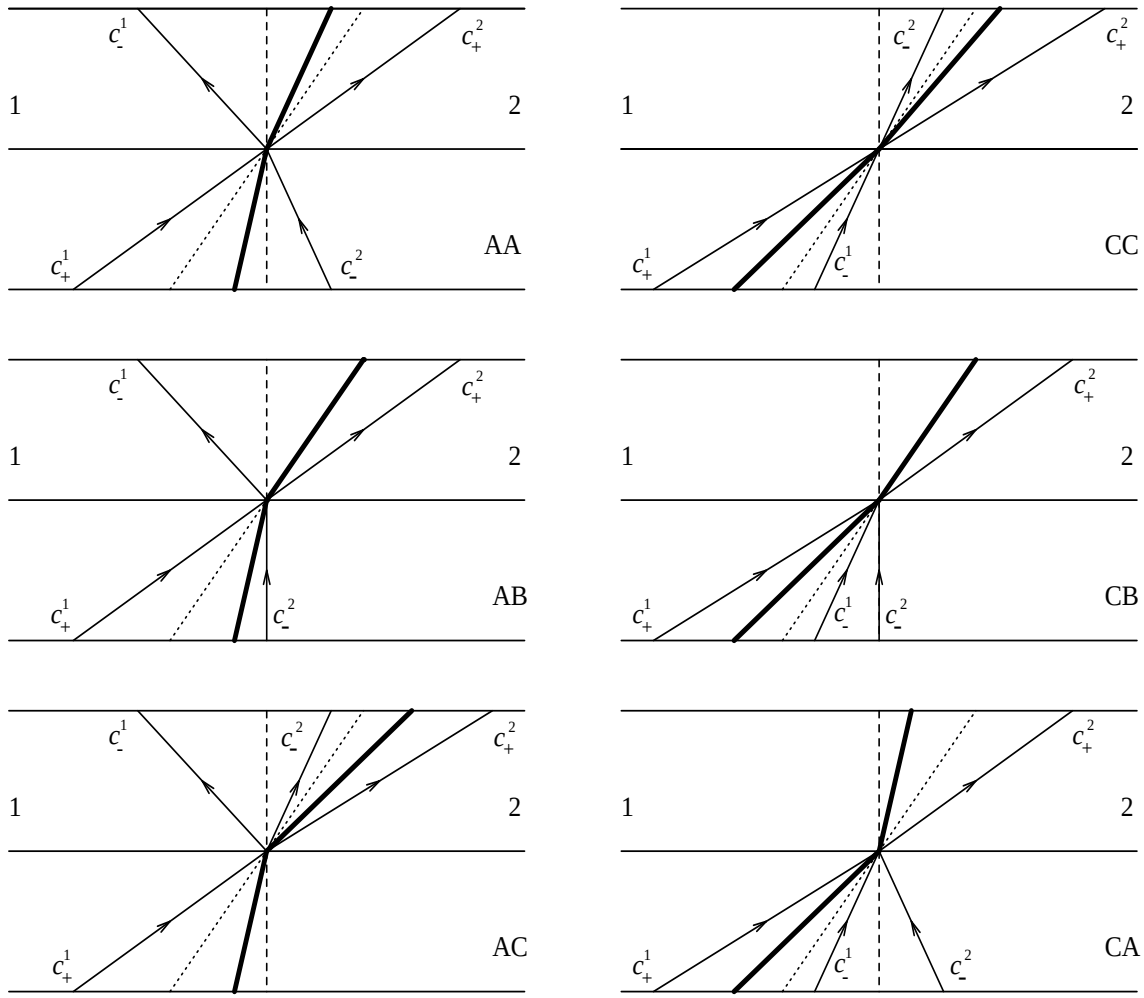

Figure 1.8 Spacetime diagrams and characteristic representations of the various types of reaction front (drawn as left propagating). Deflagrations are represented on the left and detonations on the right; the six different diagrams refer respectively to: AA: weak deflagration, AB: Chapman-Jouguet deflagration, AC: strong deflagration, CC: weak detonation, CB: Chapman-Jouguet detonation and CA: strong detonation. The diagrams are drawn relative to the front rest frame with time on the vertical axis and the space coordinate on the horizontal one. The thick solid line represents the worldline of a fluid element passing from region 1 to region 2. For each diagram, the characteristic curves are denoted with thin solid and arrowed lines ($\mathcal{C}_\pm^j$, with $j = 1,\ 2$, are the forward $(+)$ and the backward $(-)$ characteristics relative to the regions ahead of and behind the front respectively), the sound speed in the frame of the front is marked with a dotted line, while the dashed line represents the worldline of the front. (For simplicity we have assumed the sound speeds to be the same on both sides of the front.)

In this case, *there is* a mutual causal connection between the front and the medium ahead of it and the worldline of the fluid element is within the region of determinacy of the front. This mutual causal connection *is not present* when the medium ahead of the front is supersonic (*e.g.* as in the diagrams CC, CB and CA) in which case the front cannot influence the incoming flow and both the characteristic curves $\mathcal{C}_+^1$ and $\mathcal{C}_-^1$ are directed towards the front.

Similarly, from Figure 1.8 it is possible to deduce the causal connection between the front and the medium behind it, by looking at whether there is any backward characteristic curve $\mathcal{C}_-^2$ reaching the front from region 2. It is evident that this can occur only if the downstream flow is subsonic (as in diagrams AA and CA) or sonic (as in diagrams AB and CB); this latter case represents a limiting situation, with the mutual causal connection being just marginal as shown by the characteristic $\mathcal{C}_-^2$ being tangent to the worldline of the front. The front has no mutual causal connection with the medium behind when the downstream flow is supersonic (as in the diagrams AC and CC) and in this case the characteristic curves $\mathcal{C}_+^2$ and $\mathcal{C}_-^2$ are both in the direction of the flow. This difference is a fundamental one, establishing that there is a mutual causal connection between the front and the medium behind only when the flow out of it is subsonic or sonic. As a consequence, for subsonic and sonic downstream flows, the medium behind *can* respond to any perturbation produced by the front and, at least in principle, it can counteract the growth of the potential instabilities. This backreaction could then appear in the those nonlinear effects that tend to saturate the oscillations which would be present but would not grow unboundedly. This might be at the origin of the formation of the typical corrugated but stable cellular flames observed in laboratory experiments (Markestein [107], Buckmaster and Ludford [26]), which are produced by weak deflagrations.

This stabilizing mechanism *cannot* operate in weak detonations, since in this case there is no mutual interaction between the front and the media either ahead of it or behind it. We remark that this argument is simply based on the causal structure of weak detonations and is therefore independent of the order at which a perturbation analysis is performed. In the context of causal connection, Chapman-Jouguet detonations represent a limiting case but do not suffer from the causality problems discussed for weak detonations. As shown in the diagram CB of Figure 3 in fact, the front is just marginally mutually connected with the medium behind it and this could then provide the back-reaction required for saturating the potential perturbations produced at front.

Finally, the degree of underdeterminacy for the various reaction fronts can be summarized as in Table II, which shows that while strong and Chapman-Jouguet detonations are linearly stable, all the other types of reaction fronts could be unstable. While strong deflagrations are assumed to be impossible because of negative entropy production (see

Subsection 1.2.2), Table II shows that the stability of Chapman-Jouguet deflagrations, weak deflagrations and weak detonations can be assessed only if a further condition is specified.

	DETONATIONS	DEFLAGRATIONS
Weak	$4-3=1$	$4-3=1$
Chapman–Jouguet	$3-3=0$	$4-3=1$
Strong	$3-3=0$	$5-3=2$

Table II The degree of underdeterminacy for the different types of reaction front. The number is calculated as the difference between the number of unknown parameters which could be associated with a small perturbation of the front and the number of boundary conditions that the perturbation has to satisfy.

1.3.2 Stability of Detonations

The stability of classical detonation fronts has been studied quite extensively in the one-dimensional and linear regime (Lee and Stewart [96]) and attempts are currently being made to extend this analysis within a weakly nonlinear theory (see Roytburd [149] for a list of references). A more recent investigation of the stability properties of relativistic detonation fronts in cosmological phase transitions has been made by Abney [1] who has concentrated particularly on the case of Chapman-Jouguet detonations. The motivation of such a study comes from realizing that while instability modes are not allowed in the upstream flow region of a detonation front, it is not possible to exclude them in the region behind the front, where they could also grow exponentially with time. As a result of his analysis, Abney has reached the conclusion that Chapman-Jouguet detonations are unstable at all wavelengths for the relevant parameter values of a cosmological first order phase transition.

We here reconsider in more detail and removing some of the approximations which were assumed by Abney, the analysis of the stability properties of both Chapman-Jouguet and strong detonations, showing the incorrectness of the above results. In particular, we find that strong detonations are both evolutionary and stable with respect to corrugations of the front and that Chapman-Jouguet detonations are evolutionary and unconditionally

linearly stable. This is in agreement with what expected from the study of the degree of underdeterminacy of these fronts and discussed in the previous subsection.

The following analysis is rather elaborate and resembles in parts the one contained in a paper by Rezzolla [143]. We first present the general perturbed hydrodynamical equations deduced from the standard linear stability analysis of special relativistic flows and then examine the stability of generic discontinuity fronts with respect to corrugations. This can be done by requiring that the perturbed hydrodynamical equations are compatible with the conservation of energy and momentum across a front subject to a corrugation perturbation. The techniques implemented for this analysis are rather general and will be here applied to Chapman-Jouguet and strong detonations whose linear stability properties will be then established. However, minor but important modifications allow to implement the same stability analysis to any type reaction and in the next subsection we shall also discuss the case of deflagrations.

Consider a plane detonation front which is propagating in a Minkowski spacetime with $(t,\, x,\, y,\, z)$ being the inertial cartesian coordinates and which is taken to be at rest on the $(y,\, z)$ plane so that there are no three-velocity components tangent to the front (see Figure 1.1). Across this surface the fluid undergoes a transformation which can be either a chemical reaction (as in the case of combustion) or a phase transformation (as in the case of cosmological phase transitions). Assume moreover that fluids on either side of the front can be described by the standard stress energy tensor of a relativistic perfect fluid (1.1). The hydrodynamical equations can then be easily derived from the projection of the four-divergence of the stress energy tensor along the direction defined by the fluid four-velocity and orthogonal to it, so as to express local conservation of energy and momentum respectively as

$$u_{\alpha} T^{\alpha\beta}{}_{;\,\beta} = 0 \ , \tag{1.34}$$

$$P_{\gamma\alpha} T^{\alpha\beta}{}_{;\,\beta} = 0 \ , \tag{1.35}$$

where $P_{\alpha\beta} = g_{\alpha\beta} + u_{\alpha} u_{\beta}$ is the projection operator orthogonal to u^{α} (*i.e.* $P_{\alpha\beta} u^{\beta} = 0$). Making use of (1.1), equations (1.34) and (1.35) in the local Lorentz frame can be written explicitly as

$$u^{\alpha} \frac{\partial p}{\partial x^{\alpha}} + c_s^2 w \frac{\partial u^{\alpha}}{\partial x^{\alpha}} = 0 \ , \tag{1.36}$$

and

$$wu^{\alpha}\frac{\partial u_{\beta}}{\partial x^{\alpha}} + u_{\beta}u^{\alpha}\frac{\partial p}{\partial x^{\alpha}} + \frac{\partial p}{\partial x^{\beta}} = 0 \ , \tag{1.37}$$

Equations (1.36) and (1.37) represent the usual "zeroth order" hydrodynamical equations and describe the motion of fluid elements on either side of the detonation front. Following standard linear perturbation analysis, we now introduce a small perturbation in the relevant hydrodynamical variables so that, at first order in the expansion, the new perturbed (primed) variables are

$$p \quad \longrightarrow \quad p' = p + \delta p \ , \tag{1.38}$$

$$u^{\alpha} \equiv \gamma(1,\ \vec{v}) = \gamma(1,\ v_x,\ 0,\ 0) \quad \longrightarrow \quad (u^{\alpha})' = u^{\alpha} + \delta u^{\alpha} \ , \tag{1.39}$$

where $\gamma = (1 - v_x^2)^{-1/2}$ and (the flow is taken to be uniform and unperturbed along the z-axis direction),

$$(u^{\alpha})' \equiv \gamma(1 + \gamma^2 v_x \delta v_x,\ v_x + \gamma^2 \delta v_x,\ \delta v_y,\ 0) \ . \tag{1.40}$$

As a result, the perturbed expressions of equations (1.36) and (1.37) are

$$c_s^2 w\left(\gamma^2 v_x \frac{\partial}{\partial t}\delta v_x + \gamma^2 \frac{\partial}{\partial x}\delta v_x + \frac{\partial}{\partial y}\delta v_y\right) + \frac{\partial}{\partial t}\delta p + v_x \frac{\partial}{\partial x}\delta p = 0 \ , \tag{1.41}$$

$$\gamma^2 w\left(\frac{\partial}{\partial t}\delta v_x + v_x \frac{\partial}{\partial x}\delta v_x\right) + v_x \frac{\partial}{\partial t}\delta p + \frac{\partial}{\partial x}\delta p = 0 \ , \tag{1.42}$$

$$\gamma^2 w\left(\frac{\partial}{\partial t}\delta v_y + v_x \frac{\partial}{\partial x}\delta v_y\right) + \frac{\partial}{\partial y}\delta p = 0 \ , \tag{1.43}$$

which can also be written, in a more compact form, as

$$\left(\mathbf{C}_t \frac{\partial}{\partial t} + \mathbf{C}_x \frac{\partial}{\partial x} + \mathbf{C}_y \frac{\partial}{\partial y}\right)\vec{\mathbf{U}} = 0 \ , \tag{1.44}$$

where

$$\mathbf{C}_t = \begin{pmatrix} 1 & \gamma^2 w c_s^2 v_x & 0 \\ v_x & \gamma^2 w & 0 \\ 0 & 0 & \gamma^2 w \end{pmatrix} \ , \tag{1.45}$$

$$\mathbf{C}_x = \begin{pmatrix} v_x & \gamma^2 w c_s^2 & 0 \\ 1 & \gamma^2 w v_x & 0 \\ 0 & 0 & \gamma^2 w v_x \end{pmatrix} , \tag{1.46}$$

$$\mathbf{C}_y = \begin{pmatrix} 0 & 0 & w c_s^2 \\ 0 & 0 & 0 \\ 1 & 0 & 0 \end{pmatrix} , \tag{1.47}$$

and $\vec{\mathbf{U}}$ is the state-vector for the perturbations

$$\vec{\mathbf{U}} = \begin{pmatrix} \delta p \\ \delta v_x \\ \delta v_y \end{pmatrix} . \tag{1.48}$$

The most general solution of (1.44) has the form

$$\vec{\mathbf{U}}(t,\ x,\ y) = \vec{\mathbf{A}}(x) e^{-i(\omega t + k y)} , \tag{1.49}$$

with ω being a complex number, k a real number and

$$\vec{\mathbf{A}}(x) = \sum_{j=1}^{3} (c_j \vec{\mathbf{L}}_j) e^{-i(l_j x)} . \tag{1.50}$$

The l_j are the complex eigenvalues of the secular equation (1.44), $\vec{\mathbf{L}}_j$ are the corresponding eigenvectors and c_j are three real constant coefficients. Substituting the trial solution (1.49) in (1.44), leads to a homogeneous system of equations whose coefficients are in the secular matrix

$$\mathbf{D} \equiv (\mathbf{C}_t\ \omega + \mathbf{C}_x\ l + \mathbf{C}_y\ k) , \tag{1.51}$$

The eigenvalues l_j can then be found by setting to zero the determinant of $\mathbf{D}$. Doing this we obtain the dispersion relation

$$\det\,(\mathbf{D}) = (lv_x + \omega)\left[(lv_x + \omega)^2 - (\omega v_x + l)^2 c_s^2 - (1 - v_x^2)k^2 c_s^2\right] = 0\ , \tag{1.52}$$

which has the roots

$$l_1 = -\frac{\omega}{v_x}\ , \tag{1.53}$$

$$l_{2,3} = \frac{1}{v_x^2 - c_s^2}\left\{(c_s^2 - 1)\omega v_x \pm c_s(1 - v_x^2)\left[\omega^2 + \frac{(v_x^2 - c_s^2)}{1 - v_x^2}k^2\right]^{1/2}\right\}\ . \tag{1.54}$$

A first point to notice is that the eigenvalues $l_{2,3}$ become divergent for a fluid velocity normal to the front v_x equal to the local sound speed. The presence of a singularity at the sonic velocity represents the "heritage" of the hyperbolic form of the hydrodynamical equations and is a general feature of the linear stability analysis of shock waves and reaction fronts (Anile [12], Landau and Lifshitz [90]). Nevertheless, particular care should be taken examining these limiting cases. It is easy to realize that the singularity in the eigenvalues $l_{2,3}$ is only an apparent one and it can be avoided if one solves equation (1.52) directly with $v_x = c_s$. In this case there are only two roots and the new eigenvalues (which we denote with a bar) then are: $\bar{l}_1 = l_1$ and

$$\bar{l}_2 = \frac{c_s k^2}{2\omega} - \frac{(1 + c_s^2)}{2c_s}\omega\ . \tag{1.55}$$

Using the eigenvalue (1.55) in the downstream region of the flow solves the problem of the singularity at the sonic velocity, but necessarily restricts the analysis to Chapman-Jouguet detonations only. (This is the choice made by Abney.) In order to investigate the stability properties of generic detonation fronts, it is necessary to make use of the solutions (1.53) and (1.54) for fluid velocities near to the sound speed. For this purpose we can write the velocity normal to the detonation front as

$$v_x = c_s + \epsilon\ , \tag{1.56}$$

with ϵ being a small positive or negative real number. The value of ϵ must in principle lie in the range $0 < \epsilon < (1 - c_s)$ for the upstream region ($x < 0$) and in the range $-c_s < \epsilon < (1 - c_s)$ for the downstream region ($x > 0$). Making use of (1.56), it is possible to expand both the numerators and the denominators of solutions (1.53) and (1.54) around the sonic velocity so as to obtain the new eigenvalue expressions (marked with a tilde)

$$\tilde{l}_1 \cong -\frac{\omega}{c_s+\epsilon}\ , \tag{1.57}$$

$$\tilde{l}_2 \cong -\frac{1}{\epsilon(2c_s+\epsilon)}\left\{\omega\left(1+c_s^2-\frac{k^2c_s^2}{\omega^2}\right)\epsilon+\omega c_s\left[1-\frac{k^2}{2\omega^2}+\frac{k^4c_s^2}{2\omega^4(1-c_s^2)}\right]\epsilon^2\right\}\ , \tag{1.58}$$

$$\tilde{l}_3 \cong \frac{1}{\epsilon(2c_s+\epsilon)}\left\{2\omega c_s(c_s^2-1)+\omega\left(3c_s^2-1-\frac{k^2c_s^2}{\omega^2}\right)\epsilon \right. \\ \left. +\omega c_s\left[1-\frac{k^2}{2\omega^2}+\frac{k^4c_s^2}{2\omega^4(1-c_s^2)}\right]\epsilon^2\right\}\ . \tag{1.59}$$

Although approximate, these expressions are suitable for a generic value of the fluid velocity near the interface and provide a starting point for the stability analysis of both strong and weak detonations. It is important to notice that $\tilde{l}_2$ is not singular for $\epsilon \to 0$ and that it reduces to $\bar{l}_2$ at first order; for this reason a second order expansion is necessary. This is not the case for $\tilde{l}_3$ which represents the singular root of (1.54) and for which the first order expansion is, in fact, sufficient.

Next, it is necessary to find the form of the eigenvectors $\vec{\mathbf{L}}_j$ contained in (1.50). This requires solving the matrix equation

$$\begin{pmatrix} (\omega+\tilde{l}_j v_x) & \gamma^2 w(\omega v_x+\tilde{l}_j)c_s^2 & wc_s^2 k \\ (\omega v_x+\tilde{l}_j) & \gamma^2 w(\omega+\tilde{l}_j v_x) & 0 \\ k & 0 & \gamma^2 w(\omega+\tilde{l}_j v_x) \end{pmatrix} \begin{pmatrix} \vec{\mathbf{L}}_{j\,1} \\ \vec{\mathbf{L}}_{j\,2} \\ \vec{\mathbf{L}}_{j\,3} \end{pmatrix} = 0\ , \\ j = 1,\ 2,\ 3 \tag{1.60}$$

which leads to the following eigenvectors

$$\vec{\mathbf{L}}_1 = \begin{pmatrix} 0 \\ 1 \\ -\dfrac{\tilde{l}_1}{k} \end{pmatrix}\ , \tag{1.61}$$

$$\vec{\mathbf{L}}_n = \begin{pmatrix} 1 \\ -\dfrac{(\omega v_x + \tilde{l}_n)}{\gamma^2 w(\omega + \tilde{l}_n v_x)} \\ -\dfrac{k}{\gamma^2 w(\omega + \tilde{l}_n v_x)} \end{pmatrix} , \qquad n = 2,\ 3 \tag{1.62}$$

It is now necessary to ascertain the values of the coefficients c_j for which the solution (1.49), with eigenvalues (1.57)–(1.59) and eigenvectors (1.61)–(1.62), satisfies the necessary boundary conditions. For this reason we have to check that, if there are time growing instabilities, the effects of these should be limited in space and not extend to infinity, so that

$$\lim_{x \to \pm\infty} |\vec{\mathbf{U}}(t, x, y)| = 0 \ . \tag{1.63}$$

After a few algebraic transformations, it is possible to verify that

$$\begin{aligned} &\text{(a)} \qquad \text{Im}\ (\omega) > 0 \quad \Longleftrightarrow \quad \text{Im}\ (\tilde{l}_1) < 0 \ , \\ &\text{(b)} \qquad \text{Im}\ (\omega) > 0 \quad \Longleftrightarrow \quad \text{Im}\ (\tilde{l}_2) < 0 \ , \\ &\text{(c)} \qquad \text{Im}\ (\omega) > 0 \quad \Longleftrightarrow \quad \text{Im}\ (\tilde{l}_3) < 0 \qquad \text{for } 0 < \epsilon < (1 - c_s) \end{aligned} \tag{1.64}$$

and

$$\begin{aligned} &\text{(d)} \qquad \text{Im}\ (\omega) > 0 \quad \Longrightarrow \quad \text{Im}\ (\tilde{l}_1) < 0 \ , \\ &\text{(e)} \qquad \text{Im}\ (\omega) > 0 \quad \Longrightarrow \quad \text{Im}\ (\tilde{l}_2) < 0 \ , \\ &\text{(f)} \qquad \text{Im}\ (\omega) > 0 \quad \Longrightarrow \quad \text{Im}\ (\tilde{l}_3) > 0 \qquad \text{for } -c_s < \epsilon \leq 0 \ . \end{aligned} \tag{1.65}$$

In order for (1.63) to be satisfied, it is necessary that Im $(\tilde{l}_j) > 0$ or that the corresponding coefficients c_j are zero for $x < 0$ and that Im $(\tilde{l}_j) < 0$ or $c_j = 0$ for $x > 0$. For modes with Im $(\omega) > 0$ we then have

$$
\begin{array}{lllll}
\text{(a)} & c_1 = c_2 = c_3 = 0 & \text{for } x < 0 \ , & & \\
\text{(b)} & c_1 \neq 0, \quad c_2 \neq 0, \quad c_3 = 0 & \text{for } x > 0 \ \text{ and } \epsilon \leq 0 & & \text{(strong, C} - \text{J)} \ , \\
\text{(c)} & c_1 \neq 0, \quad c_2 \neq 0, \quad c_3 \neq 0 & \text{for } x > 0 \ \text{ and } \epsilon > 0 & & \text{(weak)} \ .
\end{array}
\tag{1.66}
$$

In other words, the conditions (1.66) signify that no perturbations can grow ahead of the detonation front (*i.e.* $\vec{\mathbf{U}}(t, x, y) = 0$ for $x < 0$), while this is not necessarily the case for the positive x half-plane, where growing modes are allowed to exist since only one coefficient needs to be zero in the case of strong and Chapman-Jouguet detonations, and none in the case of weak detonations. This latter result represents an important difference between strong and weak detonations and will be further underlined in the following. The condition (1.66-a) on the coefficients c_j has its physical interpretation in the fact that in the negative x half-plane the flow is supersonic and "entering" the front and, as a consequence, no sonic signal (and therefore no perturbation) can be transmitted upstream of this flow. This can also be seen making use of Figure 1.8 which shows that the backward characteristic $\mathcal{C}^1_-$ has always a positive slope in the case of detonations.

Within the theory of shock wave stability, it is known that the conditions for a shock to be evolutionary (*i.e.* $v_1 > c_{s1}$, $v_2 < c_{s2}$), Landau and Lifshitz [90]) are only necessary but not sufficient to prove that it will not develop instabilities. This means that an evolutionary shock could become unstable with respect to small perturbations of the discontinuity surface, which would then appear as *"corrugations"* of the front[14] (see Figure 1.9).

Corrugation stability analyses of the type presented here have been performed in the past both for a non-relativistic shock (D'yakov [38], Kontorovich [78], Erpenbeck [44], Landau and Lifshitz [90]) and for a relativistic Chapman-Jouguet detonation (Abney [1]). A rather different approach for a relativistic shock wave has been proposed by Anile and Russo [10, 12] where the intuitive definition of corrugation stability introduced by Whitham [168] has been translated into a more rigorous form (we recall that according to Whitham, a corrugated shock wave is stable if the shock velocity decreases where the front in expanding and increases where it is contracting).

We next discuss the corrugation stability of relativistic strong detonation fronts and show how these relate to the special case of Chapman-Jouguet detonations. The

[14] We note that it is possible, in principle, to write necessary and sufficient conditions for a shock wave not to decay into a number of different discontinuity surfaces (Gorenstein and Zhdanov [51]). However, these conditions do not provide information about the evolution of the shock when this is subject to corrugations of the front.

first step consists in establishing the correct eigenvalues to choose. Making use of the conditions (1.64)–(1.65), together with (1.66), it is evident that it is necessary to use the eigenvalues $\tilde{l}_1,\ \tilde{l}_2$ (and the corresponding eigenvectors) in the case of strong and Chapman-Jouguet detonations ($\epsilon \leq 0$) while all of the eigenvalues $\tilde{l}_1,\ \tilde{l}_2,\ \tilde{l}_3$ would need to be used in the case of weak detonations ($\epsilon > 0$). The second step consists of requiring that the perturbed hydrodynamical equations satisfy junction conditions at the front expressing the conservation of energy and momentum respectively. These have already been introduced in Section 1.1 [*i.e.* as equations (1.4)–(1.5)], but we present them here in the new compact form:

$$\left[\gamma^2 w v_x\right]^{\pm} = 0 \ , \tag{1.67}$$

$$\left[\gamma^2 w v_x^2 + p\right]^{\pm} = 0 \ , \tag{1.68}$$

$$\left[v_y\right]^{\pm} = 0 \ , \tag{1.69}$$

where[15] $[A]^{\pm} = A^{+} - A^{-} = A_1 - A_2$. Note that these junction conditions need always to be expressed in the front rest frame and that the latter coincides with the coordinate frame only when the front is unperturbed.

Let us now suppose that the front is perturbed with a periodic oscillation in the y-axis direction of the type (see Figure 1.9)

$$\Delta = \Delta_0 e^{-i(\omega t + k y)} \ , \tag{1.70}$$

and let us calculate the resulting form of the perturbed junction conditions. For this purpose it is convenient to introduce orthogonal unit three-vectors normal ($\underline{\mathbf{n}}$) and tangent ($\underline{\mathbf{t}}$) to the front (see Figure 1.9) which, at the first order in the perturbation, have components

$$\underline{\mathbf{n}} \equiv (1,\ -\frac{\partial \Delta}{\partial y},\ 0) = (1,\ ik\Delta,\ 0) \ , \qquad \underline{\mathbf{t}} \equiv (\frac{\partial \Delta}{\partial y},\ 1,\ 0) = (-ik\Delta,\ 1,\ 0) \ . \tag{1.71}$$

[15] Hereafter upper indices + and − will be used to indicate quantities immediately ahead of and behind the front.

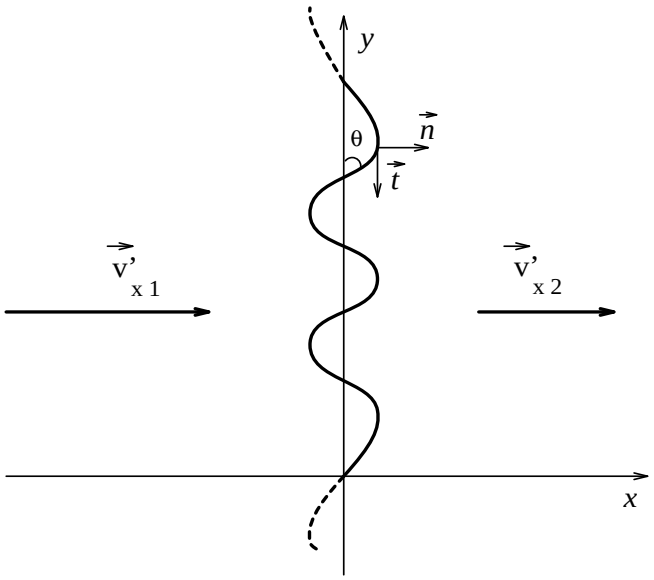

Figure 1.9 Schematic representation of a corrugated detonation front. $\underline{\mathbf{n}}$ and $\underline{\mathbf{t}}$ are orthogonal unit three-vectors, normal and tangent respectively to the discontinuity surface.

It is now necessary to evaluate the perturbed expressions for the fluid velocities on either side of the front, as these are viewed in the front rest frame. For this purpose it is necessary to perform a relativistic velocity transformation with respect to the detonation velocity $\vec{v}_f = (\partial\Delta/\partial t)\,\underline{\mathbf{n}} = (-i\omega\Delta)\,\underline{\mathbf{n}}$, so as to obtain the following expressions for the perturbed normal and tangential velocities relative to the front

$$\vec{v}_j{}' \cdot \underline{\mathbf{n}} = \left(\frac{v_{xj} + \delta v_{xj} + i\omega\Delta}{1 + i\omega v_{xj}\Delta},\ \delta v_{yj},\ 0 \right) \cdot \underline{\mathbf{n}} \cong v_{xj} + \delta v_{xj} + \frac{i\omega\Delta}{\gamma_j^2}\ , \tag{1.72}$$

$$\vec{v}_j{}' \cdot \underline{\mathbf{t}} \cong \delta v_{yj} - ikv_{xj}\Delta\ , \tag{1.73}$$

$$j = 1,\ 2$$

and to which corresponds a perturbed gamma factor

$$\delta\gamma_j \cong \gamma_j^3 v_{xj} \left(\delta v_{xj} + \frac{i\omega\Delta}{\gamma_j^2} \right)\ , \tag{1.74}$$

$$j = 1,\ 2$$

It is now convenient to introduce the new state vector of the perturbations near to the front and in downstream region of the flow

$$\vec{\mathbf{V}}_2(t,\ y) = \begin{pmatrix} \delta p_2 \\ \\ \delta v_{x2} \\ \\ \delta v_{y2} \end{pmatrix} , \tag{1.75}$$

where, as discussed above, each component of the corresponding $\vec{\mathbf{V}}_1(t,\ y)$ is automatically zero. Making use of (1.72)–(1.74) in (1.67)–(1.69), it is possible to write out the perturbed junction conditions and to use the resulting system of three equations in order to derive the components of $\vec{\mathbf{V}}_2(t,\ y)$. If there is a surface tension σ present (as in the case of a phase interface), it is necessary to modify the momentum balance across the front to take account of the effect of this (Zeldovich et al. [172]). While the energy balance at the front is unaffected by a constant surface tension (Miller and Pantano [113]). This contribution appears in the expressions for the negative x half-plane with the form $\sigma(\partial^2/\partial y^2 - \partial^2/\partial t^2)\Delta$, where the first term is related to the surface curvature, while the second is related to its "inertia". Omitting here the lengthy algebra, the three components of $\vec{\mathbf{V}}_2(t,\ y)$ are found to be

$$\delta p_2 = \frac{1+v_2^2}{\Gamma_- + \Gamma_+ v_2^2}\left[2i\omega w_2 \frac{(v_1 - v_2)(1 - v_1 v_2)}{(1+v_2^2)}\frac{\gamma_2^2 v_2}{v_1} + \sigma(\omega^2 - k^2)\right]\Delta , \tag{1.76}$$

$$\delta v_{x2} = -\frac{1-v_2^2}{\Gamma_- + \Gamma_+ v_2^2}\left[i\omega \frac{(v_1 - v_2)(1 - v_1 v_2)}{v_1}\Gamma_+ + \sigma(\omega^2 - k^2)\frac{\Theta_2}{w_2}v_2\right]\Delta , \tag{1.77}$$

$$\delta v_{y2} = -ik\Delta(v_1 - v_2) , \tag{1.78}$$

where $\Gamma_\pm = (1 \pm \Theta_2 \gamma_2^2 v_2^2)$, with $\Theta_2 = (\delta w_2/\delta p_2) = 1 + 1/c_{s_2}^2$ for a relativistic fluid (note that for compactness we have written $v_{1,2} \equiv v_{x1,x2}$ for the zeroth order velocities). Expressions (1.76)–(1.78) represent the special relativistic generalization of the equivalent expressions discussed in §90 of Landau and Lifshitz [90] and reduce to these when the Newtonian limit is taken. It is important to remark that the term $(\Gamma_- + \Gamma_+ v_2^2) = 1 + v_2^2(1 - \Theta_2)$, in the denominators of (1.76)–(1.77), vanishes whenever $v_2 = c_{s2}$, giving a singular behaviour at the sonic velocity similar to the one seen in the Newtonian case (Landau and Lifshitz [90]). We note that the corresponding expressions derived by Abney [1], differ from

(1.76)–(1.77) and do not show this singular behaviour except in their Newtonian limit. This discrepancy is due to the fact that in Abney's treatment the transformation to the front rest frame is a simple Galileian one and that the perturbation in the squared gamma factor is neglected. Unfortunately, we believe that these omissions, which radically change the nature of the solution at the sonic velocity and strongly influence the analysis, cannot be considered satisfactory.

We have already mentioned that a singular behaviour for a velocity behind the front equal to the local sound speed is a standard feature of the stability analysis of discontinuity surfaces. Nevertheless, great care must be taken when discussing these limiting cases, such as the present Chapman-Jouguet detonations. Some physical insight into the properties of Chapman-Jouguet detonations can already be gained when looking at the perturbed expressions for the hydrodynamical variables in terms of the perturbation Δ [*i.e.* inverting expressions (1.76)–(1.77)]. In this case, in fact, we could conclude that the corrugations produced on a Chapman-Jouguet detonation front by perturbations in the downstream fluid variables, are always zero and independent of the strength of the perturbations (*i.e.* independent of the magnitude of $\vec{\mathbf{V}}_2$). In other words, expressions (1.76)–(1.77) seem to indicate that at linear order a Chapman-Jouguet detonation is *unconditionally stable* (an identical conclusion will be drawn also from the study of the full dispersion relation for a Chapman-Jouguet detonation).

At this stage it is possible to deduce the form of the dispersion relation by requiring that the hydrodynamical perturbations present in the fluid adjacent to the phase interface are compatible and coincide with the perturbations produced by the corrugations of the front, *i.e.*

$$\vec{\mathbf{U}}(t,\ 0^+,\ y) \equiv \sum_{j=1}^{3} (c_j \vec{\mathbf{L}}_j) e^{-i(\omega t + k y)} = \vec{\mathbf{V}}_2(t,\ y)\ . \tag{1.79}$$

Writing out (1.79) explicitly results in a system of three equations with unknowns being given by the coefficients c_j, and by the amplitude of the surface displacement Δ_0. Whether equations (1.79) are sufficient to determine the dispersion relation depends on the number of nonzero coefficients c_j or, equivalently, on the degree of underdeterminacy of the detonation front (see Subsection 1.3.1)

In the case of a strong or Chapman-Jouguet detonation there exist three free parameters (which correspond to the unknowns $c_1,\ c_2$ and to Δ_0) and the front then has zero degree of underdeterminacy (see Table II). In this case, equation (1.79) has a solution provided that the determinant of the matrix of coefficients vanishes, *i.e.*

$$\det \begin{pmatrix} 0 & 1 & \delta p_2 \\ 1 & -\dfrac{(\omega v_x + \tilde{l}_2)}{\gamma_2^2 w_2(\omega + \tilde{l}_2 v_x)} & \delta v_{x2} \\ -\dfrac{\tilde{l}_1}{k} & -\dfrac{k}{\gamma_2^2 w_2(\omega + \tilde{l}_2 v_x)} & \delta v_{y2} \end{pmatrix} = 0 \ . \tag{1.80}$$

After some algebra, the general form of the dispersion relation is found to be

$$\begin{aligned} &\frac{w_2}{\Gamma_- + \Gamma_+ v_2^2}\Bigg\{ i\frac{(v_1 - v_2)}{v_1}\Bigg[\omega^3 \frac{(1 - v_1 v_2)(\Gamma_+ - 2\gamma_2^2 v_2^2)}{v_2} + \omega^2 (1 - v_1 v_2)(\Gamma_+ - 2\gamma_2^2)\tilde{l}_2 \\ &+\omega\left[2v_2(1 - v_1 v_2) - v_1\left(\Gamma_- + \Gamma_+ v_2^2\right)\right]\gamma_2^2 k^2 - \gamma_2^2 v_1 v_2 k^2 \left(\Gamma_- + \Gamma_+ v_2^2\right)\tilde{l}_2\Bigg] \\ &+\sigma\frac{(\omega^2 - k^2)}{w_2}\left[\omega^2\left(\Theta_2 - 1 - v_2^2\right) - \frac{\omega}{v_2}\left(\Gamma_- + \Gamma_+ v_2^2\right)\tilde{l}_2 + (1 + v_2^2)k^2\right]\Bigg\} = 0 \ , \end{aligned} \tag{1.81}$$

which provides a relation $\omega = \omega(k)$ once the free variables v_1, v_2, c_{s2} and σ/w_2 are specified.

On the other hand, in the case of a weak detonation there exist four free parameters (corresponding to the unknowns c_1, c_2, c_3 and Δ_0) and this forces the introduction of a suitable fourth boundary condition in order to make the solution fully determined. In this respect, weak detonations are similar to weak deflagrations and in order to be fully determined require an equation describing the microscopic burning mechanism or, in the case of phase transitions, the rate of transformation of the old phase into the new one. This feature of weak detonations does not allow for a *general* discussion of their stability properties and restricts the analysis to the specific situations in which the fourth boundary condition can be expressed. For this reason, in the following we will limit ourselves to discuss the general stability properties of Chapman-Jouguet and strong detonations only.

Recalling the definition (1.58) of $\tilde{l}_2$, it is possible to see that a strong detonation naturally evolves into a Chapman-Jouguet detonation when the velocity behind the front passes from being subsonic to being equal to the sound speed. This is the case which we will discuss first. We set $\epsilon = 0$, $v_2 = c_s$ (hereafter $c_s \equiv c_{s2}$) and (1.81) then reduces to

$$\frac{w_2}{\Gamma_- + \Gamma_+ c_s^2}\left\{ i\frac{(v_1 - c_s)}{v_1}\left[2\omega^3\frac{(1 - v_1 c_s)}{c_s} + 2\omega(1 - v_1 c_s)\gamma_2^2 c_s k^2\right]\right.$$
$$\left. +\sigma\frac{(\omega^2 - k^2)}{w_2}\left[\omega^2\frac{(1 + c_s^2)}{\gamma_2^2 c_s^2} + (1 + c_s^2)k^2\right]\right\} = 0 \, . \tag{1.82}$$

Note that the dispersion relation (1.82) does not contain the eigenvalue $\tilde{l}_2$ (which is always multiplied by vanishing terms) and that, in order to avoid a singularity, the content of the curly brackets in (1.82) has to be zero. This condition can be imposed by requiring that

$$(\omega^2 + \gamma_2^2 c_s^2 k^2)\left[2i\omega\frac{(v_1 - c_s)(1 - v_1 c_s)}{v_1 c_s} + \sigma\frac{(\omega^2 - k^2)}{\gamma_2^2 c_s^2 w_2}\right] = 0 \, , \tag{1.83}$$

which has the four distinct roots

$$\omega_{1,2} = \pm\, i\gamma_2 c_s k \, , \tag{1.84}$$

$$\omega_{3,4} = -\frac{\gamma_2^2 c_s w_2}{v_1 \sigma}\left\{ i(v_1 - c_s)(1 - v_1 c_s) \mp \right.$$
$$\left. \left[\left(\frac{v_1\sigma}{\gamma_2^2 c_s w_2}\right)^2 k^2 - (v_1 - c_s)^2(1 - v_1 c_s)^2\right]^{1/2}\right\} . \tag{1.85}$$

We note that it is a common experience in dealing with the solution of dispersion relations that spurious roots can be introduced, which then need to be discarded on the basis of physical or conceptual considerations. An example of this is the root ω_1 which has positive imaginary part and would lead to an exponentially growing unstable mode. However, ω_1 should be rejected since it does not satisfy energy boundary conditions at short wavelengths and would lead to a "high frequency catastrophe". It is well known, in fact, that the surface energy associated with a perturbation of amplitude Δ is proportional to $\sigma k^2 \Delta^2$ and a cutoff wave number, above which instabilities are not allowed, is necessary in order to avoid accumulation of infinite energies at high frequencies.

The physical mechanisms which operate this limitation depend on the specific situation under examination and can be either dissipative effects, such as a fluid viscosity, or can be the consequence of surface tension. However, the root ω_1 does not contain any

contribution coming from the surface tension and this has the consequence that even an infinitely stiff front (*i.e.* one with $\sigma \to \infty$) would appear to be unstable at all wavelengths. This behaviour suggests that the roots $\omega_{1,2}$ cannot provide a physical description of detonation fronts and will be discarded here. Further evidence of the inapplicability of the roots (1.84) comes from realizing that the term $(\omega^2 + \gamma_2^2 c_s^2 k^2)$ in (1.83) is the consequence of a Doppler frequency transformation relative to a medium moving at the sound speed; with a few simple calculations it is easy to see that this term should always be different from zero (see the Appendix A).

On the other hand, after some algebraic manipulations (the details of which are also presented in the Appendix A), it is possible to show that the other two roots $\omega_{3,4}$, which are clearly dependent on σ, both have negative imaginary parts and therefore lead to *stable* solutions. As discussed when imposing the validity of the junction conditions across the detonation front, this is a further and more direct proof that at first order a Chapman-Jouguet detonation is *unconditionally stable*. We remark that this conclusion is in contrast with the results presented by Abney in [1] which indicated that Chapman-Jouguet detonations are effectively unstable at all wavelengths. As mentioned before, the origin of this discrepancy is to be found in the approximations adopted in [1] for the derivation of the perturbed hydrodynamical quantities behind the detonation front, which have artificially removed the singular properties of this class of detonations and have led to erroneous conclusions.

The situation is not very different when the more general strong detonations are discussed. In this case, all of the expressions in the dispersion relation (1.81) need to be expanded around the sound speed, with terms up to the second order being retained. This is a consequence of the fact that at first order Chapman-Jouguet detonations and strong detonations are indistinguishable and a second order expansion is therefore necessary. The complete general dispersion relation, which results from lengthy algebraic manipulations, is presented in the Appendix A. Here, we limit ourselves to discussing the equivalent expression obtained by setting $c_s^2 = 1/3$

$$\left\{\frac{2\sigma}{w_2}\left(\frac{4}{3}-7c_s\epsilon+4\epsilon^2\right)\omega^7+i\left[8c_s-v_1\left(1+\frac{1}{v_1^2}\right)(2+3c_s\epsilon)+12c_s\epsilon^2\right]\omega^6\right.$$
$$-\frac{\sigma k^2}{w_2}\left(\frac{4}{3}-19c_s\epsilon+\frac{17}{2}\epsilon^2\right)\omega^5+ik^2\left[4c_s-v_1\left(1+\frac{1}{v_1^2}\right)\right.$$
$$\left.+\left(10-\frac{3v_1c_s}{2}\left(5+\frac{7}{v_1^2}\right)\right)\epsilon+\left(54c_s-\frac{69}{4}\left(1+\frac{1}{v_1^2}\right)\right)\epsilon^2\right]\omega^4$$
$$-\frac{\sigma k^4}{w_2}\left(\frac{4}{3}+5c_s\epsilon+\frac{\epsilon^2}{4}\right)\omega^3-i\frac{k^4\epsilon}{2}\left[1-3v_1c_s-\left(\frac{v_1}{4}\left(11+\frac{1}{v_1^2}\right)-\frac{13}{2}c_s\right)\epsilon\right]\omega^2$$
$$\left.+\frac{3k^6\sigma\epsilon^2}{4w_2}\omega+i\frac{3k^6}{8}(c_s-v_1)\epsilon^2\right\}\frac{w_2}{3\epsilon(2c_s+\epsilon)}=0\ . \tag{1.86}$$

As for the case of (1.82), equation (1.86) can be satisfied only if the content of the curly brackets is set equal to zero and this results in a seventh order equation in ω with complex coefficients. [It is straightforward to check that (1.86) reduces to (1.83) when $\epsilon = 0$.] The roots of (1.86) can only be computed numerically and for this we have implemented an algorithm which makes use of a variant of Laguerre's Method (NAG Fortran Library C02AFF [106]). The computations can be performed only after all the parameters have been specified and for this purpose we have set $v_1 = (3/2)c_s$ and $\epsilon = -0.01$. We stress that only the solution of the complete polynomial allows one to deduce a consistent picture of the functional dependence of the growth rate on the wavenumber k. Any analysis which studies the dispersion relation (1.86) in the approximate expressions which it assumes in the long and short wavelength *limits* (as done by Abney [1]) can easily give rise to confusing outcomes.

We present in Figure 1.10 (a) results of the numerical computations for the long wavelength region and in Figure 1.10 (b) for the short wavelength one, with the wavenumber being expressed in units of w_2/σ. Figure 1.10 (a) and (b) indicate that there is always a root of (1.86) which has positive imaginary part (all of the others have either negative or constant imaginary part).

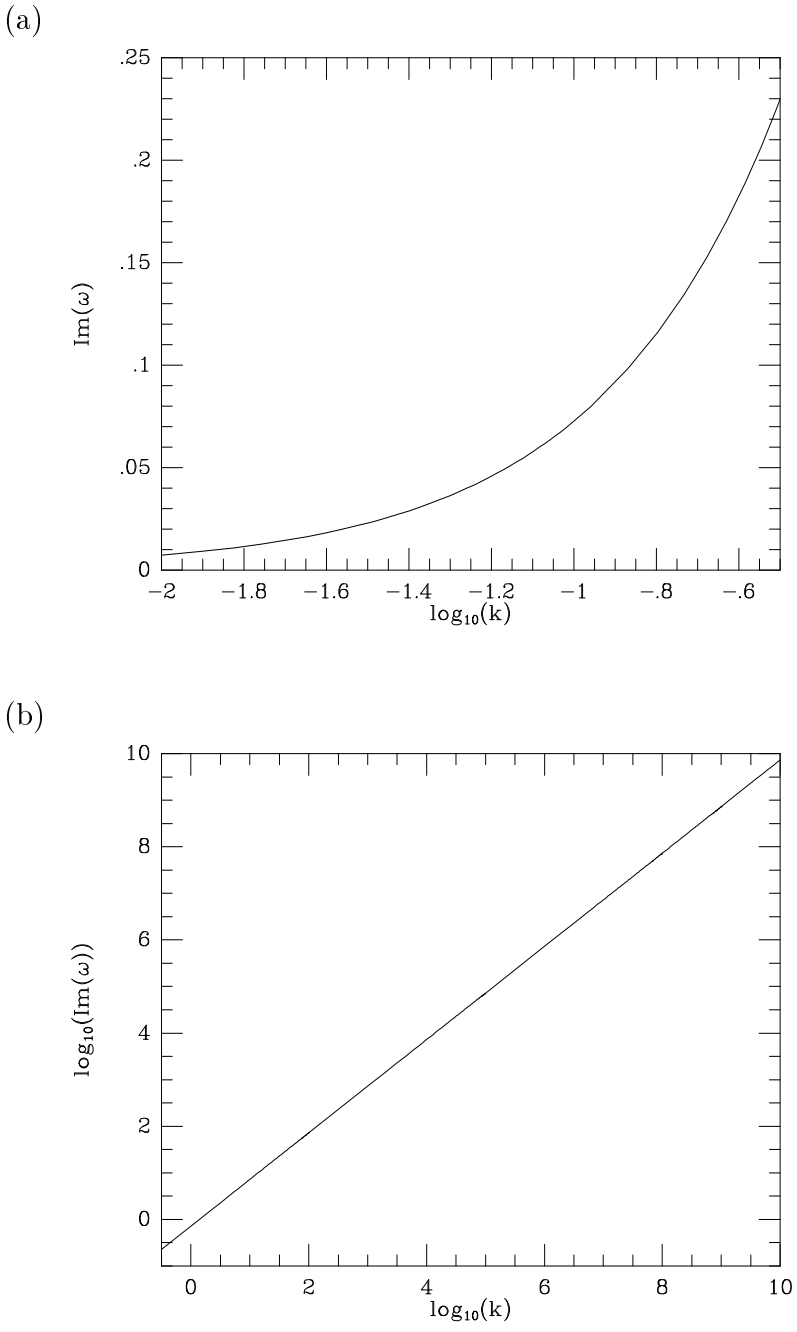

Figures 1.10 Perturbation growth rate Im (ω) plotted as a function of the logarithm of the real wavenumber k expressed in units of w_2/σ. Figure (a) refers to the long wavelength region, while Figure (b) to the short wavelength one. The curves have been calculated assuming $v_1 = (3/2)\ c_s$, $c_s = 1/\sqrt{3}$ and $\epsilon = -\ 0.01$.

The instabilities described by this root have a growth rate which is independent of σ, increases linearly with the wavenumber k and produces an inevitable energy divergence at high frequencies. They clearly represent the relics of the unstable modes contained in the root ω_1 of the dispersion relation (1.83) and, in analogy with what deduced for Chapman-Jouguet detonations, the results shown in Figure 1.10 refer to a physically inconsistent solution and should be discarded.

As a result, we can conclude that strong detonations also are linearly *stable* to corrugations of the front and in this they resemble Chapman-Jouguet detonations to which they reduce for $\epsilon \to 0$. A similar result (*i.e.* that an evolutionary front is also stable with respect to corrugations), has been obtained also by Anile and Russo [11, 12, 10] in the context of the stability of shock waves. Proceeding within the theory of singular hypersurfaces, they came to the conclusion that the linear stability conditions for planar relativistic shock waves coincide with those obtained in the framework of corrugation stability.

Before turning to the discussion of the stability of deflagration fronts, a comment should be made on strong detonations and the possibility of employing them for the growth of new phase bubbles during cosmological phase transitions. We have just proved that strong detonations are both evolutionary and stable with respect to corrugation instabilities, however it is possible to demonstrate that such flow configurations cannot be realized during bubble growth as they cannot satisfy the required boundary conditions for a self similar solution. Proofs of this have been given by Landau and Lifshitz [90] for nonrelativistic planar and spherical fronts, by Steinhardt [153] for relativistic spherical fronts and by Laine [85] for the case of relativistic planar fronts. The impossibility of having this class of reaction fronts as representative of the motion of the surface of a "bubble" can be shown also with simpler arguments. Consider a fluid element which is immediately behind a strong detonation and which has just been transformed into the new phase (we here make the implicit assumption that the sound speeds are constant on either side of the front). This fluid element, which was initially at rest, has been put into motion by the front which will be seen by the fluid element as receding at a subsonic velocity. Symmetry and the presence of an origin for the bubble, require that the fluid velocity behind the front becomes zero somewhere in the flow profile and this could occur either via a rarefaction wave, or via a shock wave. However, the front edge of the rarefaction wave or the discontinuity surface would be seen as moving at the sound speed or faster relative the fluid element and as a consequence either one would inevitably overtake the detonation front. As a result, neither of these two flows can be established behind a strong detonation front which is then unable to adjust itself to the required boundary conditions and so cannot be produced in practice as a stationary solution for

bubble growth.

1.3.3 Stability of Deflagrations

The linear stability of classical planar deflagration fronts was first studied by Landau in a seminal work of 1944 [89] in which he showed that, at linear order in the perturbation, a "slow combustion front" (weak deflagration) is unstable at any wavelength. This result was compatible with the observed irregularities in propagating planar combustion fronts and indicated that higher order effects were probably responsible for the saturation of the oscillations and the production of the globally stable cellular fronts. In his derivation, Landau concentrated on a weak deflagration and made use of the hypothesis of continuity of the pressure field across the deflagration front. This approximation allowed him to reduce to zero the degree of underdeterminacy of the front and to obtain the solution of the problem. Such a choice is certainly reasonable when the fluid *is not* relativistic and the perturbations produced at the front are not so significant so as to alter the continuity of the pressure across the front. However, when the fluid *is* relativistic, this approximation ceases to be a good one and the problem needs to be solved taking into account the pressure variation along with the conservation of momentum across the front (we recall that the pressure should be seen as a flux of momentum).

A linear stability analysis of relativistic deflagration fronts would resemble closely the one presented in the previous subsection, but with some important differences emerging because of the different causal structure between deflagrations and detonations. In particular, it is necessary to reconsider the values of the coefficients c_j of the solution (1.50) that satisfy the boundary conditions (1.63). In the case of a deflagration, in fact, the solution of the perturbed hydrodynamical equations does not extend to infinity only if

$$\begin{array}{lllll} \text{(a)} & c_1 = c_2 = 0, \;\; c_3 \neq 0 & \text{for } x < 0 \,, & & \\ \text{(b)} & c_1 \neq 0, \;\; c_2 \neq 0, \;\; c_3 = 0 & \text{for } x > 0 \;\; \text{and } \epsilon \leq 0 & & \text{(weak, C} - \text{J)} \,, \\ \text{(c)} & c_1 \neq 0, \;\; c_2 \neq 0, \;\; c_3 \neq 0 & \text{for } x > 0 \;\; \text{and } \epsilon > 0 & & \text{(strong)} \,. \end{array} \tag{1.87}$$

A first consequence of the conditions (1.87–a) is that it is no longer possible to assume the perturbed state vector of the fluid ahead $\vec{\mathbf{V}}_1(t,\ y)$ to be identically zero (as done for detonations) since there exists at least one coefficient which does not need to

be zero. This can also be seen making use of Figure 1.8 which shows that the backward characteristic $\mathcal{C}_-^1$ has always a negative slope in the case of deflagrations. A second consequence concerns the degree of underdeterminacy of a deflagration, which is always larger than zero. In particular, the degree of underdeterminacy of a weak or Chapman-Jouguet deflagration is one, since there are four different parameters (*i.e.* c_3 ahead of the front, c_1 and c_2 behind the front and Δ_0) that need to be specified, while it is two for a strong deflagration since there are five different parameters (*i.e.* c_3 ahead of the front, c_1, c_2 and c_3 behind the front and Δ_0) which could be associated with a small perturbation of the front (see Subsection 1.3.1).

As discussed in the previous subsection for the case of weak detonations, a finite degree of underdeterminacy of weak and Chapman-Jouguet deflagrations prevents from a *general* discussion of their stability properties and limits the analyses to those situations for which a consistent fourth boundary condition can be expressed. Attempts of the study of the linear stability properties of relativistic weak deflagrations as phase interfaces during cosmological phase transitions have been carried out in the past both in the limit of small velocities (Link [100], Kamionkowski and Freese [71], Adams et al. [7]) and in the case of small and large velocities (Huet et al. [60]). Unfortunately the results obtained from these analyses are often in conflict and this is due mainly to the strong dependence of the stability properties on the form chosen for the boundary condition on the velocity of the deflagration front (*i.e.* on the rate at which the transition proceeds).

We believe that further theoretical study is necessary in order to specify in a more precise way the microphysical processes taking place at the phase interface and that before this is done too much room to uncertainty is left in the analysis.

1.4 Appendix A

In this Appendix, details are presented of different expressions which are discussed in Subsection 1.3.2. In the first part of this Appendix, a rigorous proof is given of the physical inconsistency of the the first two roots of the dispersion relation for the perturbations of a Chapman-Jouguet detonation, while in the second part it is shown that the other two roots do not correspond to unstable modes. Finally, the third part of the Appendix is focussed on the presentation of the complete and generic expressions of the dispersion relation (1.81) in the case of strong detonations.

I. Unphysical solutions: $\omega_{1,2}$

We start with showing that the quantity $(\omega^2 + \gamma_2^2 c_s^2 k^2)$ in equation (1.83) should always be different from zero. Because in the Newtonian case the expressions are simpler and can be handled analytically we will give the proof in this limit of small velocities. However, the extension of the result to the special relativistic case is rather straightforward. As discussed in Subsection 1.3.2, the dispersion relation can be obtained once requiring that the perturbed state vector satisfies the junction conditions for the energy and momentum. In the limit of small velocities, we can neglect all the γ Lorentz factors and the components of the perturbed state vector can be simply written as [we here omit a common factor $\exp\left[-i(\omega t + k_y)\right]$ and drop the indices referring to region 2]

$$\begin{aligned}
\delta p &= c_2 \gamma^2 w \frac{(\omega + l v_x)}{(\omega v_x + l)} e^{-ilx} \simeq c_2 w \frac{(\omega + l v_x)}{l} e^{-ilx} \ , \\
\delta v_x &= c_1 e^{i(\omega/v_x)x} + c_2 e^{-ilx} \ , \\
\delta v_y &= c_1 \frac{\omega}{v_x k} e^{i(\omega/v_x)x} + c_2 \frac{k}{(\omega v_x + l)} e^{-ilx} \simeq c_1 \frac{\omega}{v_x k} e^{i(\omega/v_x)x} + c_2 \frac{k}{l} e^{-ilx} \ ,
\end{aligned} \tag{1.88}$$

where $l \equiv \tilde{l}_2$ and we have used $\tilde{l}_1 = -\omega/v_x$. Note that we have here exploited the possibility for a different normalization of the eigenvectors $\vec{\mathbf{L}}_1$, $\vec{\mathbf{L}}_2$ and we are not restricting the discussion to the case $x = 0$.

Imposing the condition (1.79) and asking for the determinant of the coefficients to be zero is equivalent to set

$$\det \begin{pmatrix} 0 & w\dfrac{(\omega + lv_x)}{l}e^{-ilx} & \delta p \\ e^{i(\omega/v_x)x} & e^{-ilx} & \delta v_x \\ \dfrac{\omega}{v_x k}e^{i(\omega/v_x)x} & \dfrac{k}{l}e^{-ilx} & \delta v_y \end{pmatrix} = 0 \ . \tag{1.89}$$

A solution of (1.89) is clearly given by

$$\omega = -lv_x = iv_x k \ , \tag{1.90}$$

where we have used, from (1.54), that $l = l_2 \simeq -ik$. However, the solution (1.90), which represents the small velocity limit of the positive root of (1.84), is a spurious one and should be discarded since it would imply that $c_1 + c_2 = 0$, and the corresponding solution (1.88) would be then identically zero.

II. Unphysical solutions: $\omega_{3,4}$

Next we show that the roots of (1.83) do not produce unstable modes. For this purpose, it is convenient to rewrite the roots $\omega_{3,4}$ as

$$\omega_{3,4} = -k_c \left[i \mp \left(\frac{k^2}{k_c^2} - 1 \right)^{1/2} \right] \ , \tag{1.91}$$

where k_c is a critical wavenumber defined as

$$k_c = \frac{\gamma_2^2 c_s w_2 (v_1 - c_s)(1 - v_1 c_s)}{v_1 \sigma} \ . \tag{1.92}$$

Since k_c is a positive real number for a detonation, the sign of the square root in (1.91) depends on whether the wavenumber for the perturbation mode k is larger or smaller than the critical wavenumber. The imaginary part of $\omega_{3,4}$ can then be

$$\text{Im } \omega_{3,4} = -k_c < 0 \, , \qquad \text{if } k \geq k_c \ , \tag{1.93}$$

or

$$\text{Im}\ \omega_{3,4} = -k_c \left[1 \mp \left(1 - \frac{k^2}{k_c^2}\right)^{1/2}\right] , \qquad \text{if } k < k_c \, . \tag{1.94}$$

It is easy to see that in both cases and irrespective of which of the two roots is chosen, the imaginary part of the solutions of the dispersion relation is always negative, thus establishing the stability properties of Chapman-Jouguet detonation.

III. General Dispersion Relation

Finally, we turn to the general expression of the dispersion relation which is deduced after lengthy but straightforward algebraic manipulations. In the case of strong detonation fronts and writing $v_2 = c_s + \epsilon$, (with ϵ being suitably small), equation (1.81) becomes

$$\begin{aligned}
&\left\{ i\left(1 - \frac{c_s+\epsilon}{v_1}\right)\left\{\left[(1-v_1c_s)\frac{2}{c_s} - \frac{(1+v_1c_s)}{c_s^2}\epsilon + \frac{(c_s^4-2c_s^2+1)}{c_s^3(1-c_s^2)^2}\epsilon^2\right]\omega^3\right.\right. \\
&\quad + k^2\left\{\frac{2c_s(1-v_1c_s)}{1-c_s^2} + \frac{[c_s(3+c_s^2)+v_1(2c_s^4-7c_s^2+1)]}{c_s(1-c_s^2)^2}\epsilon\right. \\
&\quad\left.\left. + \frac{[c_s(c_s^4+14c_s^2+1)+v_1(c_s^6-26c_s^4-7c_s^2-4)]}{2c_s^2(1-c_s^2)^3}\epsilon^2\right\}\omega \right. \\
&\quad + \left[\frac{v_1c_s}{1-c_s^2}\epsilon + \frac{[v_1(3+2c_s^2)-c_s]}{2(1-c_s^2)^2}\epsilon^2\right]\frac{k^4}{\omega} - \frac{v_1k^6c_s^2}{2(1-c_s^2)^2\omega^3}\epsilon^2\Big\} \\
&\quad + \frac{\sigma}{w_2}\left\{\left[(1-c_s^4)c_s^2 - c_s(2c_s^4+c_s^2+1)\epsilon + (1-c_s^4)\epsilon^2\right]\frac{\omega^2}{c_s^4}\right. \\
&\left.\left. + (c_s^2+1)k^2 + \frac{(2c_s^2+1)k^2}{c_s}\epsilon + \frac{(2c_s^2-1)k^2}{2c_s^2}\epsilon^2 - \frac{k^4}{2(1-c_s^2)\omega^2}\epsilon^2\right\}\right\}\frac{1}{\epsilon(2c_s+\epsilon)} = 0 \, ,
\end{aligned} \tag{1.95}$$

which reduces to (1.86) when $c_s^2 = 1/3$.

1.5 Summary

- *Discontinuity surfaces represent a typical aspect of compressible fluids hydrodynamics. They are extremely narrow regions of the flow across which fluid variables experience very high gradients. These regions are called* **shock fronts** *and* **reaction fronts** *if a fluid flow takes place across them.*

- *If the width of these regions is very small as compared with the typical hydrodynamical length scales and if the time scale set by the motion of these regions is smaller than the thermal and viscous time scales, a satisfactory physical and mathematical treatment of discontinuity surfaces can be achieved in terms of fictitious infinitesimal surfaces across which conservation laws apply.*

- *Shock fronts and reaction fronts share many properties and can be described by means of the same mathematical formalism. The main difference between the two classes of discontinuity surfaces is that the fluid flow across a reaction front is* **also** *subject to a* **chemical** *and* **physical transformation**. *As a consequence, the fluid states on either side of a reaction front are described by two* **different** *equations of state.*

- *The* **Poisson Adiabat**, *the* **Taub Adiabat** *and the* **Reaction Adiabat** *represent very useful tools to discriminate the different possible hydrodynamical solutions of the conservation laws in the case of (Newtonian and relativistic) shocks and of reaction fronts.*

- *The* **Transition adiabat**, *in particular, allows to distinguish a generic reaction front into a* **detonation** *or into a* **deflagration**. *Relative to their medium ahead, these fronts are supersonic and subsonic respectively.*

- *Detonations (deflagrations) can be further distinguished into* **weak**, **strong** *and* **Chapman-Jouguet** *detonations (deflagrations) according to whether the flow behind the front is supersonic (subsonic), subsonic (supersonic) or equal to the local sound speed as measured in the rest frame of the front.*

- *A discontinuity surface that satisfies conservation laws is* **thermodynamically stable** *and can be momentarily produced. However, this does not guarantee that it will not become* **hydrodynamically unstable**.

- *A simple indication of the stability properties of a discontinuity surface comes from the calculation of its* **degree of underdeterminacy**. *This is given by the number of underdetermined parameters that can be associated with a perturbation of the surface.*

- *While a discontinuity with a zero degree of underdeterminacy is linearly stable, the opposite is not true for a discontinuity with a finite degree of underdeterminacy.*

- *Strong and Chapman-Jouguet detonations have* **zero degree** *of underdeterminacy. Weak detonations, weak and Chapman-Jouguet deflagrations have* **one degree** *of underdeterminacy. Strong deflagrations have* **two degrees** *of underdeterminacy.*

- *The degree of underdeterminacy of a reaction front can be conveniently represented in terms of characteristic curves. Such a representation of the causal structure of reaction fronts points out the lack of any* **mutual causal connection** *between a weak detonation and the media on either side of the front.*

- *Because of their peculiar causal structure, weak detonation fronts* **cannot** *counteract the growth of any perturbation possibly produced.*

- *A finite degree of underdeterminacy has the consequence that it is* **not** *possible to perform a* **general** *stability analysis unless further equations are supplemented. The latter are generally strongly dependent on the specific problem under exam.*

- *Contrary to recent claims, we have shown that strong detonations are both* **evolutionary and stable** *with respect to corrugations of the front and that Chapman-Jouguet detonations appear to be* **evolutionary and unconditionally linearly stable**. *This is in agreement with indications coming from the degree of underdeterminacy of these fronts.*

Chapter 2

Relativistic Self Similar Solutions for Spherical Deflagrations

2.1 Introduction to Self Similar Hydrodynamics

As mentioned in the previous chapter, relativistic reaction fronts have been investigated in great detail since they could serve to describe the dynamics of the phase interface between the new, low temperature phase and the old, high temperature phase during cosmological first order phase transitions. This chapter is dedicated to the analysis of the hydrodynamics of spherical weak deflagrations which could have played a particularly important role during phase transitions in the early Universe.

The reason for this privileged role has to be found in the fact that deflagrations in general and weak deflagrations in particular require minimal conditions in order to be produced within a cosmological scenario (see Section 4.3 for a discussion of this). As a result, the hydrodynamics of spherical weak deflagrations can be used in order to describe the dynamics of the disconnected regions during first order phase transitions and in particular to follow the growth of *bubbles* of the new phase or the evaporation of *drops* of the old phase. We here will refer to as a growing bubble an *expanding* spherical system having one discontinuity surface moving as a reaction front. Conversely, we will refer to as an evaporating drop a *contracting* spherical system having one discontinuity surface moving as a reaction front. The concepts and the general solutions presented here will have a direct application in the discussion of the general relativistic hydrodynamics of the cosmological quark–hadron phase transition which will be presented in Chapter 5.

However, before discussing in detail the general solutions for bubbles and drops, it

is convenient to introduce the important and recurrently used terms of *similarity* and *self similarity*.

The concept of similarity is widely used in mechanics and hydrodynamics and relies on the possibility of modelling a physical phenomenon of interest by the study of an analogous phenomenon whose properties can be suitably rescaled. In this way, by exploiting the properties of similarity, it is possible to perform, in reduced and inexpensive laboratory conditions, experiments that would otherwise require much more considerable efforts. As in the conversion from a system of units to another one, the properties of a specific phenomenon can then be deduced from the assigned properties of another phenomenon, when the latter is *similar* to the first one (Sedov [150]).

Of course, not all phenomena can be scaled in a similar way and the definition of some *similarity criteria* is therefore relevant. For this purpose, let a given phenomenon be described by a number n of parameters some of which are dimensionless and other dimensional physical quantities. Moreover, assume that the dimensions of the physical quantities are expressed by means of k fundamental units with $k \leq n$. In the general case then, it is evident that $n - k$ is the maximum number of independent dimensionless combinations out of the n parameters. In other words, all of the dimensionless properties of the given phenomenon can be expressed in terms of the $n-k$ independent dimensionless combinations. It follows then, that a necessary and sufficient condition for two phenomena to be similar is that the number of their independent dimensionless combinations of parameters is the same for the two phenomena (Sedov [150]). For a relativistic system expressed in geometrical units (*i.e.* in which $c = G = 1$), for example, all dimensional quantities can be thought of as lengths and dimensionless parameters can be thought of as velocities.

While the condition of similarity is useful to establish a relation between two phenomena, the condition of self similarity is useful to establish a relation between a phenomenon and itself. Formally speaking, a solution to a mechanical or hydrodynamical problem is said to be self similar when it can be described by no more than two quantities with independent dimensions other than space and time. When this is the case, all of the physical quantities representative of the problem can be rewritten as a function of a *similarity variable*, which is usually a combination of the spatial and time coordinates. In other words, although a self similar solution does evolve in time (*i.e.* it is not stationary), it nevertheless evolves so that the solution at any instant is *similar* (in the sense defined above) to the solutions at neighbouring instants (Batchelor [17]). An obvious conclusion that can be drawn from the discussion above is that a self similar solution can be realized in practice only in a physical system that does not possess intrinsic length or time scales since the latter could not be expressed in terms of the similarity variable.

There are at least two important reasons in order to look for hydrodynamical self similar solutions. The first one is that it is in general much simpler to find an analytical solution to a given hydrodynamical problem when the relevant equations are written in terms of a self similar variable. The second reason is that nature seems to privilege solutions which have self similar properties. In this sense, the search for a self similar behaviour does not represent the search for an exotic and unrealistic solution, but rather the search for that peculiar behaviour of the system it would "naturally" tend to assume in the absence of length or time scales.

2.2 Self Similar Hydrodynamics of a Bubble

The classical dynamics of *boiling bubbles*[1] connected with first order phase transitions has been widely studied and represents a valuable background for the discussion of the growth of the low temperature phase bubbles during cosmological phase transitions. The main results of the theory of classical bubble dynamics are contained in a number of works (Plesset and Prosperetti [129], Plesset and Zwick [130], [131]) which represent a further development of a fundamental paper by Rayleigh [135] published in 1917. We will omit here a discussion of the solutions and strategies developed in order to follow a classical boiling bubble (see Pantano [127], and Rezzolla [136] for a review), but it is important to point out that already within a simple classical treatment, the motion of the vapour-liquid interface can become extremely complicated when the effects of viscosity and mass exchange are taken into account (Theofanus et al. [160], Prosperetti [134]). In these cases, the hydrodynamical models can be simplified by making a number of phenomenological assumptions about the efficiency of the mass transfer across the phase interface which can then be verified by means of experimental measurements. A similar phenomenological approach will be used also in Subsection 5.2.3 where a suitable equation for the transformation rate across a quark–hadron phase interface will be defined.

Self similar growth of bubbles in first order cosmological transitions has been considered in literature both in the case of detonation fronts (Steinhardt [153], Gyulassy et al. [54], Laine [85]) and deflagration fronts (Kurki-Suonio [80], Kurki-Suonio and Laine [82], Miller and Pantano [113, 114]). For bubble expansion, self similar motion can appear only when the bubble radius is small enough so that there is no interaction between neighbouring bubbles, but large enough so that surface tension effects are negligible. This

[1]Boiling bubbles are *vapour bubbles* (*i.e.* bubbles whose interiors contain only vapour of surrounding fluid) that are nucleated in a superheated fluid. Boiling bubbles should be distinguished from *cavitation bubbles* which are vapour bubbles nucleated within a cool (*i.e.* in a normal state) fluid.

is the regime we will consider here and, moreover, we assume that although the fluids are relativistic, their selfgravity does not play any important role on the scale of the bubbles being considered here. As a result, it is quite sufficient in order to obtain self similar solutions to consider only the special relativistic form of the conservation equations (1.3), (1.34) and (1.35) which can be also written in the following, geometry independent form

$$\frac{\partial}{\partial t}\left(\gamma\rho\right)+\frac{\partial}{\partial r}\left(\rho\gamma v\right) = -\frac{j}{r}\rho\gamma v\,, \tag{2.1}$$

$$\frac{\partial}{\partial t}\left[\left(e+pv^2\right)\gamma^2\right]+\frac{\partial}{\partial r}\left[\left(e+p\right)\gamma^2 v\right] = -\frac{j}{r}\left[\left(e+p\right)\gamma^2 v\right]\,, \tag{2.2}$$

$$\frac{\partial}{\partial t}\left[\left(e+p\right)\gamma^2 v\right]+\frac{\partial}{\partial r}\left[\left(ev^2+p\right)\gamma^2\right] = -\frac{j}{r}\left[\left(e+p\right)\gamma^2 v^2\right]\,, \tag{2.3}$$

where $\gamma=(1-v^2)^{-1/2}$ and $j=0,\ 1,\ 2$ distinguishes situations with planar, cylindrical or spherical symmetry. It is now convenient to introduce a similarity variable which, as mentioned before, can only be of the type $\xi=\pm\,(r/t)$, with $-1\leq\xi\leq 1$. In particular, we take $\xi=r/t$ and look for a solution in which $e=e(\xi)$, $\rho=\rho(\xi)$ and $v=v(\xi)$. Introducing the new variables

$$f = \frac{1+v}{1-v}\,, \tag{2.4}$$

$$z = \frac{1+\xi}{1-\xi}\,, \tag{2.5}$$

equations (2.2)–(2.1) can be conveniently rewritten as

$$\frac{(z+f)(f+1)}{2f}f^{'}-(z-f)\rho^{'}+j\frac{(f-1)}{(z-1)}\rho = 0\,, \tag{2.6}$$

$$(e+p)f^{'}+f(e+p)^{'}-z(e-p)^{'}+\frac{j}{z-1}(e+p)(f-1) = 0\,, \tag{2.7}$$

$$\frac{z}{f}(e+p)f^{'}+f(e-p)^{'}-z(e+p)^{'}+\frac{j}{z-1}(e+p)(f-1) = 0\,, \tag{2.8}$$

where the prime denotes d/dz. Using then the relations

$$\frac{\partial}{\partial\xi} \equiv \frac{(1+z)^2}{2}\frac{\partial}{\partial z}\,, \tag{2.9}$$

$$v' \equiv \left(\frac{1+z}{1+f}\right)^2 f' , \tag{2.10}$$

it is possible to rewrite equations (2.6)–(2.8) in the following self similar form in spherical symmetry (*i.e.* $j = 2$) (Steinhardt [153], Kurki-Suonio [80], Rezzolla et al. [139])

$$\left[(c_s^2\xi^2 - 1)v^2 + 2\xi(1 - c_s^2)v + (c_s^2 - \xi^2)\right]\frac{\mathrm{d}v}{\mathrm{d}\xi} = -\frac{2v}{\xi}c_s^2(1 - v^2)(1 - \xi v) , \tag{2.11}$$

$$\frac{c_s^2}{(e+p)}\frac{\mathrm{d}e}{\mathrm{d}\xi} = \left(\frac{\xi - v}{1 - \xi v}\right)\left(\frac{1}{1 - v^2}\right)\frac{\mathrm{d}v}{\mathrm{d}\xi} , \tag{2.12}$$

$$\frac{1}{\rho}\frac{\mathrm{d}\rho}{\mathrm{d}\xi} = \frac{1}{(e+p)}\frac{\mathrm{d}e}{\mathrm{d}\xi} . \tag{2.13}$$

The dimensionless similarity variable ξ can be viewed either as the position of a point in the solution at a given time, or as the velocity at which a given feature (*e.g.* a discontinuity surface or a reaction front) in the profile of the solution is moving. This velocity is to be clearly distinguished from the fluid velocity v at the point described by ξ. A self similar flow which is linearly expanding with time (such as the one occurring for a growing bubble) is naturally described in terms of a positive similarity variable ξ (*i.e.* $\xi \in [0,\ 1]$). Conversely, a self similar contracting flow (such as the one occurring for an evaporating drop) is described in terms of negative values of ξ (*i.e.* $\xi \in [-1,\ 0]$).

When solving equations (2.11)–(2.13) numerically, it is useful to notice their property of invariance under the simultaneous transformations

$$\xi \to -\xi \qquad \text{and} \qquad v \to -v , \tag{2.14}$$

which has the consequence that it is only necessary to solve them in one of the half-planes $\xi \in [0,\ \pm\ 1]$ in order to know the solution in the whole interval $\xi \in [-1,\ 1]$[2]. In Figures 2.1 (a) and (b) we have plotted the results of numerical integration of equations (2.11) and (2.12) for the functions $v(\xi)$ and $e(\xi)$.

The dashed lines in Figures 2.1 represent points for which the derivative $\mathrm{d}v/\mathrm{d}\xi$ in (2.11) becomes infinite, *i.e.* for which

$$(c_s^2\xi^2 - 1)v^2 + 2\xi(1 - c_s^2)v + (c_s^2 - \xi^2) = 0 , \tag{2.15}$$

[2]We recall that for a relativistic fluid $c_s = 1/\sqrt{3} \cong 0.577$

which has the roots

$$v = \frac{\xi \pm c_s}{1 \pm c_s \xi}. \tag{2.16}$$

Expression (2.16), which is also the special relativistic formula for velocity composition, expresses the fact that the fluid velocity, measured relative to an observer moving at ξ, equals the speed of sound. A physical solution for v cannot be extended across these points, since it would then be double valued, and a discontinuity must be introduced. The upper right quadrant of Figure 2.1 (a) shows the solutions of the similarity equations for an expanding system (such as a spherically expanding hadron bubble; see Kurki-Suonio [80], Miller and Pantano [114]). Similarly, the upper left quadrant shows the equivalent solutions for a contracting system (such as an evaporating spherical quark drop; see Rezzolla et al. [139]). The lower quadrants provide the corresponding solutions for negative values of the fluid velocity (note that these do not necessarily represent physically realistic configurations).

The only self similar flow solution in Figures 2.1 (a) and (b) which can be taken to extend for all ξ is the trivial solution $v = 0$, $e = const.$ Any other solution must be the result of a "patching" of different solution curves with the joins being either via a *weak discontinuity* (*i.e.* where the function is continuous but has a derivative of some order which is not continuous), or via a full discontinuity (*i.e.* where the function itself is not continuous). The first can apply in the case of the edge of a rarefaction or compression wave, while the second occurs in the case of shocks or combustion fronts.

In the case of a spherical growing bubble whose surface is represented by a weak deflagration front, the point $\xi = 0$ represents the centre of the bubble at any given time, $\xi_s = c_s$ is the *expanding sonic radius* and determines the position of a possible weak discontinuity and $\xi = 1$ is the edge of the future light cone. Symmetry imposes that the solution $v = 0$, $e = const.$ should be satisfied at the centre of the bubble and a similar requirement could be made for the unperturbed fluid far away from the surface of the bubble. As a consequence, for a non-trivial solution, *at least* two discontinuities should be introduced in the interval $\xi \in [0,\ 1]$ and junction conditions for the conservation of energy, momentum and baryon number need to be imposed across any which are not weak.

(a)

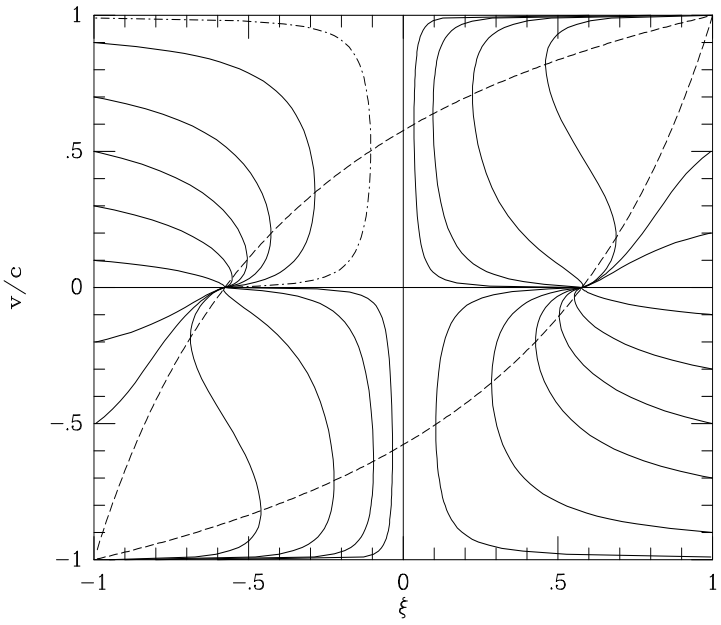

(b)

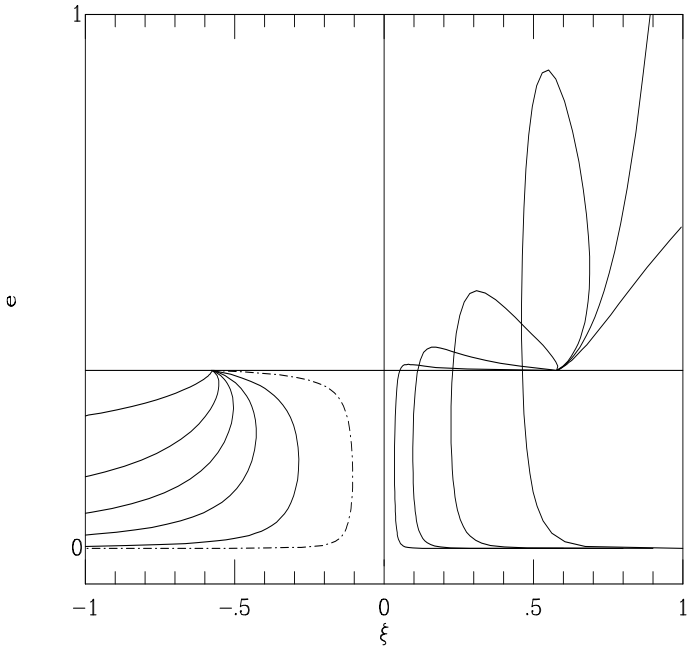

Figures 2.1 Solutions of the similarity equations for the velocity v [diagram (a)] and for the energy density e [diagram (b)]. The upper right quadrant of diagram (a) is the relevant one for a growing bubble, while upper left diagram is the relevant one for an evaporating drop. The points $\xi = \pm c_s$ represent the sonic radii, while the centre of the bubble/drop is at $\xi = 0$ at any given time. Parts of solution curves of diagram (a) are used in construction of the similarity solutions shown in Figure 2.4. The solutions for the energy density have been suitably normalized to the value of the energy density at the sonic point and correspond to solutions in the upper quadrants of diagram (a).

As discussed at length in Subsections 1.3.1, 1.2.2 and 1.3.3, weak deflagrations are underdetermined reaction fronts for which a further equation, usually establishing the motion of interface in terms of the local fluid conditions, needs to be provided. Doing this restricts the analysis to those situations for which a reasonable knowledge of the properties of the interface exists. For a cosmological first order phase transition, there are a number of ways of accomplishing this [*e.g.* either by means of energy flux across the phase interface (Miller and Pantano [113]), or by using a parameter related to the entropy production across the front (Ignatius et al. [61])] and they will be discussed in more detail in Subsection 5.2.3. What is relevant for the present discussion is that it is in principle possible to define a relation by means of which the velocity of phase interface can be specified and, in this case, the construction of a self similar solution can be obtained after imposing junction conditions across suitably located discontinuity surfaces. Doing this it is then possible to obtain the whole one-parameter family of solutions for a spherical weak deflagration, (some of which are presented in Figure 2.2) and with the parameter being essentially set by the velocity of the interface.

The two diagrams of Figure 2.2 show schematically the velocity profiles of spherical bubbles moving as weak deflagrations, with the heavy vertical lines (either continuous or dashed) marking the position of the deflagration fronts. The left diagram refers to standard subsonic deflagrations and presents two different profiles relative to a very slow (continuous line) and to a faster growing bubble (dashed line). Within a cosmological context, (see Section 4.3), the different subsonic deflagrations would be produced as a consequence of a small supercooling and of a large supercooling of the high temperature phase respectively[3]. Note that in the first case the precompression shock front has vanishingly small amplitude and effectively behaves as a weak discontinuity moving at the local sound speed ξ_s as seen from the coordinate frame (*i.e.* from the centre of the bubble).

The right diagram refers to a supersonic deflagration (continuous line) and a detonation (dotted line) is shown for comparison. As mentioned in Subsection 1.2.2, supersonic deflagrations can take place when the strength of the precompression shock front is a rather large and in this case the deflagration solution can even smoothly merge with the detonation one as the strength of the shock increases.

[3]See Section 4.3 for a definition of the degree of supercooling

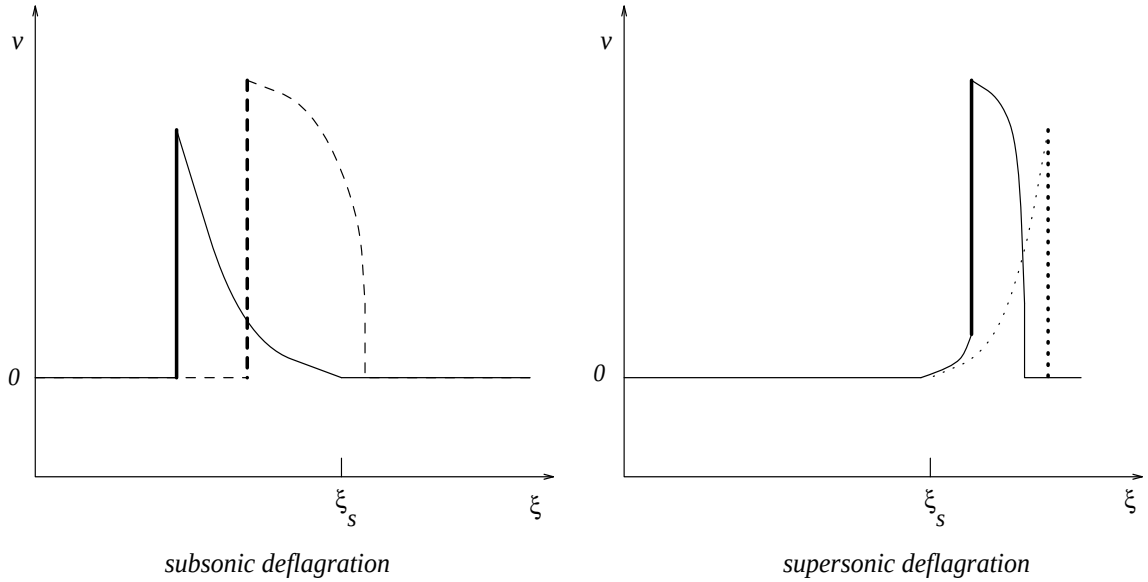

Figure 2.2 Schematic diagrams of the velocity profiles of spherical bubbles moving as weak deflagrations. The heavy vertical lines show the position of the deflagration fronts. The left diagram refers to a standard subsonic deflagration and presents two different profiles relative to a very slow (continuous line) and to a faster growing bubble (dashed line). The right diagram refers to a supersonic deflagration (continuous line) and a detonation (dotted line) is shown for comparison. (See also Figure 1.7 for a spacetime representation of the flow worldlines.)

Note also the appearance of a rarefaction wave following the supersonic deflagration front, whose tail behaves as a weak discontinuity and whose presence is necessary in order to produce a subsonic flow behind the front. Within a cosmological context, supersonic deflagrations and detonations require a larger degree of supercooling of the high temperature phase than the one necessary for subsonic deflagrations. It is interesting to underline that the self similar solutions for the energy density closely resemble the ones presented for the fluid velocity, with the only difference being given by different values of the energy density at the centre of the drop and in the unperturbed fluid; for this reason they are not reported here.

The existence and properties of the self similar solutions discussed so far for a growing bubble will be extremely useful when we need to specify initial conditions for the numerical solution of the relativistic hydrodynamical equations describing the growth of a low temperature bubble during a first order cosmological phase transition. This will be

one of the points discussed in Chapters 4 and 6 where we will also verify whether the self similar solutions (which are mathematically possible) are realised in practice.

2.3 Self Similar Hydrodynamics of a Drop

The self similar solution for a contracting and evaporating drop are radically different from the ones discussed in the previous section for an expanding bubble. The new boundary conditions will strongly influence the properties of solutions, some of which will not be present while others will be characterized by interesting new features. The first self similar solutions for a relativistic evaporating drop were presented in a recent paper by Rezzolla et al. [139, 142] and have been later confirmed also by other authors (Kurki-Suonio and Laine [83]). Also in the case of drop contraction, we expect that self similar motion should set in when the drop radius is reasonably smaller than the mean distance among neighbouring drops so that one can neglect the interaction among them, but large enough so that surface tension effects are negligible.

As mentioned in the previous section, in the case of a contracting system, we need to consider solutions of the self similar equations (2.11) and (2.12) expressed in terms of negative values of the similarity variable ξ. If we were to adopt a *positive* time coordinate we would then be forced to describe the physical system in terms of negative spatial dimensions. However, this uncomfortable point of view could be abandoned if we consider time as progressing through *negative* values and tending to zero as the radius of the contracting drop tends to zero. In this way, the instant $t = 0$ would represent an asymptotic limit in time and we can describe the dynamics of the system since $t = -\infty$. The point $\xi = 0$ would then represent the centre of the drop at any given time, $\xi_s = -c_s$ would mark, in analogy with what seen for a bubble, the position of the *contracting sonic radius* and $\xi = -1$ would finally represent the edge of the past light cone.

As for growing bubbles, self similar solutions for a contracting drop moving as a weak deflagration can be found only after a further equation, establishing the motion of the front, is provided. When this is done and the velocity of the deflagration front is specified, junction conditions across the relevant discontinuity surfaces together with the continuous solution of equations (2.11) and (2.12) provide the whole one-parameter family of self similar solutions. Notice, however, that for an evaporating drop the deflagration front is moving inwards and spherical symmetry together with the requirement for the front to be subsonic, impose that the only possible state ahead of it is one with zero velocity and constant density since the only self similar solution satisfying the condition

$v = 0$ at $\xi = 0$ is the trivial one. A consequence of this is that it is no longer possible to introduce a precompression shock ahead of the deflagration front. This is an important novel feature and points out that there are *at most* two discontinuities in the self similar solution for a contracting drop. This is quite different from what seen for the solution of growing bubbles, where there had to be *at least* two discontinuities.

The impossibility of having a precompression shock for a subsonic drop is particularly evident when looking at the upper left quadrants of the diagrams in Figure 2.1. All of the continuous solutions of (2.11) and (2.12) converge to the point $\xi = -c_s$ with positive first derivatives[4] and if the deflagration front has to be subsonic relative to the medium ahead (*i.e.* located at $\xi > -c_s$) the only possible solution ahead of it is the trivial one. A discontinuity corresponding to the subsonic deflagration front can be introduced at the drop surface, and this can then be suitably joined onto the relevant self similar solution curve for the flow behind it. In this case, (which is the physically interesting one), the self similar solution behind the front is represented by a *simple wave*[5] in which the fluid that was accelerated and expanded by the deflagration front is progressively slowed down until it is eventually taken to rest at the contracting sonic radius.

Although not self evident, the solution for the medium behind a drop surface moving as a deflagration front is effectively represented by a compression wave. This is due to the fact that a fluid element crossing the deflagration front is strongly decompressed from its original state, but it is subsequently progressively compressed up to the value in the unperturbed fluid as it moves away from the front. At the sonic radius, the solution joins (via a weak discontinuity) onto another one with zero velocity and constant energy density, with the value of the latter coinciding with the background value of the reacted fluid. As a result, the sonic radius can be thought of as tracing the edge of the perturbed flow region at any given time.

The different self similar solutions for a spherical evaporating drop moving as a deflagration are shown schematically in the different diagrams of Figure 2.3. The two upper diagrams show the velocity and energy density profiles, while the lower left diagram gives a spacetime representation of the worldline of a fiducial fluid element for a subsonic (weak) deflagration. In all of the diagrams, the heavy lines show the positions of the deflagration fronts.

---

[4]This can be easily proved by solving equation (2.11) in the low velocity limit $v \ll 1$ (Kurki-Suonio [80]).

[5]A simple wave is defined as a region of the flow in which two of the three Riemann invariants are constant and is therefore always adjacent to a flow region of constant state. Examples of simple waves are rarefaction and compression waves (Courant and Friedrichs [35]).

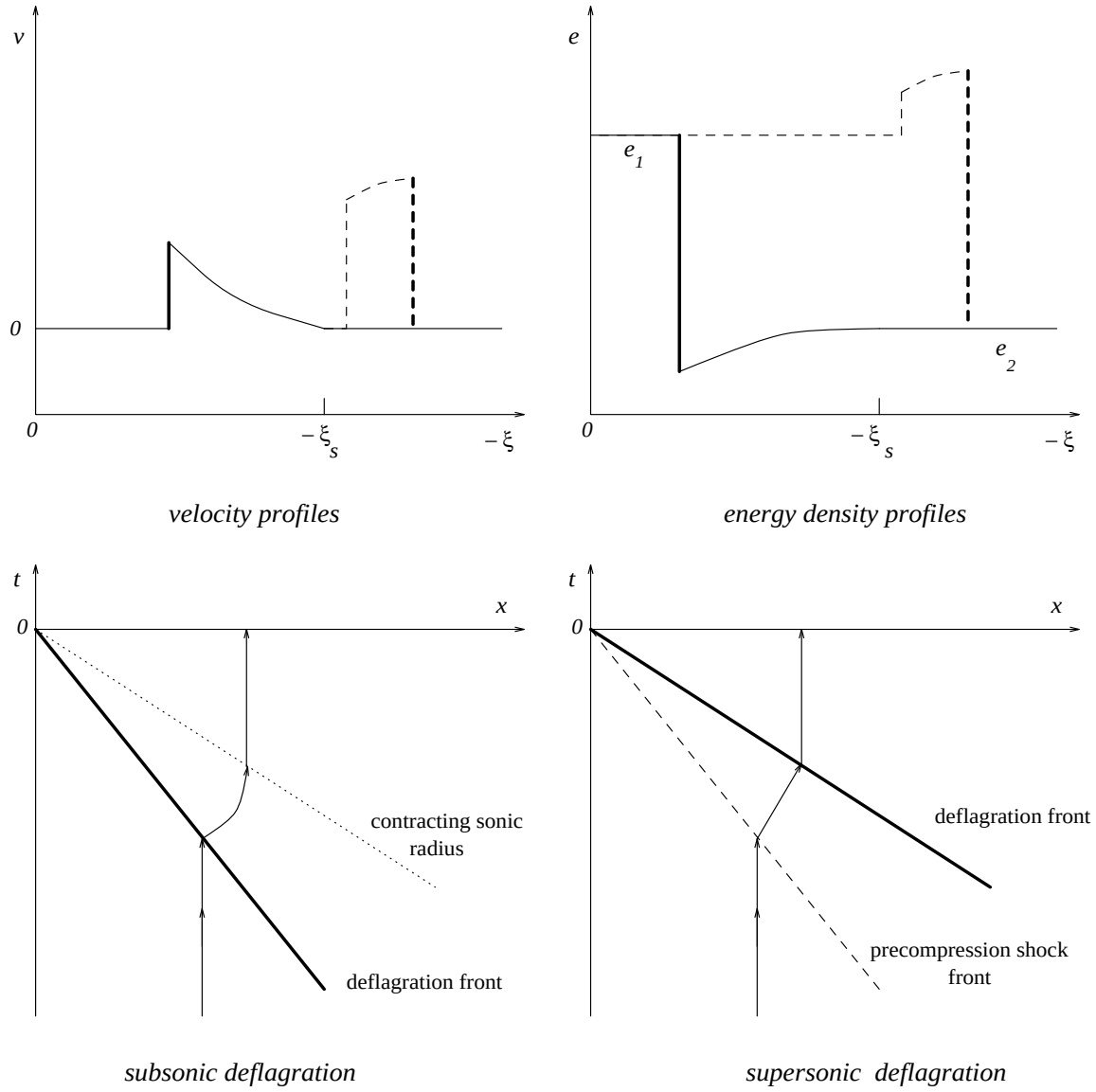

Figure 2.3 Schematic diagrams of the self similar solutions for a spherical evaporating drop moving as a deflagration. The two upper diagrams show the velocity and energy density profiles, with the continuous lines referring to a subsonic (weak) deflagration and the dashed lines to a supersonic (strong) deflagration. Similarly, the lower diagrams give a spacetime representation of the worldline of a fiducial fluid element for subsonic and supersonic deflagrations respectively. In all of the diagrams, the heavy lines show the positions of the deflagration fronts. Note that the dashed line curves in the upper diagrams refer to the self similar solution for a supersonic (strong) deflagration and that the self similar profiles for the compression ρ would be identical to the ones shown in the upper right diagram for the energy density.

Note that the self similar profiles for the compression ρ would be qualitatively identical to the ones shown in the upper right diagram for the energy density and for this reason they are not reported here.

It is interesting to notice that the limitations discussed above for the presence of a precompression shock ahead of a contracting subsonic deflagration front do not apply when the latter is supersonic relative to the coordinate frame (*i.e.* located at $\xi < -c_s$). In this case, in fact, the supersonic deflagration front can be preceded by another supersonic but slower precompression shock front with the join between the two being given by the continuous solutions of equations (2.11) and (2.12).

The fluid ahead of the precompression shock as well as the fluid behind the supersonic deflagration front would then be at rest with constant but different energy densities. As a result, solutions for supersonic evaporating drops can be constructed out of deflagration waves. Self similar solutions for drops moving as supersonic deflagrations represent a novel result which, to our knowledge, has never been discussed before in the literature and that we present for the first time in this Thesis. Such solutions are shown in the upper diagrams of Figure 2.3 where they are presented with the dashed line curves.

It is important to underline that since the fluid behind the deflagration front is at rest relative to the coordinate frame (*i.e.* relative to the centre of the drop) and since the latter is supersonic in the same frame, the fluid behind the deflagration front moves at supersonic speed relative to the front rest frame (*i.e.* $v_2 = -v_{def} > c_s$). This means that the solution of a supersonic deflagration drop would effectively correspond to a supersonic strong deflagration which, however, cannot be realized in practice because of negative entropy production.

A direct consequence of the above arguments is that it is not possible to construct self similar solutions for drops moving as detonations. A simple way of proving this is by recalling that a supersonic deflagration naturally evolves into a detonation when the deflagration front "catches up" with its supersonic precompression shock front (Subsection 1.2.2). However, if this would happen in the present case of drop evaporation, then the self similar solution would differ from a trivial one only at the detonation front which would represent the only feature of the otherwise unphysical solution. Another way of looking at this is that, on this picture, it would be impossible to have a discontinuity surface behind a detonation front since it would correspond to a "decompressive shock" which is an impossible configuration.

(a)

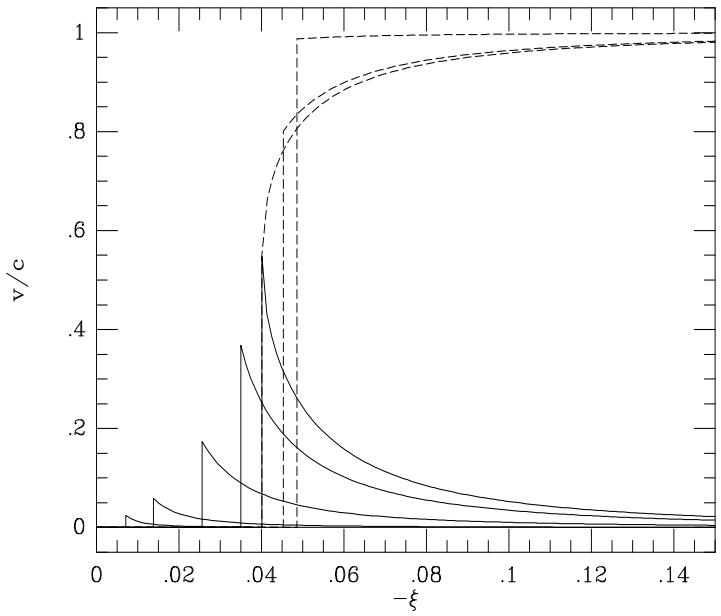

(b)

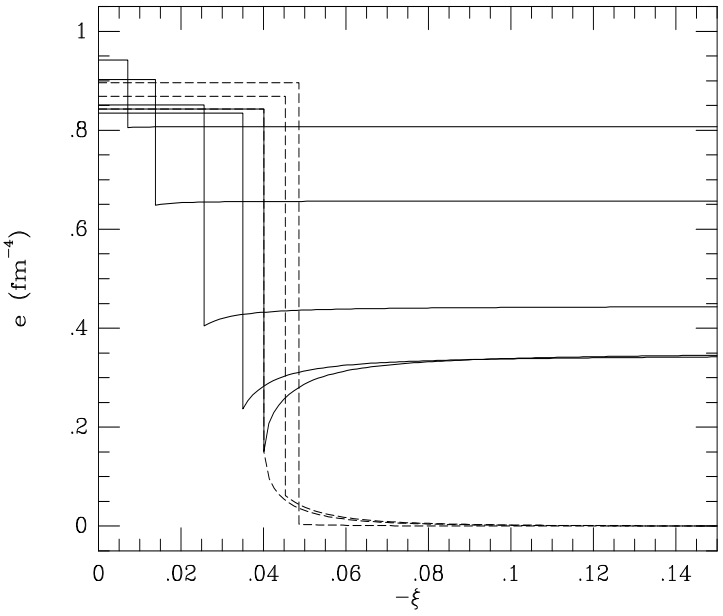

Figures 2.4 Self similar curves for the velocity and the energy density profiles of relativistic subsonic deflagrations. The solid curves represent weak deflagration solutions with the rightmost solid curve being a Chapman-Jouguet deflagration. The dashed curves represent strong deflagration solutions beyond Chapman-Jouguet limit and are physically forbidden.

The one-parameter family of self similar subsonic deflagration solutions is illustrated in Figures 2.4 (a) and (b). These curves have been effectively computed for the self similar motion of a disconnected quark drop during the cosmological quark–hadron phase transition (see also Section 6.3). The velocity of the interface has been determined after specifying the temperature in the hadron phase adjacent to the phase interface. This temperature, which is also related to the degree of supercooling of the high temperature phase, effectively ranges between $0.95T_c$ for the leftmost solid curve and $0.61T_c$ for the rightmost solid curve (T_c is the critical temperature for the transition).

Different curves are drawn for different values of the velocity of the drop surface (*i.e.* of the deflagration front) relative to a coordinate system having its origin at the centre of the drop. Solid line curves are representative of subsonic weak deflagration waves, while dashed line curves show the solution of subsonic strong deflagrations. The rightmost solid curve and the leftmost dashed curve correspond to adjacent but distinct values of the velocity of the drop surface. In particular, the rightmost solid curve represents a Chapman-Jouguet deflagration, for which the front moves at the sound speed relative to the fluid behind (Courant and Friedrichs [35]). This marks the transition from subsonic weak deflagrations (which are physically realistic) to subsonic strong deflagrations (which are physically forbidden). Note that the solution for the medium behind a subsonic strong deflagration front differs from the one behind a subsonic weak deflagration front since in this case the medium behind the front is accelerated away, reaching a velocity approaching the velocity of light at infinity, while the energy density decreases through a rarefaction wave, going to zero at infinity.

The analysis of the self similar motion of an evaporating drop whose surface moves as a deflagration front has offered a number of interesting and novel features. These are summarized in the list below, where we also point out the main differences between the self similar solutions for evaporating drops and the equivalent solutions for expanding bubbles.

i) In the case of an expanding bubble, the deflagration front (either subsonic or supersonic relative to the centre of the bubble) is always preceded by a compression wave fronted, in principle, by a shock. The latter could also have negligible amplitude in the case of a very slowly growing bubble. For a contracting drop, a subsonic deflagration can only be preceded by a solution with zero velocity and constant energy density.

ii) The deflagration front for a contracting drop can in principle be preceded by a precompression shock front. In this case, the self similar solution would correspond to a deflagration wave supersonic relative to the centre of the drop. In such a configu-

ration, the downstream flow is supersonic relative to the front and the deflagration is therefore a strong one. As discussed above, this solution would be unstable and could not be produced physically.

iii) The solution for the medium behind the deflagration front in an expanding bubble could differ from a constant state with zero velocity only if the bubble were expanding supersonically, in which case it would be represented by a rarefaction wave (Kurki-Suonio and Laine [82]). The medium just behind a subsonic deflagration front in a contracting drop is never at rest, but rather is outflowing with the velocity tending either to zero at the sonic point (in the case of subsonic weak deflagrations) or to the velocity of light at infinity (in the case of the physically forbidden subsonic strong deflagrations). The situation is different for supersonic deflagration fronts but these too are unphysical.

iv) Boundary conditions together with the properties of the continuous solutions of the hydrodynamical equations do not allow for the construction of a self similar solution for a contracting drop moving as a detonation.

v) The deflagration front in an expanding bubble could move with velocities up to the sound speed (and possibly beyond) relative to the centre of symmetry. On the other hand, weak deflagrations represent the only class of self similar solutions for an evaporating drop which could be realized in practice and, for these, the surface of the drop moves very subsonically relative to the centre of symmetry (*i.e.* at the surface, $|\xi| \ll c_s$).

As for the case of growing bubbles, the existence and properties of the self similar solutions for contracting drops will be used when specifying initial conditions for the numerical solution of the full relativistic hydrodynamical equations described in Section 6.3. There we will also be able to verify the "robustness" of the self similar solution and the physical conditions under which it will be no longer valid.

2.4 Summary

- *A physical system is said to follow a* **self similar behaviour**, *when the mathematical solution describing its physical state at a given instant is* **similar** *to the solutions at neighbouring instants. In this case, the physical state of the system at any time can be suitably* **rescaled** *from a given initial one.*

- *Self similar solutions represent* **privileged** *solutions that a physical system naturally tends to assume when there are no intrinsic* **length** *or* **time scales**.

- *Self similar solutions for a relativistic system can be described in terms of a unique dimensionless* **similarity variable**.

- *We refer to as a* **growing bubble** *an* **expanding** *spherical system having one discontinuity surface moving as a reaction front. Conversely, we refer to as an* **evaporating drop** *a* **contracting** *spherical system having one discontinuity surface moving as a reaction front.*

- *Self similar solutions for bubbles and drops moving as deflagrations can be constructed by* **joining** *the relevant* **continuous solutions** *of the self similar hydrodynamical equations with suitably located* **discontinuity surfaces** *across which junction conditions are imposed.*

- *There are* **at least** *two discontinuity surfaces for a growing bubble and* **at most** *two discontinuity surfaces for a contracting drop.*

- *Both* **subsonic** *and* **supersonic** *self similar solutions can be constructed for a* **growing bubble** *moving as a* **weak deflagration**. *In all of the solutions the medium just ahead of the deflagration front is not at rest but is set into motion by the* **precompression wave**.

- **Only subsonic** *self similar solutions can be constructed for a* **contracting drop** *moving as a* **weak deflagration**. *In all of these solutions the medium ahead of the deflagration front is at rest.* **Both supersonic** *and* **subsonic** *self similar solutions can be constructed for which the surface of the drop moves as a* **strong deflagration** *and, in the former case, the front is preceded by a* **precompression shock**. *None of these latter solutions can be realised in practice.*

Chapter 3

General Relativistic Radiation Hydrodynamics

3.1 Introduction

All the arguments discussed so far have been based on the concept of *simple fluid* (see Section 1.1 for a definition), *i.e.* on the possibility of treating a large collection of particles of the same type as a continuum described by averaged quantities. It is straightforward to extend this idea to the case of a *multicomponent fluid* (or *flow*).[1] The latter is to be understood as a fluid (or flow) whose components can be *distinguished* according to the different chemical properties of the constituents or according to the different types of physical interaction among the constituents. The formal treatment of multicomponent fluids can be rather simplified if all of the components are considered as independent. In this case, standard hydrodynamical equations can be written for each of the components and a multicomponent fluid with N different particle species can be effectively described in terms of $N+1+3$ equations accounting respectively for the continuity of the N species, (from which the continuity of the species mixture can be deduced) the conservation of energy and the conservation of momentum of the mixture (Battaner [18]).

Reactive flows are usually considered as multicomponent flows either because the fluids on both sides of the reaction front have different chemical properties, or because of the presence of "mixed phase" regions, in which the two phases coexist . However, in the case of relativistic fluids, as the ones relevant during cosmological phase transitions and that are our main interest here, the leading factor in the distinction among the different

[1] Some authors (*e.g.* Oran and Boris [125]) also refer to this as to a *multiphase* fluid (or flow).

species of a multicomponent fluid is not the chemical composition, but rather the typical interaction length scale (or mean free path) of the different particles present in the fluid. In this sense, we will consider as effectively parts of the same fluid two components having the same interaction length scale even if they are described by two different equations of state[2].

In general (and in the most interesting situations), the different species composing a multicomponent fluid are not independent but rather coupled by some kind of interaction. When this is the case, the hydrodynamical approach discussed above needs to be modified and "interaction" or "coupling" terms need to be introduced. These then account for the possibility of energy and momentum exchange among the different species or for the possibility that a species could be transformed into another one. A general hydrodynamical theory of these type of flows is no longer possible and different techniques need to be implemented in different physical situations. A simple and well known example of the "interaction" among particles of different species within a multicomponent fluid is offered by the interaction between radiation (*i.e.* meant as a fluid of photons) and matter (*i.e.* meant as a fluid of massive particles) and which usually goes under the name of *radiative transfer*. In this case, the two components of the fluid can exchange energy and momentum over some relevant length scale and the results of the "coupling" can be described by means of the *equation of radiative transfer* which accounts for the evolution of the properties of the radiation field, or, in other words, of the hydrodynamics of the radiation fluid particles.

A large literature has been produced both for classical solutions of the radiative transfer equation (Chandrasekhar [30] and references therein) and for special relativistic forms of it (Mihalas and Mihalas [110] and references therein). It is relevant to underline that when expressed in a global Lorentz frame of flat spacetime, the radiative transfer equation is identical to its standard nonrelativistic counterpart.

However, the assumptions of the classical and of the special relativistic theory of radiative transfer are no longer adequate near to astrophysical compact objects or for some cosmological situations in which the fluids can have relativistic bulk motions and the effects of spacetime curvature cannot be neglected. As a consequence, a general relativistic theory of radiation hydrodynamics is required for the study of these situations which then needs to be coupled to the standard formulation of relativistic hydrodynamics.

Consistent treatments of relativistic radiation hydrodynamics in curved spacetimes have only been developed fairly recently and among these, particular interest has been focussed on the PSTF tensor formalism devised by Thorne in 1981 [165] and the covariant

[2]This will be the case for our treatment of the hydrodynamics of the quark-gluon and hadron plasmas during the cosmological quark–hadron transition.

flux-limited diffusion theory (FLDT) approach proposed by Anile and Romano [13]. Both methods represent approximations to a problem which is too complicated to "handle" in full detail at the present time and there has been some debate about their respective merits. Because we are aiming to define a set of radiation hydrodynamical equations relevant for specific applications with spherical symmetry, we will concentrate in the following on the use of the PSTF moment formalism which presents great advantages in this respect.

In this chapter we derive a new system of Lagrangian relativistic hydrodynamic equations for describing general non-stationary spherical multicomponent flows in which a transfer of energy and momentum occurs between a perfect *standard fluid* defined as the fluid described by the stress energy tensor (1.1) and a generalized *radiation fluid* defined as a fluid composed of effectively zero rest-mass particles having longer mean free path than those of the standard fluid.

3.2 The PSTF Tensor Formalism

The PSTF tensor formalism is a technique for solving the general relativistic form of the radiative transfer equation, which, as mentioned above, describes the variation of the radiation fluid as it propagates through a standard fluid. The relativistic form of this is straightforward and can be written as[3] (Thorne [165]).

$$\frac{d\mathcal{N}}{dl} = \Sigma \,, \tag{3.1}$$

where $\mathcal{N}$ is the distribution function for the particles of the radiation fluid (a relativistic invariant) and l is a non-affine parameter measuring the proper spatial distance travelled by a particle of the radiation fluid as seen from an observer comoving with the standard fluid. Σ is a *source function* which accounts for the interaction between the radiation and the standard fluid and whose actual form depends on the specific radiative processes which are taken into examination. Note that the total derivative is taken not just in the spacetime but rather in the phase-space since $\mathcal{N} = \mathcal{N}(x^\alpha, p^\alpha)$, where $\mathbf{p}$ is the photon four-momentum, *i.e.*

$$\frac{d\mathcal{N}}{dl} = \frac{\partial \mathcal{N}}{\partial x^\alpha}\frac{dx^\alpha}{dl} + \frac{\partial \mathcal{N}}{\partial p^a}\frac{dp^a}{dl} \,, \tag{3.2}$$

The distribution function $\mathcal{N}$ can also be expressed in terms of a more familiar quantity

[3]Note that in his original papers Thorne adopted a slightly different convention in which $c = h = 1$.

in radiative transfer theory : *i.e.* in terms of the *Specific Intensity* of the radiation field I_ν, which is classically defined as the energy of the radiation field per unit time, surface, frequency and solid angle (erg cm^{-2} s^{-1} Hz^{-1} sr^{-1}). In this case, it is possible to express

$$\mathcal{N} = \frac{I_\nu}{\nu^3} \overset{\text{c.g.s.}}{=} \frac{c^3}{h^4\nu^3} I_\nu \overset{\text{c.g.s.}}{=} \frac{2h^4\nu^3}{c^3} N \ , \tag{3.3}$$

where h is the Planck constant, N is the photon occupation number and

$$\nu \equiv -\mathbf{p}\cdot\mathbf{u} \overset{\text{c.g.s}}{=} -\frac{c}{h}\, u^\alpha p_\alpha \ , \tag{3.4}$$

is the frequency of a photon with four-momentum $\mathbf{p}$ as measured by a fiducial observer with four-velocity $\mathbf{u}$. A trivial solution of (3.1) can be obtained in the case in which $\Sigma = 0$; this refers to a physical situation in which there is no interaction between radiation and the standard fluid so that the photon occupation number is conserved along each photon trajectory.

The fundamental idea of the PSTF method consists of replacing equation (3.1) (which is in a concise form but embodies enormous complexity) by a hierarchy of moment equations written in terms of Projected Symmetric and Trace-Free (PSTF) tensors which are suitably defined at each point in the projected tangent space to the fluid four-velocity $\mathbf{u}$ (see Appendix B for a definition of a PSTF tensor). PSTF moments are a trivial generalization to a four-dimensional spacetime of the "Symmetric Trace Free" (STF) tensors used in three-dimensional spacetimes (Thorne [164]). The k-th frequency integrated moment of $\mathcal{N}$ is then defined as

$$\begin{aligned}
\mathcal{M}^{\alpha_1\ldots\alpha_k} = \int_0^\infty d\nu\ \mathcal{M}_\nu^{\alpha_1\ldots\alpha_k} &= \left(\int_0^\infty d\nu \int \frac{\mathcal{N}\,\delta(2\pi\nu + \mathbf{p}\cdot\mathbf{u})}{(-\mathbf{p}\cdot\mathbf{u})^{k-2}} p^{\alpha_1}\ldots p^{\alpha_k} d\mathbf{V}_\mathbf{p}\right)^{PSTF} \\
&= \left(\int_0^\infty d\nu \int I_\nu (n^{\alpha_1} + u^{a_1})\ldots(n^{\alpha_k} + u^{a_k})\, d\Omega\right)^{PSTF} \\
&= \left(\int_0^\infty d\nu \int I_\nu n^{\alpha_1}\ldots n^{\alpha_k}\, d\Omega\right)^{TF} \ ,
\end{aligned} \tag{3.5}$$

where $d\mathbf{V}_\mathbf{p}$ is the invariant momentum-space volume element on the light cone, Ω is the solid angle in the projected tangent space to $\mathbf{u}$ and $\delta(y)$ is the Dirac delta function. $\mathbf{n}$ is the spacelike unit four-vector orthogonal to $\mathbf{u}$ (*i.e.* $\mathbf{u}\cdot\mathbf{n} = 0$, $\mathbf{n}\cdot\mathbf{n} = 1$) and fixes the direction of propagation of the radiation fluid particle as seen in the rest frame of a fiducial observer with four-velocity $\mathbf{u}$.

In a similar way, we can define the k-th frequency integrated moment of Σ as

$$\mathcal{S}^{\alpha_1\ldots\alpha_k} = \int_0^\infty d\nu\ \mathcal{S}_\nu^{\alpha_1\ldots\alpha_k} = \left(\int_0^\infty d\nu \int \frac{\Sigma\,\delta(2\pi\nu + \mathbf{p}\cdot\mathbf{u})}{(-\mathbf{p}\cdot\mathbf{u})^{k-2}} p^{\alpha_1}\ldots p^{\alpha_k} d\mathbf{V_p}\right)^{PSTF}$$
$$= \left(\int_0^\infty d\nu \int \nu^3 \Sigma\ (n^{\alpha_1} + u^{a_1})\ldots(n^{\alpha_k} + u^{a_k})\, d\Omega\right)^{PSTF}$$
$$= \left(\int_0^\infty d\nu \int \nu^3 \Sigma\ n^{\alpha_1}\ldots n^{\alpha_k}\, d\Omega\right)^{TF} . \qquad (3.6)$$

In the following, we will refer to $\mathcal{M}^{\alpha_1\ldots\alpha_k}$ and $\mathcal{S}^{\alpha_1\ldots\alpha_k}$ simply as the k-th *moment* and the k-th *source moment* respectively.

A clear physical interpretation can be given for the first three integrated moments of the hierarchy: $\mathcal{M}$ (the zeroth moment) is the energy density of the radiation, $\mathcal{M}^\alpha$ (the first moment) is the radiative energy flux, and $\mathcal{M}^{\alpha\beta}$ (the second moment) is the shear stress tensor of the radiation fluid (each quantity being measured in the local rest frame of the standard fluid). The stress energy tensor for the radiation fluid $T_R^{\alpha\beta}$ is completely defined in terms of the first three moments and higher order moments do not enter into this definition. The expression for it is

$$T_R^{\alpha\beta} = \mathcal{M} u^\alpha u^\beta + \frac{1}{3}\mathcal{M} P^{\alpha\beta} + \mathcal{M}^\alpha u^\beta + \mathcal{M}^\beta u^\alpha + \mathcal{M}^{\alpha\beta} , \qquad (3.7)$$

where $P^{\alpha\beta}$ is the projection operator orthogonal to $\mathbf{u}$. An appealing consequence of the possibility of expressing the radiation stress energy tensor in terms of the first three moments only is that, if the hierarchy is truncated at the second order, it is then possible to derive the equations governing the hydrodynamics of the radiation fluid in a particularly simple way by starting from the standard conservation laws of energy and momentum [*cf.* equations (1.34) and (1.35)]. If, on the other hand, orders higher than the second are retained, it is necessary to make direct use of the appropriate hierarchy of equations derived from (3.1) and recursive equations have been derived for this purpose.

In the case of planar or spherical symmetry, the $2k+1$ independent components of each k rank tensor depend on a single scalar variable so that the tensor formalism reduces to a purely scalar one. In this case, defining $(\mathbf{e}_{\tilde{0}},\ \mathbf{e}_{\tilde{r}},\ \mathbf{e}_{\tilde{\theta}},\ \mathbf{e}_{\tilde{\phi}})$ as the orthonormal tetrad carried by an observer comoving with the standard fluid, expressions (3.5) and (3.6) assume the simplified form

$$\mathcal{M}^{\tilde{r}\ldots\tilde{r}} = 2\pi \frac{k!(2k+1)}{(2k+1)!!} \int_0^\infty d\nu \int I_\nu P^k(\mu) d\mu \qquad (3.8)$$

and

$$\mathcal{S}^{\tilde{r}\ldots\tilde{r}} = (2\pi)^2 \frac{k!(2k+1)}{(2k+1)!!} \int_0^\infty d\nu \int \nu^3 I_\nu P^k(\mu) d\mu \ , \tag{3.9}$$

where $P^k(\mu)$ is the Legendre Polynomial of order k and $\mu = \mathbf{e}_{\tilde{r}} \cdot \mathbf{n}$. This great simplification of the tensor formalism has made it possible for the method to be used for a number of astrophysical and cosmological applications (Turolla and Nobili [167], Nobili et al. [122, 123], Rezzolla and Miller [137, 138, 140], Miller and Rezzolla [115], Zampieri et al. [171]).

The hierarchy of integrated scalar moment equations into which equation (3.1) is recast has the property that, for any k, the first k equations involve the first $k+1$ moments. In order to use this scheme for making calculations, a "judicious use of the infinite PSTF moments" is necessary (Thorne [165]). For this purpose, we need to truncate the moment hierarchy at some finite order by introducing a closure relation which specifies the value of the highest moment used in terms of lower ones and which is derived on the basis of physical considerations.

In the next section we shall use the PSTF approach to derive a new set of Lagrangian hydrodynamical equations describing the coupling between radiation and matter in the case of a non-stationary spherically symmetric flow, with the moment equation hierarchy being truncated at the second order.

3.3 Lagrangian Radiation Hydrodynamics for Spherical Flows

We here want to define general relativistic hydrodynamical equations for the radiation fluid and take into account the transfer of energy and momentum that could occur while the radiation fluid is moving through the standard fluid. While an Eulerean formulation of the hydrodynamical equations is preferable in situations with complex geometries and no symmetries, the Lagrangian formulation has great advantages for many practical applications in computations of time dependent flows having either planar, cylindrical or spherical symmetry. Here we will use a Lagrangian frame comoving with the standard fluid and the spherically symmetric line element

$$ds^2 = -a^2(t)dt^2 + b^2(\mu)d\mu^2 + R^2(\mu,\ t)(d\theta^2 + \sin^2\theta\ d\phi^2) \ , \tag{3.10}$$

where μ is a comoving radial coordinate and $R(\mu,\ t)$ is an associated Eulerean coordinate

or "Schwarzschild circumference coordinate" (Misner and Sharp [116], May and White [108], Misner [117], Miller and Sciama [112]).[4] Such a denomination for the coordinate R comes from the fact that the proper circumference at a time t of a sphere characterized by the radial coordinate μ is

$$\int ds = \int_0^{2\pi} (g_{\theta\theta})^{1/2} d\theta = 2\pi R(\mu,\ t)\ . \tag{3.11}$$

We here describe the radiation hydrodynamics using the first two moment equations together with a closure relation and the calculations then involve the first three moments, together with the first two source moments. The maximum errors in the calculated values of the radiation variables which arise when truncating at the second order, are typically of the order of $\sim 15\%$ (Turolla and Nobili [167]). In view of the fact that, in general, other uncertainties in the specification of the problem are of a comparable order, we regard this level of approximation as acceptable for the present purposes. Similar degrees of accuracy are reported for calculations using FLDT schemes (Melia and Zylstra [111], Anile and Romano [13]).

For spherical symmetry the first three moments can be written as

$$\mathcal{M} = w_0, \tag{3.12}$$

$$\mathcal{M}^{\alpha} = w_1 e^{\alpha}_{\tilde{r}}, \tag{3.13}$$

and

$$\mathcal{M}^{\alpha\beta} = w_2 \Big(e^{\alpha}_{\tilde{r}} e^{\beta}_{\tilde{r}} - \frac{1}{2} e^{\alpha}_{\tilde{\theta}} e^{\beta}_{\tilde{\theta}} - \frac{1}{2} e^{\alpha}_{\tilde{\phi}} e^{\beta}_{\tilde{\phi}} \Big), \tag{3.14}$$

where w_0, w_1 and w_2 are the first three *scalar moments*

The quantities w_0, w_1 and w_2 all have direct physical interpretations corresponding to those of the related tensor moments: w_0 and w_1 are the energy density and flux of the radiation in the fluid rest frame, while w_2 is the shear stress scalar of the radiation. The *scalar source moments* s_0 and s_1, defined in a similar way to w_0 and w_1, also have direct physical interpretations, representing respectively the transfer of energy and momentum between the two fluids. Explicit expressions for the source functions s_0 and s_1 within a cosmological scenario will be presented in Subsection (5.1.1).

---

[4] We here recall that the most general line element exhibiting spherical symmetry: $ds^2 = -\alpha^2 dt^2 - 2\alpha\beta dt d\mu + \gamma^2 d\mu^2 + R^2(d\theta^2 + \sin^2\theta\ d\phi^2)$, can be reduced to the form (3.10) when a new time coordinate t' is defined so that $\alpha' dt' = \alpha dt - \beta d\mu$.

Having restricted ourselves to the use of the first three scalar moments and the first two scalar source moments, it is convenient to derive the radiation hydrodynamical equations by means of the standard conservation laws for the energy and momentum of the radiation fluid applied to the stress energy tensor (3.7). Following this procedure, we can write the radiation hydrodynamical equations simply as

$$-u_\alpha T_{R}^{\alpha\beta}{}_{;\beta} = s_0 \ , \tag{3.15}$$

$$n_\gamma P^\gamma_\alpha T_{R}^{\alpha\beta}{}_{;\beta} = \frac{s_1}{b} \ , \tag{3.16}$$

$$w_2 = f_{_E} w_0 \ , \tag{3.17}$$

where $\mathbf{n}$ is a radial spacelike unit vector normal to $\mathbf{u}$, *i.e.* $\mathbf{n} = \mathbf{e}_{\tilde{r}}$.

The term $f_{_E}$ in the closure relation (3.17) is a *variable Eddington factor* and indicates the degree of anisotropy of the radiation fluid. It can take values ranging from 0 for complete isotropy to 2/3 for complete anisotropy. A key point in the present technique is that an expression for $f_{_E}$ has to be supplied, constructed on the basis of physical considerations and how this is done is, to some extent, *ad hoc*. In Subsection 5.1.1 we will present the explicit form of our Eddington factor implemented for studying long range energy and momentum transfer during the cosmological quark–hadron phase transition. In spite of this "freedom" in the choice of the closure relation, experience has shown that as long as its expression has the correct asymptotic behaviour in any relevant limits, results do not normally depend sensitively on the precise form used as long as it gives a suitably smooth join between the limits (Nobili et al. [122], Miller and Rezzolla [115]).

Making use of the stress energy tensor (3.7) and of the line element (3.10), equations (3.15) and (3.16) can be written explicitly as (see Appendix B for details)

$$(w_0)_{,t} + \frac{a}{b}(w_1)_{,\mu} + \frac{4}{3}\Big(\frac{b_{,t}}{b} + \frac{2R_{,t}}{R}\Big)w_0 + \frac{2a}{b}\Big(\frac{a_{,\mu}}{a} + \frac{R_{,\mu}}{R}\Big)w_1 + \Big(\frac{b_{,t}}{b} - \frac{R_{,t}}{R}\Big)w_2 = a s_0 \ , \tag{3.18}$$

$$(w_1)_{,t} + \frac{a}{b}\Big(\frac{1}{3}w_0 + w_2\Big)_{,\mu} + \frac{4a_{,\mu}}{3b}w_0 + 2\Big(\frac{b_{,t}}{b} + \frac{R_{,t}}{R}\Big)w_1 + \frac{a}{b}\Big(\frac{a_{,\mu}}{a} + \frac{3R_{,\mu}}{R}\Big)w_2 = a s_1 \ , \tag{3.19}$$

Equations (3.17)–(3.19) are our final form of the hydrodynamical equations for the radiation fluid and need to be solved together with the corresponding hydrodynamical equations for the standard fluid which will be discussed in Subsection 5.1.1.

3.4 Appendix B

In this Appendix we give a brief review of the definition of Projected Symmetric and Trace Free (PSTF) tensors and a sketch of the calculations leading from equations (3.15)–(3.16) to (3.18)–(3.19).

I. PSTF Tensors

Consider a spacetime in which there exist timelike worldlines of fiducial observers with four-velocity $\mathbf{u}$. Then $\mathbf{P} = \mathbf{g} + \mathbf{u} \otimes \mathbf{u}$ is the tensor which projects orthogonal to $\mathbf{u}$, with $\mathbf{g}$ being the metric tensor. For any k-rank tensor $B^{\alpha_1 \ldots \alpha_k}$ we define its "projected" (*i.e.* "purely spatial") part as

$$(B^{\alpha_1 \ldots \alpha_k})^P \equiv P^{\alpha_1}{}_{\beta_1} \ldots P^{\alpha_k}{}_{\beta_k} B^{\beta_1 \ldots \beta_k} \ . \tag{3.20}$$

Subsequently, from any projected k-rank tensor $C^{\alpha_1 \ldots \alpha_k}$ we can construct its "symmetric" part as

$$(C^{\alpha_1 \ldots \alpha_k})^S = C^{(\alpha_1 \ldots \alpha_k)} \equiv \frac{1}{k!} \sum_{\pi} C^{\alpha_{\pi(1)} \alpha_{\pi(2)} \ldots \alpha_{\pi(k)}} \ , \tag{3.21}$$

where the summation goes over all $k!$ permutations π of 1, 2, ..., k. Finally, for any projected and symmetric k-rank tensor $D^{\alpha_1 \ldots \alpha_k}$ we can extract its trace and make it "trace free" as

$$(D^{\alpha_1 \ldots \alpha_k})^{TF} \equiv \sum_{i=0}^{[k/2]} a_{ki} P^{(\alpha_1 \alpha_2} \ldots P^{\alpha_{2i-1} \alpha_{2i}} D^{\alpha_{2i+1} \ldots \alpha_k) \beta_1 \ldots \beta_i}{}_{\beta_1 \ldots \beta_i} \ , \tag{3.22}$$

where $[k/2]$ means the largest integer less or equal to $k/2$, we define $n!! \equiv n(n-2)(n-4)\ldots(2 \text{ or } 1)$ and the coefficient a_{ki} as

$$a_{ki} \equiv (-1)^i \frac{k!(2k-2i-1)!!}{(k-2i)!(2k-1)!!(2i)!!} \ . \tag{3.23}$$

As for the more familiar expansion of a function F in terms of multipole moments of order $(k,\ m)$

$$F = \sum_{k,m} D_{km} Y_{km}(\theta, \phi) \ , \tag{3.24}$$

[$Y_{km}(\theta,\phi)$ are the standard Spherical Harmonics of order $(k,\ m)$], we can use the $2k+1$ components of a k-rank PSTF tensor $\mathcal{F}_{\alpha_1\ldots\alpha_k}$ at an event $\mathcal{P}$ so as to express F as

$$F(\mathbf{n}) = \sum_{k=0}^{\infty} \mathcal{F}_{\alpha_1\ldots\alpha_k} n^{\alpha_1}\ldots n^{\alpha_k}\ , \tag{3.25}$$

where $\mathbf{n}$ is an arbitrary spacelike unit four-vector orthogonal to $\mathbf{u}$ at the event $\mathcal{P}$. $\mathcal{F}_{\alpha_1\ldots\alpha_k}$ is then called the k-th PSTF moment of F and can be computed by integration over the unit sphere swept, in the projected tangent space, by the vector $\mathbf{n}$, *i.e.*

$$\mathcal{F}^{\alpha_1\ldots\alpha_k} = \frac{(2k+1)!!}{4\pi k!}\Big(\int F n^{\alpha_1}\ldots n^{\alpha_k}\, d\Omega\Big)^{TF}\ . \tag{3.26}$$

II. Radiation Hydrodynamical Equations

As mentioned in Section (3.3), we use the spherically symmetric line element (3.10) and expression (3.7) for the stress energy tensor of the radiation fluid. The orthonormal tetrad carried by an observer comoving with the standard fluid: $(\mathbf{e}_{\tilde{0}},\ \mathbf{e}_{\tilde{r}},\ \mathbf{e}_{\tilde{\theta}},\ \mathbf{e}_{\tilde{\phi}})$ has then the following components

$$e^{\alpha}_{\tilde{0}} = \Big(\frac{1}{a},\ 0,\ 0,\ 0\Big)\ , \tag{3.27}$$

$$e^{\alpha}_{\tilde{r}} = \Big(0,\ \frac{1}{b},\ 0,\ 0\Big)\ , \tag{3.28}$$

$$e^{\alpha}_{\tilde{\theta}} = \Big(0, 0, \frac{1}{R}, 0\Big)\ , \tag{3.29}$$

$$e^{\alpha}_{\tilde{\phi}} = \Big(0, 0, 0, \frac{1}{R\sin\theta}\Big)\ . \tag{3.30}$$

The comoving observer's four-velocity $\mathbf{u}$ and four-acceleration $\mathbf{g}$ are given by

$$u^{\alpha} = \Big(\frac{1}{a},\ 0,\ 0,\ 0\Big) = e^{\alpha}_{\tilde{0}} \tag{3.31}$$

and

$$g^{\alpha} = \Big(0,\ \frac{a_{,\mu}}{ab^2},\ 0,\ 0\Big)\ , \tag{3.32}$$

so that $e^{\alpha}_{\tilde{r}} = g^{\alpha}/g$, where $g = (g^{\alpha}g_{\alpha})^{1/2}$ and $u^{\alpha}{}_{;\beta}u^{\beta} = g^{\alpha}$. The covariant derivative of the radiation fluid stress energy tensor is

$$T_{R}^{\alpha\beta}{}_{;\beta} = \frac{4}{3}\Big(\mathcal{M}_{;\beta}u^{\alpha}u^{\beta} + \mathcal{M}u^{\alpha}{}_{;\beta}u^{\beta} + \mathcal{M}u^{\alpha}u^{\beta}{}_{;\beta}\Big) + \frac{1}{3}\mathcal{M}^{;\alpha} + \mathcal{M}^{\alpha}{}_{;\beta}u^{\beta} + \mathcal{M}^{\alpha}u^{\beta}{}_{;\beta} + \mathcal{M}^{\beta}{}_{;\beta}u^{\alpha} + \mathcal{M}^{\beta}u^{\alpha}{}_{;\beta} + \mathcal{M}^{\alpha\beta}{}_{;\beta}\ , \tag{3.33}$$

where $\Theta = u^{\alpha}{}_{;\alpha}$ is the *expansion*. The contraction of expression (3.33) with u_{α} then gives

$$u_{\alpha}T_{R}^{\alpha\beta}{}_{;\beta} = -\mathcal{M}_{,\beta}u^{\beta} - \frac{4}{3}\mathcal{M}\Theta - \frac{g^{\beta}}{g}w_{1,\beta} + w_1\Big(\frac{g^{\alpha}}{g}\Big)_{;\beta}u^{\beta}u_{\alpha} - w_1\Big(\frac{g^{\beta}}{g}\Big)_{;\beta} + \mathcal{M}^{\alpha\beta}{}_{;\beta}u_{\alpha}\ . \tag{3.34}$$

After some further manipulation of expression (3.34) and making use of the equality

$$u_{\alpha}\mathcal{M}^{\alpha\beta}{}_{;\beta} = -\frac{(w_2)_{,\beta}}{2}\Big(e^{\alpha}_{\tilde{\theta}}e^{\beta}_{\tilde{\theta}}u_{\alpha} + e^{\alpha}_{\tilde{\phi}}e^{\beta}_{\tilde{\phi}}u_{\alpha}\Big) + w_2\Big[\Big(\frac{g^{\alpha}}{g}\Big)_{;\beta}\frac{g^{\beta}}{g}u_{\alpha} - \frac{1}{2}(e^{\alpha}_{\tilde{\theta}}e^{\beta}_{\tilde{\theta}} + e^{\alpha}_{\tilde{\phi}}e^{\beta}_{\tilde{\phi}})_{;\beta}u_{\alpha}\Big]\ , \tag{3.35}$$

it is possible to rewrite equation (3.15) in the form (3.18). We proceed in the same way with the derivation of equation (3.16). Bearing in mind that $n_{\gamma}P^{\gamma}_{\alpha} = \delta^{1}{}_{\alpha}$, it follows from (3.33) that

$$n_{\gamma}P^{\gamma}_{\alpha}T_{R}^{\alpha\beta}{}_{;\beta} = \frac{4}{3}\mathcal{M}g^{1} + \frac{1}{3}\mathcal{M}_{,1}g^{11} + \ + \mathcal{M}^{1}{}_{;\beta}u^{\beta} + w_1\frac{g^{1}}{g}\Theta + \mathcal{M}^{\beta}u^{1}{}_{;\beta} + \mathcal{M}^{1\beta}{}_{;\beta}\ . \tag{3.36}$$

Writing out each of the terms explicitly and using the expression

$$\mathcal{M}^{1\beta}{}_{;\beta} = \frac{1}{b^2}(w_2)_{,\mu} + \frac{w_2}{b^2}\Big(\frac{a_{,\mu}}{a} + 3\frac{R_{,\mu}}{R}\Big)\ , \tag{3.37}$$

equation (3.36) can finally be recast in the form (3.19).

3.5 Summary

- *We define as* **multicomponent** *fluids (or flows), those fluids (or flows) whose constituents can be distinguished according to their typical physical interaction.*
- *We here define as standard fluid a fluid described by the stress energy tensor (1.1) and as radiation fluid a fluid composed of effectively zero rest-mass particles having mean free path longer than the one of the standard fluid particles.*
- *A flow in which energy and momentum transfer occurs between a radiation fluid and a standard fluid is defined as a multicomponent flow with* **radiative transfer**.
- *Solutions to the problem of relativistic radiation hydrodynamics have been proposed only very recently and among these particular interest has been focussed on the* **PSTF tensor formalism**.
- *The fundamental idea of the PSTF method consists of replacing the* **relativistic radiative transfer equation** *by an* **infinite hierarchy** *of moment equations written in terms of PSTF tensors.*
- *The PSTF tensors become effectively* **scalars** *in the case of planar or spherical symmetry.*
- *The infinite hierarchy can be suitably truncated at a finite order and completed with a closure relation defined on the basis of physical considerations.*
- *The stress energy tensor of the radiation fluid is defined in terms of the* **first three** *moments* **only** *and standard conservation laws then provide the radiation hydrodynamical equations which we have here derived in a Lagrangian formulation.*
- *A suitable closure relation for a truncated hierarchy of moment equations can be written in terms of a* **variable Eddington factor** *which expresses at every point the degree of anisotropy of the radiation field.*
- *Results do not depend sensitively on the form chosen for the closure relation as long as it has the* **correct asymptotic limits**.

Chapter 4

Physics of the Cosmological Quark–Hadron Transition

4.1 A Cosmological Prelude

According to the *Big Bang Model*, which is the current generally accepted theoretical picture for the birth and evolution of the Universe, the history of our Universe "started" from a primordial spacetime singularity whose explosion and expansion produced our present observable world.

The Big Bang model provides a general framework for describing the evolution of the Universe and has its scientific foundations in three fundamental astronomical observations which find, in such a model, a simple and elegant explanation. These "observational evidences" are *i)* the redshift in the spectra of distant galaxies, *ii)* the existence of an isotropic cosmic microwave background radiation representative of a black-body at temperature 2.7 K and *iii)* the abundance of light elements in the Universe. All of these observations can be interpreted as indications that *i)* the Universe is subject to an isotropic expansion, *ii)* the Universe was in its past history in thermal equilibrium and at much higher temperatures, and *iii)* there was a time in the past history of the Universe at which the mean energy density dropped below the binding energy densities of light atoms so that free electrons and ionized light nuclei were able to form stable atoms and the Universe became transparent for photons. This is the epoch from which we receive information when looking at the cosmic microwave background radiation and represents the most distant epoch which could provide us with direct or indirect electromagnetic information of the early Universe.

By using Einstein's theory of gravitation and the presently known laws of elementary particles interactions it is possible to follow back in time the evolution of the Universe up to its very first instants, when it had an age of 10^{-44} s and a mean temperature of 10^{32} K, corresponding to an energy scale of about 10^{19} GeV. This age, which is called the *Planck era*, represents the actual limit of our cosmological scientific knowledge, beyond which it is not possible to proceed without a consistent quantum theory of gravity.

A frequently encountered feature of the early Universe[1] cosmology is represented by *phase transitions*, which mark many of the most important episodes of this history (see Bonometto and Masiero [23] or Kolb and Turner [79] for an introduction). The concept of phase transition within a cosmological scenario is usually associated to the loss of a given symmetry of the fields present in the Universe. This is the case, for example, of the inflaton field whose symmetry breaking possibly led to inflation, or of the order parameter field in the quartic effective potential of the electroweak transition (Kolb and Turner [79]). However, the concept of phase transition could also be introduced in order to describe the change of the intrinsic properties of a physical system when this change is related to modified thermodynamical conditions (this is the case for the more familiar phase transitions of our ordinary experience).

Among cosmological phase transitions, particular interest has been raised by *first order* phase transitions, for which, (in a certain range of temperatures) both the new and the old phase can coexist within the same volume and are separated by a narrow region called the *phase interface*. Such phase transitions proceed with the nucleation of bubbles of the new phase that then grow at the expense of the old phase. An exact description of these phenomena would require a precise knowledge of the microphysical processes taking place at the phase interface where one phase in transformed into the other, but such processes are usually so complicated that they are not known in detail not even for the simple case of a vapour bubble. However, a hydrodynamical description can be made in such a way as to circumvent the limitations posed by the ignorance of the processes at the interface and provide a satisfactory overall picture of the different stages of a cosmological phase transition. This is what will be discussed in detail in the following sections of this chapter, where the concepts and the mathematical tools developed so far will be implemented in the study of several different stages of the cosmological quark–hadron phase transition.

According to the standard Big Bang model, in fact, a phase transition at which the cosmological plasma of free quarks and gluons was transformed into a plasma of light hadrons, is thought to have occurred early in the history of the Universe. The

[1] With "early Universe" we here mean the Universe between the Planck era and that at about three minutes after the Big Bang.

physical conditions for this transition to take place, date it back to a few microseconds after the Big-Bang, when the Universe had a mean density of the same order as nuclear matter ($\rho \sim 10^{15}$ g cm^{-3}), a temperature of the order of $100 - 200$ MeV (*i.e.* $\sim 10^{12}$ K) and a particle horizon of the order of a solar mass (*i.e.* $r_H \sim 10^5$ cm). The quark–hadron transition marks the end of the exotic physics of the very early Universe and the beginning of the era of processes and phenomena which have a direct counterpart in the high energy experiments now being carried out with modern accelerators, where the physical evidence of the quark-gluon plasma is sought[2]. It is also the last of the early Universe phase transitions (at least within the standard picture) and so could be relevant both as a potential filter for the relics produced by previous transitions and also as a "best candidate" for the production of inhomogeneities which could have survived to later epochs.

The following sections are dedicated to several distinct issues on the physics of cosmological phase transitions and aim at providing the physical background necessary for the study of the quark–hadron phase transition. It is not in our intentions to present here an exhaustive discussion of the many and different physical processes involved in the transition and that can be found in the more complete review by Bonometto and Pantano [24]. Rather than that, we here want to introduce a number of important topics (such as the order of the transition, the nature of the reaction front representing the dynamics of the phase interface or the typical processes involved in the nucleation of the low temperature bubbles) and discuss the problematics around them and the solutions that have been proposed in order to untangle them. A final general overview of the probable sequence of events during the transition will then complete the picture of the physical scenario in which the cosmological quark–hadron phase transition probably took place.

4.2 Thermodynamics and Order of the Transition

All the necessary thermodynamical information about the two phases is contained in the thermodynamical potential $\Omega = \Omega\,(T,\ V,\ A,\ \mu_i,\ N_i)$ (with $i = 1,\ 2$), where A is the extension of the surface area separating the two phases, and μ_i, N_i are the chemical potentials and particle numbers of the species in the two phases, here indicated as 1 ($q$uark phase) and 2 ($h$adron phase). The thermodynamical potential is classically defined as

$$\Omega = -T \ln Z\ , \tag{4.1}$$

[2]For compactness hereafter we will refer to the quark-gluon plasma simply as the "quark plasma".

where Z is the grand partition function (Huang [59]). All of the other thermodynamical quantities can then be expressed in terms of partial derivatives of the thermodynamical potential (Landau and Lifshitz [91]). However, it can be sometimes more convenient to make use of another fundamental thermodynamical quantity: the Helmholtz free energy $F = F\,(T,\ V,\ A,\ \mu_i,\ N_i)$. F can derived from the thermodynamical potential using the relation

$$F = \Omega + \sum_{i=1,2} \mu_i N_i = -pV + \sigma A + \sum_{i=1,2} \mu_i N_i \ , \tag{4.2}$$

where σ is the surface tension of the phase interface. An infinitesimal variation of the free energy can then be expressed as

$$dF = -SdT - pdV + \sigma dA + \sum_{i=1,2} \mu_i dN_i \ , \tag{4.3}$$

where the entropy S, pressure p, surface tension σ and the chemical potentials μ_i are given by the following expressions:

$$\begin{aligned} S &= -\left(\frac{\partial F}{\partial T}\right)_{V,A,\mu_i,N_i} , & p &= -\left(\frac{\partial F}{\partial V}\right)_{V,A,\mu_i,N_i} , \\ \sigma &= \left(\frac{\partial F}{\partial A}\right)_{V,A,\mu_i,N_i} , & \mu_{1\,(2)} &= \left(\frac{\partial F}{\partial N_{1\,(2)}}\right)_{V,T,A,N_{2\,(1)}} . \end{aligned} \tag{4.4}$$

The Helmholtz free energy can be used to derive information about one of the most important quantities characterizing a phase transition and which distinguishes different physical phenomenologies: *i.e.* the *order* of the transition. A formal definition of the order of a phase transition can be done in terms of partial derivatives of specific thermodynamical quantities evaluated at the *critical temperature* of the transition T_c. The latter is then defined as the temperature at which, in the thermodynamical limit (*i.e.* in an infinitely large system in which the temperature is changed at an infinitely slow rate), the phase transition takes place. Under these assumptions, the first law of thermodynamics and the definition of the entropy density of a relativistic fluid $S/V = (e + p)/T$ allow to express the energy density in terms of the pressure and its first derivative with respect to temperature T, *i.e.* [3]

[3] We here make the underlying assumption that the background spacetime is either in an isentropic expansion or it is not expanding.

$$e = -p - \frac{T}{V}\left(\frac{\partial F}{\partial T}\right)_{V,A,\mu_i,N_i} = -p + T\left(\frac{\partial p}{\partial T}\right)_{V,A,\mu_i,N_i} , \tag{4.5}$$

where $F = eV - TS$. At the critical temperature, the new and old phases will have the same mean pressure[4]

$$p_o(T_c) = p_n(T_c) , \tag{4.6}$$

where the lower indices o and n refer to the "old" and "new" phases respectively [Expression (4.6) is sometimes used as the definition of the critical temperature T_c.] We can then define the order k of the transition according to the lowest k-th order at which the partial derivatives

$$\left(\frac{\partial^k p_n(T_c)}{\partial T^k}\right)_{V,A,\mu_i,N_i} \neq \left(\frac{\partial^k p_o(T_c)}{\partial T^k}\right)_{V,A,\mu_i,N_i} , \tag{4.7}$$

are *discontinuous* at the critical temperature, while all the other partial derivatives of lower order $k-1,\ldots,1$ are there continuous (Callen [27], Huang [59]). In this way, a first order phase transition (*i.e.* $k = 1$) will be characterized by phases with the same pressure at T_c but with different first derivatives of the pressure relative to the temperature. Similarly, in a second order phase transition the two phases will have equal pressures and continuous first derivatives at T_c, but discontinuous second order derivatives and so on (see Figure 4.1)[5].

Using the fundamental relation (4.5), it is easy to realize that discontinuity in the in the first derivatives (4.7) reflects an effective jump in the energy densities of the two phases, whose difference quantifies the *latent heat* L of a first order transition

$$L \equiv e_o(T_c) - e_n(T_c) , \tag{4.8}$$

where $L > 0$ in the case of an *exothermic* phase transition and $L < 0$ in the case of an *endothermic* phase transition.

As mentioned in the previous section, in a first order phase transition, the metastable and the stable phases may coexist within the same volume for some temperature range, occupying different regions of it and being separated by means of a phase interface. This

[4]We are here considering that both phases have vanishingly small chemical potentials so that the pressure is a function of the temperature only. Such an assumption is usually a good one for plasmas in the early Universe (see also the discussion in Section 4.4).

[5]Note that in the classical terminology of Statistical Mechanics it is common to define as "second order" any type of phase transition which is not of first order.

phenomenology is different from that of a *second order* phase transition, in which both the old and the new phases are coexistent but do not occupy different regions of the initial volume (a typical example of second order phase transition is represented by a fluid undergoing photoionization).

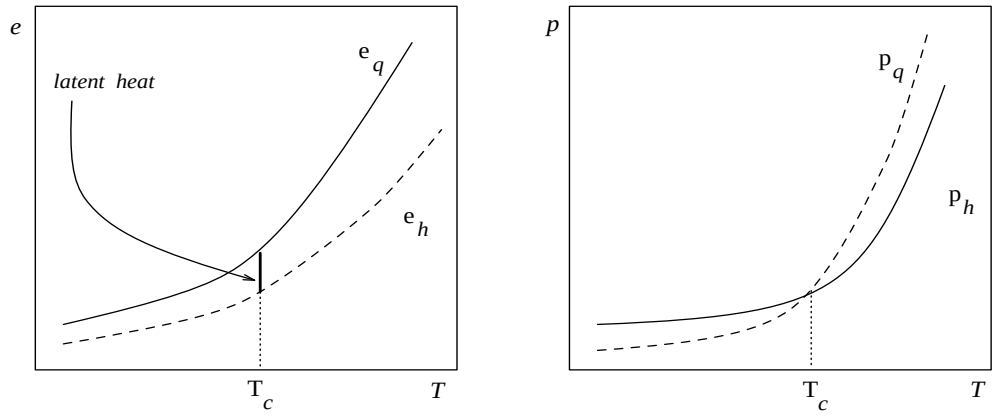

Figure 4.1 Schematic representation of different behaviours of the energy density e and of the pressure p for a first order (upper diagrams) and a second order (lower diagrams) phase transition. The diagrams are specialized to the cosmological quark–hadron phase transition.

A further and different type of phase transition is one in which the passage from the old to the new phase takes place by means of a full succession of intermediate stages each

corresponding to a different but definite symmetry. Such phase transitions are called *continuous* and are typical of lattice based physical systems and of crystals.

If the phase transition is first order and a "transition region" represented by the phase interface exists, it is then interesting to evaluate the contribution of this phase interface to the overall thermodynamics of the transition. This can be easily estimated in the hypothesis that there is no particle function excess associated with the interface *i.e.*

$$\sum_{i=1,2} \mu_i dN_{i|\Sigma} = 0 \ , \tag{4.9}$$

where the lower index Σ refers to quantities evaluated at the interface[6]. This approximation is a particularly good one in plasmas of the early Universe, in which the photon to baryon ratio is extremely high and $(\mu/T) \sim 10^{-9}$ (Kolb and Turner [79]). In this case, the phase interface contribution to the free energy is simply given by

$$F_{\Sigma} = \sigma A \ , \tag{4.10}$$

which shows that the surface tension σ represents a new *function of state* of the system and completely accounts for the variation in the free energy of the system (at constant temperature, volume and species composition) in terms of the variation of the surface area of the phase interface. In particular, evaluating (4.3) at the interface and assuming that the bulk properties of the two phases remain unaffected by a change in the surface area (*i.e.* $dN_i = dV = 0$), the change in the free energy of the phase interface is then given by

$$dF_{\Sigma} = -S_{\Sigma} dT + \sigma dA \ . \tag{4.11}$$

Differentiating equation (4.10) and comparing it with the equivalent expression (4.11) we obtain the following relation between the entropy and the surface tension of the interface

$$S_{\Sigma} = -A\left(\frac{d\sigma}{dT}\right)_A \ , \tag{4.12}$$

which shows that the surface entropy excess per unit area is a measure of the "disorder" of the phase interface region as compared to that of the bulk of the two phases. In this sense, if the bulk physical properties of the two phases extend unmodified up to the phase

[6]Note that a formal definition of the location of the phase interface can be given in terms of the separation surface at which the excess of one of the two species equals the deficit of the other (Gibbs [50]).

interface, then the surface entropy is effectively negligible, *i.e.* $S_{\Sigma} \approx 0$. Such a condition seems to be particularly good for a classical strongly first order phase transition, in which the particles of the unstable phase have rather strong atomic bindings.

A different physical quantity which can be associated to the phase interface is the *surface energy* and this can be defined in terms of the internal energy of the interface per unit area, *i.e.* $\gamma_{\Sigma} \equiv U_{\Sigma}/A$. Using then the fundamental thermodynamical relation

$$U_{\Sigma} = F_{\Sigma} + TS_{\Sigma} \,, \tag{4.13}$$

and expressions (4.10), (4.12), we can express the surface energy as

$$\gamma_{\Sigma} = \sigma - T\left(\frac{d\sigma}{dT}\right)_{A} \,, \tag{4.14}$$

which shows that the surface energy is coincident with the surface tension in the case the latter is not dependent on the temperature (*i.e.* $d\sigma/dT = 0$). Rewriting expression (4.13) as $F_{\Sigma} = U_{\Sigma} - TS_{\Sigma}$, it is possible to realize the different roles played by the internal energy and by the entropy in the minimization of the free energy. In particular, it becomes clear that while the internal energy contribution tends to favour a sharpening of the transition region (particles tend to reside in the energetically most favourable region of the phase interface adjacent to the metastable phase), the entropy contribution acts in an opposite way favouring a broadening of the transition region.

Unfortunately, it has not proved possible to determine the order of the quark–hadron transition directly from QuantumChromoDynamics (QCD) which is a non-perturbative theory at low energy and therefore *very* difficult to handle. The determination of the order of the transition depends therefore on heavy lattice gauge calculations and these necessarily rely on a number of simplifying assumptions and uncertain parameters. Because of this, any consistent modelling of the transition is immediately confronted by a major uncertainty concerning the order of the transition. It is relevant to note that while a second order or a continuous cosmological quark–hadron phase transition (Fukugita and Hogan [48], Brown et al. [25], Karsch and Laermann [76], Karsch [77]) would strongly prevent any dynamical production of primordial inhomogeneities (Crawford and Schramm [37]), the occurrence of these seems to be a rather natural consequence of a first order transition. Hereafter we will follow this latter scenario and investigate the hydrodynamical evolution of a first order cosmological quark–hadron transition. We note that this picture is favoured by recent lattice computations which include the effects of two degenerate light up (u) and down (d) quarks and a heavier strange (s) quark (of up to 400 MeV) (Iwasaki et al. [65, 66], Kanaya [72], Iwasaki et al. [67]) and clearly indicate the existence of a double state signal for the quark plasma.

4.3 Supercooling and Dynamics of the Interface

There are at least three important quantities that strongly characterize the properties of a generic first order cosmological phase transition. These are the latent heat L, the surface tension associated to the interface between the two phases σ and the *degree of supercooling* of the high temperature phase reached before the nucleation of the low temperature bubbles. In general, in fact, for an exothermic first order phase transition in which the old phase is progressively cooled, nothing really "happens" at the critical temperature and the high temperature phase just moves into a metastable supercooled state. This rather familiar behaviour is due to the fact that a certain degree of supercooling is needed in order to overcome the energy expense of forming the interface between the two phases. Therefore, only at a temperature somewhat lower than the critical one bubbles of the new phase begin to nucleate. The degree of supercooling, is formally expressed in terms of the adimensional quantity η defined as

$$\eta \equiv 1 - \frac{T_f}{T_c} = 1 - \hat{T}_f \ , \tag{4.15}$$

where $\hat{T}_f = T_f/T_c$ and $T_f \leq T_c$ represents the temperature in the bulk of the old phase at which the transition starts to take place. (Hereafter "hats" will be used to refer to temperatures normalized to the critical one.).

The roles played by L, σ and η in the quark–hadron transition are strongly correlated since they all depend on the peculiar properties of the strong interaction which is poorly know at such high temperatures. As a result, it is not simple to indicate clearly what is the contribution that each single quantity gives to the typical properties and scales of the phase transition. However, as a generic but not general rule, it is possible to associate both σ and L to the (comoving) mean distance l_n between centers of neighbouring bubbles at the time of nucleation (see also Section 4.5), while η and L can be associated with the nature of the reaction front representing the way in which the interface between the two phases moves (Ignatius et al. [61, 62]).

Although the issue of the type of reaction front which represents the way in which the phase interface moves within the high temperature medium is somewhat debated, definite clear statements can be made with reasonable confidence. As discussed in Section 1.2, because of their "internal structure", strong deflagrations and weak detonations are ruled out as physically possible within the classical theory for chemical burning (Landau and Lifshitz [90], Courant and Friedrichs [35]). We recall that the internal structure of a detonation front could be described as consisting of a shock heating up the medium to initiate combustion, immediately followed by the deflagration front. For a weak det-

onation, this deflagration would be a strong one, while it would be a weak deflagration on the case of a strong detonation. Along this line of arguments, the impossibility of strong deflagrations implies the impossibility of weak detonations. However, the internal structure of a phase transition front is different from that of a combustion front. Heating by a shock does not facilitate the phase transition, and the structure of a detonation front cannot be described as a shock followed by a deflagration. Therefore weak detonations cannot be ruled out and strong deflagrations might also be possible in some cases (Laine [85], Ignatius et al. [62]).

Detonation and deflagration solutions are obtained from the hydrodynamical conditions of energy and momentum conservation and these solutions are then physically realistic if they also satisfy the condition of non-negative entropy production. These constraints, however, do not fix the process uniquely and further conditions (usually entering as boundary conditions) need to be specified. A convenient way of handling this intrinsic freedom of the solutions is to analyze them as a function of the temperatures $\hat{T}_q^+$ and $\hat{T}_h^-$ adjacent to the phase interface in quark and hadron phases respectively[7]. Note that according to the specific type of reaction front under examination, T_q^+ and T_h^- might well not correspond to the temperatures in the bulk of the quark and hadron phases, *i.e.* to T_q and T_h respectively. In particular, the precompression wave preceding a deflagration front will produce a local increase of the temperature of the medium ahead, so that in the case of a deflagration: $T_q^+ > T_q$ and $T_h^- = T_h$[8]. On the other hand, a detonation front will produce a local increase in temperature of the medium behind it, which then decreases again through the rarefaction wave, so that in the case of a detonation: $T_q^+ = T_q$ and $T_h^- > T_h$. In view of this, it is more convenient to always refer to the temperature of the quark phase T_f at which the phase transition first takes place and bear in mind that $T_f < T_q^+$ for a deflagration and $T_f = T_q^+$ for a detonation. The multiplicity of reaction front solution for a given couple of temperatures $(\hat{T}_q^+, \hat{T}_h^-)$ is synthesized in Figure 4.2 which shows all of the relevant solutions in a $(\hat{T}_q^+, \hat{T}_h^-)$ diagram (Gyulassy et al. [54], Ignatius et al. [61, 62]).

Each point in this diagram might or might not correspond to a physically realistic solution and, for this purpose, the thick solid line is used as the locus of points for which $\Delta s = s_q - s_h = 0$ and therefore it separates regions of the diagram where the solutions are not physically possible ($\Delta s < 0$) from those where physical solutions exist ($\Delta s > 0$). Solutions in Figure 4.2 might refer to a *supercooled* quark plasma at the interface if

[7] We recall that the upper indices + and − are used to indicate quantities immediately ahead of and behind the phase interface, while lower indices q and h are used to indicate quantities in the quark and hadron phases respectively.

[8] Note that for a supersonic deflagration $T_h^- > T_h$.

$\hat{T}_q^+ < 1$ or to a "normal" (*i.e.* relative to thermodynamically a stable state) quark plasma at the interface if $\hat{T}_q^+ > 1$. Similarly, solutions for $\hat{T}_h^- < 1$ will refer to a "normal" hadron plasma at the interface, while solutions for $\hat{T}_h^- > 1$ will refer to a *superheated* hadron plasma at the interface. The shaded area shows a region of the diagram where no solution of the hydrodynamical equations is possible and it separates the regions where either only deflagrations or only detonations are allowed. The short dashed line and the dotted line mark the loci of points where Chapman-Jouguet deflagrations and Chapman-Jouguet detonations respectively occur, while the long dashed vertical and horizontal lines trace the deflagration and detonation branches respectively for phase transitions occurring with a 5% degree of supercooling.

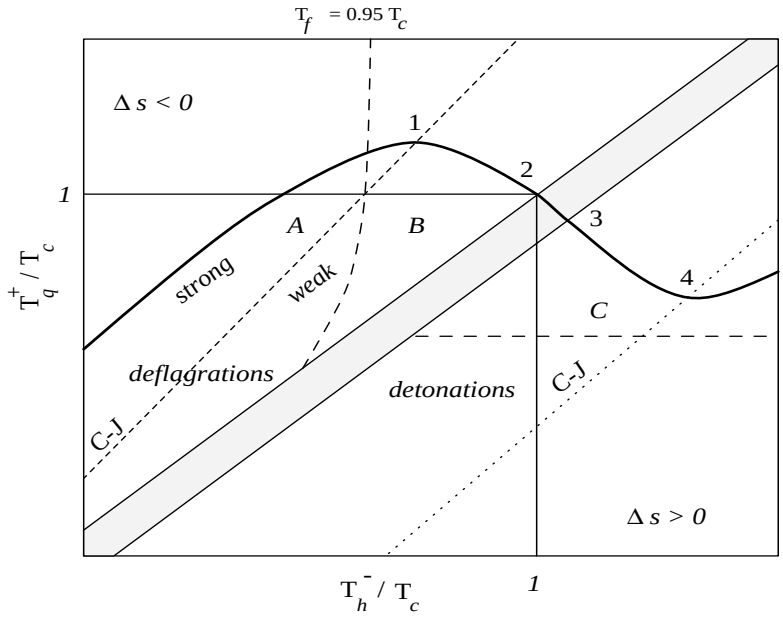

Figure 4.2 Schematic representation of the allowed types of reaction front according to the temperatures in the quark T_q^+ and hadron phases T_h^- adjacent to the phase interface. The thick solid line distinguishes regions of the diagram where the solutions are not physically possible ($\Delta s < 0$) from those where physical solution exist ($\Delta s > 0$). The short dashed line and the dotted line mark the loci of points where Chapman-Jouguet deflagrations and detonations occur respectively, while the shaded area refers to a region where no solution of the hydrodynamical equations is possible. Regions A, B and C are representative of strong deflagrations, weak deflagrations and weak detonations respectively. (A figure similar to this was first presented by Gyulassy et al. [54]

The region to the left of the short dashed line and which is indicated as A is representative of *strong deflagrations*, while the region to the right of the dashed line is indicated as B and is representative of *weak deflagrations*. Similarly, the region between the shaded area and the dotted line is representative of *weak detonations* and is indicated as C. At last, numbers from 1 to 4 are used to specify the position of special points in the diagram.

In particular, point 1 marks the temperature of the quark plasma below which deflagrations are permitted and, depending on the strength of the precompression wave, this solution might refer to an effective supercooling of the quark plasma (*i.e.* to a $\hat{T}_f < 1$). At any temperature $T_f < T_q^+(1)$, weak deflagrations, Chapman-Jouguet deflagration and strong deflagrations are in principle permitted, although the latter require a very large degree of supercooling and a very small latent heat. Point 2, on the other hand, marks a solution for which $T_q^+ = T_h^-$ and $\Delta s = 0$. Since this solution refers to a weak deflagration (for which $T_f < T_q^+$) it is certainly attained for a small but finite degree of supercooling of the quark plasma. Point 3 refers to a weak detonation solution and therefore marks the minimum amount of supercooling necessary to produce a detonation (we remind that for a detonation $T_f = T_q^+ = T_q$.) Note that in this case the temperature of the hadron plasma behind the front is that of a superheated plasma but that the rarefaction wave following the front could decompress and cool the plasma down to a stable state in the bulk of the phase. Finally point 4 marks the degree of supercooling below which also Chapman-Jouguet detonations are possible, although almost certainly these fronts would tend to leave the bulk of the hadron plasma in a superheated state.

We can summarize the results discussed so far as follows:

i) For any given temperature $T_f \leq T_c$, at which the phase transition takes place, there is a one-dimensional family of allowed reaction front processes; such a family is further distinguished into a deflagration and into a detonation branch.

ii) *Weak deflagrations* are *always* included in this family and *never* produce a superheated hadron plasma.

iii) *Strong Deflagrations* could be produced in principle. However they are very unlikely since they require a very large degree of supercooling and a rather small latent heat.

iv) This family *could* also include *weak detonations* if $T_f \leq T_q^+(3) = T_q(3)$ and *possibly* *Chapman-Jouguet detonations* if $T_f \leq T_q^+(4) = T_q(4)$.

v) While weak detonations *might* or *might not* produce a stable hadron plasma, Chapman-Jouguet detonations will most *probably* produce a superheated hadron plasma.

Which of these allowed processes actually occurs once the degree of supercooling is fixed, effectively depends on the mechanisms internal to the front. These establish the magnitude of the entropy jump across the reaction front and determine its propagation speed. Too little is known about the microphysics of the QCD phase interface for a definitive statement to be made about the nature of the interface. However, even though some thermodynamical conditions could be suitable for the production of a weak detonation (or of a strong deflagration), weak deflagrations certainly appear to require *minimal conditions* (both in the degree of supercooling and in the stability of the new phase) in order to be produced. For this reason, hereafter we will associate the hydrodynamics of the phase interface during the cosmological quark–hadron phase transition to that of a *subsonic weak deflagration front* moving within a *slightly supercooled* quark plasma.

4.4 Equations of State for the SIM

This section is dedicated to the definition of suitable equations of state for the two phases (quark and hadron) of the Strongly Interacting Matter (SIM) present in the Universe at the time of the transition. It is important to stress that our main concern here is the definition of equations of state that provide a satisfactory thermodynamical and mechanical description of the two phases but that can be easily handled in a numeric computation. This requirement will probably limit the accuracy of the expressions derived but will not alter the physical properties of the hydrodynamical solutions we are interested in evolving here.

4.4.1 Quark Phase: Bag Model

QCD is our theory of the strong interaction and, as mentioned above, it is a non-perturbative theory even at low energy and therefore very complicated to use in practice for computations. A consequence of this is that it is necessary to resort either to phenomenological models or to lattice gauge calculations in order to define an equation of state for the quark plasma. We here follow the first approach (which is also the most diffused within a cosmological context) and make use of the phenomenological *Bag Model* first proposed at MIT in 1974 (Chodos et al. [32]).

There are two main features of the quark plasma that any phenomenological model has to reproduce: *i)* the *asymptotic freedom* at short distances, when the strong coupling

constant α_s goes to zero and *ii) confinement* of quarks within hadrons for energy densities lower than ~ 500 MeV fm^{-3}. (Note that the energy density of nuclear matter is $e_{nm} \sim 150$ MeV fm^{-3}.)

Both of these features are included in the bag model, whose basic idea is that the quarks can be considered as moving freely (or with interactions treated at the level of perturbation theory) within a region of space (the "bag") in which the vacuum is different from the "true" vacuum outside. The "false" vacuum makes a positive contribution $+B$ to the energy density inside the bag and a negative contribution $-B$ to the pressure, where B is referred to as the *bag constant*.

In the limit of zero net baryon number (*i.e.* $\mu_b = 0$) and zero strong coupling constant[9] (*i.e.* $\alpha_s = 0$) we obtain the following (bag) equations of state for the energy density and pressure in the quark phase

$$e_q = g_q \left(\frac{\pi^2}{30}\right) T^4 + B \ , \tag{4.16}$$

$$p_q = g_q \left(\frac{\pi^2}{90}\right) T^4 - B \ , \tag{4.17}$$

where g_q is the number of degrees of freedom in the quark phase and depends on the number of quark flavours considered, *e.g.*

$$g_q = \begin{cases} 37 & \text{2 quark flavours} \ , \\ \\ 47.5 & \text{3 quark flavours} \ . \end{cases}$$

Insight on the form of equations (4.16) and (4.17) can be gained by looking at the derivation of the equation of state for an ideal relativistic fluid presented in the Appendix C. Other phenomenological equations of state which are defined in terms of parameters deducible from QCD lattice calculations and that have (4.16) and (4.17) as a special case, have been proposed by Bonometto and Sokołowski [22]. Miller and Pantano [114] have implemented such equations for their hydrodynamical computations of bubble growth and found only minor differences with respect to results obtained using the standard bag model equations of state.

At present it is not clear what is the exact value to take for the phenomenological bag constant and it could also be that the constant should really be temperature dependent. While a lower limit of $B^{1/4} \geq (145\text{MeV})$ is set by the stability of nuclei, especially ^{56}Fe,

[9] It was shown by Farhi and Jaffe [45] in the limit $T = 0$, that a strong coupling constant different from zero can largely be absorbed in a reduction of the bag constant.

relative to up and down (ud)-quark matter, no upper limit can be set from physical considerations. Lattice QCD calculations typically favour a value for $B^{1/4}$ above 200 MeV and hereafter we will assume $B^{1/4} \approx 220$ MeV, corresponding to a critical temperature $T_c \approx 150$ MeV.

4.4.2 Hadron Phase: Ideal Relativistic Fluid

With a level of approximation similar to the one adopted for the quark phase, we will here treat the hadron phase as a relativistic ideal fluid of massless pointlike π mesons (pions). Of course, this is not entirely correct and a number of improvements, such as the inclusion of finite volume effects, or of repulsive interaction terms between hadrons, or of a wider hadronic spectrum, could be in principle implemented. However, such improvements would mainly result into more sophisticated and complicated equations of state without providing effective novel physical behaviours (see Bonometto and Pantano [24] for a detailed discussion).

It is worth underlining that the approximation of considering the hadron phase as composed of a relativistic ideal fluid of pions is extremely good since pions with a mass $m_\pi = 137$ MeV are semi-relativistic at the time of the quark–hadron transition and represent the dominant contribution to the grand partition function of the hadron phase over the whole spectrum of hadron species. All of the other hadrons possibly present are strongly depressed in number by a Boltzmann factor $\exp(-m/T)$, where m is the hadron mass. Moreover, these heavier hadrons would be non-relativistic so that they would contribute only negligibly to the hadron pressure. A less good approximation is that of considering pions as pointlike at the time of the transition, since their mean separation $d_\pi \approx n_\pi^{-1/3} = 1.7\ T^{-1}$ is indeed just larger than their typical size $\lambda_\pi \approx m_\pi^{-1} \approx T^{-1}$. Finite volume corrections were considered by Karsch and Satz [75] for an hadron plasma of pions only, while Bonometto [21] included the contribution of protons and neutrons in the case in which $\mu \neq 0$. More sophisticated expressions retaining a wider hadronic spectrum was then proposed by Kapusta and Olive [74] and Kapusta [73].

All of these studies have shown that the hadron phase can be handled in a more sophisticated physical way than as a relativistic ideal pion fluid. However, they have also derived expressions which are rather elaborate and certainly not easy to implement in a numerical computation in which the hydrodynamics of the various stages of the phase transition is investigated. Moreover, all of the expressions proposed do not change significantly the mechanical and thermodynamical properties of the hadron plasma when

this is treated as a relativistic perfect fluid. As a result we will here implement the following standard equations of state for the hadron plasma

$$e_h = g_h \left(\frac{\pi^2}{30}\right) T^4 \ , \tag{4.18}$$

$$p_h = g_h \left(\frac{\pi^2}{90}\right) T^4 \ , \tag{4.19}$$

where $g_h = 3$ is the number of degrees of freedom of a hadron plasma of pions. A formal derivation of equations (4.18) and (4.19) is presented in the Appendix C.

4.5 Hadron Bubble Nucleation

The typical (comoving) distance between hadron bubble nucleation sites at the beginning of the transition l_n represents a major unsolved issue for the whole scenario of the quark–hadron transition. This length scale is not only relevant at the time when hadron bubbles are nucleated within the supercooled quark medium, but also represents a characteristic length scale for subsequent stages of the transition. It is the scale at which neighbouring hadron bubbles collide and percolate and it also determines the typical distance between the centres of the disconnected quark regions produced by bubble coalescence. As a consequence, it also represents the maximum length scale for the production of inhomogeneities in the baryon number density distribution that could take place during the final stages of the transition (see Subsections 5.1.2, 5.2.3 and 6.4 for further discussions of this). This section is devoted to a discussion of the most probable mechanisms for the nucleation of the new phase bubbles and to the estimates of l_n that can be derived from them.

The nucleation of the low temperature phase bubbles represents the first "episode" in the sequence of events of the transition and unfortunately embodies some of the major uncertainties that are still affecting the general scenario of the quark–hadron transition. The standard approach to the study of bubble nucleation makes use of the *classical thermal fluctuation theory* for which bubbles of the new phase are nucleated as a consequence of thermal fluctuations within the supercooled old phase medium (Landau and Lifshitz [91]). This approach is also called *homogeneous nucleation* scenario as opposed to the *inhomogeneous nucleation* scenario in which bubble nucleation is rather induced by impurities and that has been recently investigated again by Christiansen and Madsen [33].

According to the thermal fluctuation theory, the probability $p(\Delta F_c,\ T)$ of a thermal fluctuation producing a bubble nucleus can be expressed as

$$p(\Delta F_c,\, T) = C(T) \exp\left(-\frac{\Delta F_c}{T}\right) \,, \tag{4.20}$$

where the pre-exponential factor depends in detail on the model by which the bubble growth is described and ΔF_c is the minimum work necessary to produce the smallest possible growing bubble and is equal to the "critical" change in the Helmholtz free energy. In the limit of vanishing chemical potentials, the change in the Helmholtz free energy when a spherical hadron bubble of radius R is produced within a quark plasma at temperature T is equal to the change in the thermodynamical potential *i.e.* :

$$\Delta F(R,\, T) \equiv F(R,\, T) - F(0,\, T) = \frac{4\pi}{3}(p_q - p_h)R^3 + 4\pi\sigma R^2 - 8\pi\tilde{\gamma}R \,, \tag{4.21}$$

where $\tilde{\gamma} > 0$ is the *curvature coefficient* and has been introduced as a first order term in the expansion around R in order to take into account the contribution to the free energy given by massless quarks and gluons[10] (Mardor and Svetitsky [105]). Note that for a hadron bubble such a contribution has a negative sign expressing the fact that the newly nucleated bubble is favoured to grow. The radius of a critical size bubble R_c is found by putting $\partial\Delta F/\partial R$ equal to zero. Solutions of this equation are the two *critical radii*

$$R_{c,\pm} = \frac{\sigma}{(p_h - p_q)}\left(1 \pm \sqrt{1 - \frac{2(p_h - p_q)\tilde{\gamma}}{\sigma^2}}\right) \,, \tag{4.22}$$

one of which coincides with the standard expression for the critical bubble radius (DeGrand and Kajantie [40]) $R_{c,+} = 2\sigma/(p_h - p_q)$ in the case in which no curvature term is considered (*i.e.* $\tilde{\gamma} = 0$). The importance of the critical radius lies in the fact it represents the radius at which hadron bubbles are effectively nucleated. Bubbles with radius *smaller* than the critical one, in fact, will be immediately forced to shrink under the effects of surface tension, while bubbles with radius *larger* than the critical one will have exponentially decreasing probability of being produced. Typical estimates of the critical radius for the quark–hadron transition set it equal to $R_c \approx 10 - 50$ fm (Miller and Pantano [114], Christiansen and Madsen [33]).

In general, the smaller radius $R_{c,-}$ corresponds to a local minimum in the free energy, while the larger corresponds to a local maximum. As pointed out by Mardor and Svetitsky [105] and subsequently discussed by Christiansen and Madsen [33], this local minimum has some serious consequences, if it is real and not just a shortcoming of the multiple

[10] The calculation of the free energy (4.21) has been performed within the phenomenological *bag model* (see Section 4.4).

reflection expansion of the bag model (Balian and Bloch [14]), since it means that small hadron bubbles show up even above the critical temperature and no supercooling of the quark plasma is necessary. Lana and Svetitsky [88] have argued that these small radius bubbles are unstable and would therefore disappear, but at present the situation is still unclear and improved expressions for the free energy should be derived. Because of this uncertainty we will neglect this root and always refer to $R_{c,+}$.

A linear expansion of $\Delta p = p_h - p_q$ about the critical temperature gives

$$\Delta p = L\eta, \tag{4.23}$$

where L is the latent heat [*cf.* equation (4.8)], and η the degree of supercooling [*cf.* equation (4.15)] which we assume to be very small for the cosmological quark–hadron transition. The minimum work done ΔF_c can then be calculated as

$$\Delta F_c(\eta) \equiv F(R_{c,+}, T) - F(0, T) = \frac{8\pi}{3}\frac{\sigma^3}{L^2\eta^2}\left[1 - \frac{3L\tilde{\gamma}}{\sigma^2}\eta + \left(1 - \frac{2L\tilde{\gamma}}{\sigma^2}\eta\right)^{3/2}\right] . \tag{4.24}$$

By requiring ΔF_c to be always positive we obtain the following condition on the maximal degree of supercooling that can be reached

$$\eta \leq \frac{3}{8}\frac{\sigma^2}{L\tilde{\gamma}} \qquad \Longleftrightarrow \qquad \hat{T}_f \geq 1 - \frac{3}{8}\frac{\sigma^2}{L\tilde{\gamma}} . \tag{4.25}$$

The nucleation rate (*i.e.* the number of nucleations per unit volume and time) can then be calculated combining equations (4.20) and (4.24) so as to obtain, in the limit of small supercooling:

$$p(\eta) = C(\eta)\exp\left[-\frac{8\pi}{3}\frac{\sigma^3}{L^2 T_c \eta^2}\left(1 - \frac{3L\tilde{\gamma}}{\sigma^2}\eta + \left(1 - \frac{2L\tilde{\gamma}}{\sigma^2}\eta\right)^{3/2}\right)\right] . \tag{4.26}$$

Csernai and Kapusta [28, 29] have calculated the pre-exponential coefficient $C(\eta)$ in the cosmological case (*i.e.* with relativistic particles and almost zero baryon number), but without a curvature term. They obtain

$$C(\eta) = \frac{16}{3^{5/2}\pi}\frac{\sigma^{5/2}\nu^3}{\Xi_q^4 L^2 T^{3/2}}\bar{R}_c , \tag{4.27}$$

where $\bar{R}_c = R_{c,+}$ (with $\tilde{\gamma} = 0$), $\Xi_q \approx 0.7$ fm is the thickness of the bubble surface and ν is the shear viscosity given approximately by

$$\nu \simeq \frac{1.12}{\alpha_s^2 \ln \alpha_s^{-1}} T^3, \tag{4.28}$$

For the present purposes the contribution of $C(\eta)$ is much smaller than the one coming from the exponential factor and it is therefore sufficient the estimate $C(T) \approx T_c^4$. It is here important to notice that the nucleation rate $p(\eta)$ is equal to zero at the critical temperature and that it increases very rapidly with η. As a result, nearly all bubble nucleations take place at the lowest temperature T_f achieved during the supercooling phase.

It is sometimes more convenient to use as the free "flowing parameter" the time t rather than the temperature T. The relation between the two can be found by solving the Friedmann equations for a spatially flat Universe consisting of a quark plasma, of photons and of leptons and, at the order of approximation used here, such an expression is given by

$$T \simeq \left(\frac{45}{16\pi^2 g_q G}\right)^{1/4} t^{-1/2} \ , \tag{4.29}$$

where G is the gravitational constant and g_q the number of degrees of freedom in the quark phase. The nucleation rate can then be recast in the new form

$$p(t) \simeq p(\eta_f) \exp[-\alpha(t - t_f)] \ , \tag{4.30}$$

with t_f being the first instant at which the temperature in the Universe was at T_f, $\eta_f = \eta(T_f)$ and with α being defined as

$$\alpha = (41\pi G)^{1/2} \left(\frac{\pi}{3} T_c^2 \frac{C'(\eta_f)}{C(\eta)} + \frac{8\pi^2}{9} \frac{\sigma^3 T_c}{L^2 \eta_f^3} \left[2 - 3b\eta_f + (2 - b\eta_f)(1 - 2b\eta_f)^{1/2}\right]\right) \ , \tag{4.31}$$

where $b \equiv L\tilde{\gamma}/\sigma^2$ and $C' \equiv dC/d\eta$. Because of the steepness in the nucleation rate, expression (4.30) effectively represents a good approximation to the equivalent expression (4.26).

If the nucleation rate is known and the temperature evolution of the Universe is regulated by equation (4.29), it is then possible to define the mean nucleation distance l_n in terms of the total number density of nucleation sites

$$l_n \equiv n_{nuc}^{-3} = \left(\int_{t_c}^{\infty} f(t) p(t)\, dt\right)^{-3} \ , \tag{4.32}$$

where $f(t)$ is the volume fraction of the Universe in the *unaffected* metastable phase at the instant t (Kajantie and Kurki-Suonio [69], Christiansen and Madsen [33]).

There are at least two different ways of defining the functional expression for $f(t)$ and none of them is completely satisfactory. A main issue concerning the derivation of $f(t)$ is the correct definition of what should be meant as "unaffected" region of the Universe. As discussed in Subsection 1.2.2, it is most likely that the newly nucleated bubbles would grow as spherical weak deflagrations and in this case the solution of the hydrodynamical equations requires the presence of a precompression shock front preceding the deflagration. This shock front would then move at a speed slightly above the local sound speed and some authors suggest that it could reheat the quark plasma at the critical temperature. This is an argument which is often found in the literature (Gyulassy et al. [54], Bonometto and Pantano [24], Christiansen and Madsen [33]) as it provides a rather simple scenario in which define the volume fraction $f(t)$, but that is *most probably* wrong. As discussed at length in Section 2.2, the magnitude of this shock can be negligibly small in the small supercooling scenario discussed here and it would certainly be inefficient in raising the temperature in those regions it crosses. Indeed, it is not at all clear that the entire compression wave following the shock (and that certainly produces a temperature increase) would be able to raise the temperature near or above the critical one. What is usually neglected in those analyses which favour the reheating by means of the precompression shock front is that the quark plasma is an ultrarelativistic fluid with a huge energy density content and that effectively behaves as an incompressible fluid. The latent heat released at the phase transformation, although large and mostly converted into internal energy, is nevertheless only a very small contribution to the preexisting energy density of the quark plasma.

As a result, any analytic definition of the "unaffected" region of the Universe in terms of the propagation velocity of some kind of discontinuity front is rather dubious unless one is ready to consider this velocity as an effectively *undetermined* quantity, about which only reasonable upper and lower limits can be set, given by the sound speed and the propagation velocity of the deflagration front respectively.

Following Guth and Tye [53] (a slightly different approach has been proposed also by Csernai and Kapusta [28, 29]) we could describe the fraction of volume not yet swept by one or more shock fronts as

$$f(t) = \exp\left[-\int_{t_c}^{t} dt' f(t') p(T(t')) V(t', t)\right] \ , \tag{4.33}$$

where t_c is the time corresponding to the temperature T_c and $V(t', t)$ is the reheated volume at time t caused by a bubble nucleated at time t'. An approximate expression for $V(t', t)$ can then be

$$V(t',t) \approx \frac{4\pi}{3} v_{rh}^3 (t-t')^3 \ , \tag{4.34}$$

with the *reheating front* velocity v_{rh} being constrained to lie between the limits

$$v_{defl} \leq v_{rh} < c_s \ . \tag{4.35}$$

Under these simplifying assumptions, an estimate of the mean nucleation distance is then given by

$$l_n \approx (16\pi)^{1/3} \frac{v_{rh}}{\alpha} \ . \tag{4.36}$$

Finally, using the following estimates for the typical values of the surface tension and latent heat derived by lattice QCD calculations (Ignatius et al. [65], Christiansen and Madsen [33])

$$\sigma_0 = \frac{\sigma}{T_c^3} \sim 0.02 \ , \qquad\qquad L \sim 0.4B \ , \tag{4.37}$$

a critical temperature $T_c = 0.68 B^{1/4} = 150$ MeV ($B^{1/4} \approx 220$ MeV) and the upper limit for the reheating front velocity, the homogeneous nucleation scenario then leads to an estimate of the mean nucleation distance of the order of few centimeters *i.e.* :

$$l_n \approx 7 \left(\frac{220\mathrm{MeV}}{B^{1/4}} \right)^2 \left(\frac{0.4B}{L} \right) \left(\frac{\tilde{\gamma}}{0.24 B^{1/2}} \right)^3 \mathrm{cm} \ . \tag{4.38}$$

Larger values for l_n (larger by about a factor 7) can be obtained if the curvature terms are not taken into account.

It is important to underline that these estimates of l_n seem to prevent a possible impact of baryon number inhomogeneity produced at the quark–hadron transition on the subsequent cosmological nucleosynthesis, for which mean separations of the order of one meter are necessary. A discussion of this will also be presented in the following Subsection 5.1.2.

Possible ways of avoiding this conclusion have been proposed and these mainly involve the use of an inhomogeneous bubble nucleation scenario. This argument has been recently revitalized by Christiansen and Madsen [33] who have underlined the fact that classical first order phase transitions are usually triggered by the presence of impurities or "irregularities" rather than by thermal fluctuations. (It is possible to think, for example, of a charged particle entering a cloud chamber, or boiling water where bubbles are formed at the bottom of the pot.) Potential impurities for the quark–hadron transition could be

topological defects, like magnetic monopoles, and cosmic strings, primordial black-holes or relic fluctuations from the electroweak transition.

The basic idea behind the inhomogeneous bubble nucleation scenario is that the impurity tends to lower the energetic cost of creating a phase interface and therefore a bubble. As a consequence, bubbles nucleated by means of impurities would appear with a smaller degree of supercooling and their number density would then be set only by the number density of the primordial impurities and not follow the probability distribution (4.30). If one then makes the (very) strong assumption that the spherical shock produced by the newly nucleated bubbles are able to reheat the Universe and prevent any further nucleation, it becomes then clear that it is in principle possible to tune the impurity number density so as to obtain a first and unique generation of hadron bubbles nucleated at the desired separation scale. (In such a scenario thermal fluctuations may well never act so as to nucleate bubbles if the reheating is sufficiently rapid). However, as mentioned above, we doubt that the precompression shock front emitted by weak deflagrations produced at even smaller degrees of supercooling could be able to reheat the Universe and we therefore regard the present version of the inhomogeneous nucleation scenario as rather unlikely.

4.6 A General Overview

Following on from the physical scenario of the cosmological quark–hadron transition described in the previous sections, we here illustrate and comment about the most acknowledged stages of the transition. We underline that the sequence of such stages is reasonable within the framework in which the positive latent heat is large as compared with the surface tension and the transition takes place with a small degree of supercooling.

We first present a schematic sequence of "events" during the transition and then comment extensively on each of them.

1. Supercooling of the quark plasma.
2. Nucleation of bubbles of the hadron plasma.
3. Initial rapid growth of hadron bubbles as weak deflagrations; a very small spherical precompression wave is sent out in the quark phase from each hadron bubble.
4. Attainment of a self similar growth for the disconnected hadron bubbles.
5. Local coupling on the bubble length scale between standard fluid particles (*i.e.* having strong interactions) and radiation fluid particles (*i.e.* having weak and elec-

tromagnetic interactions). This coupling could occur also for a radiation fluid of neutrinos if disconnected hadron bubbles still persist at a scale of ~ 1 cm.

6. Interaction of the compression waves preceding the deflagration fronts of different bubbles and reheating of both phases near to the critical temperature.

7. Slow growth of the hadron bubbles paced by the expansion of the Universe. Different bubbles percolate into more extended structures.

8. Coalescence of percolated hadron bubbles into bigger hadron regions so as to minimize surface energy. Production of disconnected quark plasma regions.

9. Slow contraction of the disconnected regions of quark plasma which tend to become spherical.

10. Breaking of local coupling between standard fluid particles and radiation fluid particles on the length scale of the disconnected quark regions . A similar process would have happened also with a fluid of neutrinos if disconnected quark drops were produced at a scale of ~ 1 cm.

11. Final evaporation of quark drops.

After the nucleation period, the Universe is essentially populated by hadron bubbles with dimensions near the critical radius. Each bubble then starts to expand (the new, low temperature phase is thermodynamically favoured) and its surface accelerates until it reaches a steady state velocity corresponding to self similar growth for a weak deflagration front, whose solution has been presented in Section 2.2 [see diagram (a) of Figure 4.3]. The self similar growth is first broken when the dimensions of the hadron bubbles R_s become comparable with the mean free path of the radiation fluid particles λ[11]. At this stage, the long range energy momentum transfer between the standard fluid and the radiation fluid is most effective and the hadron bubbles, which were previously transparent to the radiation, start to couple with it (see also Section 6.2).

It is worth underlining that at least in principle the process of coupling between the standard fluid and the radiation fluid could take place at two different length scales λ. The smaller of these is the one set by the electromagnetic interaction and is relevant for a radiation fluid composed of photons, electrons/positrons ($e^{\pm}$), muons and their antiparticles ($\mu^{\pm}$), etc., for which $\lambda \simeq 10^4$ fm.

[11] In principle, the mean free path of the radiation fluid particles could be different in the two phases, so that it would be necessary to refer to λ_q and λ_h. However the uncertainty on this length scales is such that treating $\lambda_q \approx \lambda_h \approx \lambda$ is a reasonable approximation.

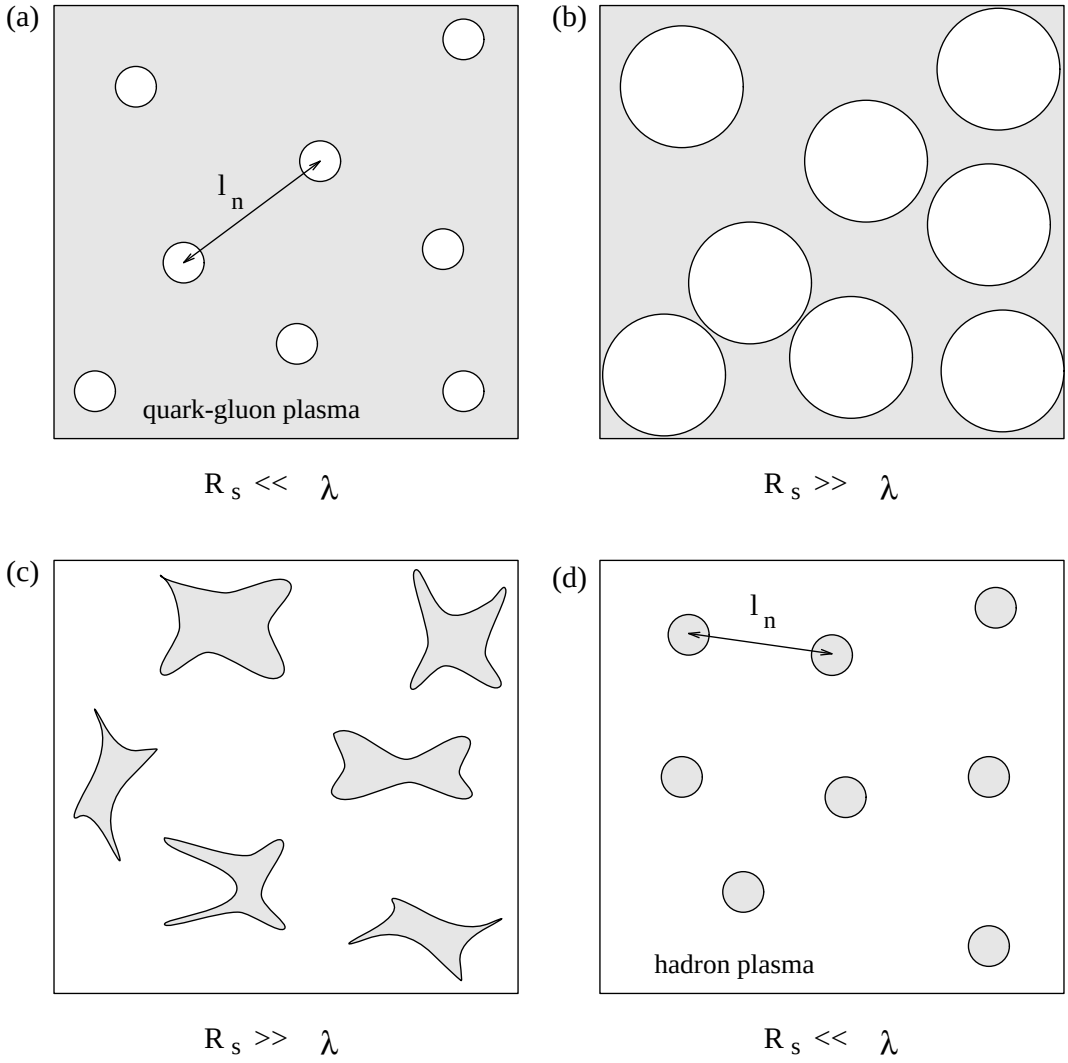

Figures 4.3 Schematic pictorial representation of the different stages of the phase transition with the quark plasma being indicated with the shaded regions. Diagram (a) shows a picture of the nucleation stage when the surviving hadron bubbles with critical radius R_c have typical comoving separation l_n within the surrounding quark plasma. Diagram (b) shows a subsequent stage when hadron bubbles meet and start percolating, while diagram (c) shows the following stage at which hadron bubble coalescence produces disconnected quark regions. Under the effects of surface tension, these regions tend to become spherical and lead to the formation of evaporating quark drops within the surrounding hadron plasma, which are shown in diagram (d). For all of the diagrams, the typical dimension of the disconnected quark or hadron regions R_s is compared with the mean interaction length scale for the radiation fluid λ.

The other larger length scale is set by the weak interaction and is relevant for a radiation fluid composed of neutrinos and antineutrinos only and for which $\lambda \simeq 10^{13}$ fm $\simeq 1$ cm. Whether the second radiative transfer can ever take place depends on the mean bubble separation distance at the time of nucleation as well as on the mean velocity of the bubble surface and, at the moment, these two quantities are not known enough to give a definitive answer.

After the hadron bubbles have grown of by about one order of magnitude past the typical radiation interaction length scale, the coupling is practically complete and the hydrodynamical solution can again recover a self similar behaviour. This newly attained similarity solution is definitively broken when the spherical compression waves preceding the deflagration fronts of neighbouring bubbles start to interact. Of course, this occurs well before the bubble surfaces themselves come into contact. As discussed in Section 4.3, the predicted amplitude of the precompression shock fronts is negligibly small for the case of spherical bubbles and small supercooling (Miller and Pantano [114], Ignatius et al. [62], Miller and Rezzolla [115], Kurki-Suonio and Laine [83]) and it is therefore rather erroneous and misleading to associate strong physical processes to the interaction of the these fronts. However, independently of whether there are significant shocks or not, the kinetic energy of the ordered motion in the compression wave will be progressively converted into internal energy, once adjacent bubbles have started to interact, and the temperatures of both phases will be raised near to the critical temperature T_c. At this stage, bubble surfaces may start to oscillate (with decaying amplitude oscillations) as a consequence of the collision with neighbouring bubbles and the new temperature phase might even be superheated as a result of the volume decrease produced by the oscillations (Kurki-Suonio and Laine [84]). What is certainly more likely is that after the collision, the hadron bubbles grow much more slowly, on a time scale which is essentially set by the expansion of the Universe leading to cooling which allows for continuation of the transition [see diagram (b) of Figure 4.3].

When the surfaces of adjacent bubbles meet, they coalesce to form larger bubbles thus minimizing the total surface energy. This coalescence then gives rise to disconnected quark regions which proceed to evaporate, tending to become spherical under the action of surface tension [see diagram (c) of Figure 4.3].

The hydrodynamical evolution of isolated evaporating quark drops has been investigated in detail in Section 2.3 and can be essentially summarized as consisting of a self similar stage followed by one in which long range energy and momentum transfer takes place and then a final decay which may be dominated by surface tension effects and become increasingly rapid. During the first stage, quark drops evaporate converting quarks into hadrons at the rate necessary to keep the internal compression constant and uniform.

In a very pictorial description, each quark drop can be viewed as behaving like a shrinking "leaky balloon" which is ejecting material at the rate necessary to avoid producing any compression.

When the quark drops reach dimensions comparable with the mean free path for the particles of the radiation fluid, the process of entropy extraction breaks the self similarity of the evaporation. Also in the case of quark drops, the decoupling could take place at two different scales, with the larger being set by the neutrinos and antineutrinos mean free path. However, it is not currently clear whether spherically isolated quark drops would have been present at that scale. The very final stages of the drop evaporation (for $R_s \lesssim 10^2$ fm) may be dominated by the surface tension σ which would tend to "squeeze" the small quark drops and could give rise to an increasingly rapid evaporation and a consequent increase of both the compression and the baryon number density. Recent lattice gauge calculations seem to indicate rather small values for the surface tension coefficient (*e.g.* $\sigma_0 = \sigma/T_c^3 \approx 0.01 - 0.02$) and, if this is correct, surface tension would then play only a minor role for the increase of baryon number density. The transition finally ends when the last quark drop has shrunk to zero dimensions and the Universe is totally filled with the new hadron phase [see diagram (d) of Figure 4.3].

There are a number of very interesting aspects of the above mentioned "events" which could be investigated by using the tools and the formalism of relativistic hydrodynamics of compressible flows. In particular, it is interesting to follow in detail the processes of long range energy and momentum transfer that take place between the standard fluid and the radiation fluid both during hadron bubble growth and during quark drop evaporation. Also, important information could be extracted by the knowledge of the hydrodynamical behaviour of the baryon number carriers, whose spatial distribution at the end of the transition could have had a strong influence on the subsequent cosmological nucleosynthesis.

All of these aspects have, in fact, been investigated by Rezzolla et al. [115, 139, 140, 145] and they will all be presented in the next chapters in which we first introduce the mathematical formalism and the original set of equations derived for the hydrodynamical solution (Chapter 5.1) and subsequently present results obtained from the numerical solution of those equations (Chapter 6).

4.7 Appendix C

Equations of state for a relativistic ideal fluid are found in almost all works concerned with the physics of plasmas in the early Universe and the derivation of such equations is rather straightforward although it is not easy to find in the literature. In this Appendix we will not present new equations nor an original derivation of equations, but rather spend few lines to rederive the standard equations of state for a relativistic ideal fluid.

Consider an ideal fluid as a large collection of identical particles and let $\mathbf{p}$ be the four-momentum associated to the i-th particle of such collection, where

$$p^\alpha p_\alpha = -p_0^2 + p_j p^j = -m_i^2 \ , \tag{4.39}$$

and where p_0 is the total energy of the i-th particle and m_i its rest mass. We can then define $f_i(x_j,\ p_j,\ t)$ to be the distribution function of the i-th particle in the phase-space where it has spatial coordinates x_j and p_j as spatial components of its four-momentum at the time t. In the presence of a diagonal metric, the stress energy tensor of the fluid can then be written as

$$T^{\alpha\beta} = \sum_i \int p^\alpha p^\beta f_i(x_j, p_j, t) \frac{dV_p}{p_0} \ , \tag{4.40}$$

where $dV_p = dp^x\, dp^y\, dp^z$ is the volume element in the momentum space and where the sum is made over the whole number of particles of the fluid. Expression (4.40) should be compared with the more familiar expression of the stress energy tensor of a perfect fluid (1.1) which we report here for convenience

$$T^{\alpha\beta} = (e+p)u^\alpha u^\beta + p g^{\alpha\beta} \ . \tag{1.1}$$

We can now write explicitly the different diagonal components of (4.40) as

$$T^{00} = \sum_i \int p_0 f_i \, dV_p = n\langle p_0 \rangle = e \ , \tag{4.41}$$

where n is the particle number density, the symbols $\langle\ \rangle$ express quantities averaged over the whole collection of particles and where the last equality in (4.41) comes from the comparison with (1.1). Similarly, we can calculate the spatial trace of (4.40) as

$$T^l{}_l = \sum_i \int \left(\frac{p_0^2 - m_i^2}{p_0} \right) f_i \, dV_p = 3p \ , \tag{4.42}$$

which leads, in the case of relativistic particles (*i.e.* for which $m_i \ll p_0$), to

$$T^l{}_l \cong \sum_i \int p_0 f_i \; dV_p = e = 3p \; , \tag{4.43}$$

thus showing the standard relation $p = e/3$ between pressure and energy density of a relativistic fluid. We can now specialize our analysis to a Bose or to a Fermi distribution function

$$f_{b,f}(T) = \frac{1}{\exp(-p/T) \mp 1} \; , \tag{4.44}$$

where $p = p^j p_j$ and the $\pm$ signs refer to a Bose and to a Fermi distribution respectively. We can then evaluate the energy density e and number density n as

$$\begin{aligned} e_{b,f} &= 4\pi T^4 \int_0^\infty \frac{x}{\exp(-x) \mp 1} \, d^3x \; , \\ n_{b,f} &= 4\pi T^3 \int_0^\infty \frac{1}{\exp(-x) \mp 1} \, d^3x \; . \end{aligned} \tag{4.45}$$

Integration of (4.45) then leads to the general expressions

$$e_{b,f}(T) = g_{b,f} \left(\frac{\pi^2}{30} \right) \; T^4 \; , \tag{4.46}$$

$$n_{b,f}(T) = g'_{b,f} \left[\frac{\zeta(3)}{\pi^2} \right] \; T^3 \; , \tag{4.47}$$

where $\zeta(3) \approx 1.202$ and

$$g_b = N_b \; , \qquad g_f = \frac{7}{8} N_f \; , \tag{4.48}$$

$$g'_b = N_b \; , \qquad g'_f = \frac{3}{4} N_f \; , \tag{4.49}$$

with N_b and N_f being the bosonic and fermionic numbers of degrees of freedom.

As a result, for a mixture of relativistic bosons and fermions the energy density and the number density are respectively given by

$$e(T) = g \left(\frac{\pi^2}{30} \right) T^4 = \left(N_b + \frac{7}{8} N_f \right) \left(\frac{\pi^2}{30} \right) T^4 \; , \tag{4.50}$$

$$n(T) = g' \left[\frac{\zeta(3)}{\pi^2} \right] T^3 = \left(N_b + \frac{3}{4} N_f \right) \left[\frac{\zeta(3)}{\pi^2} \right] T^3 \; . \tag{4.51}$$

4.8 Summary

- *According to the* **Big Bang** *model, our present Universe originated from a spacetime singularity and subsequently expanded and cooled.*
- *During its early evolution the Universe experienced a sequence of* **phase transitions** *signalling the loss of a given symmetry in the fields present or a change of the thermodynamical properties of the primordial plasma.*
- *The* **quark–hadron** *phase transition is the last in this sequence and probably took place at about* 10^{-5} *s after the Big Bang, when the mean temperature of the Universe was* $T_c \simeq 150$ *MeV.*
- *Being the* **last** *of the cosmological phase transitions, the quark–hadron transition might have produced* **relics** *that played an important role in the subsequent cosmological evolution.*
- *It is not currently known what is the* **order** *of transition, but a number of interesting features would emerge if it was* **first order** *as suggested by some recent lattice gauge calculations.*
- *We here consider the case of the quark–hadron phase transition being of* **first order**, *i.e. with both phases coexisting at the same temperature and being separated by a* **phase interface**. *The latter will be hydrodynamically described as a* **relativistic reaction front**.
- *A certain amount of* **supercooling** *is usually necessary to overcome the energy cost of producing a phase interface in a first order phase transition. A small but finite degree of supercooling most probably is necessary also in a cosmological context and according to the amount of supercooling reached, a number of different types of reaction fronts are possible.*
- **Weak deflagration fronts** *require minimal conditions (both in degree of supercooling and in the stability of the new phase) and are therefore adopted for describing the dynamics of the phase interface.*
- *It is important to stress that the* **strength** *of the* **precompression shock** *preceding the deflagration front in the solution of a growing bubble is* **negligibly small** *if the*

supercooling is small. As a result, such a shock is not able to reheat those regions which it crosses to the critical temperature.

- *Hadron bubbles can be nucleated either by means of* **thermal fluctuations** *(homogeneous nucleation scenario) or by means of* **impurities** *(inhomogeneous nucleation scenario).*

- *The nucleation mechanism basically determines the typical* **separation between nucleation sites** *and this, in turn, represents the most important scale of the transition, marking the length at which relics could have been produced. The larger this (subhorizon) scale, the stronger its cosmological impact.*

- *Homogeneous nucleation theory yields values for the bubble distance at nucleation which are typically* **smaller** *then the ones derived using a recent inhomogeneous nucleation theory. However, the latter requires a reheating of the old phase by means of the precompression shocks. Because of the weakness of these shocks, we regard the present version of the inhomogeneous scenario as unlikely.*

- *During the* **final stages** *of the phase transition, quark plasma regions become* **disconnected** *and* **evaporate** *while becoming spherical under the action of surface tension.*

- *The evaporation of single isolated quark drops represents a very interesting* **hydrodynamical configuration** *during which the simultaneous effects of* **radiation decoupling** *and* **baryon flux suppression** *at the phase interface might lead to interesting consequences for the subsequent cosmological evolution.*

Chapter 5

Relativistic Hydrodynamics of the Quark–Hadron Transition

5.1 General Relativistic Multicomponent Hydrodynamics

This chapter is dedicated to the derivation of an original and complete set of general relativistic equations describing the hydrodynamics of a multicomponent fluid in a spherical flow. In particular, we will here define a new set of equations for a three-component relativistic perfect fluid which consistently accounts for:

a) the long range energy and momentum transfer between a standard fluid and a radiation fluid (see Section 3.1);

b) the dynamics of a superposed fluid component which is collisionless and subject to diffusion only;

c) the dynamics of a discontinuity surface moving as a weak deflagration front;

d) general relativistic junction conditions across the discontinuity surface for the metric, the energy and the momentum of each of the three fluid components;

e) a characteristic form of the relevant hydrodynamical equations along the several different characteristic directions present.

The most direct application of the mathematical "apparatus" which we present here is within a cosmological scenario in general and for the quark–hadron transition in particular. However, it is important to stress that all of the equations derived here are general and could therefore be applied to any other context in which a relativistic multicomponent spherical flow takes place. Indeed, this is what has been done recently by Zampieri et al. [171] who have applied some of the above mentioned equations to the study of spherical accretion onto a black-hole.

Each of the following subsections is devoted to one of the specific issues listed above, but before going into the details of the various different derivations, it is worth to spend a few lines about the importance of a general relativistic approach for the hydrodynamics of the cosmological quark–hadron transition. It has been sometimes argued that General Relativity represents an unnecessary complication for the study of bubbles and drops in the early Universe, for which a special relativistic treatment could be sufficient. At this regard, we believe that at least two counter-arguments could be made. A first comment we would like to make is that the gravitational source terms appearing in set of hydrodynamical equations as a consequence of the general relativistic approach, introduce only a very minor additional complication. In other words, for spherical symmetry, a *general* relativistic calculation is only marginally more complicated than a *special* relativistic one. A second comment is that writing equations in a fully general relativistic form has great advantages when these equations need to be computed in an expanding background as it is the case for a cosmological phase transition. In this case, in fact, the form of the equations is totally compatible with a Friedmann-Robertson-Walker (FRW) solution, which is "automatically" recovered at large scales.

5.1.1 Two-Component Spherical Flows

In the first studies of the hydrodynamics of the cosmological quark–hadron phase transition (Miller and Pantano [113, 114], Ignatius et al. [61]) attention has been focussed on studying the growth of a single hadronic bubble during the initial stages of the transition where it makes sense to consider the material in each phase as a perfect fluid composed only of the strongly interacting matter (*i.e. standard fluid*). While the transition involves only these particles in a direct way, an important role is also played by other particles present, which can interact with them through the electromagnetic and weak interactions: primarily photons, electrons, muons and their antiparticles (electromagnetic and weak interactions) and neutrinos and antineutrinos (weak interaction only). All of these have mean free paths long compared with that of the strongly interacting matter and can provide a mechanism for long range transport of energy and momentum through the

strongly interacting fluid. Since the leptons concerned are essentially massless, both they and the photons can be treated as components of a generalized *radiation fluid* and the problem is then one of relativistic radiative transfer (Chapter 3).

During hadron bubble growth (or during quark drop evaporation), the effect of this transport is significant only when the radius R_s of the bubble (or of the drop) becomes roughly comparable with the mean free path λ of the particles concerned ($\lambda \sim 10^4$ fm for the electromagnetic interaction and $\lambda \sim 1$ cm for the weak interaction). When $R_s \ll \lambda$, the bubble (or the drop) is essentially transparent to the radiation, which can then be ignored, while when $R_s \gg \lambda$ the coupling is essentially complete on relevant length scales so that the radiation and strongly interacting matter move together as a single fluid. Clearly, the process of coupling (or of decoupling) can, in principle, occur twice during the bubble growth (or drop evaporation), but because the behaviour is similar in each case, we will discuss here only the one occurring between the strongly interacting and electromagnetically interacting particles. Identical considerations apply also for the coupling (or decoupling) with the neutrinos, the only difference, apart from the scale, being the different number of degrees of freedom into which the energy liberated by the transition is channeled.

In the following we will derive general relativistic equations accounting for the hydrodynamics of a two-component fluid composed of the standard fluids (representing the strongly interacting matter in the hadron and quark phases) and of the radiation fluid (representing weakly and electromagnetically interacting matter). Since we are interested in describing the motion of a bubble or of a drop over a number of orders of magnitude in its radius and since the underlying symmetry is a spherical one, we will make use of a Lagrangian description and adopt the same spherically symmetric line element presented in Section 3.3, which we here report for convenience

$$ds^2 = -a^2(t)dt^2 + b^2(\mu)d\mu^2 + R^2(\mu,\ t)(d\theta^2 + \sin^2\theta\ d\phi^2)\ . \tag{3.10}$$

We recall that $R(\mu,\ t)$ is the radial Eulerean coordinate and that μ is the comoving radial coordinate, whose scale needs to be fixed by means of a supplementary equation. A convenient way of doing this involves the definition of the *proper volume* V_0 contained within the spherical shell marked by μ at an initial time t_0, *i.e.*

$$V_0 = \int_0^\mu 4\pi b_0 R_0^2\, d\mu\ , \tag{5.1}$$

so that the infinitesimal volume between two spherical shells with radial separation $\Delta\mu$ (*e.g.* the volume of a fluid element) is given by

$$\Delta V_0 = 4\pi b_0 R_0^2 \Delta\mu \ . \tag{5.2}$$

The coordinate gauge freedom allows us to define (at some initial time t_0)

$$\Delta V_0 = \Delta\mu \ , \tag{5.3}$$

from which the definition for b_0 follows, *i.e.*

$$b_0 = \frac{1}{4\pi R_0^2} \ . \tag{5.4}$$

At any later instant, the proper volume will not be necessarily the same but it will rather follow the compressions and the rarefactions of the underlying medium. As a result, the general expression for the proper volume at any subsequent instant will be

$$\Delta V(t) = 4\pi b R^2(t) \Delta\mu \ , \tag{5.5}$$

and the adimensional quantity

$$\rho \equiv \frac{\Delta V_0}{\Delta V} \ , \tag{5.6}$$

will then measure the variation in the proper volume of a fluid element. Because of its definition (5.6), ρ is usually called the *relative compression factor*. For a classical standard fluid composed of non-relativistic particles, it is common practice to take μ as representing conserved rest mass $\Delta\mu = \rho_0 \Delta V_0$ with ρ representing the familiar rest mass density [*cf.* equation (7.11)]. (At later times, one then has $\rho = \rho_0 \Delta V_0 / \Delta V$ but all of the other equations presented below are formally unchanged.) Using expressions (5.3), (5.5) and (5.6) we can finally obtain the fundamental relation fixing the expression for the metric coefficient b at a general time t

$$b(t) = \frac{1}{4\pi R^2 \rho} \ . \tag{5.7}$$

The derivation of the hydrodynamical equations for the combined fluids (*i.e.* standard fluid and radiation fluids) is rather straightforward and we can start from solving Einstein field equations

$$R_{\alpha\beta} - \frac{1}{2} g_{\alpha\beta} R = 8\pi G T_{\alpha\beta}, \tag{5.8}$$

with $T^{\alpha\beta} = T_{_R}^{\alpha\beta} + T_{_F}^{\alpha\beta}$ being the *total* stress energy tensor, sum of the one for the radiation fluid (subscript R) and of that for the standard fluids (subscript F) which we here treat

as perfect. The four independent equations which follow from (5.8) can be used to write, in a more familiar form for hydrodynamics, the conservation equations for energy and momentum of the combined fluids and the continuity equation for the standard fluids, *i.e.*

$$-u_\alpha T^{\alpha\beta}{}_{;\beta} = 0 \ , \tag{5.9}$$

$$n_\gamma P^\gamma_\alpha T^{\alpha\beta}{}_{;\beta} = 0 \ , \tag{5.10}$$

$$(\rho u^\alpha)_{;\alpha} = 0 \ . \tag{5.11}$$

After some algebra, whose relevant steps are shown in the Appendix D, it is possible to write the following set of hydrodynamical equations

$$u_{,t} = -a\left[\frac{\Gamma}{b}\left(\frac{p_{,\mu} + bs_1}{e+p}\right) + 4\pi GR\left(p + \frac{1}{3}w_0 + w_2\right) + \frac{GM}{R^2}\right] \ , \tag{5.12}$$

$$e_{,t} = w\rho_{,t} - as_0 \ , \tag{5.13}$$

$$\frac{(\rho R^2)_{,t}}{\rho R^2} = -a\left(\frac{u_{,\mu} - 4\pi GbRw_1}{R_{,\mu}}\right) \ , \tag{5.14}$$

$$\frac{(aw)_{,\mu}}{aw} = -\frac{w\rho_{,\mu} - e_{,\mu} + bs_1}{\rho w} \ , \tag{5.15}$$

$$M_{,\mu} = 4\pi R^2 R_{,\mu}\left(e + w_0 + \frac{u}{\Gamma}w_1\right) \ , \tag{5.16}$$

$$\Gamma = \left(1 + u^2 - \frac{2GM}{R}\right)^{1/2} = \frac{1}{b}R_{,\mu} \ , \tag{5.17}$$

$$R_{,t} = au \ . \tag{5.18}$$

Here u is the radial component of fluid four velocity in the associated Schwarzschild (Eulerean) frame, Γ is the general relativistic analogue of the Lorentz factor, and w is the specific enthalpy

$$w = \frac{(e+p)}{\rho} \ . \tag{5.19}$$

M is a "generalized mass function", corresponding to the standard gravitational mass in the case of a classical standard fluid composed of non-relativistic particles without radiation and can also be calculated using the alternative evolution equation

$$M_{,t} = -4\pi R^2 R_{,t}\Big(p + \frac{1}{3}w_0 + \frac{\Gamma}{u}w_1 + w_2\Big) \ . \tag{5.20}$$

Equations (5.12)–(5.16) show that the interaction between the standard fluids and the radiation fluid enters through the source functions s_0 and s_1 and through the radiation contributions to the gravitational terms via the radiation energy density w_0, energy flux w_1 and anisotropy w_2. The latter quantities are calculated by considering local conservation of energy and momentum of the radiation fluid alone [*i.e.* equations (3.15) and (3.16)] and satisfy the following hydrodynamical equations for the radiation fluid and which have been derived in Section 3.3

$$(w_0)_{,\,t} + \frac{a}{b}(w_1)_{,\,\mu} + \frac{4}{3}\Big(\frac{b_{,\,t}}{b} + \frac{2R_{,\,t}}{R}\Big)w_0 + \frac{2a}{b}\Big(\frac{a_{,\,\mu}}{a} + \frac{R_{,\,\mu}}{R}\Big)w_1 + \Big(\frac{b_{,\,t}}{b} - \frac{R_{,\,t}}{R}\Big)w_2 = as_0 \ , \tag{3.18}$$

$$(w_1)_{,\,t} + \frac{a}{b}\Big(\frac{1}{3}w_0 + w_2\Big)_{,\mu} + \frac{4a_{,\,\mu}}{3b}w_0 + 2\Big(\frac{b_{,\,t}}{b} + \frac{R_{,\,t}}{R}\Big)w_1 + \frac{a}{b}\Big(\frac{a_{,\,\mu}}{a} + \frac{3R_{,\,\mu}}{R}\Big)w_2 = as_1 \ , \tag{3.19}$$

$$w_2 = f_{_E} w_0 \quad , \tag{3.17}$$

with (3.17) being the closure relation. For the two scalar source moments, we here use the following expressions

$$s_0 = \frac{1}{\lambda}(\epsilon - w_0) + (s_0)_{_{SC}} \ , \tag{5.21}$$

$$s_1 = -\frac{w_1}{\lambda} \ , \tag{5.22}$$

where λ is the effective mean free path of the radiation particles as they move through the standard fluid, $(s_0)_{_{SC}}$ is a term expressing the contribution due to scatterings, whose form depends on the specific problem, and ϵ is the energy density for radiation in thermal equilibrium with the standard fluid. Assuming that it follows a black-body law, ϵ can be written as [*cf.* equation (4.18)]

$$\epsilon = g_{_R} \left(\frac{\pi^2}{30} \right) T_{_F}^4, \tag{5.23}$$

with $T_{_F}$ being the temperature of the standard fluid. (Note that different expressions for the source functions should be used in scenarios different from the cosmological one in which we are interested here.) $g_{_R}$ is the number of degrees of freedom of the radiation fluid and has contributions coming essentially from photons, electrons (and positrons) and muons (and antimuons). A rapid calculation yields the following value for the degrees of freedom of the radiation fluid

$$\begin{aligned} g_{_R} &= g_\gamma + g_{e^\pm} + g_{\mu^\pm} \\ &= \underbrace{1}_{\gamma} \times \underbrace{2}_{helicity} + \frac{7}{8} \left[\underbrace{2}_{e^+,\,\mu^+} \times \underbrace{2}_{spin} + \underbrace{2}_{e^-,\,\mu^-} \times \underbrace{2}_{spin} \right] = 9 \end{aligned} \tag{5.24}$$

and $7/8 \times 3 \times 2 = 5.25$ $(= g_\nu)$ supplementary degrees of freedom need to be added if the contribution of neutrinos should also be taken into account.

Obtaining a suitable expression for $(s_0)_{_{SC}}$ within a cosmological scenario is less straightforward. While detailed derivations have been made for simpler astrophysical applications (Nobili et al. [122, 123]), the lack of precise knowledge about the numerous and complex interaction processes possible in the present case has led us to express $(s_0)_{_{SC}}$ by the simple absorption and emission term

$$(s_0)_{_{SC}} = \frac{\alpha_2}{\lambda} (\epsilon - w_0) \ , \tag{5.25}$$

where α_2 is an adjustable coefficient ranging between zero and one, with the latter value being the most reasonable within a cosmological context. Fortunately, the results of the numerical calculations turn out not to depend sensitively on the value chosen and a discussion of this will be given in Sections 6.2 and 6.3.3.

As mentioned in Section 3.3, the quantity $f_{_E}$ appearing in the closure relation (3.17) is the Eddington factor and gives a measure of the degree of anisotropy of the radiation fluid. In particular, it can take values ranging from 0, for complete isotropy (which could be caused by the medium being extremely optically thick), to 2/3 for complete anisotropy (which might arise when the medium is very optically thin). The expression used for it has to be arrived at on the basis of physical considerations and has to have a correct asymptotic behaviour in any relevant limits. We are here interested in studying the long

range energy and momentum transfer taking place during hadron bubble growth and during quark drop evaporation. In either case, as initial conditions, both the bubble and the drop are assumed to be immersed within a uniform and isotropic surrounding medium[1]. The radiation field interacts with the surrounding medium on suitably large scales and is in thermal equilibrium with it, so that it initially shares the properties of uniformity and isotropy, *i.e.* w_0 is constant everywhere and w_1 and w_2 are zero. The initial situation for a quark drop is however slightly more complicated than for a much smaller hadron bubble. The dimensions of the disconnected quark regions are, in fact, typically larger than the mean free path of the radiation fluid particles and a thermal equilibrium (at a slightly higher temperature, the quark plasma temperature) is present also over those regions. As a result, while still being uniform and locally isotropic in both phases, the radiation fluid is not at the same temperature everywhere (as it is the case for bubble growth) but rather follows the two different temperatures of the quark and hadron plasmas respectively.

When the hadron bubble starts to expand (or during the very final stages of the quark drop evaporation, when its dimensions are much smaller than λ), the radiation quantities deviate from their uniform initial values (or uniform final values in the case of the drop) primarily as a result of the Doppler effect arising from the motion of the standard fluid rest frames with respect to that of the radiation field (which is remaining uniform in its own frame). These Doppler corrections can be calculated analytically and the details of this derivation are presented in the Appendix D. Solely on the basis of this consideration, one finds that the optically thin regime for the radiation fluid can be described in terms of the Eddington factor

$$f_{_E} \cong \frac{8}{9}\frac{u^2}{(1+4u^2/3)} \,. \tag{5.26}$$

On the other hand, as the hadron bubble *grows* up to dimensions comparable with λ (or when the quark drop *contracts* down to dimensions smaller than λ), there is progressive coupling (or decoupling, in the case of the quark drop) between the radiation and the standard fluids on the relevant length scales and this interaction then tends in the direction of making the radiation more isotropic (or more anisotropic in the case of the drop) as seen from the standard fluids. To account for this effect in the expression for the Eddington factor, we can multiply the Doppler term in (5.26) by a correction term which has the effect of producing the right behaviour in the optically thick regime and gives a physically

[1]This surrounding medium will be the quark plasma in the case of hadron bubble growth and the hadron plasma in the case of quark drop evaporation.

plausible join with the optically thin limit[2]. The final form of our Eddington factor is then

$$f_{_E} \equiv \frac{8u^2/9}{(1+4u^2/3)} \left(\frac{\lambda}{\lambda + R} \right) \ . \tag{5.27}$$

It is worth remarking that it is common experience that results of the numerical computations do not depend sensitively on the form chosen for the Eddington factor as long as the correct asymptotic behaviours are preserved and a regular join is made between them. (Nobili et al. [122]). This is something which needs to be checked in any particular application but provided that the outcome of such a check is satisfactory, it is reasonable to proceed with confidence.

The set of hydrodynamical equations (5.7), (5.12)–(5.18) and (3.18)–(3.17) is not complete but needs to be supplemented by equations of state, relating the energy density e, the pressure p and temperature T of both phases of the standard fluids. For this purpose we will make use of the equations of state for the strongly interacting matter (4.16)–(4.19) presented in Section 4.4. In this way, the basic set of equations is finally complete and can be used for describing the transfer of energy and momentum between a standard fluid and a radiation fluid in a general non-stationary relativistic two-component spherical flow.

5.1.2 Diffusion of Baryon Number

If the cosmological quark–hadron phase transition was of first order with small supercooling then it almost certainly produced inhomogeneities of some kind in the spatial distribution of baryon number. These inhomogeneities could have had a relevant influence on the subsequent nucleosynthesis if they were produced on large enough scales, had sufficiently large amplitude and contained a significant fraction of the baryon number present in the Universe (Witten [170], Alcock et al. [8, 9], Fuller et al. [49], Kurki-Suonio [81], Bonometto and Pantano [24], Ignatius et al. [61]).

Many authors in the past years have calculated the possible consequences of baryon number inhomogeneities for the subsequent evolution of the Universe, focussing particularly on the scenarios for inhomogeneous nucleosynthesis (Malaney and Mathews [101], Fuller et al. [68]). However, in all of these studies it was necessary to introduce suitably chosen parameters in order to compensate for lack of knowledge about the spatial distribu-

[2]It should be noted that while the optically thin regime corresponds with the initial stages of the bubble growth and the optically thick regime corresponds with the final stages of the growth, exactly the opposite is true for the evaporation of the quark drop.

tion and amplitude of the baryon number peaks which might have been left behind at the end of the quark–hadron transition. There are various origins for this lack of knowledge which we will now discuss briefly. A first and major unresolved issue concerns the typical distance between nucleation sites at the beginning of the transition l_n. A discussion of this has already been given in Section 4.5 and we will not comment further here, but just recall that l_n also represents the maximum length scale for the production of peaks in the baryon number density at the end of the transition. Independently of the scale over which baryon number fluctuations are produced, the study of baryon number segregation is complicated by the presence of various mechanisms, some acting in opposite directions, which could contribute to the scale of the fluctuations.

When there is chemical equilibrium between the two phases, baryon number density is already "naturally" higher in the quark phase than in the hadron phase. This difference can be further increased as a result of various other processes which probably act together. One of these is *suppression of baryon number flow* across the phase interface (Applegate and Hogan [6], Fuller et al. [49], Kurki-Suonio [81]). Simple statistical considerations suggest that baryon number cannot be carried entirely together with the hydrodynamical flow when this moves from the quark to the hadron phase. A phenomenological explanation for this can be found in the fact that it is generally more difficult to find in a volume of 1 fm^3 and in a time of 10^{-23} sec the right triplet of up and down quarks necessary to form a color singlet nucleon (either a baryon or an antibaryon) than it is to find the doublet of quarks necessary to form the lightest hadrons (*e.g.* pions).

Another mechanism which could affect the variations in baryon number density during the final stages of the transition, is *long range energy and momentum transfer* by means of particles having long mean free path. This process, which has been investigated by Rezzolla and Miller [140] and will be discussed in detail in Subsection 6.3.3, involves the standard fluids of strongly interacting particles and the radiation fluid of particles having only electromagnetic and weak interactions.

Besides the baryon number *segregating mechanisms* mentioned above, there is also another competing process which needs to be taken into account. The formation of localized regions of high baryon number density is counteracted by *baryon number diffusion* which occurs whenever a deviation from homogeneity is produced and is effective both during the quark–hadron transition and after it.

While, from the above discussion, the formation of peaks in baryon number density appears to be a rather inevitable consequence of a first order quark–hadron transition, a number of quantitative aspects of this picture still remain to be fully investigated. For this reason, and before the microphysics of baryon number flow across the phase interface or of baryon number diffusion is known in more detail, we here discuss how the

problem of baryon number segregation and diffusion can be handled within the relativistic multicomponent framework developed so far.

The basic idea is of considering baryon number carriers as the constituents of an additional distinct collisionless "fluid" whose evolution can be followed in terms of a continuity equation for baryon number carriers, of a diffusion equation and of the underlying hydrodynamics of the standard and radiation fluids. Pictorially, baryon number carriers could be thought of as small grains advected by the bulk flow. They do not provide a pressure nor an energy contribution (just like for dust grains) but (unlike dust grains) they are subject to intrinsic motions following a diffusive law. Before illustrating the details of the new set of equations by means of which baryon number carriers will be followed during some relevant stages of the quark–hadron transition, it could be relevant to review the various stages of the transition during which baryon number segregation can either be *favoured* or *impeded*.

First, we note that even in the absence of specific mechanisms for the segregation, there is a "natural" tendency for the baryon number density to be higher in the quark phase than in the hadron phase since baryon number is carried by almost massless quarks in the quark phase, whereas in the hadron phase it is carried by heavy nucleons whose number density is suppressed by an exponential factor. An estimate for the contrast in baryon number density resulting from this can easily be calculated for stages at which global chemical equilibrium is near to holding. The chemical potentials in the two phases can then be set equal (*i.e.* $\mu_b^q = \mu_b^h = \mu_b$) signifying that, if the phase interface were not in motion, equal fluxes of baryon number would cross it in both directions.

Because of the complexity of QCD and of the spectrum of hadronic species present in the low temperature (hadron) phase, it is necessary to make approximations if we want to obtain simple analytical expressions for the baryon number density in the two phases. Using the phenomenological bag model for the quark phase (see Subsection 4.4.1), it is possible to approximate the baryon number density in the quark phase as

$$n_b^q \simeq \frac{N_c N_f}{27} \left(\frac{\mu_b}{T}\right) T^3, \tag{5.28}$$

where N_c and N_f are, respectively, the number of colours (three) and the number of quark flavours (which we will take here to be two). On a similar level of approximation, we can consider the pion contribution to the grand partition function of the hadron phase as being the dominant one coming from the whole spectrum of hadron species, neglect finite volume effects and the repulsive interaction between hadrons and describe the hadron phase as being essentially a gas of relativistic massless particles (see Subsection 4.4.2). As a result we obtain a simple and compact expression for the baryon number density in

the hadron phase as

$$n_b^h = \left(\frac{2mT}{\pi}\right)^{3/2} \sinh\left(\frac{\mu_b}{T}\right) e^{-m/T} \simeq \left(\frac{2mT}{\pi}\right)^{3/2} \left(\frac{\mu_b}{T}\right) e^{-m/T}. \tag{5.29}$$

where m is the nucleon mass.

With all of these assumptions, the contrast in baryon number density between the two phases is given by

$$R = \frac{n_b^q}{n_b^h} = \frac{N_f}{9} \left(\frac{\pi T}{2m}\right)^{3/2} e^{m/T} \sim 10 \qquad \text{for} \quad T = T_c = 150 \text{ MeV}, \tag{5.30}$$

Similar estimates of the baryon number contrast have been found also from more detailed analyses of the baryon number density in the two phases (Goyal et al. [52]).

It is important to stress that when the hypothesis of global chemical equilibrium is valid, equation (5.30) holds between any two generic points in the two phases. It is reasonable to assume that global chemical equilibrium holds when the velocity of the phase interface is much smaller than the diffusion velocity of baryon number and the length scales of the disconnected hadron or quark regions are much smaller than the baryon number diffusion length scale during the transition. This is the case, for example, soon after bubble nucleation, when most of the bubbles present have radii around the critical value.

As described in Section 4.6, after nucleation hadron bubbles start to expand and their surfaces accelerate until reaching a steady state velocity corresponding to a self similar solution (see Section 2.2). The expansion produces a deviation away from chemical equilibrium and the baryon number density can be increased in the vicinity of the interface (Kurki-Suonio [81]), piling up mostly on the quark side but also to some extent in the hadron phase as a result of the increased flux coming from the quark medium. The situation in the bulk of the two phases is not significantly modified, however. Diffusion tends to impede the accumulation of baryon number and, when the *self similar* growth stage is reached for the hydrodynamic variables, the baryon number density attains a *stationary* profile. (Note that the intrinsic length scale set by the diffusion coefficient prevents the baryon number density following a self similar solution.) Most of the excess baryon number on the quark side of the interface is then within a layer of thickness r_d with the value of the baryon number density there being joined to the background value in the bulk of the quark phase via a decaying profile. A rough estimate for r_d is given by

$$r_d \approx \frac{D}{v_f}\,, \tag{5.31}$$

where D is the baryon number diffusion coefficient and v_f is the steady state velocity of the front as measured from the centre of the bubble.

As the numerical computations will show in Section 6.2, the self similar growth is first broken by the coupling between the radiation fluid and the standard fluids when the bubble has reached dimensions of the order of λ; after the coupling, however, the similarity solution for bubble growth is restored and it ultimately ceases when the spherical compression waves preceding the deflagration fronts of neighbouring bubbles start to interact. At this stage, the temperature of the quark phase is raised again near to the critical temperature and the bubbles grow much more slowly, on a time scale which is essentially set by the expansion of the Universe whose cooling allows for the transition to continue. In this slow growth stage, global chemical equilibrium can be restored and the baryon number which has accumulated near to the phase interface can be redistributed into the bulk of the two phases. When the surfaces of adjacent bubbles meet, they coalesce to form larger bubbles thus minimizing the total surface energy. This coalescence gives rise to disconnected quark regions which then proceed to evaporate, tending to become spherical under the action of surface tension. The subsequent hydrodynamical evolution of isolated evaporating quark drops can be essentially summarized as consisting of a self similar stage followed by one in which long range energy and momentum transfer takes place and then a final decay which may be dominated by surface tension effects.

During the first stage, quark drops evaporate converting quarks into hadrons at the rate necessary to keep the internal compression constant and uniform (see Section 2.3). If baryon number were entirely carried along with the hydrodynamical flow and no suppression of baryon number flux occurred at the interface, then this stage of the evaporation would not produce any increases in the baryon number density. If, however, there *is* some flux suppression, this stage will still consist of a self similar evolution for all of the hydrodynamical variables apart from the baryon number which will accumulate ahead of the interface with diffusion to either side of it in a way similar to that discussed above for a growing hadron bubble. When the quark drop reaches dimensions comparable with the mean free path for the particles of the radiation fluid, the decoupling between the two fluids breaks the self similarity of the evaporation and, as we will see in detail in Section 6.3.3, this will produce a remarkable effect on the baryon number density in both phases. At last, the very final stages of the drop evaporation may be dominated by the surface tension σ (if this is large enough) giving rise to an increasingly rapid evaporation and a consequent increase the baryon number density in the quark phase.

We can now turn to the definition of the formal apparatus that will allow us to describe, together with the standard fluid and the radiation fluids, an additional "baryon number fluid". In particular, we need to introduce equations to describe the hydrody-

namics of a fluid which has a suppressed flow at the phase interface and which diffuses relative to the standard fluids. The effects of this diffusion can be included by introducing a diffusive flux four-vector **q** into the baryon number continuity equation which becomes

$$(n_b u^\alpha + q^\alpha)_{;\,\alpha} = 0 \ , \tag{5.32}$$

where n_b is the baryon number density, **u** is still the four velocity of the *standard* fluid. In the frame comoving with the standard fluid, $u^\alpha \equiv (1/a,\ 0,\ 0,\ 0)$ and **q** has only a spatial component [*i.e.* $u_\alpha q^\alpha = 0$ and $q^\alpha \equiv (0,\ q^\mu,\ 0,\ 0)$]. Using the property

$$V^\alpha{}_{;\alpha} = \frac{(\sqrt{-g}V^\alpha)_{,\,\alpha}}{\sqrt{-g}} \ , \tag{5.33}$$

where g is the determinant of the metric tensor and the metric relations (3.10), (5.17), we can rewrite (5.32) as

$$bR^2\left[\frac{\partial(n_b)}{\partial t} + \left(\frac{an_b}{R^2}\right)\frac{\partial(uR^2)}{\partial R}\right] = \frac{aR^2}{\Gamma}\frac{\partial(b\Gamma)}{\partial R}\frac{\partial(Dn_b)}{\partial R} + ab^2\Gamma\frac{\partial}{\partial R}\left[\frac{R^2}{b\Gamma}\frac{\partial(Dn_b)}{\partial R}\right] \ , \tag{5.34}$$

(see Appendix D for details) where the radial component of the diffusive flux is written as

$$q^\mu \equiv -\frac{1}{(b\Gamma)^2}\frac{\partial(Dn_b)}{\partial\mu} = -\frac{1}{b\Gamma}\frac{\partial(Dn_b)}{\partial R}. \tag{5.35}$$

In the Newtonian limit, $\Gamma = a = 1$ and equation (5.34) reduces to the standard Lagrangian diffusion equation in spherical coordinates. (Note that here, $\partial/\partial t$ is a Lagrangian time derivative for a location comoving with the standard fluid.). A rough estimate for the value of the diffusion coefficient D (which we take to be constant in time, uniform in space and the same in both phases) can be deduced with rather simple arguments if we rule out the possibility of the diffusion being turbulent (Alcock et al. [9] and which seems likely to be correct as discussed by Jedamzik et al. [68]). In this case, baryon number diffusion can be described as a simple Brownian motion of baryon number carriers having a mean free path of the order $\lambda_{free} \gtrsim T_c^{-1}$ (Kurki-Suonio [81]) giving a microscopic diffusion coefficient $D \sim 10^{-1} - 10$ fm.

The diffusive flux (5.35) correctly describes baryon number diffusion in the bulk of the two phases, but it is not adequate at the interface, where the diffusive flux is accompanied by a much larger flux related to the hydrodynamical flow Φ_ρ of elements of the quark gluon plasma as it is converted to the hadron phase. As mentioned earlier, this

flux could be subject to suppression processes at the interface but no exact expression is yet available for this. We therefore proceed here by defining a phenomenological expression for the net baryon number flux across the interface Φ_b in terms of the hydrodynamical flux Φ_ρ and a suitable "filter factor" F which expresses the ratio between the baryon number passing across the phase interface and the total baryon number incident on it.

In principle, F could be expressed in terms of the probability of finding (from all of the quarks and antiquarks present) three quarks of the right types within a volume of 1 fm^3 and in a time of 10^{-23} s, in terms of the "transparency" of the phase interface to the passage of a baryon number carrier from the quark phase to the hadron phase $\Sigma_{q\to h}$ and of the corresponding probability $\Sigma_{h\to q}$ that a baryon hitting the phase boundary from the hadron phase is absorbed (Fuller et al. [49]). Moreover, referring to a situation in which chemical equilibrium holds, it would be possible to express $\Sigma_{q\to h}$ in terms of $\Sigma_{h\to q}$ and this would restrict the uncertainty to this latter quantity only. (Although convenient, this approach requires that the baryon transmission probability does not vary significantly when the equilibrium is broken.)

Unfortunately, no reliable value for the baryon transmission probability $\Sigma_{h\to q}$ is known at present and, worse than this, different approaches to the study of the rates of elementary processes taking place at the phase interface seem to result in quite different estimates of it (see Fuller et al. [49], Sumiyoshi et al. [155] and Bonometto and Pantano [24] for further references). In view of this uncertainty, we will treat the filter factor as essentially a free parameter, adopting the reference value $F \sim 10^{-1}$ as estimated from the expressions presented by Fuller et al. [49] for $T_c = 150$ MeV and $\Sigma_{h\to q} \sim 10^{-3}$. (The value $F = 1$ corresponds to the case where the baryon number flow crosses the phase interface unimpeded and clearly represents an upper limit.)

The flux of elements of the standard fluids across the interface can be evaluated by projecting the flux four-vector along the unit spacelike four-vector $\mathbf{n}$ normal to the timelike hypersurface describing the time evolution of the interface, *i.e.*

$$\Phi_\rho \equiv \rho u^\alpha n_\alpha \, . \tag{5.36}$$

Neglecting diffusive contributions to the baryon number flux across the interface, we obtain that the net baryon number flux across the phase interface is then

$$\Phi_b = F\left(\frac{n_b^q}{\rho_q}\right)\Phi_\rho = F\left(\frac{n_b^q}{\rho_q}\right) u^\alpha n_\alpha \, . \tag{5.37}$$

In the next section we will give an extended presentation of the problems related with the solution of the hydrodynamical equations at the interface and there we also calculate the

components of the unit four-vectors $\mathbf{u}$ and $\mathbf{n}$ which will provide us with explicit expressions for (5.36) and (5.37).

Coupling the parabolic diffusion equation (5.34) together with the hyperbolic hydrodynamical equations (5.7), (5.12)–(5.18), (3.18)–(3.17) and (4.16)–(4.19) presented so far, provides us with a complete and consistent set of equations which allows for the hydrodynamical description of a relativistic multicomponent fluid such as the one present during the cosmological quark–hadron transition. However, this is not enough yet since all of the above equations cannot be integrated across the whole flow region, but need a special treatment in the vicinity of the phase interface as this moves within the flow domain.

Expression (5.37) represents a first example of how an hydrodynamical quantity which is suitably defined in the bulk of the flow [*e.g.* the diffusive flux of baryon number (5.35)], requires a special treatment at the phase interface. This is a very important concept that we are going to discuss extensively in the next subsections, where we will introduce the problems introduced by a phase interface treated as a discontinuity surface and present the solutions for such problems.

5.2 Solution at the Phase Interface

All of the equations derived and discussed in the previous sections [with the exception of equation (5.37)], are hydrodynamical in nature, in the sense that they refer to an ideal collection of particles considered as a *continuum*. As underlined above, these equations are *suitable* for the description of a multicomponent relativistic fluid (as the one present during the cosmological phase transition), however, they are *not enough* to describe bubble or drop dynamics if they are taken "as they stand". The reason for this is to be found in the fact that, at least within our hydrodynamical framework, the dynamics of a bubble or of a drop necessarily requires the introduction of at least one discontinuity surface across which the integration of the hydrodynamical equations cannot be taken[3].

The problems induced by the presence of a discontinuity surface within a given flow domain have already been discussed in Chapter 1, where relativistic shock waves and

[3]We note that this condition does not apply for those field-theory approaches involving a continuum order parameter to distinguish the two phases undergoing the transition. This approach, which has been proposed by the Finnish group of the University of Helsinki (Ignatius et al. [61, 62], Kurki-Suonio and Laine [82, 83, 84]) has some great advantages for the present case of cosmological phase transitions but also a number of difficulties when more complicated multicomponent flows need to be considered (see also Subsection 5.2.3).

reaction fronts have been first introduced. In the language of general relativity, the evolution of a relativistic discontinuity surface or *singular surface* can be described in terms of a three-dimensional timelike hypersurface Σ (*i.e.* the worldtube of the discontinuity surface) which divides the four-dimensional spacetime V, in which it is embedded, into the two regions V^+ and V^-. The basic idea is then that of "cutting out" the region of spacetime containing the hypersurface Σ, where junction conditions across the surface can provide suitable solutions, and of adopting the standard techniques of continuum relativistic hydrodynamics everywhere else. The use and the form of the junction conditions for classical and special relativistic fluids has been presented in Sections 1.1, 1.3.2 and 1.3.3, but further care needs to be paid when these junction conditions have to be applied across an interface treated as a singular hypersurface. The next two subsections will discuss this problem, concentrating firstly on the form of the junction conditions for the metric and secondly on the form for the energy and momentum of each of the three fluid components (*i.e.* standard fluids, radiation fluid and "baryon number fluid"). The last two subsections of this chapter are finally dedicated to two supplementary problems related with the dynamics of the interface, namely the definition of a *hadronization rate* and the derivation of a system of characteristic equations providing a correct causal framework necessary for a numerical computation using the present approach.

5.2.1 Metric Junction Conditions

Metric junction conditions basically establish the differences between the measures of an interval between two points on the surface worldtube as measured by two observers located on either side of Σ. Each observer has his set of rods to measure spatial distances and clocks to measure time intervals (May and White [108]).

Of course, both of the observers will measure the same invariant interval ds^2 which can be written as [*cf.* expression (3.10)]

$$ds^2 = -(a^-)^2 dt^2 + (b^-)^2 d\mu^2 + (R^-)^2 d\Omega^2 = -(a^+)^2 dt^2 + (b^+)^2 d\mu^2 + (R^+)^2 d\Omega^2 \ , \quad (5.38)$$

where upper indices $\pm$ refer to quantities measured in the two submanifolds V^+ and V^-, and $d\Omega^2 = d\theta^2 + \sin^2\theta d\phi^2$. If we now adopt the following convention for square and curly brackets for each quantity Ψ defined in the submanifolds

$$[\Psi]^\pm = \Psi^+ - \Psi^- \ , \qquad \{\Psi\}^\pm = \Psi^+ + \Psi^- \ , \quad (5.39)$$

then expression (5.38) will assume the more compact form

$$[a^2 dt^2 - b^2 d\mu^2 - R^2 d\Omega^2]^{\pm} = 0 \, . \tag{5.40}$$

Since $4\pi R^2$ is the proper area of a spherical shell at a given time and this quantity must be continuous across Σ, we can write

$$[4\pi R^2]^{\pm} = 0 \, , \tag{5.41}$$

from which is easy to rewrite (5.40) as the two distinct equations

$$[R]^{\pm} = 0 \, , \tag{5.42}$$

$$[f^2]^{\pm} = [a^2 - b^2 \dot{\mu}_s^2]^{\pm} = 0 \, , \tag{5.43}$$

where μ_s is the value of μ at the interface and $\dot{\mu}_s = (d\mu_s/dt)$. Since $Rd\Omega$ represents the "circumferential" proper length, equation (5.42) simply expresses the fact that meter rods lying parallel to the singular surface can be brought into contact there and be directly compared by the observers on either side. Finally, from the continuity of any R at any time t, we can deduce the further metric junction condition

$$\left[\frac{dR_s}{dt}\right]^{\pm} = [au + b\dot{\mu}_s \Gamma]^{\pm} = 0 \, . \tag{5.44}$$

5.2.2 Energy and Momentum Junction Conditions

The first studies on junction conditions for energy and momentum across a relativistic discontinuity surface with associated physical properties have been presented by Israel [63, 64] who, starting from the Gauss-Codazzi formalism (Hawking and Ellis [55], Misner et al. [118]), developed the *Singular Hypersurface Method* in 1966. This method has then found a number of cosmological applications such as the motion of a dust shell in a dust Universe (Lake [86], Lake and Pim [87], Maeda and Sato [102, 103]) or the dynamics of bubbles during early Universe phase transitions (Maeda [104]). The approach presented here is a particular application of the singular hypersurface method to the scenario of the cosmological quark–hadron phase transition (Miller and Pantano [113]) and further developments to accommodate the method within a multicomponent fluid treatment have been proposed by Rezzolla and Miller [137].

Let $\mathbf{n}$ be the unit spacelike four-vector normal to the hypersurface Σ dividing the four-dimensional spacetime V into V^+ and V^-, for which

$$n_\alpha n^\alpha = 1 \ . \tag{5.45}$$

Being embedded in a higher dimensional spacetime, the hypersurface will have an extrinsic curvature $K_{\alpha\beta}$ defined as[4]

$$K_{\alpha\beta} = h_\alpha^{\ \mu} h_\beta^{\ \nu} n_{(\mu;\nu)} \ , \tag{5.46}$$

where $h_{\alpha\beta} = g_{\alpha\beta} - n_\alpha n_\beta$ is the projection operator on Σ and describes its three-geometry, while $n_{(\beta;\alpha)} = (n_{\beta;\alpha} + n_{\alpha;\beta})/2$. We here use two different symbols for the covariant derivative, with ";" denoting the derivative with respect to $g_{\alpha\beta}$, while "$\|$" denotes the derivative with respect to $h_{\alpha\beta}$. From the Gauss-Codazzi equations we can write

$$^{(3)}R + K_{\alpha\beta}K^{\alpha\beta} - K^2 = -2G_{\alpha\beta}n^\alpha n^\beta \ , \tag{5.47}$$

$$K_\alpha^{\ \beta}{}_{\|\beta} - K_{\|\alpha} = G_{\mu\nu} h_\alpha^{\ \mu} n^\nu \ , \tag{5.48}$$

where $K = K^\alpha{}_\alpha$, is the trace of the extrinsic curvature, $G_{\alpha\beta} = R_{\alpha\beta} - \frac{1}{2}g_{\alpha\beta}R$ is the Einstein tensor in V, while $^{(3)}R$ is the Ricci scalar of the three-dimensional geometry $h_{\alpha\beta}$. An important distinction needs now to be made: if we define $K^+_{\alpha\beta}$, $K^-_{\alpha\beta}$ to be the extrinsic curvatures of Σ in the two submanifolds V^+ and V^-, then the singular hypersurface will represent the time evolution of a *surface layer* if $K^+_{\alpha\beta} \neq K^-_{\alpha\beta}$ or of a *boundary surface* if $K^+_{\alpha\beta} = K^-_{\alpha\beta}$. A typical example of a surface layer is the phase interface in first order phase transitions and, in this case, the stress energy tensor in V has a δ-function singularity on Σ. On the other hand, typical boundary surfaces are shock fronts or contact discontinuities and these have been studied extensively by Lichnerowicz [93] and Synge [156].

Let us now introduce the following two quantities $S_{\alpha\beta}$ and $\tilde{K}_{\alpha\beta}$ defined as

$$-8\pi G\left(S_{\alpha\beta} - \frac{1}{2}h_{\alpha\beta}S\right) \equiv [K_{\alpha\beta}]^\pm \ , \tag{5.49}$$

$$2\tilde{K}_{\alpha\beta} \equiv \{K_{\alpha\beta}\}^\pm \ , \tag{5.50}$$

where G is the gravitational constant and $S = S^\alpha{}_\alpha$. (Note that $S_{\alpha\beta} \neq 0$ only on Σ.) Following Israel, we interpret $S_{\alpha\beta}$ as the stress energy tensor of the matter in the discontinuity surface, thus embodying the physical properties of the singular surface. As a result, $S_{\alpha\beta}$ can also be defined as

[4] We here follow the definition of Israel which differs in sign from that of Misner et al. [118]

$$S_{\alpha\beta} = \lim_{\epsilon\to 0}\int_{-\epsilon}^{+\epsilon} T_{\mu\nu}h_{\alpha}^{\ \mu}h_{\beta}^{\ \nu}\,dx\ , \tag{5.51}$$

where x is a Gaussian coordinate in the direction of $\mathbf{n}$ and $x = 0$ on Σ. Making use of the Einstein field equations

$$G_{\alpha\beta} = 8\pi G T_{\alpha\beta}\ , \tag{5.8}$$

and of equations (5.47)–(5.50), we obtain (see Rezzolla [136] for details)

$${}^{(3)}R + \tilde{K}_{\alpha\beta}\tilde{K}^{\alpha\beta} - \tilde{K}^2 = -16\pi^2 G^2\left(S_{\alpha\beta}S^{\alpha\beta} - \frac{1}{2}S^2\right) - 8\pi G\{T^{\alpha\beta}n_\alpha n_\beta\}^{\pm}\ . \tag{5.52}$$

$$\tilde{K}_{\alpha\ \|\beta}^{\ \beta} - \tilde{K}_{\|\alpha} = 4\pi G\{T^{\mu\nu}n_\mu h_{\nu\alpha}\}^{\pm}\ , \tag{5.53}$$

$$\tilde{K}_{\alpha\beta}S^{\alpha\beta} = [T^{\alpha\beta}n_\alpha n_\beta]^{\pm}\ , \tag{5.54}$$

$$S_{\alpha\ \|\beta}^{\ \beta} = -[T^{\mu\nu}n_\mu h_{\nu\alpha}]^{\pm}\ . \tag{5.55}$$

Equations (5.52) and (5.53) can be regarded as the standard Hamiltonian and momentum constraints of a "3 + 1" formalism of General Relativity (Misner et al. [118]) considered in a fictitious spacetime $\tilde{V}$ in which $\tilde{K}_{\alpha\beta}$ is the mean curvature of the regular hypersurface Σ (Maeda [104]). On the other hand, equations (5.54) and (5.55), together with (5.8) are sufficient to describe the evolution of the singular surface and will account for the conservation of energy and momentum across Σ.

It is here convenient to make use of an orthonormal tetrad and for this purpose we assume that our system has a planar or spherical symmetry so that two orthogonal Killing vectors $\mathbf{e}_{(A)}$ (with $A = 2, 3$) exist. The tetrad is then completed if we introduce the unit timelike four-vector $\mathbf{v}$ tangent to Σ so as to obtain the tetrad $(v^\alpha,\ n^\alpha,\ e^\alpha_{(A)})$ (see Figure 5.1). Assuming that the matter in V can be treated as a perfect fluid, the expressions for the stress energy tensors in the singular surface and in the two submanifolds V^+ and V^- will be

$$S_{\alpha\beta} = (\gamma_\Sigma + \bar{\sigma})v_\alpha v_\beta + \gamma_\Sigma h_{\alpha\beta}\ , \tag{5.56}$$

$$(T_F^{\alpha\beta})^{\pm} = (e^{\pm} + p^{\pm})u^\alpha u^\beta + p^{\pm}(g^{\alpha\beta})^{\pm}\ , \tag{5.57}$$

where γ_Σ is the surface energy [*cf.* equation (4.14)] and $\bar{\sigma}$ is the bidimensional tangential pressure and it is the opposite of the more familiar surface tension (*i.e.* $\bar{\sigma} \equiv -\sigma$). Note that the stress energy tensor (5.57) is representative of the standard fluids only and does not contain contributions coming from the radiation fluid, for which a special treatment will be presented later on.

Projecting (5.55) along each of the directions of the orthonormal tetrad ($\mathbf{v}$, $\mathbf{n}$, $\mathbf{e}_{(A)}$) yields

$$[(\gamma_\Sigma + \bar{\sigma})v^\alpha]_{||\alpha} - \bar{\sigma}_{||\alpha}v^\alpha = [(e+p)(u^\alpha n_\alpha)(u^\beta v_\beta)]^\pm \ , \tag{5.58}$$

$$(\gamma_\Sigma + \bar{\sigma})n_\alpha v^\alpha{}_{||\beta}v^\beta = 0 \ , \tag{5.59}$$

$$(\gamma_\Sigma + \bar{\sigma})e^\alpha_{(A)}v_{\alpha\ ||\beta}v^\beta = 0 \ , \tag{5.60}$$

where all of the fluid quantities are meant to be evaluated on Σ. Because of the symmetries introduced, there is no acceleration on Σ, *i.e.*

$$v^\alpha{}_{||\beta}v^\beta = 0 \tag{5.61}$$

and, as a consequence, (5.59) and (5.60) are trivially satisfied. The only non trivial equation is then (5.58) which represents the energy conservation across Σ.

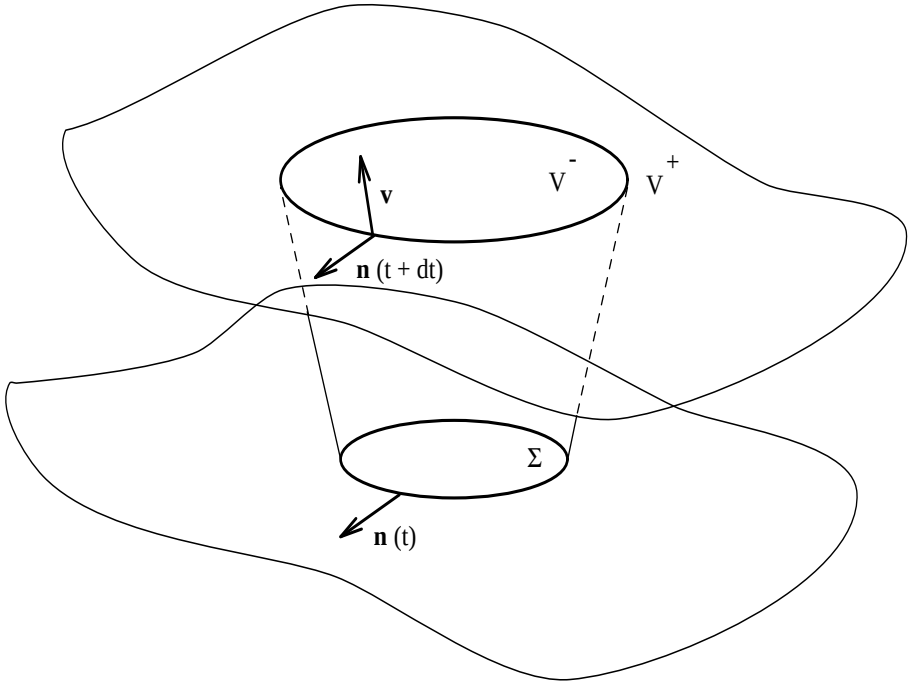

Figure 5.1 Schematic spacetime diagram of an expanding spherical singular surface Σ as it evolves from a spacelike hypersurface at time t to a subsequent one at time $t+dt$. (For convenience, one spatial dimension has been suppressed.). **n** is the spacelike unit four-vector normal to the hypersurface and **v** is the timelike unit four-vector tangent to it.

Using (5.61), it is possible to show that the acceleration vector in V is not zero, but rather expressed as

$$\frac{dv^\alpha}{d\tau} = v^\alpha{}_{;\beta} v^\beta = -n^\alpha v^\mu v^\nu K_{\mu\nu} \ , \tag{5.62}$$

where τ is the proper time of an observer on Σ. Using (5.56) and (5.62), the left-hand side of equation (5.54) can be rewritten as

$$\begin{aligned} \tilde{K}_{\alpha\beta} S^{\alpha\beta} &= [\gamma_\Sigma v^\alpha v^\beta + \bar{\sigma} e^\alpha_{(A)} e^{\beta\ (A)}]^\pm \tilde{K}_{\alpha\beta} \\ &= -\frac{\gamma_\Sigma}{2} \{ n_\alpha \frac{dv^\alpha}{dt} \}^\pm + \bar{\sigma} \tilde{K}_{\alpha\beta} e^\alpha_{(A)} e^{\beta\ (A)} \ . \end{aligned} \tag{5.63}$$

Given the spherically symmetric line element (3.10), it is simple to write the second contraction on the right-hand-side of (5.63) as

$$\tilde{K}_{\alpha\beta} e^{\alpha}_{\ (A)} e^{\beta\ (A)} = K^{\theta}_{\ \theta} + K^{\phi}_{\ \phi} = (lnR)_{,\alpha} n^{\alpha} \ , \tag{5.64}$$

from which it is possible to rewrite equation (5.54) as

$$\left\{ -\frac{\gamma_{\Sigma}}{2} n_{\alpha} \frac{dv^{\alpha}}{d\tau} + \bar{\sigma} (lnR)_{,\alpha} n^{\alpha} \Big|_{\Sigma} \right\}^{\pm} = [(e+p)(u^{\alpha} n_{\alpha})^2 + p]^{\pm} \ , \tag{5.65}$$

thus expressing the condition of momentum conservation across Σ for a spherically expanding singular surface. All of the equations of the singular hypersurface method presented so far have been derived for a general spherically symmetric metric. Next, we will specialize expressions (5.58) and (5.65) for the conservation of energy and momentum to the specific case of the metric which we are using here.

First, we calculate the components of the unit four-vectors **n** and **v** respectively normal and tangent to the singular surface whose time evolution is given by

$$\mathcal{F} = \mu - \mu_s(t) = 0 \ . \tag{5.66}$$

We then obtain the following covariant components of **n**

$$n_{\alpha} = N \frac{\partial \mathcal{F}}{\partial x^{\alpha}} = N(-\dot{\mu}_s, \ 1, \ 0, \ 0) \ , \tag{5.67}$$

where N is a normalization factor whose magnitude can be calculated by requiring that the condition (5.45) is satisfied. This then yields

$$N = \frac{ab}{(a^2 - b^2 \dot{\mu}_s^2)^{1/2}} = \pm \frac{ab}{f} \ , \tag{5.68}$$

where the $\pm$ signs reflect the choice between the two directions of the normal; this difference is however not relevant for the following calculations which are invariant under a sign change of **n**.

Similarly, the contravariant components of **v** are found to be

$$v^{\alpha} = \frac{dx^{\alpha}}{d\tau}\Big|_{\Sigma} = \frac{1}{f}(1, \ \dot{\mu}_s, \ 0, \ 0) \ , \tag{5.69}$$

while the fluid four-velocity **u** has contravariant components

$$u^\alpha = \frac{1}{a}(1,\ 0,\ 0,\ 0)\ . \tag{5.70}$$

Since we are referring to a system with spherical symmetry, the intrinsic curvature can be deduced from the line element

$$ds^2 = -d\tau^2 + R^2(\tau)d\Omega^2\ , \tag{5.71}$$

by means of which all of the covariant derivatives of the three-geometry (*i.e.* those denoted by $\|$) can be calculated. This is useful for calculating the left-hand side of equation (5.58) which is then found to be

$$\begin{aligned}[(\gamma_\Sigma + \bar{\sigma})v^\beta]^\pm_{\|\beta} &= \frac{1}{\sqrt{-h}}[\sqrt{-h}(\gamma_\Sigma + \bar{\sigma})v^\beta]_{,\beta} \\ &= \frac{1}{R^2}\frac{d}{d\tau}[(\gamma_\Sigma + \bar{\sigma})R^2]\ ,\end{aligned} \tag{5.72}$$

where $h = \det(h_{\alpha\beta}) = R^2\sin^2\theta$ and

$$\bar{\sigma}_{\|\beta}v^\beta = \frac{d\bar{\sigma}}{d\tau} = 0\ . \tag{5.73}$$

Note that the last equality in (5.73) is not general but valid only in the case in which the surface tension is considered as being independent of temperature and the surface energy equals the surface tension, *i.e.* $\gamma_\Sigma = \sigma \equiv -\bar{\sigma}$ [*cf.* equation (4.14)].

Under these assumptions, the condition of conservation of energy for the standard fluids across the reaction front (5.58) is finally expressed as

$$[(e+p)(u^\alpha n_\alpha)(u^\beta v_\beta)]^\pm = [(e+p)ab]^\pm = 0\ . \tag{5.74}$$

Next we turn to rewriting the condition of momentum conservation (5.65) for the present case. In particular, we note that

$$\begin{aligned}(lnR)_{,\alpha}n^\alpha &= \frac{ab}{f}\left(\frac{\dot{\mu}_s R_{,t}}{a^2 R} + \frac{R_{,\mu}}{b^2 R}\right) \\ &= \frac{ab}{f}\left(\frac{\dot{\mu}_s u}{aR} + \frac{\Gamma}{bR}\right)\end{aligned} \tag{5.75}$$

and

$$n_\alpha \frac{dv^\alpha}{d\tau} = n_\alpha v^\alpha{}_{;\beta} v^\beta = \frac{1}{ab}\frac{d}{dt}\left(\frac{b^2\dot{\mu}_s}{f}\right) + \frac{b\dot{\mu}_s^2}{af}\left(\frac{a_{,\mu}}{a} - \frac{b_{,\mu}}{b}\right) + \frac{f}{a^2 b} a_{,\mu}$$
$$= \frac{1}{a}\left[\frac{1}{b}\frac{d}{dt}\left(\frac{b^2\dot{\mu}_s}{f}\right) + \frac{f_{,\mu}}{b}\right], \tag{5.76}$$

while the right-hand-side of (5.65) can also be written as

$$[(e+p)(u^\alpha n_\alpha)^2 + p]^\pm = \frac{1}{f^2}[eb^2\dot{\mu}_s^2 + pa^2]^\pm . \tag{5.77}$$

Making use of the relations (5.75) and (5.76), together with the new form of the right-hand-side of (5.77), the final form for the conservation of momentum for the standard fluids across the reaction front is found to be

$$[eb^2\dot{\mu}_s^2 + pa^2]^\pm = -\frac{\sigma f^2}{2}\left\{\frac{1}{ab}\frac{d}{dt}\left(\frac{b^2\dot{\mu}_s}{f}\right) + \frac{f_{,\mu}}{ab} + \frac{2}{fR}(b\dot{\mu}_s u + a\Gamma)\right\}^\pm . \tag{5.78}$$

Equation (5.78) shows that the surface tension provides a two-fold contribution to the conservation of momentum: an *inertial* one, expressed in terms of the acceleration of the front and a *viscous* one, expressed in terms of the velocity of the front.

It should be underlined that the junction conditions for the energy and momentum (5.74) and (5.78) have been derived in terms of the stress energy tensor of the standard fluids (5.56) and are therefore valid for these fluids only. In general, it would be necessary to perform the same analysis also for the radiation fluid and for the "baryon number fluid", with the stress energy tensor (3.7) playing a role analogous to the one played by (5.56). However, the physical conditions at the quark–hadron transition are such that this is not really necessary and simpler solutions can be found.

We recall that the phase interface has a width of the order of the interaction scale length for the strong interaction, *i.e.* $\xi \sim 1$ fm. On the other hand, the typical interaction scale length for the radiation fluid particles is $\lambda \sim 10^3$ fm (or $\lambda \sim 10^{13}$ fm in the case of neutrinos). Because of the large difference in these two scales, it is reasonable to neglect any interaction of the radiation fluid particles with the interface, so that no effective energy and momentum transfer takes place when the radiation crosses the phase interface. In other words, the reaction front effectively behaves as a *boundary surface* relative to the radiation fluid. In this case, we can consider negligible the contribution of the radiation fluid to the stress energy tensor of the phase interface (*i.e.* $S_R^{\alpha\beta} = 0$), thus

greatly simplifying equations (5.54) and (5.55) for the radiation fluid which then reduce to

$$[T_{R}^{\alpha\beta} n_\alpha n_\beta]^{\pm} = 0 \ , \tag{5.79}$$

$$[T_{R}^{\alpha\beta} n_\alpha h_{\beta\gamma} v^\gamma]^{\pm} = [T_{R}^{\alpha\beta} n_\alpha v_\beta]^{\pm} = 0 \ . \tag{5.80}$$

Making use of the components of the four-vectors $\mathbf{v}$ and $\mathbf{n}$, the continuity of energy and momentum of the radiation fluid can finally be expressed respectively as

$$[T_{R}^{\alpha\beta} u_\alpha u_\beta]^{\pm} = \left[ab\dot{\mu}_s \left(\frac{4}{3} + f_{E} \right) w_0 - (a^2 + b^2 \dot{\mu}_s^2) w_1 \right]^{\pm} = 0 \ , \tag{5.81}$$

$$[T_{R}^{\alpha\beta} n_\alpha v_\beta]^{\pm} = \left[\left\{ a^2 \left(\frac{1}{3} + f_{E} \right) + b^2 \dot{\mu}_s^2 \right\} w_0 - 2ab\dot{\mu}_s w_1 \right]^{\pm} = 0 \ , \tag{5.82}$$

where we have made use of the closure relation $w_2 = f_{E} w_0$.

Similar considerations can be used also for the "baryon number fluid", whose net flux across the phase interface (5.37) can now be calculated explicitly in terms of the components (5.67) and (5.70) so as to obtain

$$\Phi_b \equiv F \left(\frac{n_b^q}{\rho_q} \right) \Phi_\rho = -F \left(\frac{n_b^q}{\rho_q} \right) \frac{\dot{\mu}_s}{4\pi R_s^2 f} \ . \tag{5.83}$$

As a first approximation it is reasonable to neglect any interaction of the baryon number carriers with the matter in the interface, so that the only junction condition for the "baryon number fluid" across the singular surface is a continuity condition, *i.e.*

$$[\Phi_b]^{\pm} = 0 \ , \tag{5.84}$$

as anticipated in Subsection 5.1.2.

It is interesting to notice that if we treat the phase interface as a boundary surface also for the standard fluids, we can neglect the contributions coming from the surface tension and the surface energy and find that the junction conditions (5.74) and (5.78) simply reduce to the relativistic Rankine-Hugoniot junction condition (May and White [108])

$$[aw]^{\pm} = 0 \ , \tag{5.85}$$

$$[eb\dot{\mu}_s \Gamma - aup]^{\pm} = 0 \ . \tag{5.86}$$

A final comment should be made on the mass function M which receives a net contribution from the surface energy, so that $M^+ \neq M^-$. At the time of nucleation of the bubble, conditions are essentially Newtonian so that

$$[M]^{\pm} = 4\pi R^2 \sigma \ , \tag{5.87}$$

but the subsequent time evolution is given by (Rezzolla and Miller [137])

$$\begin{aligned} \frac{d}{dt}[M]^{\pm} &= [M_t + \dot{\mu}_s M_\mu]^{\pm} \\ &= 4\pi R^2 \left[b\Gamma\dot{\mu}_{_S} \left\{ e + w_0 + \frac{u}{\Gamma} w_1 \right\} - au \left\{ p + \left(\frac{1}{3} + f_{_E} \right) w_0 + \frac{\Gamma}{u} w_1 \right\} \right]^{\pm} \ . \end{aligned} \tag{5.88}$$

5.2.3 Transition Rate Equation

As discussed in detail in Section 4.3, weak deflagrations require minimal conditions in order to be produced within cosmological scenarios and thus represent the most promising type of reaction front by means of which to describe the dynamics of the phase interface. However, weak deflagrations are also the physically possible reaction fronts which are most difficult to "handle" since they are subsonic with respect to their media ahead and behind (Section 1.2) and are intrinsically underdetermined (Subsections 1.2.2 and 1.3.3). Both of these difficulties will be discussed in the following two subsections and we here start with the second, *i.e.* with the definition of a suitable *hadronization rate*.

In order to completely determine a weak deflagration solution it is necessary to provide a further equation which basically establishes the velocity at which the deflagration front moves in the unreacted medium. [More formally, the extra equation effectively quantifies the entropy jump hidden in the inequality (1.7).] If the deflagration involves well known physical conditions, this equation can be based on more solid grounds and be expressed in terms of the chemical properties of the fluid undergoing the reaction (examples of classical deflagrations are given by Buckmaster and Ludford [26] and by Zeldovich et al. [172]). However, this is not possible within a cosmological scenario and a number of different approaches have been proposed for the electroweak transition (Dine et al. [41], Hua Liu et al. [58], Huet et al. [60], Heckler [56], Moore and Prokopec [119]) and for the quark–hadron transition (Applegate and Hogan [6], Bonometto and Pantano [24] and references therein, Ignatius et al. [61]).

Despite the large literature, the situation is still rather unclear and this is particularly the case for the quark–hadron transition. Applegate and Hogan [6] proposed in 1985 that the temperature of the quark phase ahead of the interface could be considered equal to the critical temperature during all of the transition, with some initial supercooling being allowed for bubble nucleation. While it is likely that the temperature ahead of the front is very close to the critical temperature during most of the transition, it is essential to note that the dynamics of transition is entirely determined by the small deviations away from this temperature and therefore this assumption is not at all satisfactory.

A more reasonable approach has been initially proposed by Ignatius et al. [61] and subsequently exploited in all of the following works by the Finnish group at the University of Helsinki (*i.e.* comprising Kajantie, Kurki-Suonio and Laine). The method basically consists in solving the hydrodynamical equations of a perfect *"cosmic fluid"* which is coupled with a scalar *order parameter* field ϕ, in analogy with the reheating problem in inflation. While the total stress energy tensor is conserved, this is not the case for the two sub-systems: cosmic fluid and order parameter. The entropy produced at the interface couples the behaviour of ϕ with the fluid, and the strength of this interaction is described by a *dissipative constant* which, at least in principle, is calculable from the theory. At the moment, no precise value of the dissipative constant is known, and this forces to use a phenomenological approach in which the constant is treated as a free parameter.

A further different solution to the problem has been proposed by Miller and Pantano [113] who adopted a more classical approach. From a physical point of view, the extra condition for a weak deflagration can be obtained relating the energy flux coming from the interface as derived from considerations of the transition process $F_{_T}$, with the effective hydrodynamical energy flux $F_{_H}$. (This is just an equivalent way of determining the entropy jump across the interface, since any other condition can be eventually related to a condition on $F_{_T}$.) The simplest expression for this energy flux can then be

$$F_{_T} = \alpha_1 \left[\Phi(T_q) - \Phi(T_h)\right] \ , \tag{5.89}$$

where $\Phi(T_q)$ represents an ideal thermal flux away from the interface (at temperature T_q) into the hadron plasma and $\Phi(T_h)$ is the corresponding flux from the hadron phase toward the interface. α_1 (with $0 \leq \alpha_1 \leq 1$) is an *accommodation coefficient* and accounts for deviations away from the ideal situation of an interface emitting hadrons as a black-body at temperature T_h (*i.e.* $\alpha_1 = 1$). Note that this approach is analogous to the one used for calculating the net mass transfer across a vapour-liquid interface in classical bubble dynamics (Theofanous et al. [160]). Also in this approach, which we will adopt hereafter, the accommodation coefficient is poorly known but is in principle calculable. Unfortunately, the hadronization rates coming from calculations of heavy ion collisions

are not useful for the present scenario as they are relative to quark matter being produced in vacuum and not in a leptonic bath (Banerjee et al. [15], Müller and Eisenberg [120]). However, it is worth underlying that we are not interested here in the microscopic structure of the phase interface, but rather in its dynamics during the transition and this can be satisfactorily investigated by treating α_1 as a free parameter.

Using the equations of state (4.16)–(4.19) presented in Subsections 4.4.1 and 4.4.2, we can then rewrite (5.89) as

$$F_{_T} = \frac{\pi^2}{30}\left(\frac{\alpha_1}{4}\right) g_h (T_q^4 - T_h^4) \; . \tag{5.90}$$

On the other hand, the hydrodynamical energy flux across the interface is defined in terms of the projection of the stress energy tensor of the standard fluids in the direction normal to the interface worldtube, *i.e.*

$$F_{_H} \equiv T_{_F}^{\mu\nu} u_\mu n_\nu \; . \tag{5.91}$$

The extra condition for weak deflagrations is then obtained after requiring that $F_{_H} = F_{_T}$ and this then finally yields

$$F_{_H} = \pm \frac{a w \dot{\mu}_s}{4\pi R_s^2 (a^2 - b^2 \dot{\mu}_s^2)} = \frac{\pi^2}{30}\left(\frac{\alpha_1}{4}\right) g_h (T_q^4 - T_h^4) = F_{_T} \; . \tag{5.92}$$

where the $\pm$ signs depend on the choice made for the unit normal to the hypersurface, with the plus sign being relevant for hadron bubble growth and the minus sign for quark drop evaporation.

5.2.4 Characteristic Equations

When we deal with a quasi-linear system of n *partial differential equations of* dependent variables $U^j(x,\, t)$, with $j = 1, \ldots, n$

$$a_{ij} \frac{\partial U^j}{\partial t} + b_{ij} \frac{\partial U^j}{\partial x} + c_i = 0 \; , \qquad\qquad i,\; j = 1, \ldots, n \tag{5.93}$$

where

$$a_{ij} = a_{ij}\,(t, x, U^1, \ldots, U^n) \; , \quad b_{ij} = b_{ij}\,(t, x, U^1, \ldots, U^n) \; , \quad c_i = c_i\,(t, x, U^1, \ldots, U^n) \; , \tag{5.94}$$

it is sometimes more convenient to rewrite them in a *characteristic form*. In other words, it is convenient to look for a linear combination of equations (5.93) such that the new system can be written as a set of *ordinary differential equations* along specific directions in the independent variable space $(x,\ t)$. These directions are then called *characteristic directions* or *curves* or simply "characteristics". The initial set of partial differential equations (5.93) will then be called *hyperbolic* if the characteristics are real and distinct, *parabolic* if the characteristics are real and coincident and *elliptic* if the characteristics are complex and conjugate (Courant and Friedrichs [35], Potter [132]). Physical problems described by hyperbolic equations are, for example, all those involving "wave-like" differential operators [*e.g.* a wave equation $\Box\phi = \{\nabla^2 - (1/v^2)\partial^2/\partial t^2\}\phi = 0$]. On the other hand, "diffusion-like" differential operators [*e.g.* $\{\partial/\partial t + (D)\partial^2/\partial x^2\}\phi = 0$] are typical of parabolic equations [*cf.* equation (5.34)], while problems involving the solution of "Poisson-like" equations [*e.g.* $\nabla^2\phi = 0$] are typical examples of elliptic differential equations.

Apart from this mathematical classification, characteristic equations can have a deep physical meaning and this is particularly evident in the case of hyperbolic systems of equations, such as our equations (5.12), (5.13), (5.14), (5.20), (3.18) and (3.19). In the case of a fluid, the characteristic curves coincide with the directions of propagation of sonic disturbances as well as with the direction of the fluid flowlines or *advective* characteristics (see also Subsection 1.3.1 where characteristics are used to investigate the causal structure of reaction fronts).

Given an event $P(x_0,\ t_0)$ in the spacetime $(x,\ t)$, it is then possible to define as *domain of dependence* of $P(x_0,\ t_0)$, the segment S between points A and B on the $t = 0$ curve (see left diagram of Figure 5.1). This then represents the *Cauchy data* for the event P or, in other words, the set of possible initial conditions from which the solution at P of the hyperbolic differential equation depends. Associated with the domain of dependence is the *domain of determinacy*; this region is limited by the *forward* $\mathcal{C}^+$ and *backward* $\mathcal{C}^-$ characteristics issued respectively from A and B and is so called because the solution at each point of it is fully determined by the initial data that has been assigned to the domain of dependence (Coulson and Jeffrey [34], Courant and Friedrichs [35]). If the Cauchy data are assigned only to a point $P(x,\ t)$ of the domain of dependence, the solution will then be determined only at that point $P(x,\ t)$, which, in turn, will influence but not determine the solution on a larger region. It is then defined as *region of influence* of the event $P(x,\ t)$ the region of spacetime I included between the characteristic curves diverging from the point $P(x,\ t)$ (see right diagram of Figure 5.1).

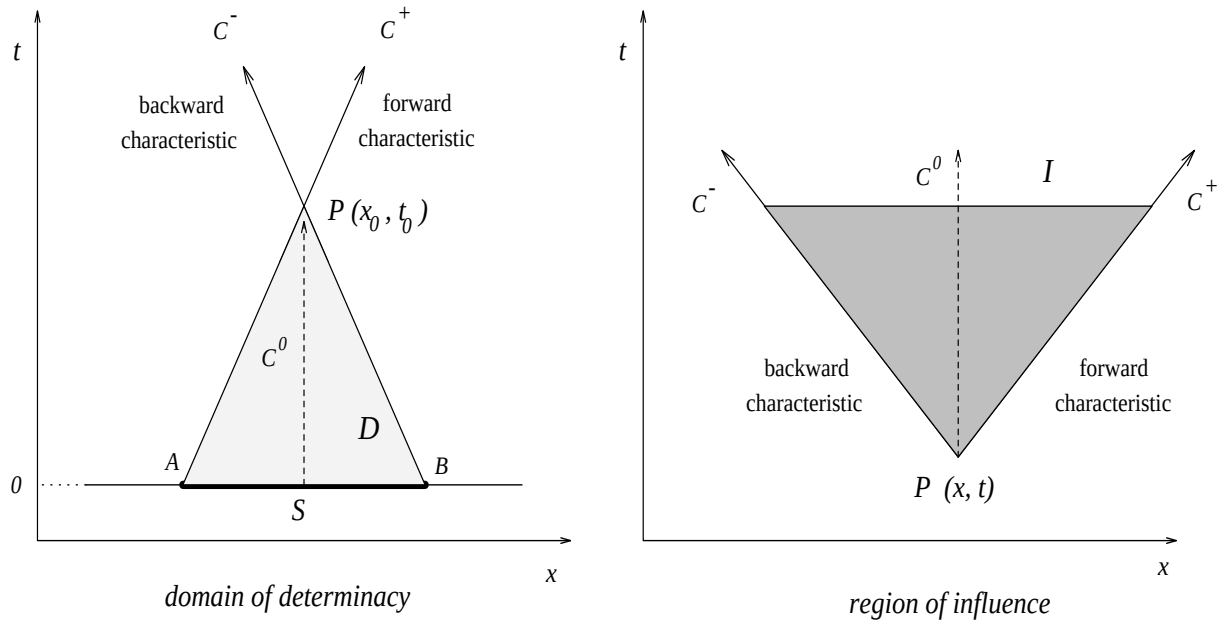

Figure 5.1 The left diagram is a spacetime illustration of the "domain of dependence" (indicated with a heavy line curve S) and of the "domain of determinacy" (indicated with the light shaded area region D) of a event $P(x_0,\ t_0)$ to which the forward $\mathcal{C}^+$, the backward $\mathcal{C}^-$ and the advective characteristic $\mathcal{C}^0$ converge. Similarly, the right diagram shows the "region of influence" (indicated with the heavy shaded area I) of the event $P(x,\ t)$, from which the characteristics are emitted. Note that for simplicity we have drawn the characteristic curves as straight lines although this is not necessarily true in the case of compressible media.

The relations among the mathematical concepts of the domain of determinacy and of region of influence with the corresponding physical concepts of past and future sound (or light) cones are rather obvious and we shall not comment on them here.

Although more complicated to implement, characteristics based approaches in hydrodynamics are often used either when a very high spatial resolution is desired (Dubal and Pantano [42]), or when an exact treatment of discontinuity surfaces is necessary (McKee and Colgate [109]). In this latter case and particularly if the discontinuities are subsonic relative to their medium ahead, a numerical computation based on a characteristic scheme represents the best (if not the only) possible approach since it automatically ensures a correct causal treatment. Miller and Pantano [113] have exploited the advantages of a

characteristic approach for studying the hydrodynamics of hadron bubble growth during the early stages of the quark–hadron transition. Their computational strategy was to use the continuum hydrodynamical equations for the solution in the bulk of each phase and to track the interface continuously through the finite difference grid using a characteristic method together with suitable junction conditions. This approach has then been extended by Rezzolla and Miller [137] to allow for a multicomponent treatment in which long range energy and momentum transfer could be followed and has been subsequently applied in a number of numerical computations studying radiative transfer during hadron bubble growth in the quark–hadron transition (Miller and Rezzolla [115], Rezzolla [144]) and the radiation decoupling during quark drop evaporation (Rezzolla and Miller [140], Rezzolla [145]).

In the following we sketch the basic lines of this strategy and present the derivation of the characteristic form of the hydrodynamical equations for the standard and radiation fluids presented in Subsection 5.1.1. Before that, however, it is worth noticing that for each two moment equations describing the radiation hydrodynamics which are retained from the infinite hierarchy, there are two families of corresponding characteristic curves with associated characteristic speeds. While including a larger number of moments in general increases accuracy, the role and relevance of the speeds associated with moments beyond the first two is controversial. Since we are using only the first two moment equations in the present context, these difficulties do not arise here.

In order to write the equations in a characteristic form, it is convenient to make use of the following equalities coming from the constraint equations obtained from the Einstein field equations (5.8) and from the conservation of momentum

$$\frac{b_{,t}}{b} = a\frac{u_{,\mu}}{R_{,\mu}} - \frac{4\pi GabR}{R_{,\mu}}w_1 \,, \tag{5.95}$$

$$\frac{a_{,\mu}}{a} = -\frac{p_{,\mu} + bs_1}{\rho w} \,, \tag{5.96}$$

so that equations (5.12), (5.13), (5.14), (3.18) and (3.19) can be written respectively as

$$u_{,t} + \frac{a\Gamma}{b\rho w}p_{,\mu} + B_0 = 0 \,, \tag{5.97}$$

$$p_{,t} + \frac{c_s^2 a\rho w}{b\Gamma}u_{,\mu} + B_1 = 0 \,, \tag{5.98}$$

$$\rho_{,t} + \frac{a\rho}{b\Gamma} u_{,\mu} + B_2 = 0 \ , \tag{5.99}$$

$$(w_0)_{,t} + \frac{a}{b}(w_1)_{,\mu} + \frac{a}{b\Gamma}\Big(\frac{4}{3} + f_{_E}\Big) w_0 u_{,\mu} - \frac{2a}{b\rho w} w_1 p_{,\mu} + B_3 = 0 \ , \tag{5.100}$$

$$(w_1)_{,t} + \frac{a}{b}\Big(\frac{1}{3} + f_{_E}\Big)(w_0)_{,\mu} - \frac{a}{b\rho w}\Big(\frac{4}{3} + f_{_E}\Big) w_0 p_{,\mu} + \frac{2a}{b\Gamma} w_1 u_{,\mu} + B_4 = 0 \ , \tag{5.101}$$

where

$$B_0 = a\Big\{4\pi G R\Big[p + \Big(\frac{1}{3} + f_{_E}\Big) w_0\Big] + \frac{GM}{R^2} + \frac{\Gamma}{\rho w} s_1\Big\} \ , \tag{5.102}$$

$$B_1 = a c_s^2 \Big[s_0 + \rho w\Big(\frac{2u}{R} - \frac{4\pi G R}{\Gamma} w_1\Big)\Big] \ , \tag{5.103}$$

$$B_2 = a\rho\Big(\frac{2u}{R} - \frac{4\pi G R}{\Gamma} w_1\Big) \ , \tag{5.104}$$

$$B_3 = 2a\Big(\frac{\Gamma}{R} - \frac{1}{\rho w} s_1\Big) w_1 + \frac{au}{R}\Big(\frac{8}{3} - f_{_E}\Big) w_0 - \frac{4\pi G a R}{\Gamma}\Big(\frac{4}{3} + f_{_E}\Big) w_0 w_1 - a s_0 \ , \tag{5.105}$$

$$B_4 = -\frac{a}{\rho w}\Big(\frac{4}{3} + f_{_E}\Big) w_0 s_1 + 2a\Big(\frac{u}{R} - \frac{4\pi G R}{\Gamma} w_1\Big) w_1 + \frac{3a\Gamma}{R} f_{_E} w_0 - a s_1 + \frac{a}{b} w_0 (f_{_E})_{,\mu} \ . \tag{5.106}$$

In deriving equations (5.97)–(5.101), the relations $R_{,t} = au$ and $R_{,\mu} = b\Gamma$ have been used and we have introduced the local sound speed in the standard fluids $c_s = (\partial p/\partial e)^{1/2}$. If we now introduce the *state vector*

$$\mathbf{U} \equiv \begin{pmatrix} u \\ p \\ \rho \\ w_0 \\ w_1 \end{pmatrix} , \tag{5.107}$$

equations (5.97)–(5.101) can then be written in the symbolic form

$$\frac{\partial \mathbf{U}}{\partial t} + \mathcal{A}\frac{\partial \mathbf{U}}{\partial \mu} + \mathbf{B} = 0 , \tag{5.108}$$

where $\mathbf{B}$ is the vector whose components are given by (5.102)–(5.106).

If the expression chosen for the Eddington factor $f_{_E}$ is dependent on components of the state vector $\mathbf{U}$, it is necessary to rewrite the partial derivative of $f_{_E}$ in (5.106) in terms of the derivatives of the component variables. In doing this the elements of the matrix $\mathcal{A}$ are obviously modified. We recall that for our specific application, the expression which we have chosen for the Eddington factor is

$$f_{_E} = \frac{8u^2/9}{(1+4u^2/3)}\left(\frac{\lambda}{\lambda+R}\right) , \tag{5.27}$$

so that equation (5.101) needs to be modified so as to obtain

$$(w_1)_{,t} + \frac{a}{b}\Big(\frac{1}{3}+f_{_E}\Big)(w_0)_{,\mu} - \frac{a}{b\rho w}\Big(\frac{4}{3}+f_{_E}\Big)w_0 p_{,\mu} + \frac{2a}{b\Gamma}(1+K)w_1 u_{,\mu} + B_4 = 0 , \tag{5.109}$$

with

$$B_4 = -\frac{a}{\rho w}\Big(\frac{4}{3}+f_{_E}\Big)w_0 s_1 + 2a\Big(\frac{u}{R} - \frac{4\pi G R}{\Gamma}w_1\Big)w_1 + \frac{3a\Gamma}{R}f_{_E}w_0 - a s_1 - \frac{a\Gamma f_{_E} w_0}{\lambda+R} , \tag{5.110}$$

and where, for compactness, we have defined

$$K = f_{_E} \frac{\Gamma w_0}{u(1+4u^2/3)w_1} \; . \tag{5.111}$$

Having done this, the matrix $\mathcal{A}$ takes the form

$$\mathcal{A} = \begin{pmatrix} 0 & a\Gamma/b\rho w & 0 & 0 & 0 \\ c_s^2 a\rho w/b\Gamma & 0 & 0 & 0 & 0 \\ a\rho/b\Gamma & 0 & 0 & 0 & 0 \\ aw_0(4/3+f_{_E})/b\Gamma & -2aw_1/b\rho w & 0 & 0 & a/b \\ 2aw_1(1+K)/b\Gamma & -aw_0(4/3+f_{_E})/b\rho w & 0 & a(1/3+f_{_E})/b & 0 \end{pmatrix} . \tag{5.112}$$

Next, we introduce l_i, the set of left eigenvectors of $\mathcal{A}$, and λ_i, the corresponding eigenvalues satisfying the relations

$$l_i \mathcal{A} = \lambda_i l_i \; . \tag{5.113}$$

Equation (5.113) has five distinct eigenvalues (the system is hyperbolic)

$$\lambda_0 = 0 \; , \tag{5.114}$$

$$\lambda_{1,2} = \pm \frac{a}{b} c_s \; , \tag{5.115}$$

$$\lambda_{3,4} = \pm \frac{a}{b} \sqrt{\frac{1}{3} + f_{_E}} \; , \tag{5.116}$$

to which correspond the five eigenvectors

$$l_0 = k\Big(0, \; \pm \frac{1}{c_s^2 w}, \; 1, \; 0, \; 0\Big), \tag{5.117}$$

$$l_{1,2} = k\Big(\pm \frac{c_s \rho w}{\Gamma}, \; 1, \; 0, \; 0, \; 0\Big) \; , \tag{5.118}$$

$$l_{3,4} = k\Big(\pm \frac{2(c_s^2 - 1 - K)(1/3 + f_E)^{1/2}}{\Gamma(c_s^2 - 1/3 - f_E)} w_1 + \frac{1}{\Gamma}\Big(\frac{4}{3} + f_E\Big) w_0, \\ \frac{2(f_E - 2/3 - K)}{\rho w (c_s^2 - 1/3 - f_E)} w_1,\ 0,\ \pm\Big(\frac{1}{3} + f_E\Big)^{1/2},\ 1\Big)\ . \tag{5.119}$$

where k is an arbitrary constant.

The eigenvalues (5.114)–(5.116) effectively determine the five relevant characteristic directions of this physical system. While λ_0 and $\lambda_{1,2}$ are rather straightforward to interpret since they represent respectively the advective, the forward and the backward characteristics of the standard fluids and the latter are proportional to the local sound speed of the standard fluids,[5] the interpretation of the eigenvalues $\lambda_{3,4}$ appears to be less obvious. However, recalling that the Eddington factor can take values in the range $0 \leq f_{_E} \leq 2/3$, it is easy to realize that the eigenvalues (5.116) effectively refer to the forward and backward characteristics of the radiation fluid, whose local sound speed can effectively range between $c_{s,R} = \sqrt{1/3}$ in the case of an isotropic radiation fluid (*i.e.* $f_{_E} = 0$) and $c_{s,R} = 1$ in the case of *free streaming* radiation fluid (*i.e.* $f_{_E} = 2/3$).

The configuration of characteristic curves adjacent to the interface is shown in Figure 5.2 for evolution of the system from time level t to a subsequent time level $t + \Delta t$. The dashed lines represent the forward and backward characteristics for the radiation fluid **r**, the full narrow lines are the equivalent characteristics for the standard fluids **f**, the vertical dotted line is the advective characteristic for strongly interacting matter in the quark phase and the heavy line is the worldline of the interface. (Figure 5.2 should be compared with diagram AA of Figure 1.8.) Note the differences introduced by the two possible directions in which the discontinuity can move as shown in the right diagram for an outward moving phase interface (*e.g.* as in the case of bubble growth) and in the left diagram for an inward moving one (*e.g.* as in the case of drop evaporation). Such differences force the use of two different schemes for the solution of the system of characteristic equations and the use of modified algorithms for the calculation of quantities in the grid zones immediately adjacent to the interface according to whether the interface is inward or outward moving (see also Subsection 6.1.1). Note also that since the front is always subsonic, the domain of dependence of the event immediately ahead of the front is not completely contained in one phase only.

---

[5]Note that the metric coefficients a and b appearing in the eigenvalues (5.114)–(5.116) are necessary to convert coordinate distances and time intervals into "proper distances" and "proper times" relative to the standard fluids.

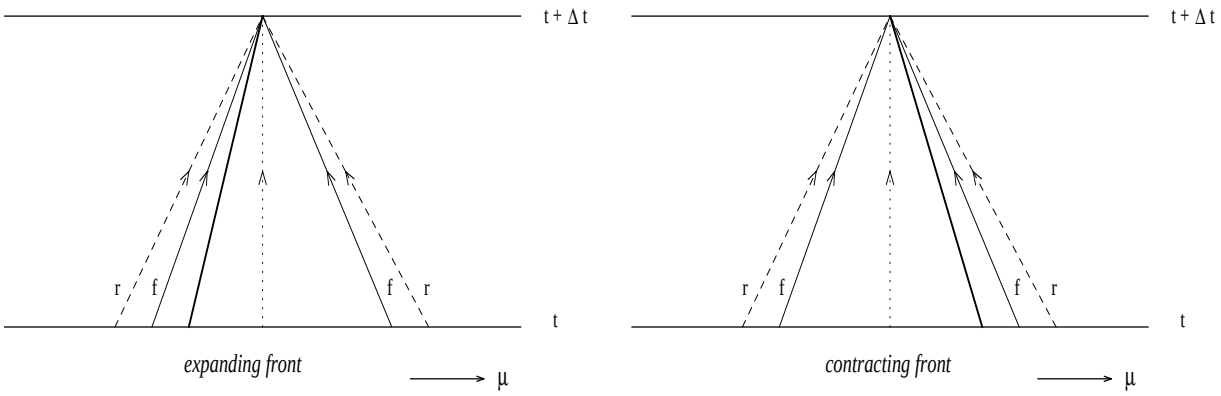

Figure 5.2 Spacetime configuration of characteristic curves near the phase interface drawn in the Lagrangian coordinate frame. The left diagram refers to an expanding weak deflagration and is therefore representative of a hadron bubble, while the right one refers to a contracting front and is representative of a quark drop. The dashed lines represent the forward and backward characteristics for the radiation fluid **r**, the full narrow lines are the equivalent characteristics for the standard fluids **f**, the vertical dotted line is the advective characteristic and the heavy line is the worldline of the interface. For simplicity we have drawn the characteristics of the same type of fluid as having the same slope in both phases of the SIM.

It is important to underline that some of the components of the eigenvectors (5.119) of the radiation fluid could become nearly singular in the case in which the radiation fluid is almost isotropic (*i.e.* $f_{_E} \to 0$) and the standard fluid is relativistic (*i.e.* $c_s \to 1/\sqrt{3}$). The singularity is an inevitable by-product of the hyperbolic nature of the equations (*cf.* discussion in Subsection 1.3.2) and is effectively related to the difference between the sound speeds in the standard fluids (c_s) and in the radiation fluid ($c_{s,R} = \sqrt{1/3 + f_{_E}}$). Such a difference is rather large when the standard fluids are non-relativistic but, unfortunately, in the present case the standard fluids *are* relativistic and the difference between the sound speeds is frequently small. This singular nature of the eigenvectors will be reflected directly on the characteristic equations of the radiation fluid, leading to some serious complications in numerical solution of the equations. This will be further discussed in Subsection 6.1.2.

Once the eigenvectors are known, equation (5.108) can then be multiplied on the left by l_i so as to obtain the new symbolic expression

$$l_i \left[\frac{\partial \mathbf{U}}{\partial t} + \lambda_i \frac{\partial \mathbf{U}}{\partial \mu} \right] + l_i \mathbf{B} = 0 \, . \tag{5.120}$$

in which each component involves derivatives only along the characteristic direction given

by $d\mu/dt = \lambda_i$. Writing out system (5.120) explicitly we then get the following characteristic form of the equations (5.97)–(5.101)

$$du \pm \frac{\Gamma}{\rho w c_s} dp + a\Big\{\frac{\Gamma}{\rho w}(s_1 \pm c_s s_0) \\ +4\pi G R\Big[p + \Big(\frac{1}{3} + f_{_E}\Big) w_0 \mp c_s w_1\Big] + \frac{GM}{R^2} \pm \frac{2\Gamma u c_s}{R}\Big\} dt = 0 \ , \tag{5.121}$$

which are to be solved along the forward and backward characteristics of the standard fluid $d\mu = \pm\, (a/b) c_s\, dt$, and

$$dw_1 \pm \Big(\frac{1}{3} + f_{_E}\Big)^{1/2} dw_0 + \Big[\Big(\frac{4}{3} + f_{_E}\Big) w_0 \pm \frac{2(c_s^2 - 1 - K)(1/3 + f_{_E})^{1/2}}{c_s^2 - 1/3 - f_{_E}} w_1\Big] \frac{1}{\Gamma} du \\ + \Big[\frac{2(f_{_E} - 2/3 - K)}{\rho w (c_s^2 - 1/3 - f_{_E})}\Big] w_1 dp + a\Big\{\Big(\frac{2u}{R} - \frac{4\pi G R w_1}{\Gamma}\Big) \times \\ \times \Big[\frac{2[(1/3 + f_{_E})(c_s^2 - 1) - K c_s^2]}{c_s^2 - 1/3 - f_{_E}} w_1 \pm \Big(\frac{4}{3} + f_{_E}\Big)\Big(\frac{1}{3} + f_{_E}\Big)^{1/2} w_0\Big] \\ + \Big[4\pi R\Big(p + w_0\Big(\frac{1}{3} + f_{_E}\Big)\Big) + \frac{M}{R^2}\Big] \times \\ \times \Big[\Big(\frac{4}{3} + f_{_E}\Big) w_0 \pm \frac{2(c_s^2 - 1 - K)(1/3 + f_{_E})^{1/2}}{c_s^2 - 1/3 - f_{_E}} w_1\Big] \frac{G}{\Gamma} - \frac{K u (1 + 4u^2/3)}{\lambda(1 + R/\lambda)} w_1 \\ - \frac{1}{R}\Big\{3 f_{_E}\Big[\pm\Big(\frac{1}{3} + f_{_E}\Big)^{1/2} u - \Gamma\Big] w_0 \ - 2\Big[\pm\Big(\frac{1}{3} + f_{_E}\Big)^{1/2} \Gamma - u\Big] w_1\Big\} \\ + \Big[\frac{2c_s^2}{\rho w (c_s^2 - 1/3 - f_{_E})}\Big(f_{_E} - \frac{2}{3} - K\Big) w_1 \mp \Big(\frac{1}{3} + f_{_E}\Big)^{1/2}\Big] s_0 \\ + \Big[\pm \frac{2}{\rho w (c_s^2 - 1/3 - f_{_E})}\Big(f_{_E} - \frac{2}{3} - K\Big)\Big(\frac{1}{3} + f_{_E}\Big)^{1/2} w_1 \ - \ 1\Big] s_1\Big\} dt = 0 \ , \tag{5.122}$$

which are to be solved along the forward and backward characteristics of the radiation fluid $d\mu = \pm\, (a/b)(1/3 + f_{_E})^{1/2} dt$, and finally

$$d\rho - \frac{1}{c_s^2 w} dp - \frac{a s_0}{w} dt = 0, \tag{5.123}$$

which is an advective equation and is to be solved along the flowlines of the standard fluid $d\mu = 0$. Finally, R and M are calculated from advective equations

$$dR = au\, dt\ , \tag{5.124}$$

$$dM = -4\pi R^2 au \left[p + \left(\frac{1}{3} + f_{_E} \right) w_0 + \frac{\Gamma}{u} w_1 \right] dt\ , \tag{5.125}$$

and the metric coefficient a is calculated from (5.15) which is a constraint equation on the constant t hypersurface (*i.e.* it is to be integrated along the direction $dt = 0$).

We conclude this subsection by summarizing the overall strategy of the solution at the interface, in which the characteristic equations need to be solved together with the junction conditions. In practice, the numerical solution of the hydrodynamical equation across the phase interface involves the simultaneous calculation (*i.e.* on each time slice) of the ten components of the state vectors $\mathbf{U}^{\pm}$ (*i.e.* $u^{\pm}$, $p^{\pm}$, $\rho^{\pm}$, $w_0^{\pm}$, $w_1^{\pm}$), of the metric coefficients $a^{\pm}$, of the mass function $M^{\pm}$, of the baryon number flux $\Phi_b^{\pm}$ and of the interface location R_s (or equivalently μ_s) and velocity $\dot{\mu}_s$, giving a total number of 18 unknowns. These are then determined by using 4 equations along the backward and forward characteristics of the standard and radiation fluids [*i.e.* equations (5.121) and (5.122)], 3 equations along the advective characteristics [*i.e.* equations (5.123)–(5.125)], 1 equation for the net baryon flux at the interface [*i.e.* equation (5.83)], 2 metric junction conditions [*i.e.* equations (5.43) and (5.44)], 4 energy and momentum junction conditions [*i.e.* equations (5.74), (5.78), (5.81) and (5.82)], 1 continuity equation for the baryon flux [*i.e.* equation (5.84], 1 evolution equation for the mass function [*i.e.* equation (5.88)], 1 constraint equation [*i.e.* equation (5.15)] and finally 1 rate equation [*i.e.* equation (5.92)]. For compactness, a detailed description of the sequence of computational procedures adopted for the numerical solution at the interface will not be presented in this Thesis.

5.3 Appendix D

In this Appendix we give a brief sketch of the calculations leading from the Einstein field equations (5.8) and the conservation equations (5.9)–(5.11) to the hydrodynamical equations (5.12)–(5.20). Also, we present the basic steps that allow for the derivation of our expressions for the Eddington factor and for the initial conditions for the radiation fluid in the case of an expanding bubble. A final comment will be dedicated to the calculation of the relativistic diffusion equation for the baryon number (5.34) and to a convenient finite difference form for its numeric integration.

I. The Combined Fluids

Expressions for the non-zero contravariant components of the total stress energy tensor ($T^{\alpha\beta} = T_{R}^{\alpha\beta} + T_{F}^{\alpha\beta}$) can be calculated using the expression for the stress energy tensor of the radiation fluid (3.7) and the components (3.27)–(3.30) of the comoving tetrad. This then gives

$$T^{00} = \frac{1}{a^2}(e + w_0) \,, \tag{5.126}$$

$$T^{01} = \frac{w_1}{ab} \,, \tag{5.127}$$

$$T^{11} = \frac{1}{b^2}\left(p + \frac{w_0}{3} + w_2\right) \,, \tag{5.128}$$

$$T^{22} = \frac{1}{R^2}\left(p + \frac{w_0}{3} - \frac{w_2}{2}\right) \,, \tag{5.129}$$

$$T^{33} = \frac{1}{R^2 sin^2\theta}\left(p + \frac{w_0}{3} - \frac{w_2}{2}\right) \,, \tag{5.130}$$

where it is easy to see the contributions coming from the standard fluids and the radiation fluid respectively.

After straightforward but particularly tedious calculations it is possible to obtain the following non-zero components of the Christoffel symbols of the metric (3.10):

$$\Gamma^0_{00} = \frac{a_{,t}}{a} \quad , \quad \Gamma^0_{01} = \frac{a_{,\mu}}{a} \quad , \quad \Gamma^1_{00} = \frac{a a_{,\mu}}{b^2} \quad , \quad \Gamma^1_{11} = \frac{b_{,\mu}}{b} \, ,$$

$$\Gamma^1_{10} = \frac{b_{,t}}{b} \quad , \quad \Gamma^0_{11} = \frac{b b_{,t}}{a^2} \quad , \quad \Gamma^2_{20} = \frac{R_{,t}}{R} \quad , \quad \Gamma^2_{21} = \frac{R_{,\mu}}{R} \, ,$$

$$\Gamma^0_{22} = \frac{R R_{,t}}{a^2} \quad , \quad \Gamma^1_{22} = -\frac{R R_{,\mu}}{b^2} \quad , \quad \Gamma^3_{30} = \frac{R_{,t}}{R} \quad , \quad \Gamma^3_{31} = \frac{R_{,\mu}}{R} \, ,$$

$$\Gamma^3_{32} = \frac{\cos\theta}{\sin\theta} \quad , \quad \Gamma^0_{33} = \frac{R \sin^2\theta R_{,t}}{a^2} \quad , \quad \Gamma^1_{33} = -\frac{R \sin^2\theta R_{,\mu}}{b^2} \quad , \quad \Gamma^2_{33} = -\sin\theta\cos\theta \, , \tag{5.131}$$

while the relevant components of the Ricci tensor and scalar are respectively

$$R_{00} = \frac{a}{b}\left[\left(\frac{a_{,\mu}}{b}\right)_{,\mu} - \left(\frac{b_{,t}}{a}\right)_{,t} - \frac{2b}{R}\left(\frac{R_{,t}}{a}\right)_{,t} + \frac{2}{bR} a_{,\mu} R_{,\mu}\right] , \tag{5.132}$$

$$R_{01} = \frac{2}{R}\left(\frac{a_{,\mu}}{a} R_{,t} + \frac{b_{,t}}{b} R_{,\mu} - R_{,t\mu}\right) , \tag{5.133}$$

$$R_{22} = \left(\frac{R_{,t}}{a}\right)^2 - \left(\frac{R_{,\mu}}{b}\right)^2 + \frac{R}{a}\left(\frac{R_{,t}}{a}\right)_{,t} - \frac{R}{b}\left(\frac{R_{,\mu}}{b}\right)_{,\mu} + \frac{R}{ab}\left(\frac{R_{,t} b_{,t}}{a} - \frac{R_{,\mu} b_{,\mu}}{b}\right) + 1 \, , \tag{5.134}$$

$$R_{33} = \sin^2\theta R_{22} \, , \tag{5.135}$$

and

$$R = \frac{2}{ab}\left[\left(\frac{b_{,t}}{a}\right)_{,t} - \left(\frac{a_{,\mu}}{b}\right)_{,\mu}\right] + \frac{4}{R}\left[\frac{1}{a}\left(\frac{R_{,t}}{a}\right)_{,t} - \frac{1}{b}\left(\frac{R_{,\mu}}{b}\right)_{,\mu}\right]$$
$$+ \frac{2}{R^2}\left[\left(\frac{R_{,t}}{a}\right)^2 - \left(\frac{R_{,\mu}}{b}\right)^2 + 1\right] + \frac{4}{abR}\left(\frac{R_{,t} b_{,t}}{a} - \frac{R_{,\mu} b_{,\mu}}{b}\right) \, . \tag{5.136}$$

Using then all of these components, we obtain the following form of the four independent Einstein equations

$(T^0{}_0)$:

$$8\pi G(e+w_0)R^2R_{,\mu}+\frac{8\pi GbR^2R_{,t}}{a}w_1=\left\{R\left[\left(\frac{R_{,t}}{a}\right)^2-\left(\frac{R_{,\mu}}{b}\right)^2+1\right]\right\}_{,\mu}\,, \quad (5.137)$$

$(T^1{}_1)$:

$$8\pi G\left(p+\frac{w_0}{3}+w_2\right)+\frac{8\pi GaR^2R_{,\mu}}{b}w_1=-\left\{R\left[\left(\frac{R_{,t}}{a}\right)^2-\left(\frac{R_{,\mu}}{b}\right)^2+1\right]\right\}_{,t}\,, \quad (5.138)$$

$(T^2{}_2\equiv T^3{}_3)$:

$$8\pi G\left(p+e+\frac{4}{3}w_0-2w_2\right)=\frac{1}{ab}\left[\left(\frac{a_{,\mu}}{b}\right)_{,\mu}-\left(\frac{b_{,t}}{a}\right)_{,t}\right]+\frac{1}{R^2}\left[\left(\frac{R_{,t}}{a}\right)^2-\left(\frac{R_{,\mu}}{b}\right)^2+1\right]\,, \quad (5.139)$$

$(T^0{}_1)$:

$$8\pi G\frac{b}{a}w_1=-\frac{2}{a^2R}\left(\frac{a_{,\mu}}{a}R_{,t}+\frac{b_{,t}}{b}R_{,\mu}-R_{,t\mu}\right)\,. \quad (5.140)$$

(the symbol in brackets identifies the component referred to). Equation (5.140) is a *constraint equation* which, in the form

$$\frac{b_{,t}}{b}=-\frac{1}{R_{,\mu}}\left(R_{,\mu t}-\frac{a_{,\mu}}{a}R_{,t}-4\pi GabRw_1\right)\,, \quad (5.141)$$

has been used frequently in the course of the calculations outlined in this Appendix. Writing out explicitly the time derivative on the right-hand side of equation (5.138) and making use of the (5.141), the following expression

$$\Gamma\Gamma_{,t}=\frac{R_{,\mu}}{b}\left[4\pi GRaw_1-\frac{R_{,t}}{b}\left(\frac{p_{,\mu}+bs_1}{e+p}\right)\right]\,, \quad (5.142)$$

can be obtained and this can then be further transformed, by means of equation (5.17), so as to arrive at the form (5.12), which represents the relativistic form of the standard Euler equation.

Next we turn to writing out explicitly the hydrodynamic conservation equations (5.9)–(5.10) which take the form

$$-u_\alpha T^{\alpha\beta}{}_{;\beta} = 0 = s_0 + (e+p)_{,\beta}u^\beta + (e+p)\Theta - p_{,\beta}g^{\alpha\beta}u_\alpha \ , \tag{5.143}$$

$$n_j P^j{}_\alpha T^{\alpha\beta}{}_{;\beta} = 0 = \frac{1}{b}s_1 + (e+p)n_j u^j{}_{;\beta}u^\beta + (g^{\alpha\beta}+u^\alpha u^\beta)p_{,\beta} \ , \tag{5.144}$$

$$(\rho u^\alpha)_{;\alpha} = 0 = \rho_{,\alpha}u^\alpha + \rho u^\alpha{}_{,\alpha} + \rho u^\alpha \frac{\left(\sqrt{\det(-g^{\alpha\beta})}\right)_{,\alpha}}{\sqrt{\det(-g^{\alpha\beta})}} \ . \tag{5.145}$$

Using the expressions $\Gamma = R_{,\mu}/b$ and $u = R_{,t}/a$ together with (5.141), equations (5.143)–(5.145) can be converted to the final form given in equations (5.13)–(5.15). Finally, we note that if we rewrite equations (5.10) and (5.11) as

$$\left\{\frac{R}{2G}\left[\left(\frac{R_{,t}}{a}\right)^2 - \left(\frac{R_{,\mu}}{b}\right)^2 + 1\right]\right\}_{,\mu} = 4\pi R^2 R_{,\mu}(e + w_0 + \frac{u}{\Gamma}w_1) = M_{,\mu} \tag{5.146}$$

and

$$\left\{\frac{R}{2G}\left[\left(\frac{R_{,t}}{a}\right)^2 - \left(\frac{R_{,\mu}}{b}\right)^2 + 1\right]\right\}_{,t} = -4\pi R^2 R_{,t}\left(p + \frac{1}{3}w_0 + \frac{\Gamma}{u}w_1 + w_2\right) = M_{,t} \ , \tag{5.147}$$

this gives expressions (5.16) and (5.20) for the generalized mass function M and which reduce to the familiar expressions for the standard mass function when the radiation terms are omitted.

II. Eddington Factor and Initial Conditions for the Radiation

As mentioned in Sections 3.3 and 5.1.1, a particularly important point in the PSTF approach is the truncation of the infinite hierarchy of moment equations by means of a suitably defined closure relation derived on the basis of physical considerations. We have used the closure equation (3.17) and, for our particular problem, an appropriate expression for f_E is given by equation (5.27). Here we give our justification for making this choice and refer, in particular, to the initial conditions for the radiation fluid for hadron bubble growth.

A key point in choosing an expression for $f_{_E}$ is that it should have the correct asymptotic behaviour in the optically thin and optically thick limits. Consider the case of a single spherical hadronic bubble which is initially nucleated at rest with a radius small compared with the mean free path of the radiation. Under these circumstances, the radiation field will be everywhere rather accurately uniform and isotropic (unless there is some other perturbing influence) and since the bubble radius is very small compared with the horizon scale, it is also a good approximation to neglect cosmological expansion. Since w_0, w_1 and w_2 are all measured with respect to the local rest frames of the standard fluid, the values which they take during the early part of the bubble expansion are those produced by motion of the fluid rest frames with respect to the essentially uniform radiation field.

When the radiation is isotropic in its mean rest frame, its stress energy tensor takes the perfect fluid form

$$T_{_R}^{\alpha\beta} = (e_{_R} + p_{_R})v^\alpha v^\beta + p_{_R} g^{\alpha\beta} \ , \tag{5.148}$$

where $e_{_R}$ and $p_{_R}$ are the radiation energy density and pressure ($p_{_R} = e_{_R}/3$), measured in the mean rest frame of the radiation, and $v^\alpha = dx^\alpha/d\tau$ is the four-velocity of this frame relative to some specific observer. For purely radial motion in our metric

$$d\tau^2 = -ds^2 = \left(1 - \frac{b^2\dot{\mu}^2}{a^2}\right)a^2 dt^2 = \frac{a^2}{\gamma^2}dt^2 \ , \tag{5.149}$$

and the non-zero components of four-velocity are

$$v^\alpha = \left(\frac{dt}{d\tau}, \frac{d\mu}{d\tau}\right) = \frac{\gamma}{a}(1, \dot{\mu}) \ , \tag{5.150}$$

where

$$\gamma = \frac{1}{\sqrt{1 - v^2}} \qquad \text{and} \qquad v = \frac{b\dot{\mu}}{a} \ . \tag{5.151}$$

To find the value of $\dot{\mu}$ for the radiation frame with respect to the standard fluid, we note that since each element of the radiation fluid is remaining at a constant value of R

$$dR = R_{,t}dt + R_{,\mu}d\mu = au dt + b\Gamma d\mu = 0 \tag{5.152}$$

and so

$$\dot{\mu} = -\frac{au}{b\Gamma} \ , \tag{5.153}$$

which leads to the following expressions

$$v = -\frac{u}{\Gamma} , \qquad \gamma^2 = \frac{\Gamma^2}{\Gamma^2 - u^2} . \tag{5.154}$$

If we now write the stress energy tensor (5.148) in the frame comoving with the standard fluid, we can compare the new expressions for the components with the ones appearing in equation (3.7), thus obtaining the following system of equations

$$T^{00}_{R} = \frac{w_0}{a^2} = \frac{4}{3} e_{R} \left(\frac{\gamma^2}{a^2} \right) + \frac{1}{3} e_{R} \left(-\frac{1}{a^2} \right) , \tag{5.155}$$

$$T^{01}_{R} = \frac{w_1}{ab} = \frac{4}{3} e_{R} \left(\frac{\gamma^2}{a^2} \dot{\mu} \right) , \tag{5.156}$$

$$T^{11}_{R} = \frac{1}{b^2} \left(\frac{w_0}{3} + w_2 \right) = \frac{4}{3} e_{R} \left(\frac{\gamma^2}{a^2} \dot{\mu}^2 \right) + \frac{1}{3} e_{R} \left(\frac{1}{b^2} \right) . \tag{5.157}$$

The solution of this system then leads to the expressions

$$w_0 = \frac{\gamma^2}{3} (3 + v^2) e_{R} , \tag{5.158}$$

$$w_1 = \frac{4}{3} \gamma^2 v e_{R} , \tag{5.159}$$

$$w_2 = \frac{\gamma^2}{3} (1 + 3v^2) e_{R} - \frac{w_0}{3} . \tag{5.160}$$

If we now define $(w_0)_{N} = e_{R}$ to be the radiation energy density at the bubble nucleation time (when there is no fluid motion), equations (5.158)–(5.160) can be suitably transformed so as to give the following expressions for the energy density, flux and shear stress scalar of the radiation as seen from the standard fluid

$$w_0 = \left(1 + \frac{4}{3} \frac{u^2}{\Gamma^2 - u^2} \right) (w_0)_{N} \simeq \left(1 + \frac{4}{3} u^2 \right) (w_0)_{N} , \tag{5.161}$$

$$w_1 = -\frac{4}{3} \frac{\Gamma u}{\Gamma^2 - u^2} (w_0)_{N} \simeq -\frac{4}{3} \Gamma u (w_0)_{N} , \tag{5.162}$$

$$w_2 = \frac{8}{9} \frac{u^2}{\Gamma^2 - u^2} (w_0)_{N} \simeq \frac{8}{9} u^2 (w_0)_{N} . \tag{5.163}$$

The approximate forms of the expressions (5.161)–(5.163) result from noting that since the dimensions of the bubble are small compared with the horizon scale, $\Gamma^2 - u^2 \simeq 1$.

Equations (5.161) and (5.163) together with the definition (3.17), give the following analytic expression for the variable Eddington factor during the first stages of the bubble expansion

$$f_{_E} = \frac{8u^2/9}{(1+4u^2/3)} \, . \tag{5.164}$$

This is the "optically thin" limit. At the other extreme, the "optically thick" limit arises when the radius of the bubble is large compared with the radiation mean free path and complete coupling has been attained between the radiation and the standard fluids over length scales comparable with the radius of the bubble. When this happens, interactions make the radiation isotropic in the local fluid rest frame so that $w_2 \to 0$ and $f_{_E} \to 0$. A suitable smooth join is required in between the two asymptotic limits and to do this we have multiplied the expression in (5.164) by $\lambda/(\lambda + R)$ which then gives equation (5.27). Experiment has shown that reasonable variation in the form of the join makes an insignificant change in the results obtained.

III. Baryon Diffusion

Finally, we briefly show some intermediate steps leading to equation (5.34), the relativistic diffusion equation for baryon number. Using the standard property of four-divergences (5.33), equation (5.32) can be written as

$$bR^2 \left[(n_b)_{,\,t} + n_b \left(\frac{b_{,\,t}}{b} + \frac{2R_{,\,t}}{R} \right) \right] = -ab \left[R^2 q^\mu \left(\frac{a_{,\,\mu}}{a} + \frac{b_{,\,\mu}}{b} \right) + (R^2 q^\mu) \right] \, . \tag{5.165}$$

The $T^0_{\ 1}$ component of the Einstein field equations (5.140) provides the useful relation (5.141) and, for the present purposes, we can neglect the term containing the gravitational constant $G \ll 1$ so as to obtain the simpler expression

$$\frac{b_{,\,t}}{b} \approx \frac{R_{,\,\mu t}}{R_{,\,\mu}} - \frac{a_{,\,\mu}}{aR_{,\,\mu}} = \frac{a}{b\Gamma} u_{,\,\mu} \, . \tag{5.166}$$

Making then use also of the identity

$$\frac{b_{,\,\mu}}{b} = \frac{R_{,\,\mu\mu}}{b\Gamma} - \frac{\Gamma_{,\,\mu}}{b\Gamma} \, , \tag{5.167}$$

and of the definition (5.35), it is then possible to rewrite equation (5.165) in the final form (5.34).

An attractive feature of Lagrangian schemes is that advection is treated exactly. Exploiting this, it is convenient to use for the finite-difference representation of equation (5.34) the simple and compact expression:

$$4\pi(n_b)^{n+1}_{j+1/2}\left[\frac{(R^2)^{n+1}_{j+1/2}}{\Gamma^{n+1}_{j+1/2}}\right]\Delta R^{n+1}_{j+1/2} = 4\pi(n_b)^{n}_{j+1/2}\left[\frac{(R^2)^{n}_{j+1/2}}{\Gamma^{n}_{j+1/2}}\right]\Delta R^{n}_{j+1/2}$$
$$-\frac{4\pi}{\Gamma^{n+1/2}_{j+1/2}}\left[(R^2)^n_{j+1}(\Phi_{_D})^n_{j+1} - (R^2)^n_j(\Phi_{_D})^n_j\right]a^{n+1/2}_{j+1/2}\Delta t^{n+1/2}_{j+1/2}\ , \tag{5.168}$$

where the superscripts refer to the time level at which the quantity is calculated and the subscripts to the position in the spatial grid, $\Delta R^n_{j+1/2} = R^n_{j+1} - R^n_j$ and

$$(\Phi_{_D})^n_j = -D\left[\frac{(n_b)^n_{j+1/2} - (n_b)^n_{j-1/2}}{R^n_{j+1/2} - R^n_{j-1/2}}\right]\ , \tag{5.169}$$

is the diffusive flux of baryon number at any grid zone boundary j.

5.4 Summary

- *The relativistic hydrodynamics of the cosmological quark–hadron transition can be described in terms of a* **multicomponent fluid approach** *in which the dynamics of two* **standard fluids**, *a* **radiation fluid** *and a* **"baryon number fluid"** *are followed simultaneously.*
- *The relativistic hydrodynamical equations for the standard fluids are obtained after coupling the* **Einstein field equations** *with* **conservation equations** *expressed in terms of the total stress energy tensor of the standard and radiation fluids.*
- *The dynamics of the* **radiation fluid** *and the energy and momentum exchanges with the standard ones are followed by means of a coupled system of radiation hydrodynamical equations written using the* **PSTF** *formalism.*
- *The dynamics of the* **"baryon number fluid"** *is followed by means of a relativistic diffusion equation for baryon number in spherical symmetry.*
- *The hydrodynamical equations* **cannot be integrated across** *the phase interface which is here treated as a* **discontinuity surface**. *This forces the use of a particular strategy for the* **solution at the interface**.
- *At the interface junction conditions for the* **metric functions**, *for the energy and momentum of the* **standard fluids** *and of the* **radiation fluid** *as well as a continuity equation for the* **net baryon number flux** *need to be solved. The junction conditions are derived following the* **Singular Hypersurface Method**.
- *The* **underdeterminacy** *of the weak deflagration describing the motion of the phase interface can be eliminated by specifying an* **extra condition**. *A convenient expression for this can be derived in terms of the* **energy flux** *and the* **hydrodynamical flux** *across the interface.*
- *Since weak deflagrations are* **subsonic**, *it is particularly important to have a* **correct causal treatment**. *This can be accomplished by means of* **characteristic scheme** *involving the solution of the hydrodynamical equations written as ordinary differential equations along characteristics curves.*
- *The* **characteristic curves** *in a fluid can be associated with the directions in spacetime along which sonic disturbances propagate (forward and backward characteristics) and with the fluid flowlines (advective characteristic).*

Chapter 6

Numerical Strategies and Results

In all of the previous chapters we have presented and discussed the basic structures and the formal details of a new general relativistic multicomponent fluid formalism in spherical symmetry. Such a formalism allows for a consistent description of a relativistic fluid consisting of a number of component species with different interaction scales and interaction types. The different components can exchange energy and momentum on the relevant length scales and could be affected by peculiar kinematical properties such as diffusion. Special attention has also been paid to the possibility of introducing, besides the continuum hydrodynamical equations, a careful treatment of a subsonic relativistic discontinuity surface moving as a weak deflagration. We have finally pointed out the relevance of such a mathematical apparatus for the study of the relativistic hydrodynamics of the cosmological quark–hadron phase transition, in which the dynamics of bubbles and drops and the long range energy and momentum transfer represent important features to investigate.

In a sense, all of the previous chapters could be considered as *introductory* to the present one, in which the formal and theoretical framework finds concrete applications in the numerical computations of the hydrodynamics of the cosmological quark–hadron transition under several physical conditions. In the following, we firstly discuss the numerical strategies that have been introduced in order to solve the hydrodynamical equations and secondly present the results obtained from such calculations and comment on their influence on the cosmological scenario after the transition.

6.1 The Basic Codes

For following the growth of an isolated spherical hadron bubble and the evaporation of an isolated spherical quark drop, we have written a number[1] of hydrodynamical codes, which represent an extended evolution of a previous relativistic code developed by Miller and Pantano [114]. Indeed, the number of new routines and strategies introduced effectively make the new codes rather different from the original one on which they were modelled. The new codes have been produced over the last four years, following the logic of the research project in which we have been involved and each new code represents a further development of the previous ones and allows for a numerical solution either of new equations or of "almost" the same set of equations but under different physical conditions. In particular, the different codes have been implemented for studying

i) Bubble dynamics and long range energy and momentum transfer during the growth of an isolated spherical hadron bubble (Rezzolla and Miller [137], Miller and Rezzolla [115]).

ii) The evaporation of quark drops at the end of the cosmological quark–hadron transition and the stability of the analytic solutions for a self similar evaporating system (Rezzolla et al. [139]).

iii) Drop dynamics and radiation decoupling during the final stages of the evaporation of a cosmological quark drop (Rezzolla and Miller [140]).

iv) Baryon number segregation produced during the very final stages of the quark–hadron transition by evaporating quark drops (Rezzolla [145]).

All of codes make use of a composite numerical technique in which a standard Lagrangian finite-difference method is used to solve the hydrodynamical equations in the bulk of both phases, while a system of characteristic equations and a set of junction conditions are solved in the grid zones adjacent to the phase interface as this moves across the grid. In particular, we use a spherically symmetric Lagrangian grid having comoving coordinate μ and with its origin at the centre of the bubble or of the drop according to the specific situation under investigation [*cf.* expression (3.10)]. The grid has variable spacing with the width of each zone being twice that of the zone inside it, *i.e.*

$$\Delta\mu_{j+1/2} \equiv \mu_{j+1} - \mu_j = 2\Delta\mu_{j-1/2} \,, \qquad j = 0, \ldots, j_{_G} - 1 \tag{6.1}$$

[1] They are effectively four distinct numerical codes.

where j_G denotes the grid point at the outer edge of the grid. The only exception to the spacing given by (6.1) is made for the two central zones which have equal width (*i.e.* $\Delta\mu_1 = \Delta\mu_2$) as necessary for the regridding routines which we will discuss in the next subsection. This exponential arrangement of the grid spacing has a number of advantages. Firstly, it allows to perform numerical computations of bubble expansion or drop contraction through many orders of magnitude change in radius and with only minimal memory expenses. Secondly, it provides a natural solution to the problem of the acoustic disturbances produced by the subsonic deflagration front we evolve in time and that could induce instabilities when reflected by the edge of the computational grid. With our grid choice, in fact, the acoustic disturbances are always contained within the grid.

The numerical integration is made following a standard explicit *Two-Level* finite difference scheme (May and White [108], Richtmyer and Morton [147], Potter [132], Oran and Boris [125], Miller and Pantano [114]) which is suitably modified in the grid zones adjacent to the phase interface for implementing the characteristics based solution. This scheme is *second order accurate* in the time step and makes use of a staggered grid which enables the calculation of time-centered derivatives together with the space-centered derivative on each time slice. In Figure 6.1 we give a schematic picture of the spacetime structure of our computational grid. Note the presence of the two staggered grids, with the primary time levels being indicated with horizontal solid lines and integer numbers and the intermediate and shifted time levels being indicated with dashed horizontal lines and non-integer numbers.

As is standard for Lagrangian hydrodynamics, the different variables are evaluated either at *midzone grid points* (indicated with non-integer numbers and crosses on the spatial grids in Fig. 6.1) or at the *zone boundaries* (indicated with integer numbers and circles on the spatial grids) according respectively to their *extensive* or *intensive* nature. In this way, the thermodynamic variables e, p, ρ, w, w_0 and w_2 are calculated as midzone quantities, while u, w_1, R, a, Γ and M are carried as zone boundary quantities. Figure 6.1 is also useful to illustrate the basic logic of the method in centering time derivatives. The diagram, in fact, shows how a midzone quantity evaluated on the primary time level n is evolved to the following time level $n+1$ by making use of the spatial derivative evaluated at the $n + 1/2$ time shifted level (solid arrowed lines). Similarly, a zone boundary quantity evaluated on the secondary time level $n + 1/2$ is evolved to the subsequent time level $n + 3/2$ by making use of spatial derivatives evaluated at the time level $n + 1$ (dotted arrowed lines).

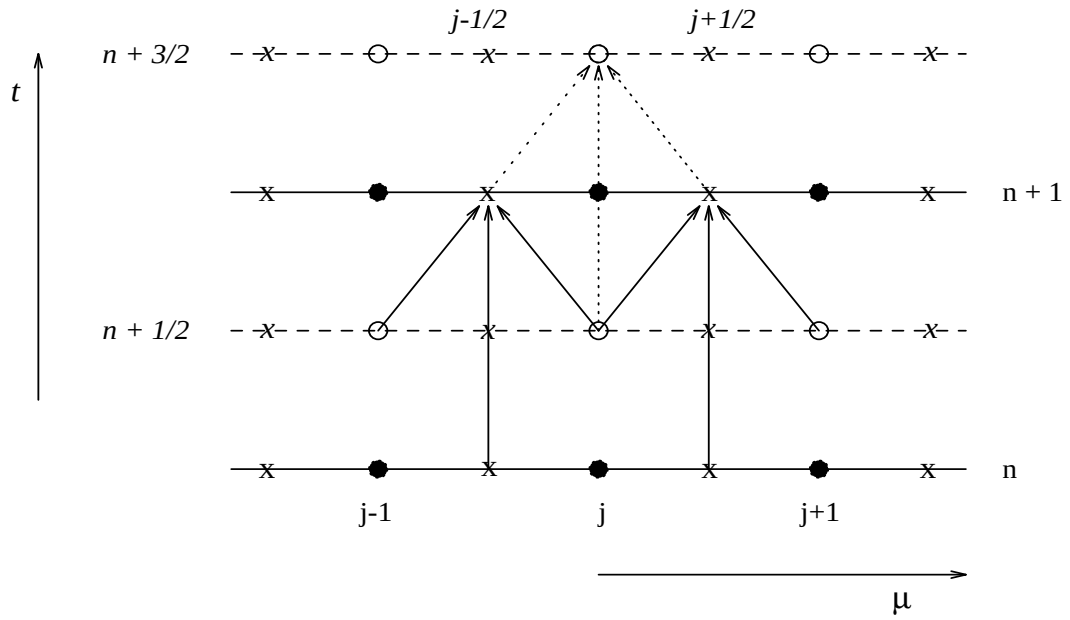

Figure 6.1 Schematic spacetime structure of our computational grid. Note the presence of two staggered grids, with the primary one being indicated with horizontal solid lines and the intermediate time-shifted one, being indicated with dashed horizontal lines. *Zone boundary* and *midzone* grid points are shown with circles and crosses respectively, while fundamental time levels are indicated with integer numbers on the right of the diagram and intermediate time levels with non-integer numbers on the left. Also shown with arrows is the typical time evolution strategy for midzone variables (continuous arrowed lines) and for zone boundary variables (dotted arrowed lines).

On each time slice, the set of the hydrodynamical continuum equations is solved in all of the grid zones except those adjacent to the phase interface and limited by the grid points $[j_s - 1,\ j_s]$ and $[j_s,\ j_s + 1]$, with j_s being the grid point closest to the phase interface. For those grid zones, the characteristic method described in Subsection 5.2.4, together with the set of junction conditions presented in Subsections 5.2.1 and 5.2.2 is used, with the characteristic equations being solved according to the spacetime scheme shown in Figure 5.2. Once the solution is known on a time slice, it is then evolved to the following one, with the time step being set by the relativistic generalization of the *Courant condition*

$$\Delta t = k\frac{b}{a}\left(\frac{\Delta\mu}{c_s}\right) = k\frac{1}{4\pi R_s^2 \rho a}\left(\frac{\Delta\mu}{c_s}\right), \tag{6.2}$$

where $k < 1$ is a constant coefficient to be chosen according to the specific features of the problem under examination; in our computations $k = 0.2$. The Courant condition (6.2) is a stability condition and establishes that the computational domain of dependence determined by (6.2) is always larger than its physical domain of dependence or, in other words, that a sonic perturbation cannot propagate out of a grid zone in a single time step.

A detailed description of the sequence in which the different hydrodynamical quantities are integrated in space and evolved in time would require a rather extended discussion which we cannot offer in this Thesis. We therefore limit ourselves to present in the following list just a schematic description of the main steps involved in the numerical solution.

i) w_0, e and ρ are evolved from the time level n to the new time level $n+1$ for all of the midzone grid points $j+1/2$, with $j = 0, \ldots, j_s-2$ and $j = j_s+1, \ldots, j_G-1$. Similarly, R at the new time level is calculated at each grid point j, with $j = 0, \ldots, j_s - 1$ and $j = j_s + 1, \ldots, j_G$.

ii) The mass function M is calculated on the new time level from the origin of the grid up to the grid point $j_s - 1$.

iii) The characteristic equations together with the junction conditions are solved simultaneously in the grid zones $[j_s - 1, j_s]$ and $[j_s, j_s + 1]$, providing at the new time level the values of the interface quantities: $\dot{\mu}_s$, μ_s, R_s, $a^{\pm}$, $M^{\pm}$, $\Phi_b^{\pm}$ $e^{\pm}$, $p^{\pm}$, $\rho^{\pm}$, $u^{\pm}$, $w_0^{\pm}$ and $w_1^{\pm}$.

iv) The metric coefficient a is calculated from the constraint equation on each grid point at the new time level.

v) The calculation of the mass function M on the new time level is now completed from the grid point $j_s + 1$ up to the outer edge at j_G.

vi) The new time step Δt is set according to the Courant condition and the fractional increment in the last time step of the spatial gradients of e and ρ.

vii) The new values of u and w_1 on the shifted time level $n + 1/2$ are evolved to the following time level $n + 3/2$.

viii) The generalized Lorentz factor Γ is calculated on the new time level. The new sequence can now start again from point *i*).

A final comment is reserved for our treatment of possible shocks appearing in the flow domain and about the use of artificial viscosity to handle them. In principle, our characteristic based approach (Subsection 5.2.4) would allow for the *exact* treatment

of any shock possibly produced during the numerical computation. The situation, in this case, would be much more simple than the one discussed for weak deflagrations and, being supersonic relative to its medium ahead, the shock front could be effectively treated as a strong detonation, with the domain of the dependence of the state ahead being entirely contained in the medium ahead. (see Figures 1.8 and 5.2 for the causal structure of strong and weak deflagrations). However, in order to do this we would need to know the position of the shock when it first forms. Rather than doing this, in the present codes we prefer to handle possible shocks by means of an *artificial viscosity* (Richtmyer and Morton [147]). The basic idea behind its introduction is rather simple and artificial viscosity essentially amends for the fact that non-dissipative hydrodynamical equations are inevitably inadequate to describe physical processes occurring when large compressions in the fluid take place. It is an important feature of the non-linearity of the hydrodynamical equations for compressible fluids that the kinetic energy associated with acoustic disturbances is channelled into progressively higher frequency modes. A natural limit to this process of energy concentration is set by all those "non-ideal" dissipative terms that we here neglect and that suitably convert this kinetic energy into internal energy. Such a conversion, however, cannot take place in the present "ideal fluid" framework, in which the kinetic energy builds up in the highest possible wavenumber mode allowed by the computational grid and corresponding to a wavelength of two zones. In order to avoid this, which has the only effect of rapidly destroying the solution, an artificial viscosity can be explicitly introduced, which is effective only on the largest wavenumber modes and that essentially spreads the discontinuity over several zones of the computational grid.

For the present situations of relativistic fluids in a spherical Lagrangian grid we use an artificial viscosity for the standard fluids originally proposed by May and White [108] and here modified as

$$Q_{_F} = \begin{cases} k^2 (e/\Gamma) \left[(\Delta\mu / R^2) \, (u R^2)_{,\mu} \right]^2 & \text{if} \quad \rho_{,t} > 0 \ , \\ \\ 0 & \text{if} \quad \rho_{,t} \leq 0 \ , \end{cases}$$

where $k^2 = 2$ in our computations. Note that the artificial viscosity operates only if there is a compression and, in this case, $Q_{_F}$ is added to the pressure. In our multicomponent fluid approach, we need to specify an artificial viscosity also for the radiation fluid which, in analogy with the one for the standard fluids, we define as

$$Q_{_R} = \begin{cases} k^2 (1/\Gamma) \left[(\Delta\mu / w_0 R^2) \, (w_1 R^2)_{,\mu} \right]^2 & \text{if} \quad (w_1 R^2)_{,t} > 0 \ , \\ \\ & \text{if} \quad (w_1 R^2)_{,t} \leq 0 \ , \end{cases}$$

and that we could add to the Eddington factor $f_{_E}$ every time a flux of radiation energy takes place from a grid zone. However, experience has shown that the behaviour of the radiation fluid never necessitates of an artificial viscosity and its evolution is always very smooth.

6.1.1 Boundary Conditions and Regridding Techniques

The numerical solution of the hydrodynamical (hyperbolic) equations discussed so far represents a typical *initial value problem* (Press et al. [133]), for which it is necessary to define a starting solution on the initial time slice (*i.e.* the initial conditions) as well as boundary conditions to be imposed at the edges of the computational grid and on each time slice. The definition of the initial conditions could represent at times a "problem within the problem" and it is usually strongly dependent on the type of problem under examination (*e.g.* to whether we are interested in following a hadron bubble growth or a quark drop evaporation). For this reason, initial conditions will be presented in detail in Subsections 6.2.1 and 6.3.1 before discussing the numerical strategies and the results of computations of bubble and drop dynamics.

On the other hand, boundary conditions are more straightforward and do not depend sensitively on whether we are considering bubble growth or drop contraction. For this reason, we always set at the origin of the grid and corresponding to the centre of either the bubble or the drop (*i.e.* at $\mu = 0$)

$$\begin{aligned} M &= 0 \,, & R &= 0 \,, \\ u &= 0 \,, & w_1 &= 0 \,, \end{aligned} \tag{6.3}$$

while, at the outer edge of the grid we impose (*i.e.* at $\mu = \mu_{j_G}$)

$$\begin{aligned} f_{_E} &= 0 \,, & a &= 1 \,, \\ w_1 &= 0 \,, & p_{,\mu} &= 0 = p \,. \end{aligned} \tag{6.4}$$

Note that the choice of setting the metric coefficient a equal to one at the edge of the grid is effectively equivalent to synchronize the coordinate time t with the time measured by a comoving observer at the outer edge of the grid (who is a FWR fundamentalobserver)

In our analysis a fundamental role is played by the dynamics of a phase interface that can either move outward or inward. It is therefore important that the computational grid should always allow for an accurate description of both phases and through a number of order of magnitudes in the dimensions of the disconnected phase. For this purpose, suitable regridding procedures have been implemented so that the solution can always be recast on a accurate enough grid every time this is necessary. Note that regridding can be quite a delicate matter and, if the implementation is not a good one, there is a danger of introducing instabilities into the solution, particularly if function fitting routines are used. With our choice of grid structure, it is possible to avoid the use of any fitting algorithm and solve the problem of the regridding in a simple and very efficient way.

Indeed, we need to implement two different regridding routines according to whether we are studying bubble growth or drop contraction, but the basic logic is the same in the two cases and essentially consists in maintaining constant the number of grid zones within the bubble or the drop as required for maintaining accuracy. In particular, in the case of bubble growth and every time that the phase interface crosses a zone boundary in the outward direction, we merge the two central zones and relabel all of the other zones as

$$\begin{aligned} j &\rightarrow j-1, && \text{with} \quad j = 2, \ldots, j_G \\ j+3/2 &\rightarrow j+1/2, && \text{with} \quad j = 1, \ldots, j_G - 2 \end{aligned} \tag{6.5}$$

(see upper diagram of Figure 6.2). On the other hand, in the case of drop evaporation and every time the interface crosses a zone boundary during its inward motion, a new zone inside the quark phase is created with the central zone being divided into two equal parts and all of the other zones being relabelled as

$$\begin{aligned} j &\rightarrow j+1, && \text{with} \quad j = 1, \ldots, j_G - 1 \\ j+1/2 &\rightarrow j+3/2, && \text{with} \quad j = 1, \ldots, j_G - 2 \end{aligned} \tag{6.6}$$

(see lower diagram of Figure 6.2). This latter strategy maintains intact the structure of the grid (the first two central zones still have the same width, while the others are increasingly spaced) and limits the recalculation of new quantities only to the central zones. However, in the case of drop evaporation, this grid structure leads to the zones immediately outside the drop surface being rather wide since the compression factor in the hadron phase (outside the drop surface) is considerably lower than that in the quark phase. In order to avoid a loss of accuracy due to this, suitable function fitting is carried out in these zones and this turns out to be crucial for the success of the code.

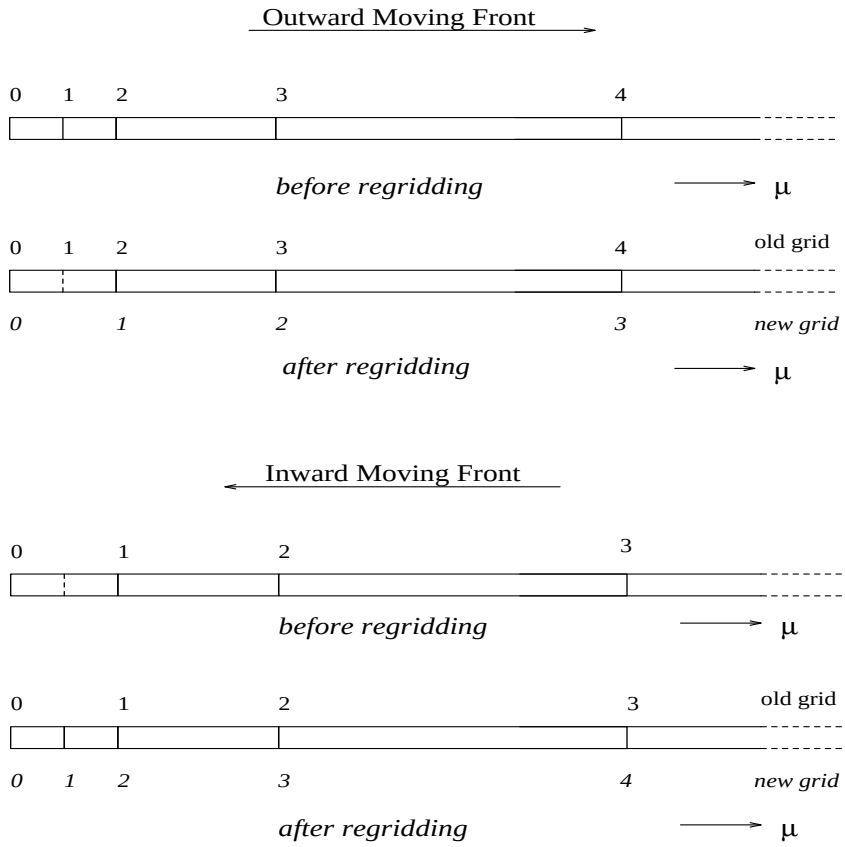

Figure 6.2 Regridding strategies for an outward moving front (upper diagram) used in the case of bubble growth and for an inward moving front (lower diagram) implemented in the case of drop evaporation.

A final important detail to note is that for the relabelling used in the case of bubble growth (6.5), the number of grid zones decreases of one unit every time that the regridding routine is used, even though the spatial extension of the computational domain does not vary. This is different from what happens in the relabelling (6.6) used for a contracting drop. In this case, in fact, the grid would gain a new zone and, in order to keep constant the total number of zones (and thus avoid increases in the computational time), the outermost zone is removed every time the central zone is divided into two. Experience has shown that the loss of information involved in this does not create any problem since the outer edge of the grid is always very distant from the interface.

As a conclusion, the regridding schemes presented here have several advantages: they are extremely simple to implement, they are suitable for use during changes of many

orders of magnitude in the bubble or drop radius and they keep constant the number of zones within the bubble or the drop, hence maintaining resolution and numerical accuracy.

6.1.2 Cancellation Errors and Solutions

The hydrodynamical equations for the radiation fluid presented in Sections 3.3, 5.1.1 and 5.2.4 are general in nature and can be applied to a variety of situations (*e.g.* to spherical accretion onto black-holes, Zampieri et al. [171]). Normally, there would be no problem in doing this but some particular difficulties have arisen when applying them to the present case of bubble growth and drop contraction at the cosmological quark–hadron phase transition. Here, direct use of the radiation equations in the form given above leads to rapidly growing instabilities which destroy the solution. After a series of experiments it was found that the difficulty originates in the very small deviation of w_0 and w_1 away from their initial values during the early part of the evolution and in the fact that the characteristic sound speed in the radiation fluid $(1/3 + f_{_E})^{1/2}$ becomes very close to the sound speed in the standard fluids c_s when the radiation is nearly isotropic in the rest frame of the standard fluids (*i.e.* when $f_{_E} \to 0$). These features lead to production of cancellation errors in the solution of equations (3.18) and (3.19) and near divergences in the characteristic form of the equations (5.122) [the expression $(c_s^2 - 1/3 - f_{_E})$ appears in the denominator of several terms]. Note that the near equality of the sound speeds only arises when the standard fluids are, themselves, relativistic (with $c_s \sim 1/\sqrt{3}$). Also, it is a peculiarity of the situation for bubble growth that, initially, the radiation is nearly isotropic in the rest frame of the standard fluids not because the medium is optically thick on the scale of the bubble but, rather, because of the assumed isotropy of the Universe.

For overcoming the cancellation errors, we have introduced new radiation variables defined as the difference between the energy density, the flux and the shear of the radiation fluid and some reference values (indicated below by the superscript *) with the aim of performing an analytic cancellation of large terms in the equations leaving behind smaller "difference" terms. It turns out to be convenient to take these reference values to be those which would be measured if the only effect were that resulting from the motion of the fluid relative to a uniform radiation field having an energy density equal to that at the time of nucleation of the bubble, $(w_0)_{_N}$. (These are the pure Doppler values mentioned in Chapter 5 and calculated in the Appendix D.) Using a tilde to denote the new variables, we have

$$\widetilde{w}_0 = w_0 - (w_0)^* = w_0 - \left(1 + \frac{4}{3}u^2\right)(w_0)_N \ , \tag{6.7}$$

$$\widetilde{w}_1 = w_1 - (w_1)^* = w_1 + \frac{4}{3}u\Gamma(w_0)_N \ , \tag{6.8}$$

$$\widetilde{w}_2 = w_2 - (w_2)^* = w_2 - \frac{8}{9}u^2(w_0)_N \tag{6.9}$$

and equations (3.18) and (3.19) can then be rewritten as

$$\begin{aligned}(\widetilde{w}_0)_{,t} + a\widetilde{w}_0\left[\frac{1}{R^2}\left(\frac{4}{3}+f_{_E}\right)(uR^2)_{,R} - \frac{3uf_{_E}}{R}\right] + \frac{\Gamma}{aR^2}(\widetilde{w}_1 a^2R^2)_{,R} \\ +a\frac{4}{3R}(w_0)_N\left[f_{_E}(\frac{3}{4}+u^2) - \frac{2}{3}u^2\right]\left[\frac{1}{R}(uR^2)_{,R} - 3u\right] - as_0 \\ -\frac{4}{3}a(w_0)_N G\left[4\pi uR\left(2p - e - \frac{w_0}{3} + 2w_2 - \frac{u}{\Gamma}w_1\right) - \frac{M}{R}\left(2u_{,R} + \frac{u}{R}\right)\right] \\ -\frac{4\pi aGR}{\Gamma}\left(\frac{4}{3}w_0 + w_2\right)w_1 = 0\end{aligned} \tag{6.10}$$

and

$$\begin{aligned}(\widetilde{w}_1)_{,t} + 2\widetilde{w}_1\frac{a}{R}(uR)_{,R} + a\Gamma\left(\frac{\widetilde{w}_0}{3} + \widetilde{w}_2\right)_{,R} + \Gamma\left(\frac{4}{3}\widetilde{w}_0 + \widetilde{w}_2\right)a_{,R} + \frac{3a\Gamma\widetilde{w}_2}{R} \\ -as_1 + \frac{4}{3}a(w_0)_N\Gamma G\left[4\pi R\left(p + \frac{w_0}{3} + w_2 - \frac{u}{\Gamma}\ w_1\right) + \frac{M}{a^2R^2}(a^2R)_{,R}\right] - \frac{8\pi aGR{w_1}^2}{\Gamma} = 0 \ ,\end{aligned} \tag{6.11}$$

where the partial derivatives with respect to μ have been replaced by the equivalent derivatives with respect to R [*i.e.* $\partial/\partial R = (4\pi R^2\rho/\Gamma)\partial/\partial\mu$]. Equations (6.10) and (6.11) are the new radiation hydrodynamical equations for the bulk of each phase; once the "tilde" variables have been computed, the values of w_0, w_1, w_2 can be calculated from (6.7)–(6.9). Note that in (6.10) and (6.11) the radiation variables which are multiplied by G are not transformed according to (6.7)–(6.9). This has been done to keep the expressions in a simpler form and because the contribution of these terms is small under the present circumstances.

Using the new variables, the radiation characteristic equations (5.122) become

$$d\widetilde{w}_1 \pm (\frac{1}{3}+f_{_E})^{1/2} d\widetilde{w}_0 + \mathbf{BU}du + \mathbf{BP}dp + \mathbf{BT}dt = 0, \tag{6.12}$$

where

$$\mathbf{BU} = \frac{a}{\Gamma}\Bigg\{\left(\frac{4}{3}+f_{_E}\right)\widetilde{w}_0 + \frac{8}{3}(w_0)_{_N}\left(\frac{GM}{R} - \frac{u^2R}{3(l+R)}\right)$$
$$\pm 2(\frac{1}{3}+f_{_E})^{1/2}\left\{\frac{2\Gamma}{u}\left[\frac{\widetilde{w}_0}{(1+4u^2/3)} - (w_0)_{_N}\frac{R}{l}\left(1+\frac{4}{3}u^2\right)\right] + \frac{4\widetilde{w}_1}{3f_{_E}}\right\}\Bigg\}, \tag{6.13}$$

$$\mathbf{BP} = \frac{2\Gamma}{\rho w}\Big[\frac{\widetilde{w}_0}{u(1+4u^2/3)} + \frac{2\widetilde{w}_1}{3\Gamma f_{_E}}\left(1-\frac{3}{2}f_{_E}\right) - (w_0)_{_N}\frac{R}{u\lambda}\left(1+\frac{4}{3}u^2\right)\Big] \tag{6.14}$$

and

$$\mathbf{BT} = \Bigg\{(\mathbf{BU})\Big\{4\pi GR\Big[p+\left(\frac{1}{3}+f_{_E}\right)w_0\Big] + \frac{GM}{R^2} + \frac{\Gamma}{\rho w}s_1\Big\} + \frac{2ac_s^2}{\rho w}(\mathbf{BP})\Big[s_0$$

$$+\rho w\left(\frac{2u}{R} - \frac{4\pi GRw_1}{\Gamma}\right)\Big] + a\Big\{\widetilde{w}_0\Big[\Gamma f_{_E}\frac{(3\lambda+2R)}{R(\lambda+R)} - \frac{s_1}{\rho w}\left(\frac{4}{3}+f_{_E}\right) \pm \sqrt{\frac{1}{3}+f_{_E}}\frac{u}{R}\left(\frac{8}{3}-f_{_E}\right)\Big]$$

$$+2\widetilde{w}_1\left[\frac{u}{R} - \frac{4\pi GRw_1}{\Gamma} \pm \sqrt{\frac{1}{3}+f_{_E}}\left(\frac{\Gamma}{R} - \frac{s_1}{\rho w}\right)\right] - \frac{8\Gamma u^2}{9(\lambda+R)}\left[\frac{(4\lambda+3R)}{(\lambda+R)} \mp \sqrt{\frac{1}{3}+f_{_E}}\frac{u}{\Gamma}\right](w_0)_{_N}$$

$$+\frac{4}{3}(w_0)_{_N}\Big\{4\pi G\Gamma R\Big[\left(p+\frac{w_0}{3}+\frac{u}{\Gamma}w_1+w_2\right) \mp \frac{u}{\Gamma}\sqrt{\frac{1}{3}+f_{_E}}\left(2p-e-\frac{w_0}{3}-\frac{u}{\Gamma}w_1+2w_2\right)\Big]$$

$$+\frac{\Gamma GM}{R^2}\left(1 \pm \sqrt{\frac{1}{3}+f_{_E}}\frac{u}{\Gamma}\right) \pm \sqrt{\frac{1}{3}+f_{_E}}s_0\Big\} - s_1\left[1+\frac{(w_0)_{_N}}{\rho w}\left(\frac{8GM}{3R} - \frac{8u^2R}{9(\lambda+R)}\right)\right]$$

$$\mp\sqrt{\frac{1}{3}+f_{_E}}\frac{4\pi GRw_0w_1}{\Gamma}\left(\frac{4}{3}+f_{_E}\right)\Big\}\Bigg\} = (\mathbf{BU})\Big\{4\pi GR\Big[p+\left(\frac{1}{3}+f_{_E}\right)w_0\Big] + \frac{GM}{R^2} + \frac{\Gamma}{\rho w}s_1\Big\}$$

$$+\frac{2ac_s^2}{\rho w}(\mathbf{BP})\left[s_0 + \rho w\left(\frac{2u}{R} - \frac{4\pi GRw_1}{\Gamma}\right)\right] + a\overline{\mathbf{BT}}\,. \tag{6.15}$$

The new form of the radiation junction conditions (5.81) and (5.82) is

$$\left[ab\dot{\mu}_{S}\left(\frac{4}{3}+f_{E}\right)\tilde{w}_{0}-(a^{2}+b^{2}\dot{\mu}_{S}^{2})\tilde{w}_{1}+(w_{0})_{N}\left\{ab\dot{\mu}_{S}\left(1+\frac{4}{3}u^{2}\right)\left(\frac{4}{3}+f_{E}\right)\right.\right.$$
$$\left.\left.+\frac{4}{3}u\Gamma(a^{2}+b^{2}\dot{\mu}_{S}^{2})\right\}\right]^{\pm}=0\,, \tag{6.16}$$

$$\left[\left\{a^{2}\left(\frac{1}{3}+f_{E}\right)+b^{2}\dot{\mu}_{S}^{2}\right\}\tilde{w}_{0}-2ab\dot{\mu}_{S}\tilde{w}_{1}\right.$$
$$\left.+(w_{0})_{N}\left\{\left(1+\frac{4}{3}u^{2}\right)\left[a^{2}\left(\frac{1}{3}+f_{E}\right)+b^{2}\dot{\mu}_{S}^{2}\right]+\frac{8}{3}abu\Gamma\dot{\mu}_{S}\right\}\right]^{\pm}=0\,. \tag{6.17}$$

Note that the characteristic equations (6.12) no longer have terms with $(c_s^2 - 1/3 - f_{E})$ in the denominator but they *do* have terms containing the ratio $\tilde{w}_1/f_{E}$ and these still give rise to numerical instabilities. However, this can be countered by further rewriting the equations in a form in which $\tilde{w}_1/f_{E}$ only appears as the coefficient of expressions which are small when $f_{E} \to 0$. The central point in our strategy consists in isolating the group of terms which appears on the left-hand-side of the fluid characteristic equations (5.121) (and hence tends to zero when $f_{E} \to 0$ and the fluid and radiation characteristics coincide). Details of the manipulation involved are given in the Appendix E. This group of terms can then be conveniently handled using the differences between parameter values at the feet of the fluid and radiation characteristics. The revised form of the radiation characteristic equations (which is the one actually implemented in the code) is

$$d\tilde{w}_{1}\pm(\frac{1}{3}+f_{E})^{1/2}d\tilde{w}_{0}+\mathbf{BU}du-\frac{2\tilde{w}_{1}}{(e+p)}dp+\mathbf{BT}dt$$
$$+\frac{c_{s}}{\Gamma}\left\{\frac{2\Gamma}{u}\left[\frac{\tilde{w}_{0}}{1+4u^{2}/3}-(w_{0})_{N}\frac{R}{\lambda}\left(1+\frac{4}{3}u^{2}\right)\right]+\frac{4\tilde{w}_{1}}{3f_{E}}\right\}\times$$
$$\times\left\{du\pm\frac{\Gamma}{\rho w c_{s}}dp+a\left\{\frac{\Gamma}{\rho w}(s_{1}\pm c_{s}s_{0})+4\pi GR\left[p+\left(\frac{1}{3}+f_{E}\right)w_{0}\mp c_{s}w_{1}\right]\right.\right.$$
$$\left.\left.+\frac{GM}{R^{2}}\pm\frac{2\Gamma u c_{s}}{R}\right\}dt\right\}=0\,, \tag{6.18}$$

where

$$\mathbf{BU} = \frac{a}{\Gamma}\Bigg\{\left[\left(\frac{4}{3}+f_{_E}\right)\widetilde{w}_0 + \frac{8}{3}(w_0)_{_N}\left(\frac{GM}{R}-\frac{u^2R}{3(l+R)}\right)\right]$$
$$\pm\left(\frac{(1/3+f_{_E})^{1/2}}{c_s}-1\right)\frac{c_s}{\Gamma}\left\{\frac{2\Gamma}{u}\left[\frac{\widetilde{w}_0}{1+4u^2/3}-(w_0)_{_N}\frac{R}{\lambda}\left(1+\frac{4}{3}u^2\right)\right]+\frac{4\widetilde{w}_1}{3f_{_E}}\right\}\Bigg\}, \tag{6.19}$$

$$\mathbf{BT} = (\mathbf{BU})\left\{G\left\{4\pi R\left[p+\left(\frac{1}{3}+f_{_E}\right)w_0\right]+\frac{M}{R^2}\right\}+\frac{\Gamma}{\rho w}s_1\right\}$$
$$-\frac{2a}{\rho w}c_s^2\left[s_0+\rho w\left(\frac{2u}{R}-\frac{4\pi GRw_1}{\Gamma}\right)\right]\left(\frac{4}{3}\Gamma u(w_0)_{_N}-w_1\right)+a\overline{\mathbf{BT}} \tag{6.20}$$

and where $\overline{\mathbf{BT}}$ is the same as in (6.15). Note that the last two lines of (6.18) are the terms on the left-hand-side of the standard fluids characteristic equations (5.121).

6.2 Growth of a Hadron Bubble

This section presents the numerical techniques and the results obtained in the computation of the hydrodynamics of a spherical isolated hadron bubble during the initial stages of the quark–hadron transition. The theoretical framework is the one discussed in the previous chapters of this Thesis and involves the study of a multicomponent relativistic fluid composed of a radiation fluid and of two standard fluids, one for each of the phases of the SIM. We first discuss the initial conditions implemented on the zero time slice and then illustrate the tests made and the results obtained.

6.2.1 Initial Conditions

Making use of the experience gained in the earlier work of Miller and Pantano [114], the setting of initial conditions can be quite straightforward. We start with a single supercooled hadronic bubble nucleated in mechanical and thermal equilibrium with its surroundings at a temperature $T_{_N}$ slightly below the critical temperature for the transition T_c. The equilibrium is an unstable one and any perturbation (*e.g.* continuing expansion of the Universe) will cause it to start growing. However, this growth is extremely slow and,

in practice, it is not easy to follow with our code as numerical noise rapidly dominates. Our strategy is then to introduce a small artificial perturbation, decreasing the fluid temperature inside the bubble by a small amount $\Delta T < T_c - T_{_N}$ below its equilibrium value, and analytically tracing the effect of this on related quantities.

We can start with evaluating the perturbed expression for the critical radius of the bubble [*cf.* equation (4.22) with $\tilde{\gamma} = 0$]

$$\Delta R_s = \frac{2\sigma}{[p_h(T_{_N}) - p_q(T_{_N})]^2}\Delta p_h = \frac{8\sigma p_h(T_{_N})}{[p_h(T_{_N}) - p_q(T_{_N})]^2}\left(\frac{\Delta T}{T_{_N}}\right) \ , \tag{6.21}$$

The thermal perturbation is just of second order in the metric coefficient a and in the Γ factor near the interface and these can then be taken as those of a locally flat spacetime (*i.e.* $\Gamma_- = \Gamma_+ = a_- = a_+ = 1$). Next, from the rate equation (5.92), we can calculate the velocity of the interface which, at the first order, is given by

$$\dot{\mu}_s = 4\pi R_s^2 a_+ \alpha_1 \frac{e_h(T_{_N})}{w_+}\frac{\Delta T}{T_{_N}} \ . \tag{6.22}$$

From (6.22) and equation (5.43), the velocity immediately ahead of the phase interface can be calculated as

$$u_+ = [b_-(T_{_N}) - b_+(T_{_N})]\dot{\mu}_s \ , \tag{6.23}$$

while for the whole flow region outside the hadron bubble we can impose the *solenoidal flow* condition

$$uR^2 = \text{const.} = u_+ R_s^2 \ , \tag{6.24}$$

which is exact in the case of an incompressible fluid and represents a very good approximation in the present case. The condition (6.24) is applied out to the point where the value for u given by this becomes less than that for the background Universe, which is taken to follow the spatially flat Friedmann-Robertson-Walker solution [*i.e.* obtained from (5.17) for $\Gamma \approx 1$]

$$u = \left(\frac{2GM}{R}\right)^{1/2} \tag{6.25}$$

and which effectively expresses the *Hubble expansion law*. It is reasonable to take the fluid inside the bubble as not dynamically affected by the thermal perturbation and therefore at rest [*i.e.* $u(R < R_s) = u_- = 0$]. The initial conditions for the standard fluids can

be finally completed by establishing the values of the compression factors on the whole spatial grid, which, under the hypothesis of uniform compression, can be derived from those immediately ahead of and behind the phase interface. From the junction condition for the energy of the standard fluids (5.74) expanded at first order it is possible to write

$$\rho_- = \rho_+ \eta \left[1 + \frac{1}{2} b_-^2 \dot{\mu}_s^2 \left(\frac{1}{\eta} - 1 \right) \right] , \tag{6.26}$$

where

$$\eta = \frac{(e+p)_-}{(e+p)_+} = \frac{g_h}{g_q} \left(\frac{T_h}{T_q} \right)^4 . \tag{6.27}$$

Note that the condition (6.26) can be solved only after the value of ρ_+ has been fixed; indeed, there is freedom in this (the compression factor is just a *relative* measure of compression) and we choose to set $\rho_+ = 1$, in line with the discussion of equation (5.6).

The last quantities to define on the zero-time slice are those relative to the radiation fluid. However, since at this stage the radius of the bubble is small compared with λ, the radiation fluid is not significantly affected by the thermal perturbation and remains uniform and isotropic in its own frame. The initial conditions for w_0, w_1, w_2 (measured in the rest frames of the standard fluid) are then those calculated from the Doppler formulae discussed earlier and presented in the Appendix D [*i.e.* equations (5.161)–(5.163)]. These finally complete the definition of the initial data, whose time evolution can start in a smooth and consistent way and will produce the solutions which will be discussed in the next subsection.

6.2.2 Tests and Results

As usual in numerical computations, the construction of the computer code has been followed by a series of tests to eliminate errors and verify that the strategies used were satisfactory. One important test consisted in turning off the source functions and checking that the computed values of the radiation variables agreed with the analytical Doppler expressions. This revealed the problems discussed earlier. When these had been satisfactorily solved, the source functions were then turned on again and complete runs of the code were carried out. As the radius of the bubble increased (leading to increased coupling between the radiation and the standard fluids on relevant length scales) care was required as increasingly steep gradients of w_0 appeared in the vicinity of the interface

prior to complete coupling. Since structure on a scale smaller than the grid spacing can obviously not be resolved, it is necessary to be ready to switch on complete coupling in the equations at the appropriate moment. Some experimentation was required in order to do this in the best way. When this had been done, further tests were carried out in order to examine the sensitivity of the results to changes in the physical parameters and assumptions. In the following, we will first present results for a set of "standard" parameter values and then discuss the effect of varying some of these.

In Figures 6.3 and 6.4, we show results from a run with $T_C = 150$ MeV, $\hat{T}_N = 0.98$, $\sigma_0 = 1$, $\alpha_1 = \alpha_2 = 1$ and $\lambda = 10^4$ fm. Following Witten [170], we here measure the relative strength of the surface tension in terms of the coefficient $\sigma_0 = \sigma/T_c^3$. The value which we are taking for this is larger than currently preferred ones but we give results for this case to allow direct comparison with those of Miller and Pantano [114].

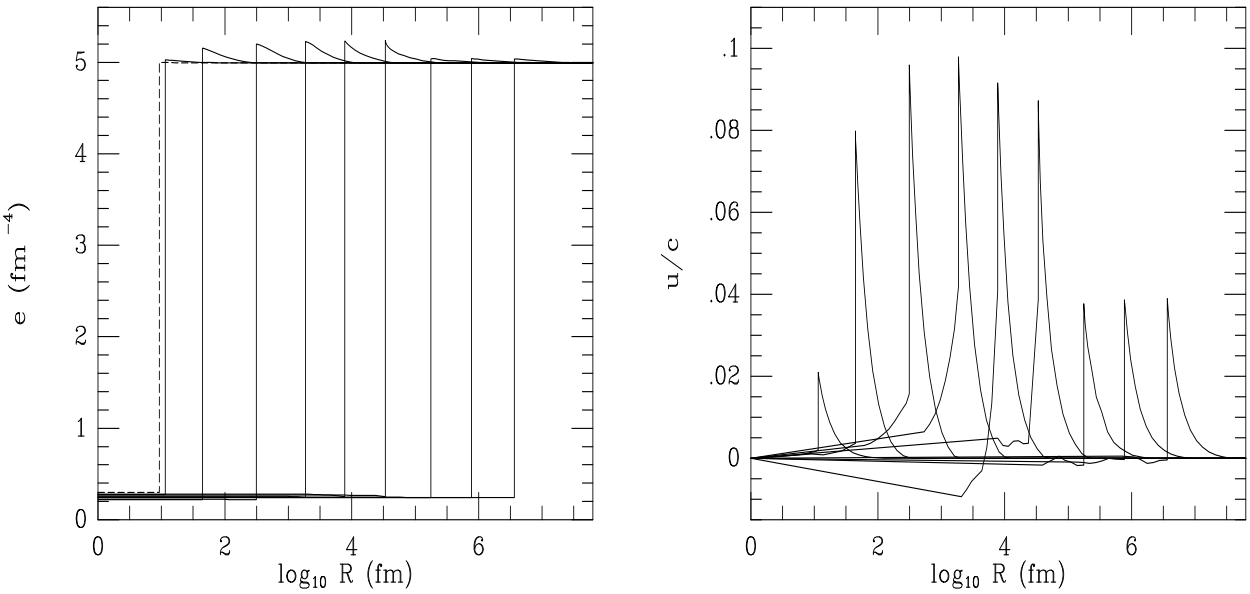

Figure 6.3 Energy density e and radial component of the standard fluid four-velocity in the Eulerean frame u. Different curves are for different times during the bubble growth; the dashed lines represent the values at the initial time. Here $\alpha_1 = \alpha_2 = 1$ and $\lambda = 10^4$ fm. The phase interface is represented by the vertical discontinuity, with the quark phase always being to the right of it and with the different curves referring to different stages during the contraction.

Figure 6.3 shows the behaviour of the energy density e and of the radial component

of the standard fluid four-velocity in the Eulerean frame u at various times during the bubble growth, while Figure 6.4 shows the corresponding behaviour of the radiation energy density w_0 and flux w_1. (Note that for convenience in drawing these figures and the following ones, the values of the variables at the centre of the bubble have been plotted at $\log_{10} R(\text{fm}) = 0$ rather than at $R = 0$.)

During the first part of the bubble expansion (*i.e.* for $R_s \lesssim 10^2$ fm), the standard fluids variables behave in an identical way to that seen previously in the calculation with no radiative transfer: the velocity of the interface progressively increases and a compression wave is pushed out into the surrounding quark medium. The velocity profile in the quark phase is approximately solenoidal (*i.e.* $u \propto 1/R^2$). The radiation variables at this stage have profiles which are almost exactly the Doppler ones produced by the motion of the fluid relative to an essentially uniform radiation field.

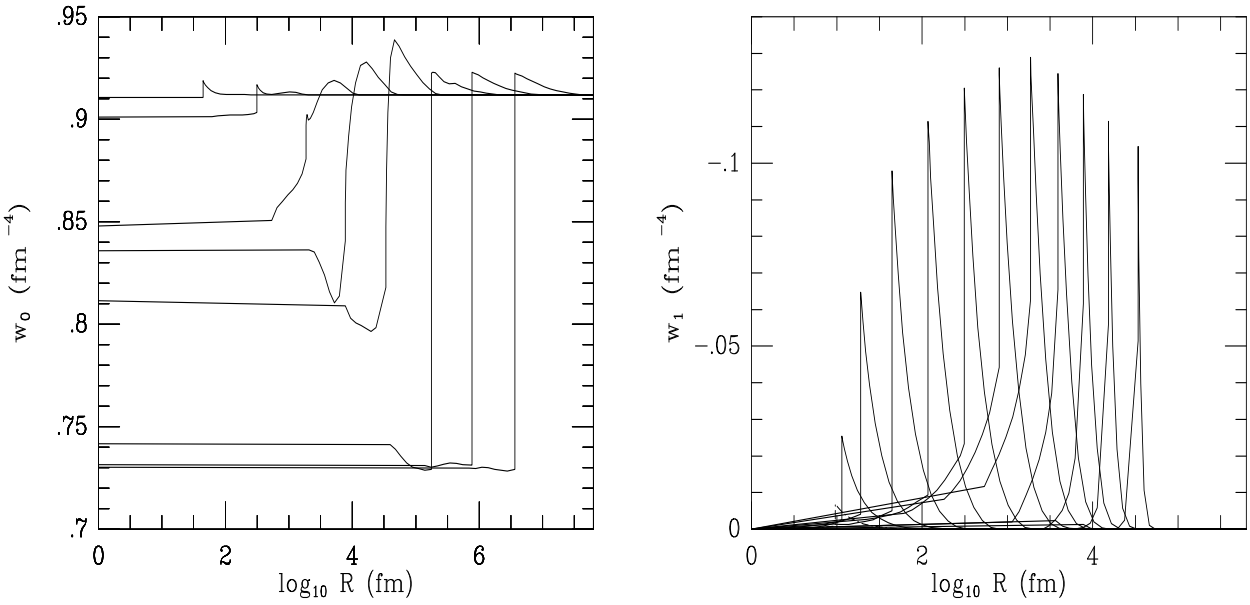

Figure 6.4 Radiation fluid energy density w_0 and energy flux w_1. Here $\alpha_1 = \alpha_2 = 1$ and $\lambda = 10^4$ fm.

In the calculations carried out by Miller and Pantano [114], in which radiative transfer was not included, the standard fluids variables tended towards the similarity solution for a growing bubble (*cf.* discussion in Section 2.2) which was effectively attained for $R_s \gtrsim 10^3$ fm. In the present calculations, the coupling together of the radiation and the

standard fluids (which can be clearly seen in the left diagram of Figure 6.4) starts to be effective before the former similarity solution is fully reached, causing first a distortion of the velocity profile and subsequently a decrease in the peak velocity. (If a smaller value is used for σ_0, both bubble nucleation and the attainment of the similarity solution occur at smaller values of R_s.) As the coupling becomes more complete on the relevant length scales (*e.g.* when $R_s \sim 10^4$ fm), the peak of the radiation flux profile becomes very narrow (the main part of the flux is concentrated exactly at the interface) and when it is no longer possible to resolve this on the grid we switch to total coupling. This involves setting to zero the radiation flux w_1, the Eddington factor f_E and the source functions s_0 and s_1 in the bulk of each phase and augmenting the number of degrees of freedom for the standard fluids at the interface to include also those of the coupled radiation. The behaviour of the radiation at the interface is then included together with that of the standard fluids. Following the total coupling, the variables tend rapidly to the same similarity solution for a growing bubble characterized, however, by smaller velocities (the front now has to push a medium having larger "inertia") and a smaller temperature jump across the interface.

A very important feature to underline again here[2] is that long range energy and momentum transfer out of the disconnected hadron regions is absolutely negligible when the latter have dimensions much smaller than the radiation fluid particles mean free path λ. On the other hand, the radiative transfer is also effectively irrelevant (because the coupling is maximally efficient) when the disconnected regions are much larger than λ. Therefore, the present computations have revealed that the radiative transfer is effective *only* in a rather *short range* in the dimensions of disconnected regions (*i.e.* for $R_s \sim \lambda$). This feature has often been neglected in the literature and has led to models of energy extraction via neutrino flows (Applegate and Hogan [6], and subsequent corrections by Miller and Pantano [113], Bonometto and Pantano [24]) which seem now not to be realistic.

Next, we turn to a discussion of the effect on the results of varying the values taken for some of the physical parameters and, in particular, we concentrate here just on the roles played by the mean free path for the radiation particles λ (whose value, we recall, has an uncertainty of about an order of magnitude), and on the non-conservative scattering coefficient α_2 appearing in the expression (5.21) for the source moment s_0.

The effect produced by varying λ is illustrated in Figure 6.5 (upper diagrams), which shows the behaviour during the bubble expansion of the values of w_0 and u measured just ahead of the interface and just behind it (*i.e.* $w_0^{\pm}$, $u^{\pm}$). The different values of λ used (which are represented with the different styles of line) are 5×10^3 fm (dotted line), 10^4 fm (dashed line) and 10^5 fm (continuous line), proceeding from left to right.

---

[2]See also Subsection 5.1.1.

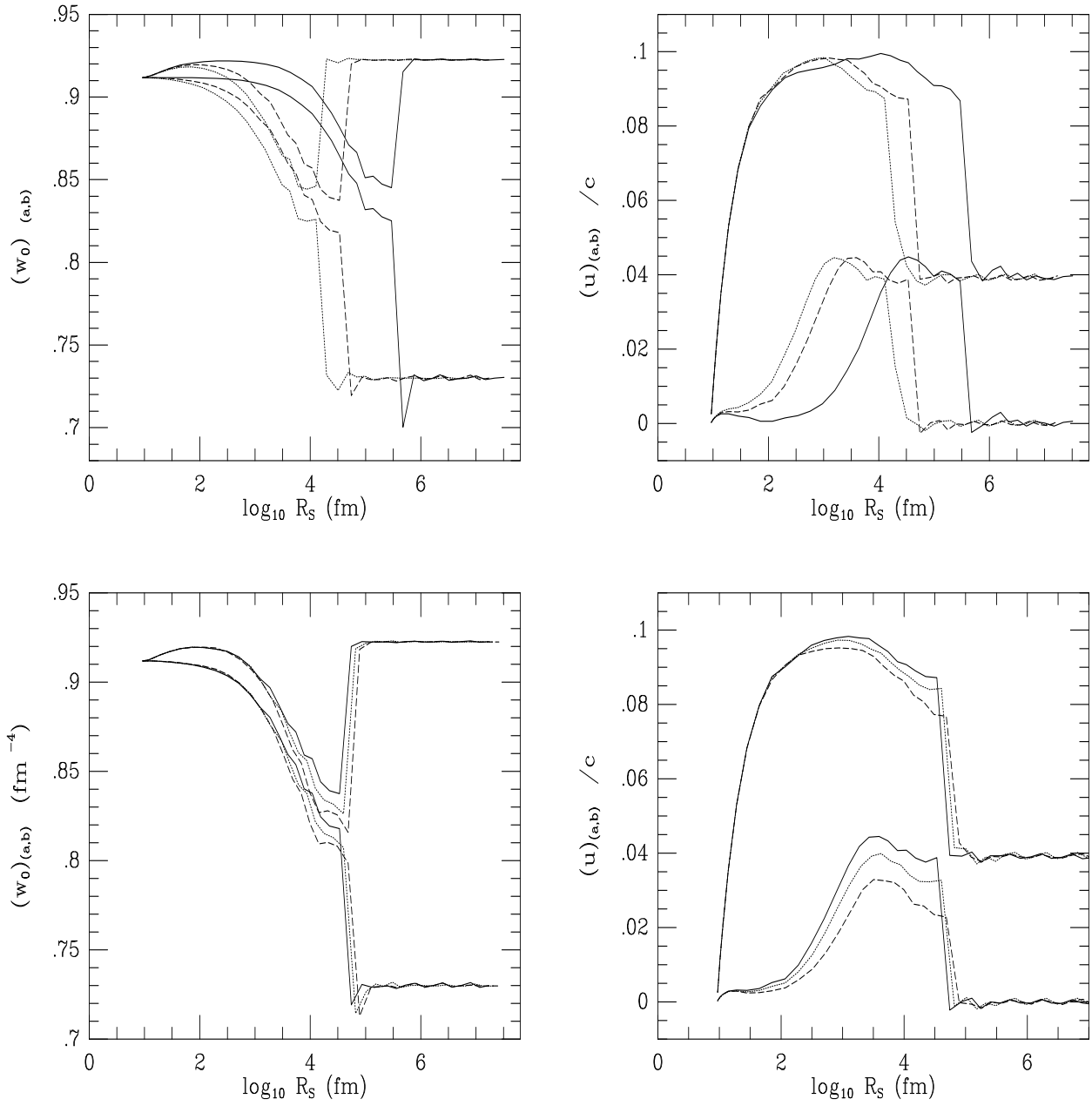

Figures 6.5 – 6.6 Radiation energy density w_0 and standard fluids velocity u just ahead of the phase interface and just behind it (higher and lower curves respectively). The curves are the result of calculations with different values of λ (upper diagrams) and of the non-conservative scattering coefficient α_2 (lower diagrams). R_s is the bubble radius and the curves are plotted so that the hadronic region is on the left of the discontinuity tracing the phase interface.

As one would expect, use of a larger value of λ has the only effect of delaying the coupling between the two fluids, causing it to occur when the bubble has reached a progressively larger value of R_s. Figure 6.6 (lower diagrams), on the other hand, shows the effect of varying the coefficient for the non-conservative scatterings α_2. The different values of α_2 used are 0 (dashed line), 0.5 (dotted line) and 1 (continuous line). Also in this case it is easy to realize that the larger values give an increased efficiency of the energy transfer between the radiation and the standard fluids and make the total coupling occur earlier.

These tests show that although the results can indeed be influenced by different choices of the parameters, there is no serious qualitative change. We have also checked on the sensitivity of the code to the form chosen for the Eddington factor f_E. In our investigation, we have modified the form given in equation (5.27) by replacing the monotonic correction term $\lambda/(\lambda + R)$ with a more sophisticated expression having a maximum whose position and the amplitude could be suitably tuned in different combinations. Paying attention to producing a smooth join between the optically thin and optically thick limits, we have found that reasonable variations in this joining function lead to only minor differences in the results, confirming previous experience (Nobili et al. [122, 123]).

The results of the computations presented here have a double importance. In the first place and from a cosmological point of view, they provide us with very interesting indications on the delicate process of long range energy and momentum transfer taking place during hadron bubble growth. They clearly show the progressive coupling together of the strongly interacting matter and the radiation fluid as the bubble expands. When the complete coupling occurs, there is no dramatic effect on the bubble which simply decreases its expansion velocity and the eventually approaches a similarity solution. Before these results were published, this stage of the transition was rather unclear and discussions of the role of radiative transfer in the extraction of energy out the disconnected hadron regions were often erroneous. (Examples of the misinterpretation of the effects of radiative transfer are found in those models of energy extraction via neutrinos proposed by Applegate and Hogan [6] and partially corrected by Miller and Pantano [113]). On the other hand and more from an hydrodynamical point of view, these computations give a direct proof that the elaborate and theoretical multicomponent fluid approach developed in the previous chapters, is self consistent and can lead to a rather complicated but affordable numerical computation. This "voluminous apparatus" for studying the relativistic hydrodynamics of multicomponent fluid has also found other applications within the quark–hadron transition and these are discussed in the following sections.

6.3 Evaporation of a Quark Drop

The following Subsections 6.3.1–6.4 present the numerical techniques and the results obtained in the computation of the hydrodynamics of a spherical isolated quark drop during the final stages of the quark–hadron transition. While for the hydrodynamics of bubble growth a number of works in the literature (Kurki-Suonio [81], Kajantie and Kurki-Suonio [69], Miller and Pantano [114]) had laid the basis for such a study, the hydrodynamics of an evaporating drop during a cosmological phase transition represented a rather unexplored field prior to our studies, both from the theoretical and the computational point of view. For this reason, the investigation of the final stages of the quark–hadron phase transition, during which the disconnected quark regions evaporate, has required a thorough study which has started with the search for analytical self similar solutions and has ended with complete multicomponent hydrodynamical computations in which two standard fluids, a radiation fluid and a "baryon number fluid" are simultaneously evolved in time.

The first stage of this research has already been discussed in Section 2.3, where the self similar hydrodynamics of a drop has been presented. In Subsection 6.3.2 we present complete hydrodynamical computations which aimed at verifying the validity of the similarity solution for an evaporating quark drop and for which the radiation decoupling was neglected. As a development of this, the following Subsection 6.3.3, introduces the superposed hydrodynamics of the radiation fluid and discusses the effects it has on the final flow properties. This series of investigations is eventually concluded in Section 6.4 with the analysis of the combined contributions of radiation decoupling and of baryon flux suppression to the segregation of baryon number during the final stages of the transition.

6.3.1 Initial Conditions

As mentioned above, the specification of initial conditions in a time dependent calculation can be very delicate and difficult. Sometimes, when there is no obvious physical solution, it can be useful to extract information from the code itself by observing its response to trial initial data. This has been the case with the present calculation, in which the initial conditions (which have turned out to correspond to self similar solutions for an evaporating drop), were originally "suggested" by the code itself. Before initial data based on a self similar solution was implemented, other choices of initial data were observed to relax, after some readjustments, to a solution having a flat density profile and zero velocity within the quark region, and an outward velocity profile falling off roughly as $1/R^2$ in the hadron region. The subsequent evolution of this solution exhibited self similar features and this

then stimulated the investigation for the similarity solution that we have presented in detail in Section 2.3[3].

It is important to stress that it could happen that a self similar solution which is mathematically possible might nevertheless not be realized in practice. In this respect, the weak deflagration similarity solution for a contracting drop has turned out to be strikingly "robust". As a test, initial conditions with an inward-pointing velocity field inside the drop and zero velocity outside, were specified on the zero-time hypersurface. After some excursions, the solution converged towards the corresponding similarity one. Identical results have been obtained also in the case when the solution was started with very irregular and noisy initial conditions.

During the last stages of the transition, the reduced quark volume fraction of the Universe is no longer able to provide the amount of energy necessary to keep the increased hadron volume fraction at the critical temperature for the transition. As a consequence, the temperature of the hadron phase is free to decrease and a small non-zero temperature jump drives the following hydrodynamical evolution of the disconnected quark regions. In view of this, at the time of commencement of our calculations we assume that all quantities have reached a high degree of homogeneity in each phase and then the situation is regulated by the temperature jump between the two phases. All of the variables, except for the fluid velocity u, are therefore taken to have "step-like" profiles. Note that this is consistent with the self similar solution for small supercooling and low interface velocity (see Figure 2.4).

Working within this scenario, we first specify the drop radius R_s and the temperature of the hadron phase T_h so that the corresponding temperature in the quark phase T_q is then calculated from the special relativistic form of the junction conditions (Pantano [128]). The next quantity to calculate is the value of the interface velocity $\dot{\mu}_{_S}$ which is obtained from the rate equation (5.92) as[4]

$$\dot{\mu}_{_S} = -4\pi R_s^2 \rho_+ a_+ \frac{(1+\chi^2)^{1/2} - 1}{\chi} \,, \tag{6.28}$$

where

$$\chi = \frac{\alpha_1 \pi^2 (g_h + g_{_R})}{60} \frac{(T_+^4 - T_-^4)}{(e + p + 4\pi^2 g_{_R} T^4/90)_+} \,, \tag{6.29}$$

[3]When the similarity solutions discussed in Section 2.3 are used for the quark phase, one should replace the energy density e by $(e - B)$ and the pressure p by $(p + B)$ everywhere.

[4]Note that the different geometry for a drop has led us to use here the expression of the rate equation (5.92) with the minus sign. This is the opposite of what was done for a hadron bubble.

and, using the freedom in the choice of reference values for ρ and a, we have set $\rho_+ = a_+ = 1$. Rewriting the junction condition (5.74) as

$$\rho_- = \rho_+ \frac{(e+p)_-}{(e+p)_+} x \ , \tag{6.30}$$

where $x = a_-/a_+$ and combining this with (5.43), it is possible to obtain the following equation

$$x^4 - \left[1 - \left(\frac{b_+ \dot{\mu}_S}{a_+}\right)^2\right] x^2 - \left[\frac{(e+p)_+}{(e+p)_-}\left(\frac{b_+ \dot{\mu}_S}{a_+}\right)\right]^2 = 0 \ , \tag{6.31}$$

whose solution provides the required value for a_- and consequently for ρ_-. The last quantity to calculate is u_-, and the expression for this follows directly from (5.44) with $\Gamma_\pm = 1$, *i.e.*

$$u_- = \frac{\dot{\mu}_S}{a_-}(b_+ - b_-) \ , \tag{6.32}$$

where, following the similarity solution, we have taken $u_+ = 0$ and also for all points inside the quark drop [*i.e.* $u(R < R_s) = 0$]. From the similarity solutions for weak deflagrations shown in Figure 2.4, it can be seen that the velocity profile just behind the phase interface can be well approximated by the solenoidal flow expressed by [*cf.* equation (6.24]

$$uR^2 = \text{const.} = u_- R_s^2 \ , \tag{6.33}$$

and which represents an excellent approximation in the case of small supercooling. Equations (6.28)–(6.25) provide all of the data required on the zero-time hypersurface.

As discussed in Section 4.3, we expect that the degree of supercooling would be rather small and this case is our primary interest. However, in order to gain a good overall perspective of the situation, it is interesting to consider also what would happen if the supercooling were greater and so we have investigated values of $\hat{T}_h$ ranging between 0.999 and the Chapman-Jouguet point ($\hat{T}_h = 0.61$). We found it convenient and satisfactory to continue to specify the initial data as outlined above also in these cases.[5]

[5] At this stage in the writing of his Thesis, the author has become father of Anna (Trieste, August 5th 1996, 2:40 a.m.).

6.3.2 Computations of Self Similar Evaporation

When studying the hydrodynamics of an evaporating quark drop it can be useful to compare this process with the evaporation of a water drop. The main difference between the two situations is that while the first is exothermic, the second is endothermic. This means that the water drop will continue to evaporate as long as there is an efficient transport of heat from the inner regions to the surface where it will be lost during the evaporation. In a similar way, it is important that during the quark drop evaporation there should be an efficient mechanism in the hadron phase for transporting the latent heat away from the phase interface. The geometry of the process and the complexity of the phenomena at the deflagration front prevent any simple but accurate analysis being possible and only a numerical simulation can give a deeper insight into the details of the evolution. The calculations reported here were the first complete relativistic computations of an evaporating cosmological quark drop and have modified and corrected a previous more simplified analysis carried out by Kajantie and Kurki-Suonio [69].

We will first discuss the results obtained for the following combination of values for the free parameters in our model: we consider an initial quark drop of radius $R_{s,0} = 10^5$ fm, surrounded by a hadron plasma at temperature $\hat{T}_h = 0.990$, to which is associated a phase interface with surface tension parameter $\sigma_0 = \sigma/T_c^3 = 1$. (We take $T_c = 150$ MeV.) As expected from the properties of the self similar solution, calculations with larger values for $R_{s,0}$ show exactly similar hydrodynamical behaviour. Also, computations performed with values closer to T_c (*e.g.* $\hat{T}_h = 0.999$) show only minor differences (of the order of a few per cent) after deviation away from the similarity solution has occurred, but are much more time consuming[6]. On the other hand, for greater supercooling, the quantitative differences can be larger (up to 50 per cent), but the underlying hydrodynamical behaviour remains the same. We first discuss the situation for $\sigma_0 = 1$ as this corresponds to the value used in our previous computations (Miller and Pantano [114], Miller and Rezzolla [115]) and also allows one to see clearly the main features of the hydrodynamical scenario. Results for lower values of σ_0 will be discussed later.

During the initial stages of the drop evaporation, the evolution of the hydrodynamical variables in both phases is in very good agreement with the similarity solution. As the evaporation proceeds and the drop reaches dimensions of the order of $R_s \approx 10^2$ fm, the hydrodynamics starts to deviate significantly from the similarity solution (the evolution is no longer scale-free). The surface tension starts to cause the compression inside the shrinking drop to increase, raising the temperature jump between the two phases which has been constant up to this stage. The value of $\hat{T}_h^-$ is not significantly changed by this,

[6]It is worth noticing that the supercooling at this stage of the transition does not need to be extremely small as is the case during bubble percolation and coalescence.

however. This deviation from the similarity solution is at the origin of a run-away mechanism which amplifies the temperature difference between the two sides of the interface and increases the quark evaporation rate. Although the area of the drop surface is reduced, the velocity of the evaporating matter has become larger and this preserves a significant outward flux away from the surface. As a consequence, the contraction is accelerated and the drop experiences an increasingly rapid evaporation which ends with its complete disappearance.

Figures 6.7 and 6.8 synthesize the results from a calculation for a drop contracting from 10^5 fm to 1 fm by showing the time evolution of the energy density e of the standard fluid radial velocity u and of the compression ρ.[7]

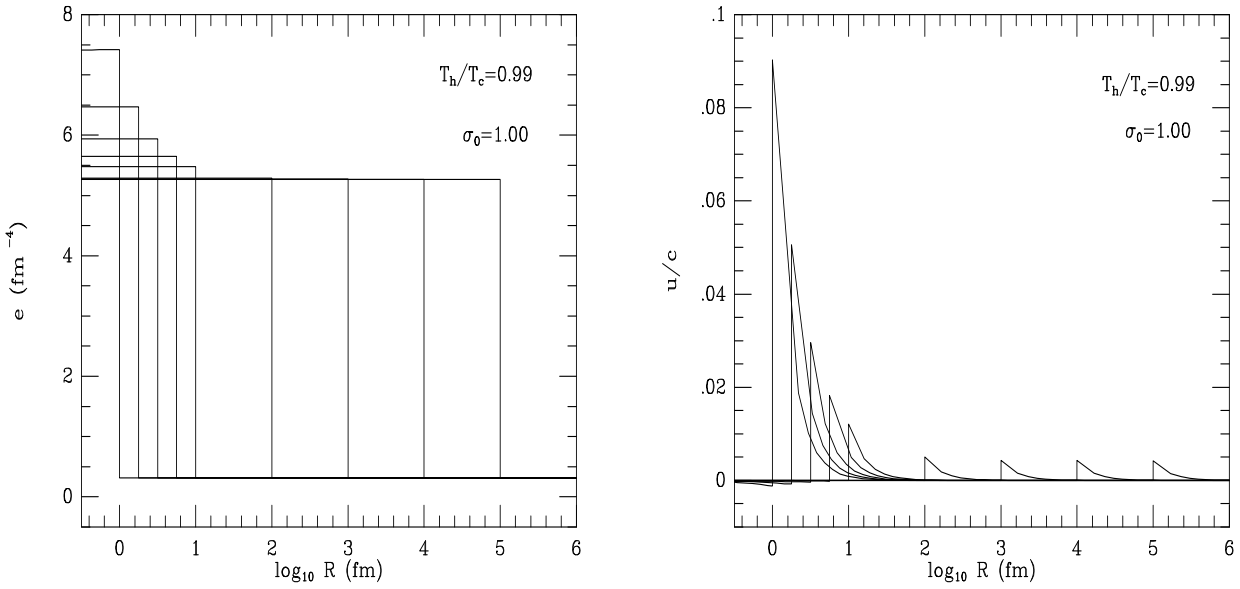

Figure 6.7 Time evolution of the profile of the energy density e and of u. The hadron phase is on the right of the vertical discontinuity. Note that the similarity solution is preserved until to values of the drop radius of the order of 10^2 fm.

In this scenario then, the final stages of the evaporation are not regulated by the expansion of the Universe, as suggested by Kajantie and Kurki-Suonio [69], but rather by

[7]It is important to underline that we here stop our computations at $R_s \approx 1$ fm because at these length scales the whole underlying hydrodynamical approach is ceasing to be valid and our results for the smallest radii should only be treated as indicative. In other words, it is no longer sensible to use a *fluid* description for a quark drop containing only very few quarks.

the run-away mechanism which allows the temperature jump across the phase interface to increase. One way of understanding this process is by taking into account the larger outward flow produced by a higher evaporation rate from the drop surface. This can, in turn, increase the efficiency in the removal of the latent heat released, preventing the temperature in the hadron phase rising above T_c, while allowing the temperature in the quark phase to grow above T_c. The hydrodynamical behaviour described above has been observed for all of the allowed values of the hadron temperature and although the use of lower initial values for $\hat{T}_h$ (to which correspond larger temperature jumps between the two phases) produces a more dramatic and rapid evolution for the shrinking quark drop, all of the results obtained share the above features. A physical lower limit to the values of $\hat{T}_h$ is given by $\hat{T}_h = 0.61$ which corresponds to a deflagration front moving at the sound speed with respect to the medium behind (*i.e.* a Chapman-Jouguet deflagration).

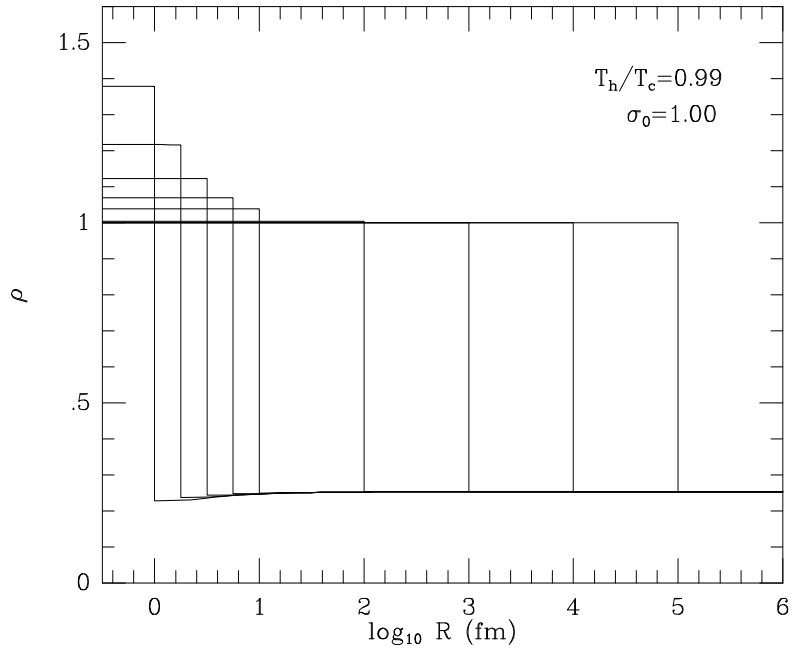

Figure 6.8 Time evolution of the compression factor ρ. Note that during the contraction of the drop from 10 fm to 1 fm, a depression appears in the hadron phase.

The deviation of the hydrodynamical solution away from the self similar one can be seen as a consequence of the existence of a surface tension σ. When the drop dimensions

become comparable with the characteristic length $l \approx \sigma/(e_q + p_q)$, the drop evolution can no longer be considered as scale-free and surface effects start to become dynamically relevant. When σ_0 is taken to be exactly zero, the similarity solution continues to hold all the way down to the complete disappearance of the drop. A numerical computation of this situation has been performed and the self similar solution was preserved with a precision close to the sixth decimal place. If $\sigma_0 = 0.02$, as suggested by recent lattice gauge simulations (Ignatius et al. [65], Iwasaki et al. [65], Christiansen and Madsen [33]), the breaking of the similarity solution starts to become relevant later, for drop dimensions $R_s \approx 10$ fm, with the subsequent evolution following the lines described for the case $\sigma_0 = 1$. A main difference between these two situations is given by the magnitude of the relative change in the hydrodynamical variables as the contraction proceeds. Bearing in mind that the sooner the self similar solution is broken, the more the variables can grow away from their initial values, we report in Table III the total relative change of the most relevant quantities as calculated between the initial value (*i.e.* the value at the time the computation is started) and the final value (*i.e.* the one obtained when $R_s = 1$ fm), for different values of σ_0. A graphical representation of the behaviour of the radial component of the interface four-velocity in the Eulerean frame $u_{_S}$, and of $\hat{T}_{q,h}$ is also given in the two diagrams of Figure 6.9.

Q	$\sigma_0 = 1.00$	$\sigma_0 = 0.10$	$\sigma_0 = 0.02$	$\sigma_0 = 0.00$
$u_{_S}$	12.46	1.22	0.31	2.10×10^{-3}
e_q	0.41	4.01×10^{-2}	8.07×10^{-3}	$< 10^{-6}$
ρ_q	0.38	2.99×10^{-2}	7.90×10^{-3}	$< 10^{-6}$
$\hat{T}_h$	-1.21×10^{-3}	-1.01×10^{-4}	$< 10^{-6}$	$< 10^{-6}$
$\hat{T}_q$	0.11	9.62×10^{-3}	2.30×10^{-3}	$< 10^{-6}$

Table III The relative change ($\Delta Q/Q_0$) of the hydrodynamical variables for different values of the surface tension σ_0. The relative variation is evaluated between the final and the initial values of the relevant variable which is shown in the first column. Here $u_{_S}$ is the radial component of the interface four-velocity as measured by an Eulerean observer. All variations have been calculated for an initial $\hat{T}_h = 0.990$.

One way of looking at the results in Table III is that of considering the self similar

solution as a perfect balance between competing effects. As long as the similarity holds, there is a dynamical equilibrium by means of which the evaporation flux reduces the dimensions of the quark drop without increasing the compression or the energy density inside it (see also Section 2.3 for a discussion of this). When the self similar solution is broken, the balance is lost and the run-away mechanism sets in. Although these very final stages in the life of the quark drop represent only a small fraction of its whole evolution, they can be extremely important since a considerable change in the fluid variables might occur then.

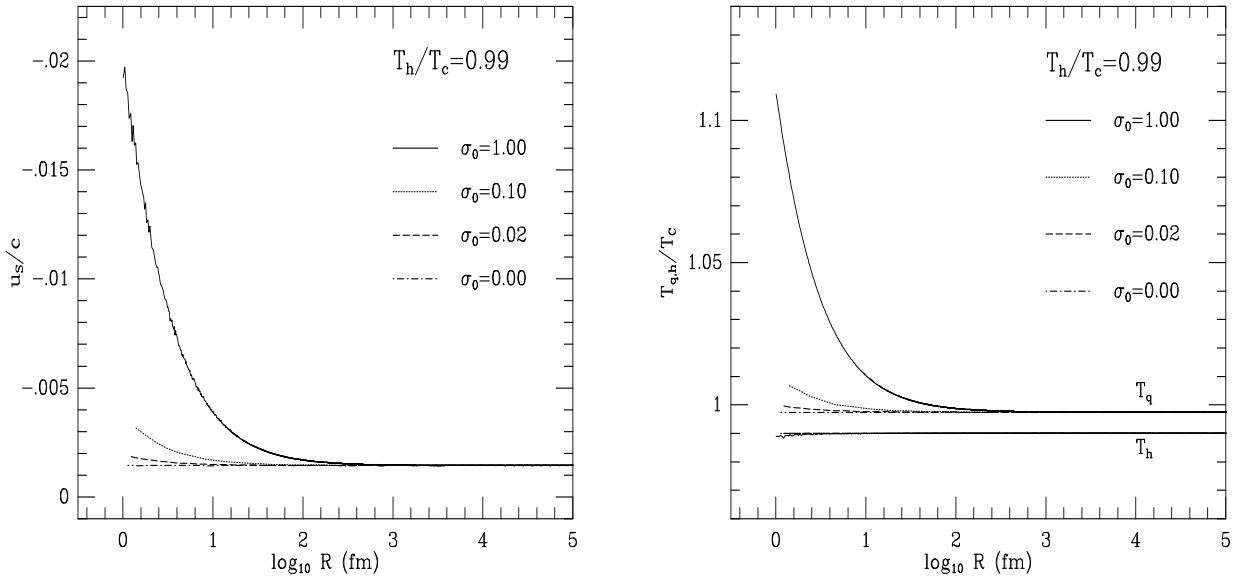

Figure 6.9 Behaviour of u_S and of the temperature in the two phases $\hat{T}_{h,q}$ for different values of the surface tension parameter σ_0. Note that the deviation away from the self similar solution becomes extremely small for smaller values of σ_0.

A comment should be made on the results obtained for low initial values of the hadron temperature (*i.e.* $\hat{T}_h \leq 0.80$). Although these cases probably have no cosmological relevance, as they require a strongly supercooled quark plasma, they provide important information about the hydrodynamics of weak deflagration fronts near the stability threshold given by the *Chapman-Jouguet point*, at which Chapman-Jouguet deflagrations take place. In the present scenario this occurs for an initial value $\hat{T}_h = 0.61$ and has turned out to be the limit for the numerical solution. It is interesting to note, when looking at

the sequence of the different solutions in the range of low $\hat{T}_h$, that the hydrodynamical evolution becomes less stable and regular as values of $\hat{T}_h$ closer to the Chapman-Jouguet point are used. It is particularly interesting to note the behaviour of u_S, which is larger for lower initial values of $\hat{T}_h$. In this case, the presence of oscillating modes is very clear and these can perhaps be related to the instabilities which are known to appear from the linear perturbation analysis of two-dimensional deflagration fronts (Landau and Lifshitz [90], Link [100]). At the Chapman-Jouguet point, the solution is extremely unstable and is almost immediately dominated by instability modes with very large amplitude and very short time scale. As stated before, it was not possible to calculate any numerical solution beyond this limit. Figure 6.10 shows the behaviour of u_S for $\hat{T}_h = 0.80$ and $\hat{T}_h = 0.61$.

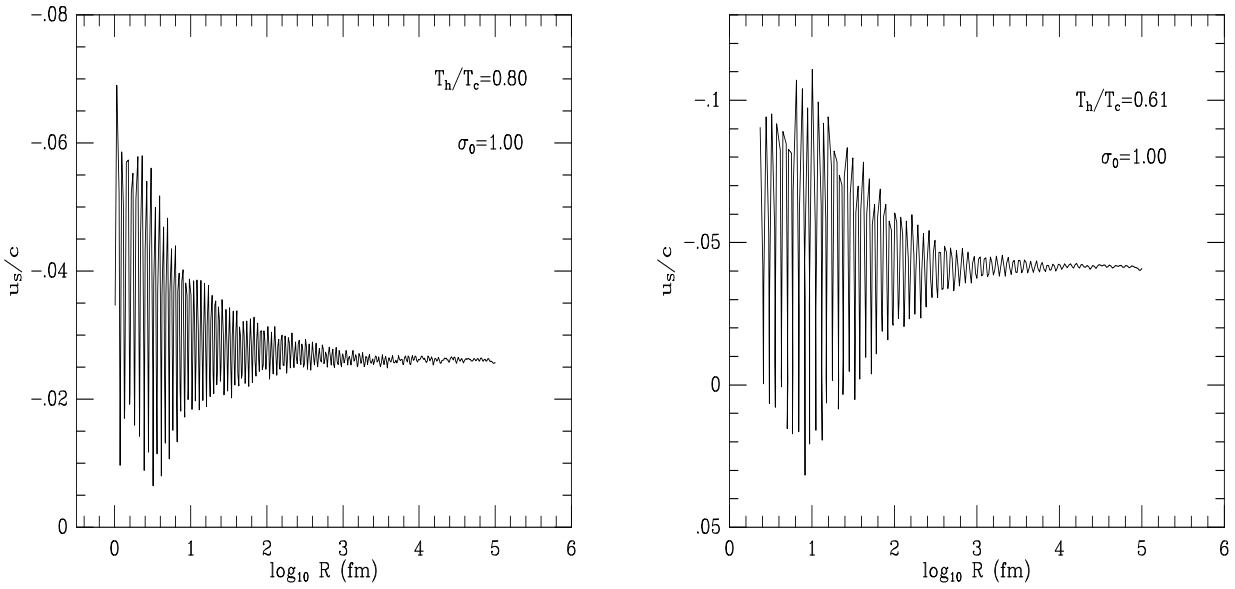

Figure 6.10 Time evolution of the radial component of the interface four-velocity in the Eulerean frame for large supercooling. This should be compared with Fig. 8, where $\hat{T}_h = 0.990$.

It is important to point out that, despite the dramatic oscillatory behaviour seen for u_S at low $\hat{T}_h$, the solution for the other quantities remains comparatively smooth and regular up until the Chapman-Jouguet point, beyond which stability is lost completely. This sort of behaviour seems to be characteristic of deflagrations and is related to phenomena observed in laboratory experiments (Buckmaster and Ludford [26]). The complete loss of stability past the Chapman-Jouguet point (*i.e.* for strong deflagrations), may be related

to the fact that in this case the front ceases to be in mutual causal connection with the fluid behind, relative to which, the front is supersonic.

As discussed in Subsection 5.1.2, much of the astrophysical interest in a first order quark–hadron phase transition concerns baryon number segregation within the shrinking quark drop and the consequent generation of inhomogeneities in the baryon number density. With the present calculations, in which we neglect the effects of long range energy and momentum transfer, we have aimed to establish whether, by means of purely hydrodynamical mechanisms, the contraction could significantly aid baryon concentration. With regard to this, a key result is the demonstration of the existence of self similar solutions which tend to keep constant the values of the compression factor in the two phases. If one makes the (very idealised) assumption that baryon number is carried along exactly with the hydrodynamical flow and limits attention to material which was within the disconnected quark regions at the time when chemical equilibrium was broken, then the baryon number density will be found to follow the same behaviour as the compression factor. As can be seen from Figure 6.8, no strong enhancement of the compression factor seems to appear. For a standard quark drop of $\sigma_0 = 1$ and initial $\hat{T}_h = 0.990$, the relative increase of the compression at the end of the contraction is $\Delta\rho/\rho_0 \sim 0.38$ (see Table III). Slightly larger compressions have been found for lower values of $\hat{T}_h$ (*e.g.* $\Delta\rho/\rho_0 \approx 0.55$ for $\hat{T}_h = 0.80$), but such low values of the temperature seem unlikely to be relevant in the cosmological situation.

Our conclusion is that hydrodynamical compression "on its own" can do little to enhance baryon number concentration. If there is to be a concentration of the magnitude discussed in the literature (Sumiyoshi et al. [155], Malaney and Mathews [101], Cheng and Olinto [31]), then this must result mainly from the role of the long range energy transfer or from suppression of the flux of baryon number across the interface. These will be the subjects of the numerical investigations illustrated in the next two subsections.

A concluding remark could be made about recent calculations performed by Kurki-Suonio and Laine [83] of the very final stages of the evaporation of a quark drop. Using a general framework rather different from the one presented here and which is based on a coupled system of hydrodynamical equations and of evolution equations for a scalar order parameter, the Finnish group was able to reproduce the self similar solution proposed by Rezzolla et al. [139] and the hydrodynamical behaviour described above and to follow the evaporation down to dimensions of the quark drop below the limit of 1 fm presented in this subsection. Although we are skeptical about the validity of a hydrodynamical approach for infinitesimal quark drops, the results of Kurki-Suonio and Laine for the bigger drops represent an important confirmation of the validity of our approach and of the "robustness" of the self similar solution found.

6.3.3 Evaporation with Radiation Decoupling

This subsection presents and discusses numerical computations aimed at following the evaporation of a quark drop, taking into account the progressive exchange of energy and momentum which at a certain stage will take place between the radiation fluid and the strongly interacting fluids. For this purpose, we have here made use of the experience and numerical codes developed for studying the related problems of radiative transfer for a growing hadron bubble (Section 6.2) and of evaporation of a quark drop in the absence of long range energy and momentum transfer (Subsection 6.3.2). The result of this has produced a code which embodies the main features of the previous ones.

The specification of the initial conditions for the system of hydrodynamical equations has been guided by the existence of a self similar solution for an isolated contracting physical system which was demonstrated in Section 2.3. In the case of an evaporating quark drop during the cosmological quark–hadron phase transition, it is reasonable to expect that a self similar solution will first set in after the quark drops become physically disconnected, so that the distance between the centers of two neighbouring drops is larger than the sum of their respective "sonic radii" (see Section 2.3 for a definition). The value of this distance is not yet established and its determination would require a detailed hydrodynamical study of the intermediate stages of the transition, which we consider to be the ones after the hadron bubbles have coalesced and the quark regions have started to become disconnected. Simple geometrical considerations suggest that the mean separation between quark regions at bubble coalescence should be of the order of the mean separation of bubble nucleation sites $l_n \sim 10$ cm [*cf.* expression (4.38)]. Bearing in mind the uncertainty in this, we here take a conservative view and consider a quark drop of initial dimensions $R_{s,0} = 10^5$ fm, much below the above range (but still comfortably larger than λ, by which radius the similarity solution will have broken due to radiation decoupling from the standard fluids). Considering such a small quark drop implies restricting our analysis to the very final stages of the transition, but it is only then that the self similarity is expected to break down and a change in the hydrodynamical evolution is expected to occur.

As initial conditions for the time evolution with the full hydrodynamical equations, we again use the general form of the self similar solutions, which is determined once the degree of supercooling in either one of the two phases has been established. All of the models which we present here refer to a quark drop having initial temperature $\hat{T}_q = 0.998$, surrounded by a hadron plasma at initial temperature $\hat{T}_h = 0.990$. (Results obtained with a smaller degree of supercooling, *e.g.* down to 0.1%, show only minimal overall differences for e, ρ and w_0, always below a few percent).

An important feature of the present simulations is the transition between total cou-

pling of the radiation and standard fluids and their effective decoupling. While in nature this process would take place in a rapid but gradual way, the start of it is necessarily discontinuous when simulated by means of a numerical calculation on a grid. This is just the consequence of the fact that, within the context of a numerical calculation, the concept of the phase interface as a perfect discontinuity surface needs careful interpretation and cannot be considered as strictly infinitesimal. In the present situation, in which the computer code follows the drop evaporation with an increasing spatial resolution through a number of orders of magnitude in radius, the interface should be thought of as having an effective width which is always smaller than the minimum length scale resolvable on the grid. This means that the numerical code will treat as discontinuous any change in the physical variables which cannot be resolved on the grid. This feature is particularly relevant at the decoupling, because at that stage the long range energy and momentum transfer introduces features of the flow on length scales which were not previously resolved when the standard fluids and the radiation fluid were considered as coupled. When the decoupling is allowed to start, the effective width of the phase interface is abruptly decreased to that appropriate for the strongly interacting matter alone and, as a consequence, changes across it which were previously discontinuous are allowed to smooth down and assume the profiles produced by the radiative transfer.

Allowing for the decoupling to start requires particular care and for this reason it has been necessary to introduce a free parameter R_d, referred to as the *"decoupling radius"*, fixing the drop radius at which the change is made from one regime to the other. For drop radii $R_s > R_d$ the two fluids are considered as totally coupled and moving as a single fluid. The phase interface is taken to have a width related to the mean free path of the radiation fluid particles and the characteristics of the radiation fluid are taken to coincide with the ones of the standard fluids. As for bubble growth (*cf.* Section 6.2), the coupling is treated by adding the number of degrees of freedom of the radiation fluid particles to the number of degrees of freedom in the two phases of the strongly interacting matter and by setting to zero the contribution of the source functions s_0 and s_1 and the energy flux w_1. Also, the jump in w_0 at the interface is then calculated in terms of that for e. Conversely, for drop radii $R_s < R_d$ the two fluids are considered as not being totally coupled and the calculation of the radiation fluid variables adjacent to the interface is made using the radiation characteristics which are now distinct from those of the standard fluids. At this stage the radiation fluid evolves separately from the standard ones and long range energy and momentum transfer can start to take place.

It is worth pointing out that while in the above procedure the decoupling between the two fluids *starts* in a discontinuous manner, the decoupling in itself is *gradual* and is governed by the radiation hydrodynamic equations. The abrupt switch is certainly an

approximation but, as discussed in next subsection, it is a rather good one and numerical results show that the hydrodynamical evolution quickly recovers from the perturbation introduced by the sudden decoupling.

The presentation of the results obtained from the numerical integration of the hydrodynamical equations for the radiation and the standard fluids is divided into two subsections. In the first one (A), we present results for a standard set of the parameters of the problem, while in the second one (B) we discuss the changes introduced when these parameters are allowed to vary.

A. The Standard Parameters

As discussed above, we first consider an isolated quark drop of initial radius $R_{s,0} = 10^5$ fm, surrounded by a hadron plasma at temperature $\hat{T}_h = 0.990$ and to which is associated a phase interface with surface tension parameter $\sigma_0 = \sigma/T_c^3 = 1$. We stress that the effects of the surface tension appear only during the very final stages of the evaporation [*i.e.* for $R_s \lesssim \sigma/(e_q + p_q)$] when the effects of the radiative transfer are no longer important. Large values of the surface tension make the very final stages of the evaporation occur more rapidly than for smaller values, and a discussion of this has already been given in the previous subsection (and by Rezzolla et al. [139]).

We consider the phase interface as a perfect black-body (*i.e.* $\alpha_1 = 1$) and the non conservative scattering contribution in the first source function as maximal (*i.e.* $\alpha_2 = 1$). The decoupling radius is related to the mean free path of the radiation fluid particles and we here set $R_d = \lambda = 10^4$ fm.

Figure 6.11 shows the time evolution of the radial component of the Eulerean four-velocity u and the energy density e of the standard fluids. The decoupling is allowed to start at a drop radius of 10^4 fm; as can be seen from the graphs, the solution is not particularly perturbed by the new conditions and quickly returns to a regular behaviour. These graphs are quite similar to the ones presented in Figure 6.7 even though in this case the self similar solution during the contraction is more weakly preserved after the decoupling. When the drop reaches dimensions comparable with the intrinsic length scale $\sigma/(e_q + p_q) \approx 10^2$ fm, the self similar behaviour is irreversibly lost and the evaporation then proceeds through the accelerated stages already observed in the previous subsection. This is related to the contribution of the surface tension which has become overwhelming and produces a compression within the quark phase with a consequent temperature increase.

In this case also and despite the reduced dimensions of the drop surface, the increased

temperature jump between the two phases of the strongly interacting matter is able to preserve a considerable hydrodynamical flux away from the surface, thus allowing for an increasingly rapid evaporation which ends with the complete disappearance of the drop[8].

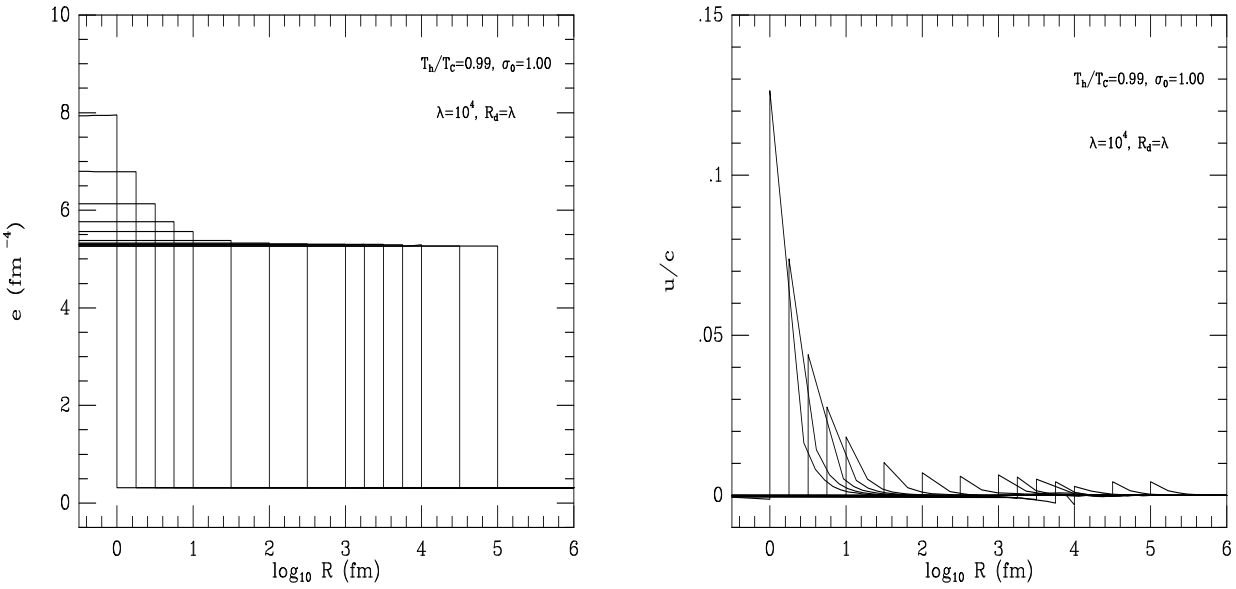

Figure 6.11 Time evolution of u, the radial component of the fluid four-velocity in the Eulerean frame and of the energy density of the standard fluids e. The quark phase is to the left of the vertical discontinuity. The decoupling between the radiation fluid and the standard fluids is allowed to start at $R_s = 10^4$ fm. These diagrams should be compared with those of Figure 6.7

The two diagrams of Figure 6.12 show the time evolution of the radiation energy density w_0 and of the radiation energy flux w_1. Before the decoupling starts, w_0 obviously follows the self similar evolution of the energy density of the standard fluids and the energy and momentum transfer between the two types of fluid is so efficient that they can be considered as in local thermodynamic equilibrium, giving $w_1 = 0$. The situation changes when the drop becomes smaller then 10^4 fm. At this stage the decoupling starts and this has the effect of smearing out the step in the radiation energy density which was present before. Now the radiative transfer is able to carry away some of the energy stored within the radiation fluid in the quark phase.

[8]Note that also for these computations, our results for the smallest radii should only be treated as indicative.

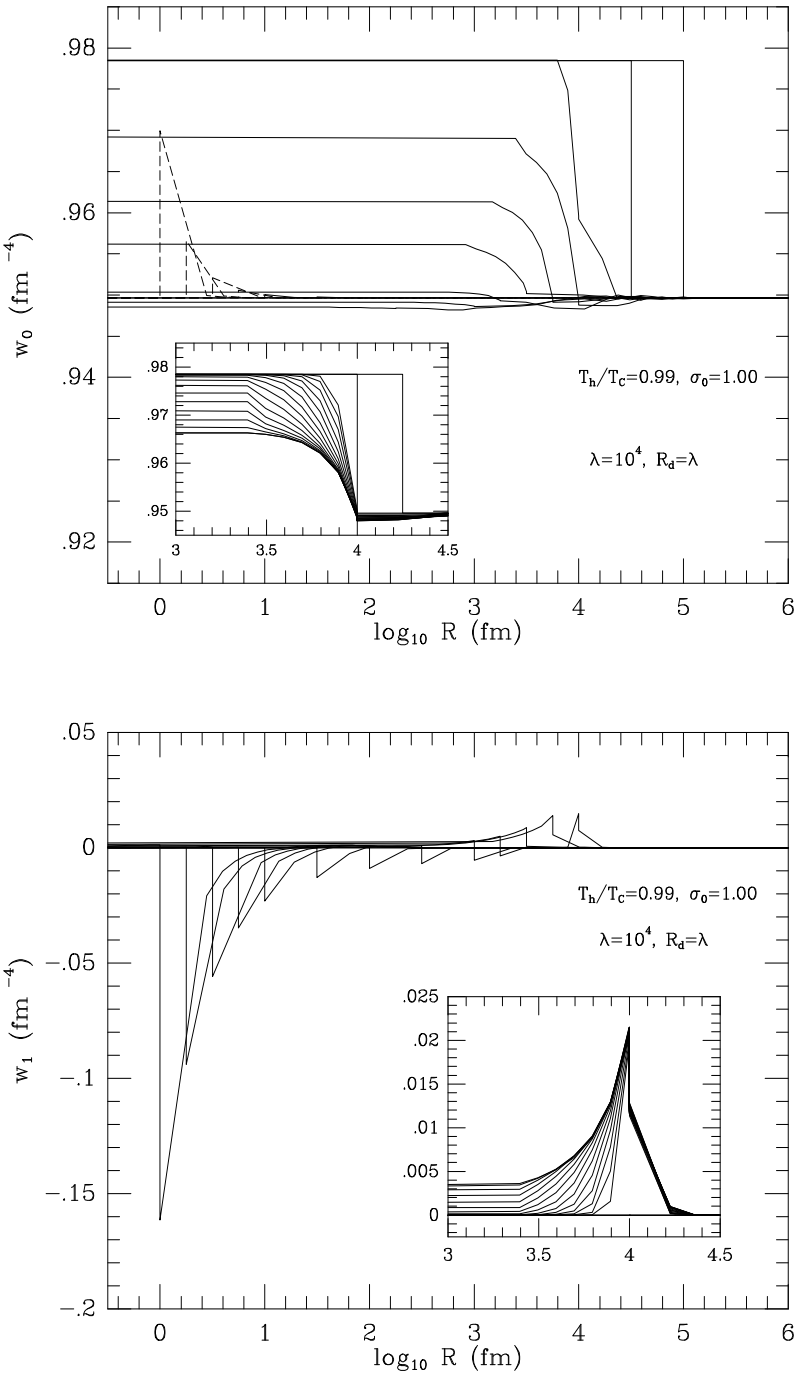

Figure 6.12 Time evolution of the radiation energy density w_0 and energy flux w_1. The dashed curves on the figure for w_0 are the result of dominant Doppler effects at the very end of the drop evaporation. The curves in the small diagrams show the rapid evolution of w_0 and w_1 immediately after the decoupling has started.

As can be seen from the magnifications in the diagrams in Figure 6.12, which show the evolution of w_0 and w_1 immediately after the decoupling has started, this process is quite rapid and before the drop radius has decreased by one order of magnitude, the radiation energy density profile has flattened out, equalizing with the value at infinity. The energy flux w_1 deviates from zero and becomes positive as soon as the decoupling starts and then progressively decays as the step in the radiation energy density is smeared out. This process is somewhat similar to the rapid release of the radiative energy contained within an optically thick, hot but non-emitting gas sphere which suddenly starts to become optically thin and is allowed to emit.

The dashed curves in the upper diagram of Figure 6.12 correspond to the very final stages of the drop evaporation (*i.e.* for drop dimensions of the order of a few fm). The increase in the radiation energy density which is seen there is related to the motion of the Lagrangian observers with respect to an essentially uniform radiation field and therefore has a pure Doppler nature [In the Appendix D we have shown that under these circumstances $w_0 \simeq (1 + 4u^2/3)(w_0)_{_N}$ and $w_1 \simeq -(4\Gamma u/3)(w_0)_{_N}$]. Note that Doppler contributions are always present after the decoupling and are more evident in the energy flux, where they enter at the first order in u and are responsible for the increasing negative flux observed for drop radii smaller than 10^3 fm.

Some of the most interesting effects produced by the decoupling between the radiation fluid and the standard fluids regard the evolution of the compression factor ρ. As discussed in the previous subsection, a key property of the self similar solution is that of preserving the values of the compression factor in the two phases of the strongly interacting matter, reflecting a perfect balance between the competing effects of the compression which would tend to be produced by the reduction in size of the quark drop and the evaporation processes which extract matter from it. An increase in the compression within the quark phase is possible only when the self similar solution is broken and this can occur either when the long range energy and momentum transfer takes place or, later on, when the drop radius becomes comparable with the intrinsic length scale related to the surface tension. If the decoupling between the radiation fluid and the standard fluids is neglected, (as in Figure 6.8), the compression produced is purely hydrodynamical and this takes place only during the very final stages of the drop evaporation. In that case, the relative increase of ρ^+ at the end of the contraction of a standard quark drop with $\sigma_0 = 1$ and initial $\hat{T}_h = 0.990$, was computed to be of the order of 40%.

The situation changes dramatically if the radiative transfer between the standard fluids and the radiation fluid is consistently taken into account. Figure 6.13 shows the time evolution of the compression factor in both phases of the strongly interacting matter (*cf.* Figure 6.8).

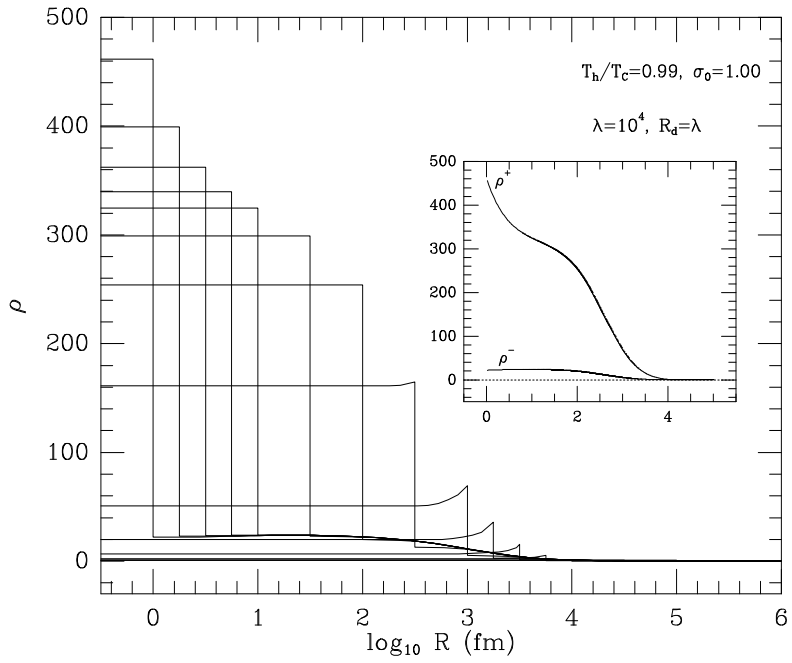

Figure 6.13 Time evolution of standard fluids compression factor ρ. The curves in the small diagram represent the values of the compression factor immediately ahead of the phase interface (ρ^+) and immediately behind it (ρ^-). This Figure should be compared with the corresponding one 6.8, calculated neglecting the radiative transfer.

With the magnified scale it is not possible to see the initial values of the compression factors which are the same as those in Figure 6.8, with $\rho_h = 0.253$ for the hadron phase and $\rho_q = 1.0$ for the quark phase (our reference value). It is evident that as soon as the decoupling is allowed to take place at 10^4 fm, the compression within the quark phase starts to increase progressively and, at the end of evaporation, it has reached values which are more than two orders of magnitude larger (*i.e.* with an increase of $\sim 5 \times 10^4$ %). The small diagram in Figure 6.13 traces the values of the compression just ahead of the phase interface (ρ^+) and just behind it (ρ^-).

The explanation for this striking behaviour is related to the fact that the long range radiative transfer is able to extract energy from within the quark phase without extracting the strongly interacting matter. As a consequence, the relation between the compression factor and the pressure (and hence between the compression factor and the temperature)

is altered and the evaporation evolves in a radically non-adiabatic manner. The main effect produced by the radiative transfer is then that of reducing the specific entropy of the quark-gluon plasma, so that it is possible to enhance the quark compression without significantly changing its temperature.

It is interesting that the growth in the quark compression factor continues to occur also *after* the radiation energy density in the quark phase has been levelled down to the value in the hadron phase and the outward energy flux from the quark phase has become very small (*e.g.* even for $R_s < 10^3$ fm). This is due to the fact that when the energy density of the radiation fluid within the quark phase has reached the same value as in the hadron phase, there is a local temperature difference between the radiation fluid and the quark-gluon plasma which drives a very small but finite energy flux from the quark plasma into the radiation fluid, where it is then redistributed very efficiently. In this way the process of entropy extraction from the quark phase is able to operate even when the outward radiation energy flux from the quark phase is very small.

A limit to this mechanism is, of course, introduced by the intrinsic dimensions of the drop and by the length scale for the interactions of the particles of the radiation fluid. If the drop is too small, it becomes effectively transparent to the radiation particles and the entropy extraction is no longer efficient; at this stage the decoupling between the two fluids can be considered to be *complete*. For the typical quark drop under consideration here, this happens for a drop radius of about 10^2 fm, where the increase in the compression factor temporarily slows down (see the small diagram in Figure 6.13). At this stage the solution would become self similar again, but for the fact that the quark drop is now small enough for the surface tension to take over and dominate the final stages of the evaporation, producing the last compression enhancement. In the next subsection it will be shown that it is possible to recover the self similar solution again after the total decoupling has taken place if a suitable choice of the decoupling radius and of the mean free path λ is made (Figure 6.18).

A special comment should be made concerning a result which we consider to be particularly important. As discussed before, our treatment of the long range energy and momentum transfer between the radiation fluid and the standard fluids leads to an increase in the compression factor of the *quark* phase by about two orders of magnitude. It should be kept in mind, however, that this peak value is limited to a very small volume (of the order of 1 fm^3) and that it would be probably dispersed by the rarefaction wave formed following the complete disappearance of the drop (see Section 6.4 for further discussions). As a consequence, if a relic inhomogeneity from the transition is to be investigated, this should rather concern the compression seen in the *hadron* phase before the disappearance of the drop.

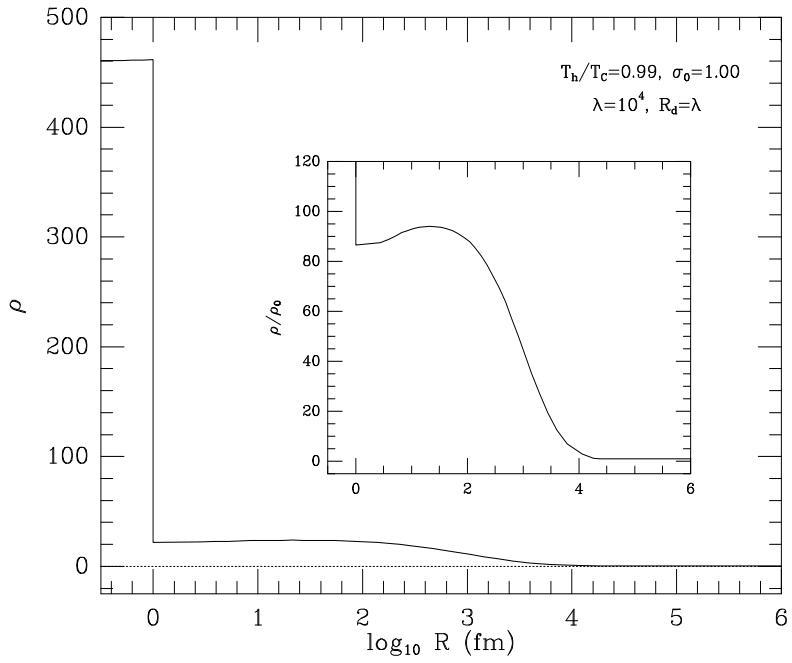

Figure 6.14 Final profile of the compression factor ρ; the computation has been stopped when the quark drop has a radius of 1 fm. The small diagram shows, with a different vertical resolution, the same profile after it has been normalized to the value of the hadron compression at infinity.

Figure 6.14 shows the final profile of the compression factor ρ computed when the quark drop has reached a radius of 1 fm. It is interesting to note that besides the large peak in the quark phase, the compression factor has been increased also in the hadron phase, where it appears as a plateau of comparatively smaller magnitude. However, if one selects a vertical scale with greater resolution and normalizes the values of the compression factor to the background hadron compression (see the small diagram of Figure 6.14), it is clear that the plateau does indeed have an intrinsic profile, with a maximum about two orders of magnitude larger than the background value. More important, the hadron compression extends over a much larger length scale, which coincides with the interaction length scale of the radiation fluid particles. Figures 6.13 and 6.14 could give a misleading impression as they seem to show that the most important effect is the compression increase in the quark phase whereas, in fact, the relative compression increase in the hadron phase is also substantial and is more significant in that it extends over a volume which is twelve orders

of magnitude larger.

The compression increase in the hadron phase is not produced directly by the radiation, but rather results from the fact that "over-compressed" quark fluid elements (with decreased specific entropy) give rise to "over-compressed" hadron fluid elements after they have undergone the phase transformation in accordance with the junction condition (5.74). (Note that the entropy *increase* which naturally occurs as fluid elements cross the phase interface is much smaller than the *decrease* introduced by the radiative transfer, so that fluid elements in the hadron phase near the drop have smaller specific entropy than those far from it). A key point to stress is that the over-compressed hadron plasma is in pressure balance (and therefore in temperature balance) with the surrounding hadron medium. This is a consequence of the decrease of specific entropy which took place while the fluid elements concerned were still inside the drop. At the end of the transition a spherical region of over-compressed hadron plasma is left behind which is in equilibrium with the surrounding medium. This is the region where a baryon number concentration could be produced and this would then only be dispersed by diffusion on the time scale relevant for that. The mechanisms for the production of baryon number inhomogeneities at the end of the transition will be discussed in more detail in Section 6.4.

B. The Parameter Space

In this section we discuss the changes introduced for the drop evaporation by variation of the set of the parameters within the allowed parameter space. The effect of varying σ_0 is in line with what one would infer from the discussion in 6.3.2 and we defer presenting results for this until the next section. We start here by commenting on the hydrodynamical evolution of a quark drop for which the coefficient α_1, which relates the hydrodynamical flux to the thermal flux in the hadron phase, is not equal to unity as in the case of a perfect black-body surface. In general, reducing α_1 has the effect of decreasing the "transparency" of the drop surface to the phase transformation and therefore of slowing down the drop evaporation and favouring the long range energy and momentum transfer away from the quark phase.

Figure 6.15 shows the variation, as a function of α_1, of the compression factors immediately ahead of and behind the phase interface when the radius of the quark drop has decreased to 1 fm (the other input parameters are left unchanged from the values discussed in the previous subsection). While the solid curves fit points obtained by single computations, the dashed curves are an extrapolation of these to values of α_1 for which the computations would have been exceedingly time consuming (the computational time

tends to infinity as α_1 tends to zero).

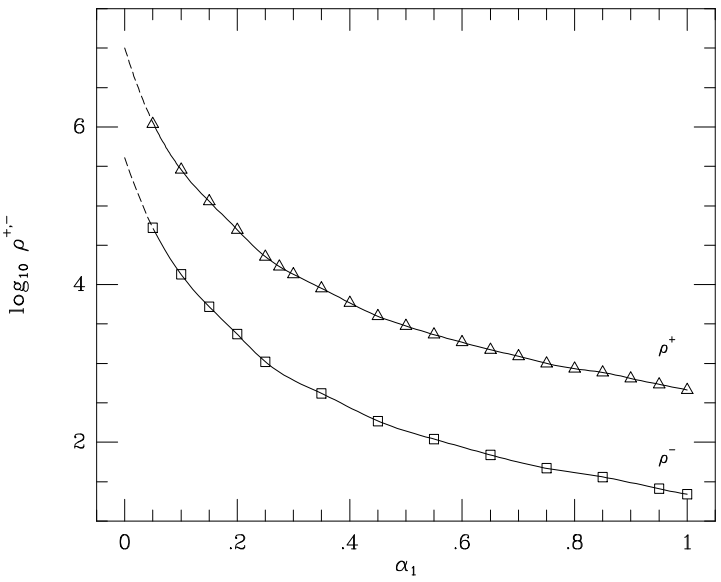

Figure 6.15 Logarithms of the compression factors immediately ahead of and behind the phase interface when the radius of the quark drop has decreased to 1 fm, as a function of the adjustable coefficient α_1. The dashed curves extrapolate the numerical results to very small values of α_1, for which computations are not possible.

It is interesting to notice that the formation of high compressions in the quark and hadron phases is a general feature and that the relative increase of the compression factors in the two phases can easily be of six or seven orders of magnitude, thus giving a stronger cosmological relevance to this process. We also note that the use of values of α_1 less than unity does not significantly alter the qualitative and quantitative evolution of the hydrodynamical variables presented in Figures 6.11–6.14 except for the compression factor, which is suitably rescaled while preserving the same qualitative behaviour.

Let us now consider the changes brought about by variation of the non-conservative scattering coefficient α_2 in the energy source moment (5.21). As mentioned in Subsection 5.1.1, rough estimates indicate that $\alpha_2 \approx 1$ in the present cosmological scenario, but it is nevertheless interesting to consider situations for smaller values of α_2. It is obvious that a larger non-conservative scattering coefficient will enhance the efficiency of the radiative transfer processes and, in turn, the formation of compressed regions of the

strongly interacting fluids.

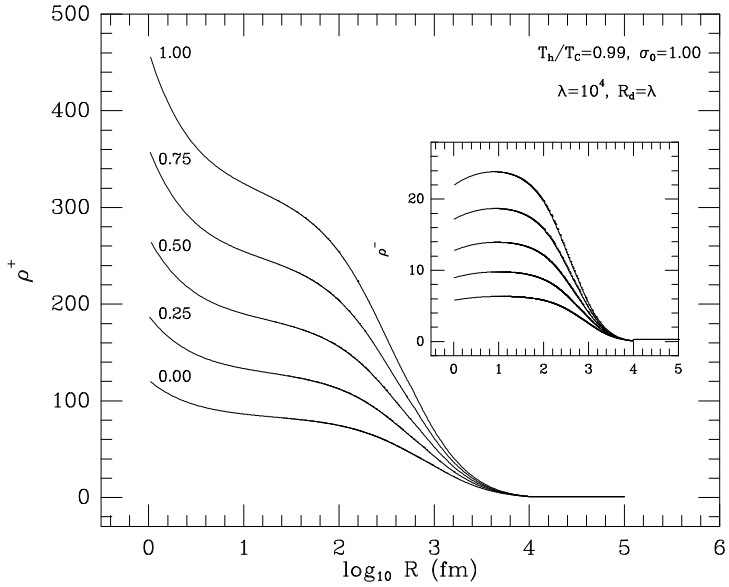

Figure 6.16 Compression factor immediately ahead of the phase interface for computations with different values of the adjustable coefficient α_2. The small diagram shows the equivalent curves for the compression factor immediately behind the phase interface.

As shown in Figure 6.16, where results of computations performed with five different values of α_2 are presented, the hydrodynamical evolution is not qualitatively changed and although a value of $\alpha_2 = 1$ maximizes the compression, a relative compression increase (at the end of the drop evaporation) of about two orders of magnitude is present also in the total absence of the scattering contribution.

All of the results discussed so far are from simulations in which the decoupling between the radiation fluid and the standard fluids was allowed to start at a "decoupling radius" R_d equal to the mean free path λ of the electromagnetically interacting particles. As mentioned in the previous subsection, the decoupling radius is a free parameter which in principle does not represent a precise physical length scale, but rather needs to be introduced as a consequence of having to study the decoupling between the two fluids on a finite grid. In principle, an extremely fine grid would allow one to observe the very gradual onset of decoupling when the drop is still rather large, corresponding to large values of R_d. In practice however, one has to choose a value of R_d which is small enough

to be compatible with a reasonable grid spacing, while still being large enough to give a good approximation to the ideal situation which could be followed with an infinitely fine grid. In order to determine an appropriate value, it is necessary to study the behaviour of a suitable representative quantity in the solution as a function of the different values of R_d.

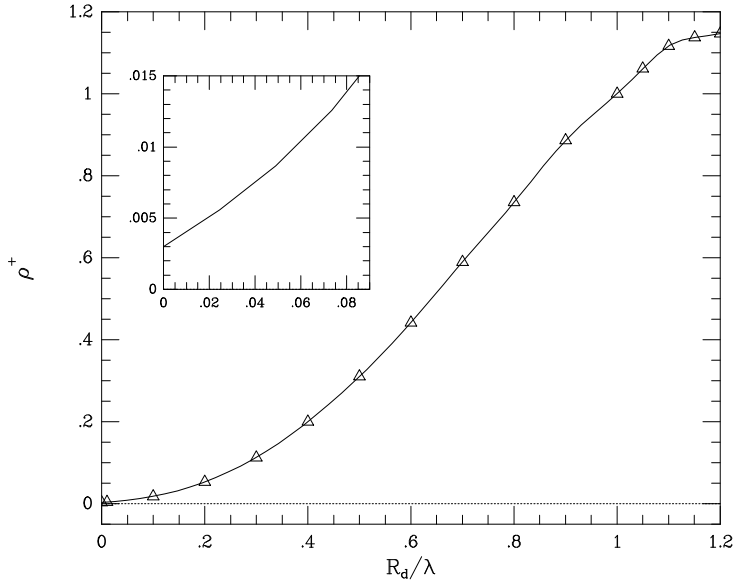

Figure 6.17 Compression factor immediately ahead of the phase interface when the radius of the quark drop has decreased to 1 fm, as a function of the decoupling radius R_d. The vertical axis is normalized to the value of ρ^+ obtained for $R_d = \lambda$. The solid line fits points obtained by single numerical simulations and the small diagram magnifies the results for small values of the decoupling radius.

We chose the quark compression ρ^+ when $R_s = 1$ fm as a suitable representative quantity and Figure 6.17 shows our results for the variation of this with varying R_d. The values of ρ^+ presented in the diagram are normalized to the one obtained for $R_d = \lambda$ and $R_d = 1.2\ \lambda$ is the largest value for which a satisfactory numerical solution could be obtained with our grid. Note the appearance of a plateau in the graph for the largest values of R_d, indicating that the asymptotic solution is being reached. Values of R_d larger than the ones shown here would not lead to any further significant change in the solution. $R_d = \lambda$ gives a more regular behaviour of the hydrodynamical quantities than occurs

for larger values and so this was used for the standard run presented in the previous subsection.

The interpretation of Figure 6.17 is straightforward: making the decoupling at smaller values of the drop radius has the effect of reducing the time interval during which the long range energy and momentum transfer away from the quark phase takes place. As a consequence, the specific entropy in the quark phase is changed less, leading to a smaller final compression. If the value of R_d/λ is taken to be very small, the hydrodynamical behaviour tends to the one observed when the decoupling is totally neglected and ultimately coincides with the solution obtained in Subsection 6.3.2 when $R_d/\lambda = 0$ (see small diagram of Figure 6.17). This is a satisfying result and shows that the numerical modelling has an overall physical consistency.

Another example of this coherence appears when a self similar solution can be recovered after decoupling between the radiation fluid and the standard fluids is complete. This can be produced if λ is artificially increased so as to be much larger than the length scale associated with the surface tension, thus separating the two possible regimes during which a compression can be produced.

Figure 6.18 shows the profiles of the compression factors immediately ahead of and behind the phase interface for values of $\lambda = R_d$ ranging between 10^4 fm (the physically realistic value) and 10^7 fm. (In all simulations the quark drop has initial dimensions $R_{s,0} = 10\lambda$.) It is evident that with the standard set of parameters, (shown with the continuous line), the two different compression growth stages join together and that self similar evolution (represented by a constant compression factor state) cannot set in. The situation is rather different for the (unrealistic) choice of $R_d = \lambda = 10^7$ fm. In this case it is possible to distinguish clearly between the initial compression growth (produced by the relativistic radiative transfer), and the final compression enhancement (a consequence of the accelerated evaporation driven by the surface tension) which in all of the simulations takes place for $R_s \lesssim 10^2$fm. The evolution between the two stages clearly follows a self similar solution and this seems to be a further example of the widespread occurrence of the self similar solution for an isolated contracting spherically symmetric system.

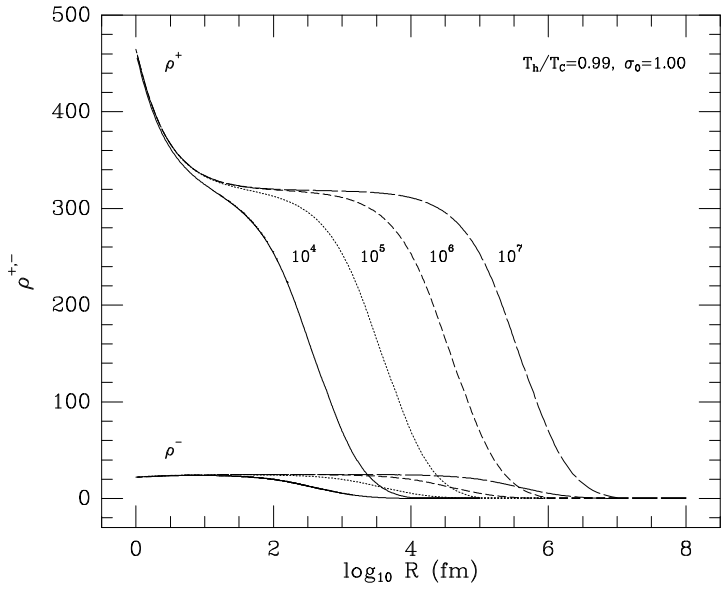

Figure 6.18 Compression factors immediately ahead of and behind the phase interface. Different curves refer to different values of the mean free path of the radiation fluid particles (expressed in fm) and show that if a large enough value is chosen, a self similar evolution is reached. All curves are drawn for $R_d = \lambda$ and initial quark drop dimensions one order of magnitude larger than λ.

A final comment in this subsection should be made concerning the role played by the neutrinos in the process of long range energy and momentum transfer away from the quark phase. Neutrinos have been neglected in the present calculations because of the much larger length scale at which they interact ($\lambda_\nu \approx 10^{13}$ fm). Nevertheless, on this scale they can be considered as particles of a generalized radiation fluid and could operate a radiative transfer process similar to the one discussed so far for the electromagnetically interacting particles and produce a compressed hadron medium at the end of their decoupling.

In order to investigate the amplitude of this compression, we have performed a computation in which we simulate the decoupling between a radiation fluid composed only of neutrinos, and a standard fluid composed of strongly and electromagnetically interacting particles. It should be noted that this is a rather speculative investigation since it assumes the existence of isolated, spherical quark regions of dimensions at least comparable with λ_ν, and it is not clear whether the disconnection of quark regions happens

at a scale large enough for this to occur. However, bearing this reservation in mind, results of our calculations for the effects of neutrino decoupling on the compression profiles are presented in Figure 6.19.

It is evident that entropy extraction by means of neutrinos is less effective than for the case of the electromagnetically interacting particles and this is the result of the different combination of the number of the degrees of freedom in the two cases (for neutrinos $g_\nu = 5.25$ as compared with $g_R = 9$ for the electromagnetically interacting particles). Nevertheless, the decoupling produces a non negligible compression in both phases, giving a compression in the hadron plasma which is about five times greater than the background one.

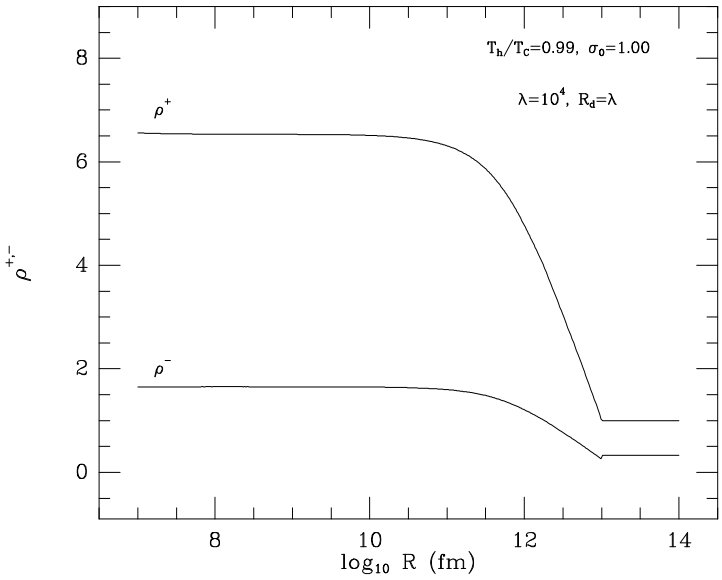

Figure 6.19 Compression factors immediately ahead of and behind the phase interface. Here $R_d = \lambda_\nu = 10^{13}$ fm.

Reduction of α_1 would lead to further amplification of the compression in the same way as already discussed for the decoupling of the electromagnetically interacting particles. This result could be also relevant for considerations of the baryon number density profile which is left behind by the quark–hadron transition and whose formation will be discussed in the next section.

6.4 Baryon Number Segregation at the End of the Transition

We conclude this chapter with the presentation of numerical computations aimed at studying quantitatively the segregation of baryon number at the end of the cosmological quark–hadron transition, as discussed qualitatively in Subsection 5.1.2. For this purpose, we have implemented here all of the formal tools developed in the previous chapters in order to follow simultaneously the processes of entropy extraction by means of particles having long mean free path and the process of baryon number flux suppression at the phase interface. From a computational point of view, the numerical codes presented and discussed earlier for the evaporation of a quark drop have been here modified so as to include the solution the parabolic diffusion equation (5.34) at each time step.

As is frequently the case for numerical computations in which a diffusion equation needs to be solved, we are here faced with the problem of performing calculations with a mixed set of equations and avoiding excessive restrictions placed on the time step by the von Neumann criterion for stability in solving the parabolic equation. Obeying this criterion, which is more stringent than the usual Courant one [*cf.* equation (6.2)] since it depends quadratically on the minimum grid spacing and is inversely proportional to the diffusion coefficient (Potter [132]), allows one to perform an explicit integration of equation (5.168) without any further constraint. However, for the present case, implementing the von Neumann condition produced computational times for each simulation which were not affordable. The reason for this is connected with the particular organization of our grid which has an exponentially increasing spacing in order to facilitate following the dynamics of the drop through several orders of magnitude change in the radius. To avoid this problem, we have implemented a standard "flux limiter" scheme in which a control is set on the diffusive flux in the quark phase preventing it from evacuating the baryon number content of any grid zone within a single time step (Oran and Boris [125]). The results obtained in this way were found to be in excellent agreement with ones from a comparison calculation without the flux limiter and using the von Neumann condition (but which required a computational time longer by a factor of twenty).

Another concern in the present calculations has been that of preserving as closely as possible the overall conservation of baryon number. Clearly, results for the final distribution of baryon number at the end of the transition will be worthless if the integration of the diffusion equation (5.168) is not accurate enough and is significantly producing or destroying baryon number. This equation has been written in a nearly conservative form but special attention needed to be paid to the calculation of interpolated values for a and Γ (for which we used function fitting procedures) and to the implementation of the

regridding procedure (see Subsection 6.1.1). Having done this, our computations preserve the total baryon number in the grid to an accuracy of a few parts in 10^8 for runs of about 10^6 time steps.

In the following and in analogy with what was done in the previous section, we present results from computations which have been performed evolving from initial data given by the self similar solutions for a spherical quark drop with initial dimensions $R_{s,0} = 10^7$ fm, at an initial temperature $\hat{T}_q = 0.998$, surrounded by a hadron plasma at temperature $\hat{T}_h = 0.990$. The similarity solution provides suitable initial conditions for all of the variables apart from the baryon number which does not necessarily follow the bulk hydrodynamical flow. We decided to start with the baryon number density in each phase being uniform and given by the expressions (5.28) and (5.29) presented in Section 5.1.2 which correspond to conditions of chemical equilibrium. This is very approximate because global chemical equilibrium does not apply for a situation with a moving interface such as the one which we are considering but, nevertheless, initial conditions imposed in this way are sufficiently good to allow the solution to relax rapidly to a consistent one.

We have examined the effects on the overall solution of varying the values of important input parameters and we will be discussing this in detail but first we concentrate on the results obtained for a set of fiducial parameter values. This "standard" run follows the evaporation of a quark drop with surface tension parameter $\sigma_0 = 0.01$, filter factor $F = 0.3$ [*cf.* equation (5.83)] and diffusion coefficient $D = 1$ fm [*cf.* equation (5.169)][9]. The decoupling radius R_d is set to be 10^4 fm, which corresponds to the average mean free path of the electromagnetically interacting particles. We do not consider here a decoupling with neutrinos which, however, would follow a similar hydrodynamical behaviour except for the different number of degrees of freedom involved.

The results presented here should be confronted with those for the fundamental hydrodynamics (as discussed in the previous section) which forms the background against which the segregation of baryon number takes place. Equivalent results to those presented in Subsection 6.3.3 but for the present case of $\sigma_0 = 0.01$ are summarized in Figure 6.20. The main features of the hydrodynamical solution can then be synthesized as follows: *i)* the presence of a similarity solution until the radiation decoupling starts at $R_s = R_d$; *ii)* the recovering of an "almost" self similar solution for the energy density e and the fluid velocity u after decoupling; *iii)* the significant increase of the compression factor in both phases caused by the extraction of entropy by the radiation fluid; *iv)* the smoothing out of the step in the profile of the radiation energy density when decoupling occurs.

[9]Note that we here adopt as our reference value for σ_0 a much smaller number than the one discussed in the previous subsection. This is because we prefer here to reduce the effects related to the surface tension and adopt a value closer to the ones derived from current lattice gauge calculations.

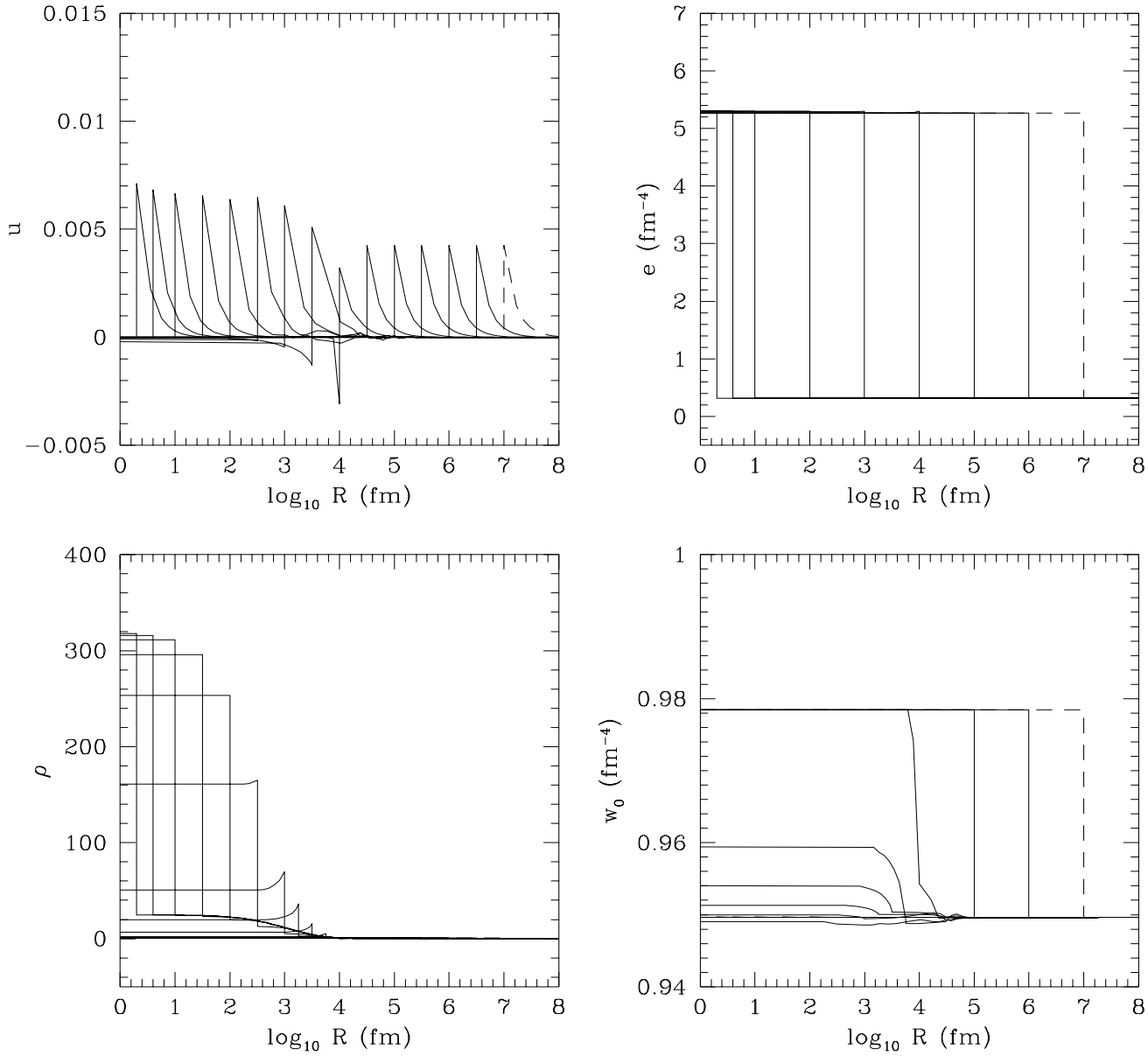

Figure 6.20 Time evolution of the most significant hydrodynamical variables for a surface tension $\sigma_0 = 0.01$. Starting from the upper left-hand window and proceeding clockwise, the frames show: the radial component of the fluid four-velocity in the Eulerian frame u, the energy densities of the standard fluids e and of the radiation fluid w_0 and the compression factor ρ. The decoupling between the radiation fluid and the standard fluids is allowed to start at $R_s = 10^4$ fm.